SYNTHÈSE ET MAÎTRISE DE LA CROISSANCE DE NANOCRISTAUX : APPLICATIONS AUX COMPOSANTS A BASE DE SEMI-CONDUCTEURS A GRANDE BANDE INTERDITE

Eric Vinod Sandana

Thèse Présentée pour obtenir

Le GRADE de DOCTEUR de l'ÉCOLE POLYTECHNIQUE

Discipline : PHYSIQUE

par

Eric Vinod SANDANA

SYNTHÈSE ET MAÎTRISE DE LA CROISSANCE DE NANOCRISTAUX : APPLICATIONS AUX COMPOSANTS A BASE DE SEMI-CONDUCTEURS A GRANDE BANDE INTERDITE

CONTROLLED NANOCRYSTAL SYNTHESIS: APPLICATION TO WIDE BANDGAP SEMICONDUCTORS

Date de soutenance : 28 Juin 2011

Devant le jury composé de :

Michaël Molinari	Président du jury
Gille Patriarche	Rapporteur
Philippe Lecoeur	Rapporteur
Philippe Bove	Examinateur
David Rogers	Examinateur
Henri-Jean Drouhin	Directeur de thèse
Manijeh Razeghi	Co-directeur de thèse

Thèse préparée au Laboratoire des Solides Irradiés (LSI) de l'École Polytechnique en cotutelle
en cotutelle avec le Laboratoire Center for Qantum Devices de Northwetern University, États-Unis

Remerciements

Arrivé au moment de remercier tous ceux qui m'ont aidé et soutenu durant cette thèse, je suis surpris de constater combien ces trois ans ont pu passer si vite. Pourtant, que de chemin parcouru ! Je me dois de commencer par Féréchteh H. Teherani et David Rogers, fondateurs de Nanovation, grâce à qui j'ai passé trois merveilleuses années toujours intéressantes et pleines de surprises. Infaillibles lorsque j'avais besoin d'aide et prêts à me laisser libre quand je le voulais, ils ont toujours fait preuve d'un soutien moral sans faille. On dit souvent qu'une thèse comporte des moments difficiles, mais ça n'est qu'à moitié vrai avec eux ! Si ces trois années ont été si agréables, c'est bien sûr grâce à eux.
Je voudrais aussi dire un grand merci à toutes les personnes du LSI de l'École Polytechnique pour leur accueil. Un grand merci au Professeur Henri-Jean Drouhin qui a accepté d'être mon directeur de thèse, ainsi qu'au Professeur Guillaume Petite et Martine Soyer de m'avoir accueilli au sein de leur laboratoire.
Un grand merci au Professeur Manijeh Razeghi directrice du laboratoire CQD de Northwestern university, pour m'avoir fait l'honneur d'être en cotutelle pour mes travaux de thèse.

Ces travaux démontrent qu'ils sont avant tout le fruit d'une collaboration enrichissante et je tiens à remercier l'ensemble des personnes qui m'ont aidé au cours de cette thèse.
Les analyses ont été effectuées dans différents laboratoires, un grand merci aux personnes qui m'ont aidé à réaliser et à interpréter les résultats.

Au sein du LSI je tiens à remercier Marie-Claude Clochard pour sa formation au FE-SEM, Nadège Ollier et Bruno Boizot pour l'utilisation de la PL. Vincent Metayer pour son aide lors des recuits de mes échantillons et Travis Wade pour la métallisation.
Au sein du CQD, un grand merci à Ryan McClintock, Can Bayram et Binh Minh Nguyen pour leurs aides avec la XRD, la PL et l'AFM.
Un grand merci à Alain Lusson du GEMaC pour son aide avec la PL.
Un grand merci à l'ensemble du groupe du Professeur Teresa Monteiro de Universida de Aveiro pour leur aide sur les caractérisations optiques est notamment la réflectométrie.
Merci au Professeurs Michel Troyon et Michael Molinari du LMEN pour leurs aides sur la cathodoluminescence.
Merci à Anthony Martinez et Abderrahim Raman du LPN pour leur collaboration sur les mesures d'effet Hall.

Je tiens à remercier Vincent Sallet et Farid Falyouni du GEMaC pour la croissance de ZnO par MOCVD.
Un grand merci au Professeur Abdallah Ougazzaden, Simon Gautier et Tarik Moudakir de Georgia Tech Lorraine pour la croissance de GaN par MOVPE.
Merci au Professeur Gérard Demazeau et Alain Largeteau de l'ICMCB pour nous avoir fourni des cristaux de ZnO massif.
Merci à Colin Scott d'Arcelor-Mittal pour nous avoir fourni des substrats d'acier.

L'ensemble des outils de croissance utilisés au cours de cette thèse ont nécessité l'intervention de

nombreuses personnes que je tiens à remercier.
Eléonore Caristan du PICM pour ses conseils avisés au sujet de la mise en place d'une chambre d'évaporation thermique. Merci à Guy Garry de Thales R & T pour son prêt d'une pompe turbo-moléculaire. Merci à Michel Chamberlin, qui m'a tout appris sur le fonctionnement d'un laser excimer et un grand merci à Philippe Bove pour l'ensemble de ses conseils.

Un grand merci au Professeur Philippe Lecoeur de l'IEF et au Professeur Gille Patriarche du LPN pour avoir accépté d'être rapporteur pour mon jury de thèse.

Et je souhaite remercier aussi l'ensemble des personnes que j'ai rencontré au cours de cette thèse, Michel Marceau et Michel Robiolle de Captronic-Jessica France. Un grand merci à Pierre Basséras et Jacqueline Thomas du CFI pour leur soutien.

Un grand merci à l'ensemble des personnes que j'ai rencontré lors des conférences et qui m'ont permis d'approfondir mes connaissances sur mon sujet de thèse. Professeur Lorenz de Universität Leipzig, Professeur David Look de Wright State University, Professeur Yicheng Lu de Rutgers University, Professeur Zhong Lin Wang of Georgia Tech, Professeur Masashi Kawasaki de Tohuku University, Professeur Jean-Jacques Delaunay de Tokyo University et Professeur Bruno Meyer de Universität Giessen.

Et bien sûr un grand merci à l'ANRT qui a contribué au financement de cette thèse.

SOMMAIRE

Liste des abréviations 1
Introduction 3
I Contexte 5
1.1 Avant propos : Nanovation 5
1.2 La PLD, la MOCVD et la PVT 5
1.3 L'oxyde de zinc 11
1.4 Applications à l'optoélectronique 13
1.4.1 Les diodes électroluminescentes 13
1.4.2. Les cellules photovoltaïques 17
1.4.3 Oxydes conducteurs et transistors couches minces 19
II ZnO et ses applications en optoélectronique 23
ZnO Thin Films & Nanostructures for Emerging Optoelectronic Applications 26
Conclusion 37
III Mise en place d'une approche pour la fabrication de ZnO nanostructuré 39
3.1 MOCVD Growth of ZnO Nanowires Using Au Droplets as Catalysts 43
3.2 Comparison of ZnO nanostructures grown using pulsed laser deposition, metal organic chemical vapor deposition, and physical vapour transport 50
Conclusion 60
IV Dépôts de ZnO par PLD pour la fabrication de LEDs et de PVs 61
4.1 Fabrication of Nanostructured Heterojunction LEDs Using Self-Forming "Moth-Eye" Type Arrays of n-ZnO Nanocones Grown on p-Si (111) Substrates by Pulsed Laser Deposition 64
4.2 Morphological and optical studies of self-forming ZnO nanocolumn and nanocone arrays grown by PLD on various substrates 74
4.3 Growth of "moth-eye" ZnO nanostructures on Si (111), c-Al_2O_3, ZnO and steel substrates by PLD 80
4.4 Use of "moth-eye" ZnO nanostructures on Si (111) as templates for MOVPE growth of GaN 88
Conclusion 95
VI Dépôts de ZnO par PLD pour la fabrication de TFT et TCO 97
5.1 Thin film transistors with wurtzite ZnO channels grown on Si_3N_4/SiO_2/Si (111) substrates by pulsed laser deposition 98
5.2 Amorphous ZnO Films Grown by Room Temperature Pulsed Laser Deposition on Paper and Mylar for Transparent Electronics Applications 103
Conclusion 110
Conclusions de ce travail de recherche 111
Etape 1 : Choix d'approche de croissance de nanostructures 111
Etape2 : Etude de la croissance de réseaux de nanostructures de ZnO sans catalyseur sur different substrats 112
Etape 3 : Fabrications de composants 112
ANNEXE I Outils de Caractérisations 115
I.1 Microscopie électronique à balayage 115
I.2 Photoluminescence 117
I.3 Microscopie à force atomique 118
I.4 Diffractométrie de rayons X 121

I.5 Cathodoluminescence 122
I.6 Réflexion spéculaire 124
ANNEXE II Les matériaux semi-conducteurs 125
ANNEXE III Structure de bande de ZnO 127
ANNEXE IV Luminescence d'un semi-conducteur et extraction de la lumière 129
ANNEXE V *Novel Green Light Emitting Diodes: Exploring Droop-free Lighting Solutions for a Sustainable Earth* 139
ANNEXE VI *Epitaxial MOVPE growth of highly c-axis oriented InGaN/GaN films on ZnO-buffered Si (111) substrates* 203

Liste des abréviations

AFM	Microscope à force atomique
Al_2O_3	Saphir
AMLCD	Ecran cristaux liquides à matrice active
AOS	Semi-conducteur oxyde amorphe
AZO	Oxyde de zinc dopé à l'aluminium
CAS	Semi-conducteur amorphe covalent
CL	Cathodoluminescence
EDX	Analyse dispersive en énergie
FET	Transistor à effet de champ
GaN	Nitrure de gallium
IRC	Indice de rendu des couleurs
ITO	Oxyde d'indium dopé à l'étain
LCD	Ecran cristaux liquides
LED	Diode électroluminescente
MEB	Microscope électronique à balayage
MOCVD	Dépôt chimique en phase vapeur de composés organométalliques
MOVPE	Dépôt en phase vapeur de composés organométalliques
OLED	Diode électroluminescente organique
OM	Organométallique
PL	Photoluminescence
PLD	Dépôt par ablation laser
PV	Cellule photovoltaïque
PVT	Dépôt par transport physique en phase vapeur
SEM	Microscope électronique à balayage
Si	Silicium
TCO	Oxyde transparent conducteur
TFT	Transistor couche mince
TTFT	Transistor couche mince transparent
UV	Ultraviolet
XRD	Diffraction de rayons X
ZnO	Oxyde de zinc

Introduction

Les travaux de recherches présentés dans ce mémoire ont été réalisés au sein de la société Nanovation et du Laboratoire des Solides Irradiés de l'Ecole Polytechnique en cotutelle avec le Center for Quantum Devices de Northwestern University (Etats-Unis). Le premier chapitre introduit les objectifs de cette thèse, la démarche de recherche qui a été suivie et les principales étapes définies. Les résultats obtenus sont décrits de façon détaillée sous la forme d'articles publiés dans des revues internationales.

Objectifs

Deux grands objectifs étaient fixés :
1. la mise en place d'un procesus d'élaboration de réseaux de nanostructures d'oxyde de zinc (ZnO).
2. la réalisation de composants pour l'optoélectronique à partir de réseaux de nanostructures ou de couches minces d'oxyde de ZnO déposés par ablation laser (PLD). Ces composants sont :
- Les diodes électroluminescentes (LED)
- Les couches antireflets
- Les cellules photovoltaïques (PV)
- Les transistors couches minces (TFT)
- Les oxydes Amorphe conducteurs (AOS).

Démarche de recherche suivie

La démarche suivie peut être divisée en trois grandes étapes comme décrit dans la figure 1.1. Chaque étape est validée par les résultats obtenus à l'aide des différents outils de caractérisation utilisés (Annexe I).

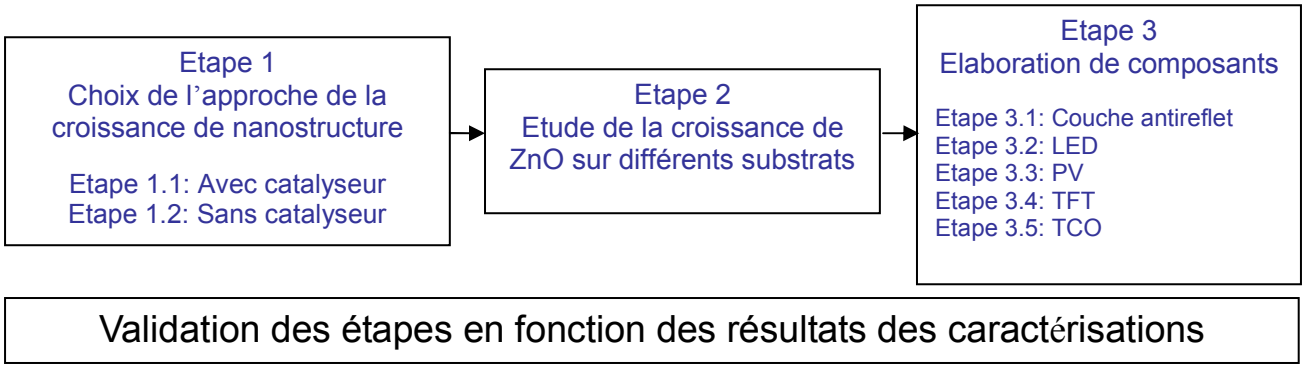

Figure 1.1 Schéma du plan de travail suivi au cours de cette thèse.

Etape 1 : Trois procédés de fabrication de nanostructures de ZnO sont étudiés : dépôt chimique en phase vapeur de composés organométalliques (MOCVD), dépôt par ablation laser et dépôt par

transport physique en phase vapeur (PVT) (voir chapitre III pour plus de détails). Les substrats utilisés pour cette étude sont le saphir (Al_2O_3) et silicium (Si) car ils sont les plus couramment utilisés dans l'industrie de l'optoélectronique. [1] Des dépôts avec ou sans catalyseur sont effectués (respectivement étapes 1.1 et 1.2). La validation du procédé est fonction des résultats obtenus en termes de caractérisations optique, morphologique, cristalline et électrique des nanostructures de ZnO.

Etape 2 : Une fois qu'un des procédés est validé l'étude de la croissance de dépôts de ZnO est approfondie. Cette étude s'effectue sur six substrats qui sont Al_2O_3, Si, ZnO massif, acier austénitique, mylar et papier. Chacun de ces substrats est choisi en fonction des applications potentielles qui sont développées en étape 3 (voir chapitre I.2 pour plus de détail).

Etape 3 : Lorsque les paramètres de croissance sur les six types de substrats utilisés sont maitrisés, l'étude de la réalisation de composants optoélectroniques commence. Le tableau suivant met en relation les types de composants développés, ZnO couche mince ou nanostructuré déposé et les substrats :

Etape	Composant optoélectronique	Dépôt	Substrat
3.1	Couche antireflet	Nanostructures de ZnO	Si, Al_2O_3, ZnO massif et acier
3.2	LED	Nanostructures de ZnO	Si
3.3	PV	Nanostructures de GaN sur Nanostructures de ZnO	Si
3.4	TFT	Couche mince de ZnO	SiO/SiN4/Si
3.5	TCO	Couche mince de ZnO	Papier et Mylar

Tableau 1.1 Composants optoélectroniques en fonction du dépôt ZnO et des substrats utilisés.

Chacun des composants est validé selon des résultats de caractérisations qui lui sont propres (voir chapitre I.3 pour plus de détails). Le tableau suivant représente les composants développés en fonction des caractéristiques recherchées dans le cadre de cette étude:

Etape	Composant optoélectronique	Caractéristique recherchée
3.1	Couche antireflet	~ 95% d'absorption de la lumière visible
3.2	LED	Electroluminescence et caractéristique électrique rectifiante
3.3	PV	Reprise de croissance épitaxiale
3.4	TFT	Caractéristique de transfert rectifiante
3.5	TCO	Transparence (~ 90%) et résistivité électrique minimale (< 1 Ω.cm)

I Contexte

1.1 Avant propos : Nanovation

Nanovation est une SARL fondée en 2001. Nanovation est le fruit de la collaboration de quatre entrepreneurs-chercheurs spécialisés dans le développement de matériaux innovants aux propriétés adaptées aux besoins des nouvelles applications du marché de l'optoélectronique. [1-3]

Le produit de Nanovation est un substrat recouvert d'un semi-conducteur transparent : ZnO. Il est déposé soit sous forme de couches minces, soit sous forme de nanostructures. La fabrication se fait par PLD.

1.2 La PLD, la MOCVD et la PVT

La PLD

Le principe de ce procédé de dépôt (cf. figure ci-dessous), basé sur l'ablation d'une cible par un faisceau laser, [4] en fait une technique souple, peu coûteuse et facile à mettre en œuvre [5]. La PLD, ou « ablation laser », est aussi connue pour [6, 7]:
- sa capacité à reproduire en couche mince la composition de la cible (méthode congruente) ;
- la croissance cristalline à une température de substrat bien plus basse que par les techniques couramment utilisées dans l'industrie des semi-conducteurs (MBE, CVD, Pulvérisation) ;
- sa rapidité d'élaboration des films minces et donc son plus haut rendement.

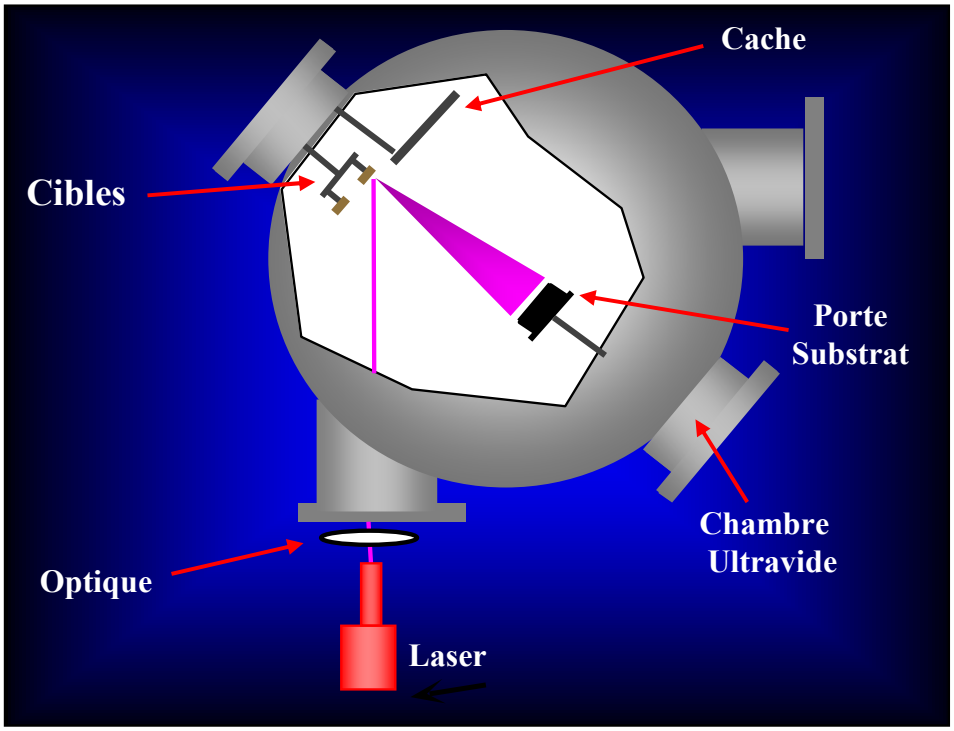

Figure 1.1: Schéma d'une chambre de croissance par PLD.

Un faisceau laser pulsé (dans le cas de cette étude un laser excimère KrF (λ = 248 nm) de haute énergie (~ 20 mJ) est focalisé sur une cible (à base de poudre de ZnO (5N) comprimée et frittée). La cible est située dans une enceinte sous vide (typiquement $<10^{-5}$ Torr). Sous l'effet des impulsions du laser (entre 0.1 et 100 Hz), les constituants de la cible vont être ablatés et forment ainsi un plasma, qui est projeté dans une direction perpendiculaire à la surface de la cible (représenté en violet sur la figure ci-dessus). Les constituants de la cible vont ainsi être déposés sur le substrat situé en face de la cible. La figure suivante est une série de photos de l'evolution du plasma suite à une impulsion laser.

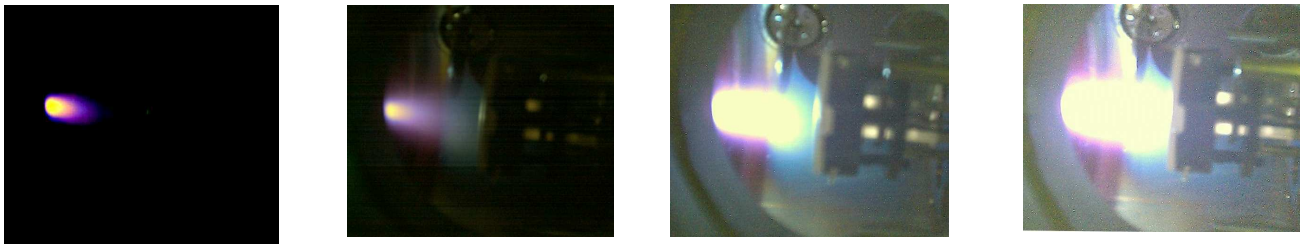

Figure 1.2 : Photo de la plume de plasma.

Un grand avantage de la PLD comparé à d'autres procédés de croissance par voie physique est que l'énergie cinétique des éspèces dans le plasma est plus élevée. Elle est comprise entre 10 et 100 eV, alors que par MBE et CVD elle est géneralement comprise entre 0,1 et 1 eV. Ainsi, la mobilité de surface des atomes et leur réactivité est plus élevée, ce qui permet a) une cristallisation à une température plus basse que dans d'autres procédés et b) une plus grande souplesse dans le contrôle de l'incorporation d'oxygène à travers la pression en O tout en conservant une mobilité de surface

suffisament élevée pour bien cristalliser.

Dans la figure 1.2 on peut constater que la plume est anisotrope et eccentre au moment de l'impact avec le subtrat (c.a.d. au moment du depot). Avec des balayages motorisés (et simultanés) de la cible, du substrat et de l'optique dirigeant le faisceau laser il est possible, cependant, de compenser cette nature inhomogène du dépôt.

La figure 1.4 illustre l'homogénéité des plaques (ϕ = 50 mm) fabriquées par Nanovation après optimisation de ces mouvements.

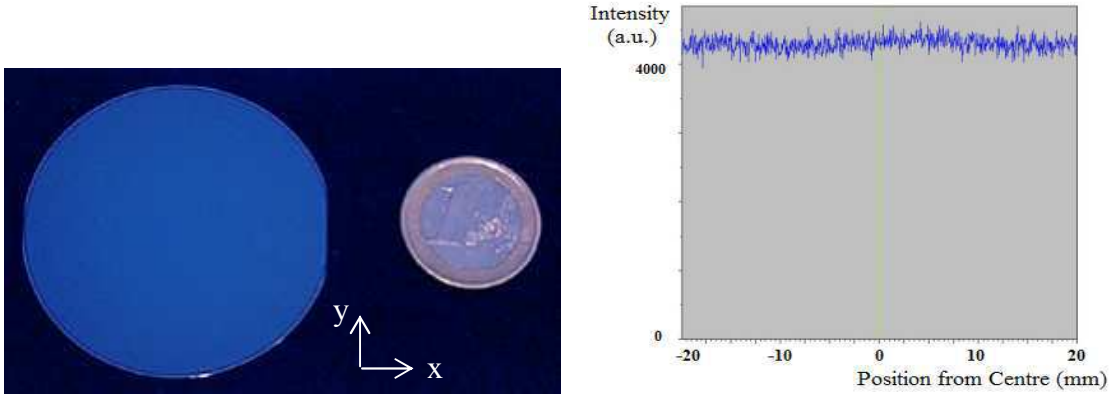

a) b)

Figure 1.3 a) Photographie d'une plaque de ZnO/Si après dépôt par PLD. La coloration bleue provient d'un effet d'interference entre la lumière refléchi à la surface de la couche et à l'interface entre la couche et le substrat. Ainsi, la couleur est déterminée par l'épaisseur du film b) Profil d'intensité (du pic (0002)) de diffraction X pour un balayage du faisceau sur l'échantillon selon l'axe x.

L'homogeneité de la couleur bleue, et le peu de variation d'intensité en XRD indiquent que l'epaisseur et la qualité cristalline sont relativement homogènes, avec une variation « in-wafer » estimé a < 5%.

La MOCVD

La MOCVD est une technique de croissance en phase vapeur utilisant des organométalliques (OM) comme sources pour les éléments à déposer. Elle permet l'épitaxie de matériau, sur un substrat orienté, par la décomposition thermique des OM [dans ce cas du diméthylzinc-triéthylamine (DMZn : TEN) et diéthylzinc (DEZn) fournissent le Zn] et des réactants [L'eau (H_2O) et (N_2O) fournissent l'O]. La figure 3.5 schématise les différentes étapes de croissance de matériau par MOCVD :

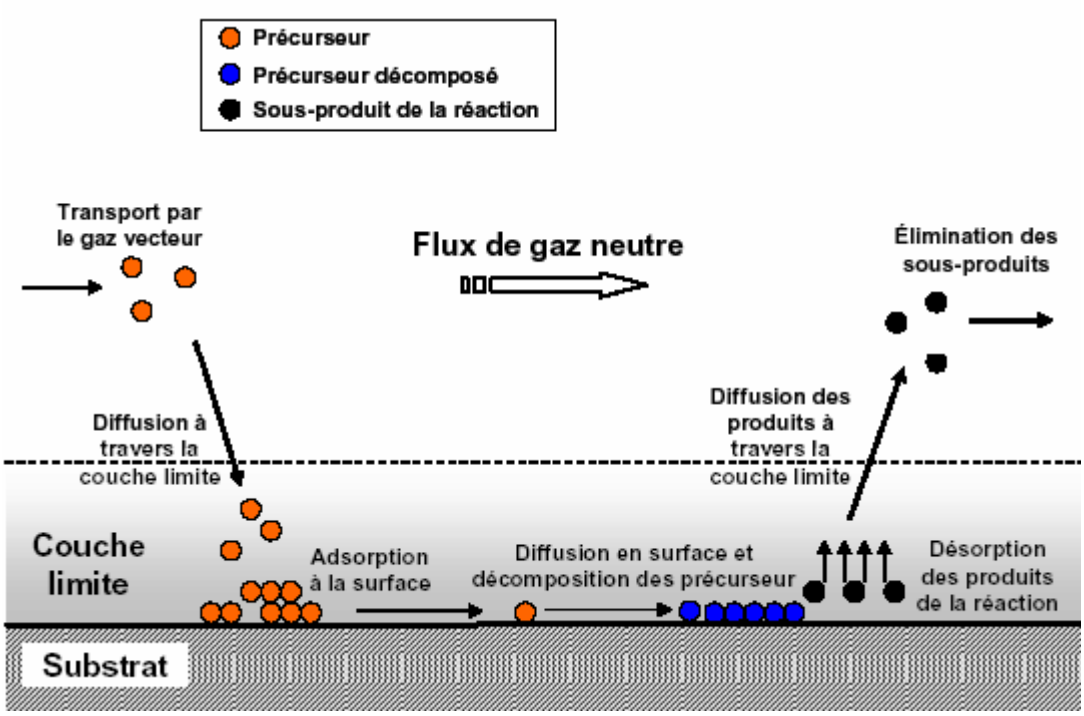

Figure 3.5 : Schéma de principe du processus MOCVD. [8]

a) Un gaz vecteur (azote ou hydrogène) amène les précurseur (OM et réactant) dans la chambre de réaction ;
b) Les précurseurs sous formes gazeuses diffuses à travers la couche limite ;
c) Un ou plusieurs des précurseurs sont adsorbé à la surface du substrat ;
d) Les précurseurs diffusent à la surface du substrat et les précurseurs réagissent entre eux ;
e) Formation d'une couche continue et agrégats ;
f) Désorption des produits de la réaction ;
g) Elimination des sous produits vers le système de récupération.

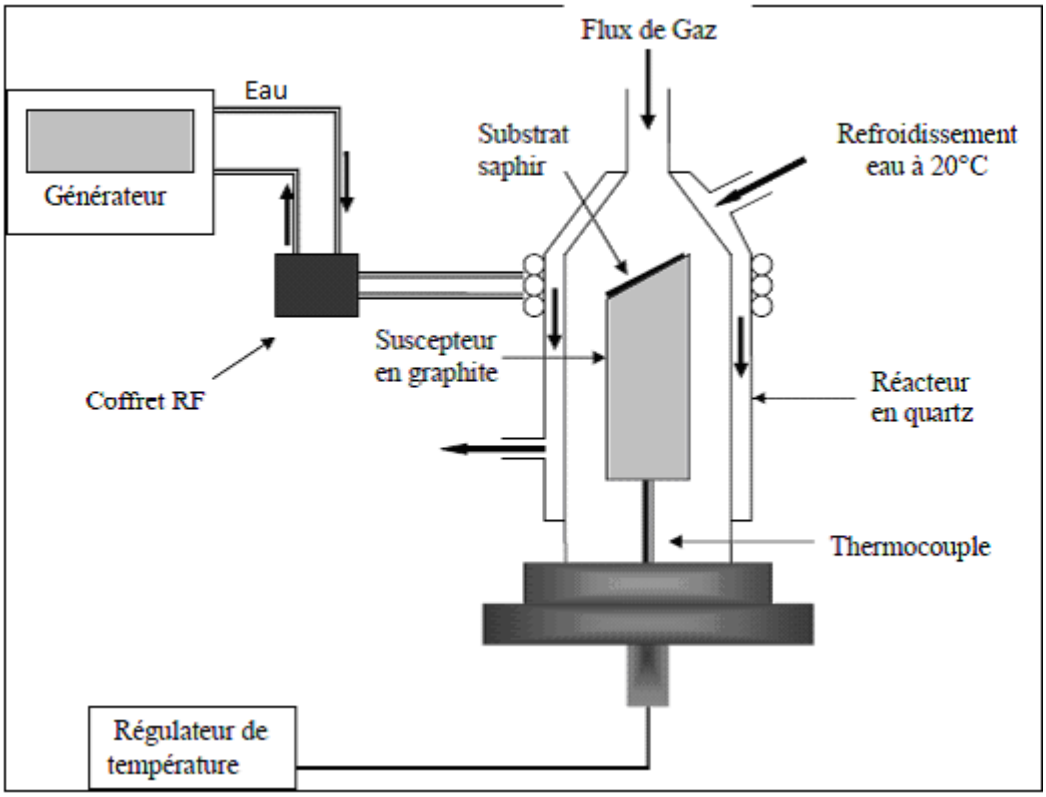

Figure 3.6 : Schéma de réacteur de croissance utilisé.

Les réactions chimiques qui entrent en jeu lors de la formation de ZnO à partir de ces OM sont nombreuses et complexes. Les sources d'éléments sont susceptibles de se décomposer par pyrolyse à des températures modérées, en libérant les groupes éthyl ou méthyl dans la phase gazeuse sous forme d'alcanes gazeux, permettant ainsi le dépôt de l'atome métallique sur le substrat.

La PVT

La figure suivante décrit le procédé utilisé dans cette étude de la croissance par PVT.

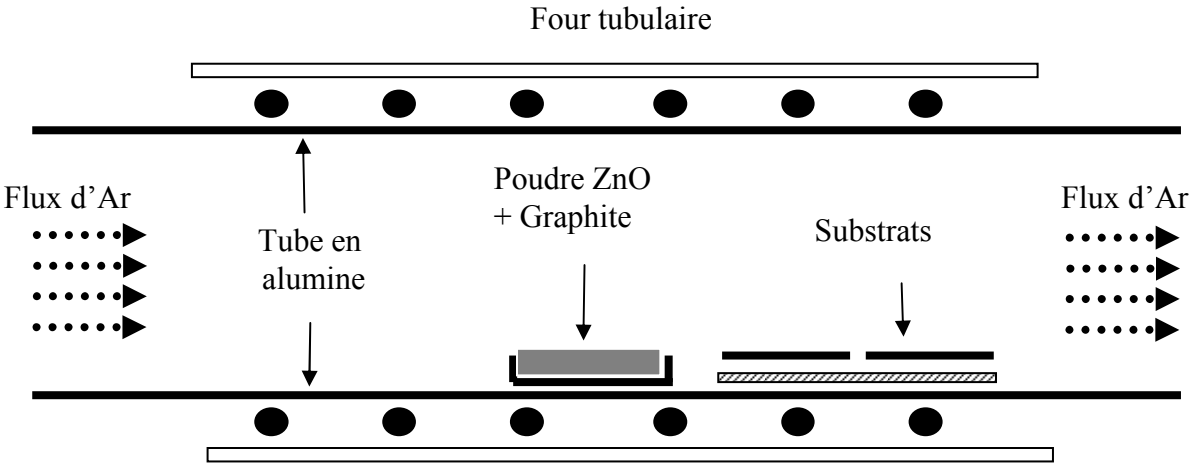

Figure 3.7 : Schéma du four tubulaire utilisé pour la croissance par PVT.

Le procédé suit les étapes suivantes :
1) Réduction de la poudre de ZnO: ZnO+C➔ Zn+ CO
2) Transport par flux d'Ar de Zn en phase vapeur
3) Oxydation sur le substrat du Zn en phase vapeur: Zn+O➔ZnO

Références

Références

[1] Optics Valley, *Les Marchés de l'optique-photonique : Eclairage affichage* (2004).
[2] Yole Développement, *Nouvelles technologies avancées pour la réalisation de LED blanches et leur impact sur le marché de l'éclairage*, Conférence Eclairage, Troyes (2008).
[3] Nanomarket.net, *New Reports from Nanomarket Foresees Continued Growth in the Zinc Oxide Electronics*.
[4] H. M. Smith and A. F. Turner, Appl. Optics **4** (1965) 147.
[5] J. F. Bednorz and K. A. Müller, Z Phys. B Condens Matter. **64** (1986) 189.
[6] M. Kanai, T. Kawai, S. Kawai, H. Tabata, Appl. Phys. Lett. **54** (1989) 1802
[7] H. Tabata, T. Kawai, M. Kanai, O. Murata and S. Kawai, Jap. J. Appl. Phys. **28** (1989) L823.
[8] J. Thery, Mémoire de thèse : Elaboration par MOCVD à injection pulsée d'oxydes de fer et de BiFeO3, Université de Grenoble, Ecole doctorale: EEATS (2006).

1.3 L'oxyde de zinc

À température ambiante, ZnO a une structure de type würtzite (hexagonale). Ses liaisons chimiques ont un fort caractère ionique. Ainsi ZnO est-il très résistant mécaniquement et son point de fusion est relativement élevé (2248 K). [4] La structure cristalline würtzite de ZnO est présentée dans la figure ci-dessous.

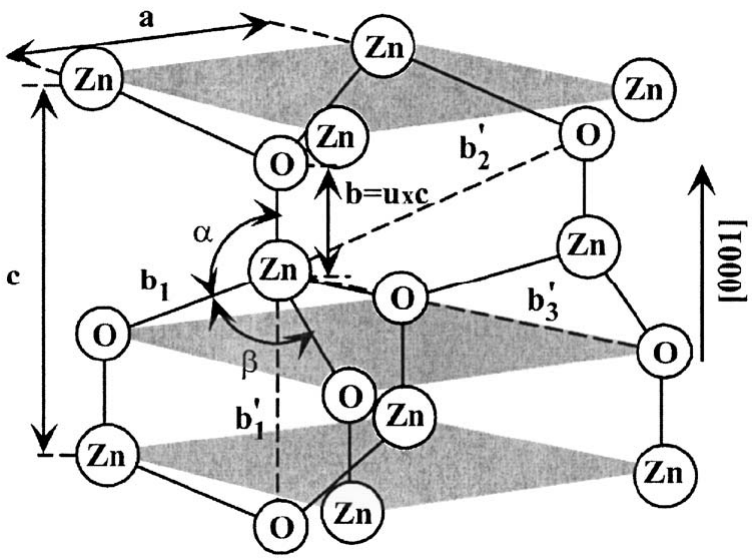

Figure 1.5 : Schéma de la maille élémentaire de la structure würtzite de ZnO ; a et c sont respectivement les paramètres de maille dans le plan et la direction de base. Le paramètre u est défini comme le rapport entre la distance du plus proche voisin, noté b, divisé par le paramètre c (u = 0.375 dans un cristal parfait) ; α et β sont les angles entre les liaisons. [4]

ZnO est polaire et montre une très forte réponse piézo-électrique (parmi les plus élevées de tous les semi-conducteurs) [5] qui mène à diverses applications industrielles telles que les transducteurs et les composants à onde de surface.

ZnO est également transparent (85%-95%) à la lumière visible et sa conductivité peut être modulée entre semi-isolant et semi-métallique, ce qui mène à son utilisation comme électrode transparente conductrice. [6]

ZnO est également un semi-conducteur (annexe II) à grande bande interdite directe (annexe III). Le tableau 1.1 compare les principales caractéristiques des semi-conducteurs à grande bande interdite (ou « grand gap ») les plus courants.

Matériaux	Structure Cristalline	Paramètre de maille		Energie de bande interdite (eV)	Energie d'excitons E_b^{ex}. (meV)	Point de fusion T_f (K)
		A (Å)	C (Å)			
ZnO	Würtzite	3,249	5,020	3,37	60	2248
ZnS	Würtzite	3,824	6,261	3,80	39	2103
ZnSe	Zinc Blende	5,668	-	2,70	20	1793
GaN	Würtzite	3,189	5,185	3,39	21	2500
6H-SiC	Würtzite	3,081	5,117	2,86	-	>2100

Tableau 1.1 : Caractéristiques des matériaux à grande bande interdite pour l'optoélectronique. [7]

Le semi-conducteur à grand gap le plus utilisé par l'industrie est le nitrure de gallium (GaN). Comme nous le voyons dans ce tableau, ZnO présente beaucoup de similarités avec GaN, ayant la même structure cristalline et des paramètres de maille similaires. De plus, ces deux matériaux ont des énergies de bandes interdites qui sont quasiment identiques. Dans le cas de ZnO la recombinaison radiative (« bord-de-bande », voir annexe IV) des paires électrons-trous donne une émission dans l'UV proche (~375 nm). Parmi tous les semi-conducteurs II-VI et III-V, on constate que l'énergie de liaison de l'exciton pour ZnO (60meV) est nettement plus élevée. Ceci suggère que ZnO a le potentiel pour une plus forte émission lumineuse que GaN (E_b^{ex} ~ 21 meV). D'autre part, l'engouement qui a suivi l'observation d'émissions stimulées excitoniques jusqu'à 500 K dans ZnO en 1998 [8] a propulsé le développement d'un savoir-faire « matériau » qui, aujourd'hui, permet de disposer de couches minces d'excellentes qualités structurales pouvant servir de briques élémentaires pour le développement d'un matériau photonique aux propriétés exaltées et aux fonctions multiples. Pour ces raisons, ZnO est proposé comme un candidat pour les applications optoélectroniques UV (cf. p. 12). De plus, à l'heure actuelle, un autre aspect important de ZnO est sa biocompatibilité car contrairement au GaN (et la plupart des semiconducteurs), l'administration de produit pharmaceutique/alimentaire américaine (Federal Drug Administration ou « FDA ») a classifié le ZnO comme biocompatible (literalement « GRAS » ou Generally Regarded As Safe). Il est d'ailleurs présent dans des produits pharmaceutiques (e.g le talc) ainsi que des aliments (e.g. les pilules vitaminées).

1.4 Applications à l'optoélectronique

1.4.1 Les diodes électroluminescentes

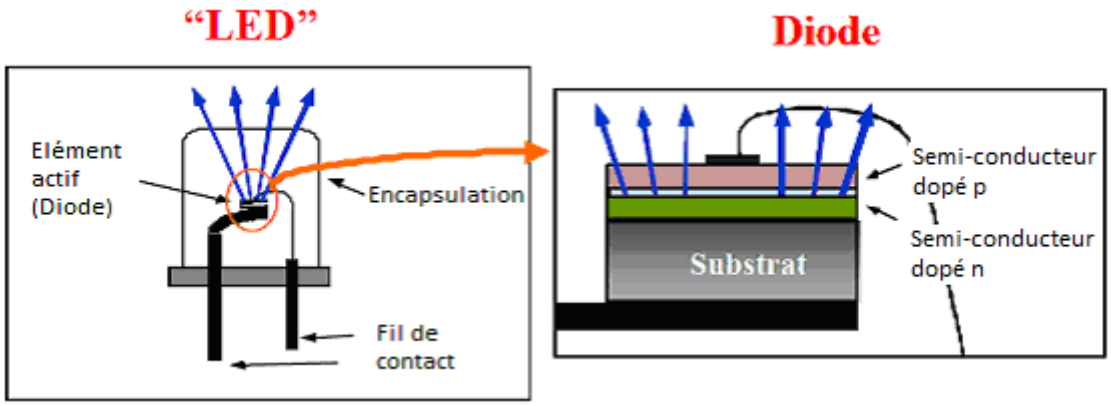

Figure 1.6: Schéma d'une LED.

Il existe à l'heure actuelle deux méthodes utilisés dans l'industrie permettant d'obtenir des LEDs blanches. [1]

Méthode 1 : Mélange de LEDs de couleurs
La mise au point, par l'entreprise Nichia, [9] de LEDs bleues permet de produire de la lumière blanche à partir d'un mélange de LEDs rouges, vertes et bleues dans un même luminaire, spot ou « tableau » à LEDs. [1] Cette méthode à deux avantages : d'une part l'efficacité lumineuse globale est bonne et, d'autre part, elle permet de faire varier les intensités lumineuses de chaque groupe de LEDs afin d'obtenir la température de couleur et d'indice de rendu des couleurs (IRC) désirée (un bon IRC est proche de 100 et un bonne température de couleur est proche de 550k). C'est aussi la méthode la plus efficace en terme de consommation d'énergie pour le moment mais minoritaire sur le marché car trop onéreuse pour être intégrée à grande échelle. [2]

Méthode 2 : LED bleue et phosphore
Cette méthode est utilisée dans la majorité des LEDs blanches. [1] Elle est basée sur le principe de la fluorescence. Ces LEDs blanches sont fabriquées à partir d'une jonction p-n (diode) (voir annexe IV) à l'interface d'un empilement de couches minces de GaN en alliage avec l'indium ($In_xGa_{1-x}N$). Intrinsèquement, ces LEDs à base de $In_xGa_{1-x}N$ donnent une émission bleue. Une couche luminescente à base de phosphore, déposée au-dessus, permet de convertir une partie du rayonnement émis en un rayonnement jaune. La lumière visible résultante est donc un mélange de bleu et de jaune, perçu par l'oeil comme un pseudo-blanc. Ces LEDs ont une efficacité lumineuse jusqu'à 90 lumens par watt selon les annonces de presse des grands fabricants (Nichia, CREE, Lumiled/Philips, OSRAM), ce qui est comparable avec une lampe fluorescente à basse consommation. Il faut noter, cependant, que ces valeurs d'efficacité sont pour des courants

relativement faibles et que l'efficacité a tendance a chuter brusquement avec l'augmentation de courant injecté, à cause d'un phènomène qui s'appelle le « droop » (voir annexe V).

État de l'art

Actuellement, un déficit de luminosité de ces LEDs fait que le prix d'achat, pour un éclairage équivalent, est 50 fois supérieur à celui de lampes incandescentes (toutefois la consommation énergétique est nettement réduite, typiquement d'un facteur 4 comparé à une lampe à incandescence). [1]

La figure 1.7 est un diagramme en baton présentant les différentes pertes lors de la conversion du courant injecté dans une LED. Ces pertes ont lieu sous forme de chaleur. On constate que l'extraction de la lumière (« Extrakc. Eff. ») reste un problème majeur.

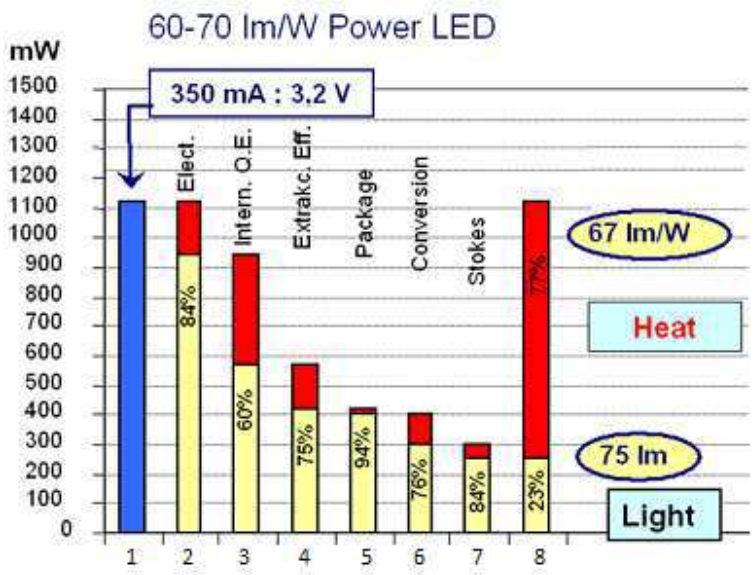

Figure 1.7 Diagramme en bâton des différentes pertes en puissance dans une LED de puissance blanche à base de phosphore de chez OSRAM [10]. Selon l'axe des ordonnées est représentée la puissance injectée en milliwatt dans une LED. Selon l'axe des abscisses sont représentées les différentes pertes dans une LED. Les parties rouges indiquent les conversions du courant injecté sous forme de chaleur et en jaune les conversions du courant injecté sous forme de lumière. Le bâton 1 représente 100% de courant injecté et le bâton 8 représente la conversion totale du courant injecté, soit 23% en lumière et 77% sous forme de chaleur. Les bâtons 2 à 7 représentent les pertes intermédiaires.
1 : Bâton d'injection dans la LED d'un courant de 350 mA et 3,2 V (correspondant à 100% de courant) ;
2: Bâton des pertes électriques lié à la conversion du courant alternatif en courant continue, où 84% du courant injecté sont convertis en lumière et 16% convertis sous forme de chaleur ;
3: Bâton des pertes liées à l'efficacité quantique interne où 60% du courant restant suite aux pertes électrique (bâton 2) sont convertis en lumière ;
4 : Bâton des pertes liées à l'efficacité d'extraction lumineuse où 75% du courant restant suite aux pertes liées à l'efficacité quantique interne (bâton 3) sont convertis en lumière ;
5 : Bâton des pertes liés à la mise en forme de la LED sous forme de composant, où 94% du courant restant

suite aux pertes liées à l'efficacité d'extraction lumineuse (bâton 4) sont convertis en lumière ;
6 : Bâton des pertes liées aux taux de conversion de photon émis par la LED en lumière blanche via le phosphore, où 76% du courant restant suite aux pertes liées à la mise en forme du composant (bâton 5) sont convertis en lumière ;
7 : Bâton des pertes liées à la conversion Stokes, où 84% du courant restant suite aux pertes liées aux taux de conversion via le phosphore (bâton) sont convertis en lumière ;
8 : Bâton représentant l'ensemble des pertes et conversion en lumière du courant initialement injecté soit 77% en chaleur et 23% en lumière.

Problématique de l'extraction de la lumière d'une LED

La figure 1.8 illustre la problématique de l'extraction de la lumière d'une LED.

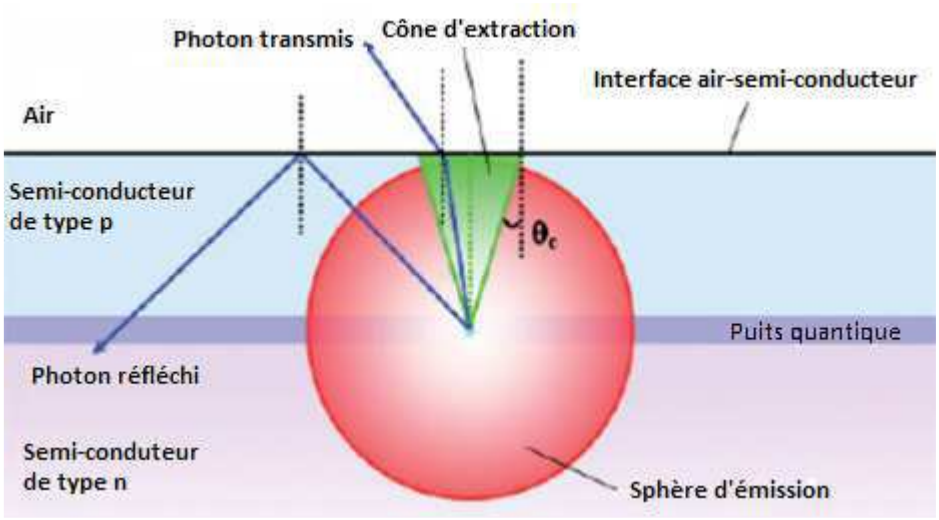

Figure 1.8 Représentation du cône d'extraction (en vert) d'angle solide θ_c , dans le cas d'une interface air-semi-conducteur. La sphère d'émission des photons est représentée en rouge [11].

A cause de la réflexion interne lorsqu'un photon passe d'un milieu de fort indice optique à l'air, seule la lumière située dans le cône d'extraction est susceptible d'être émise. Une émission isotrope donne alors un rendement d'extraction de la lumière noté $\theta_{extract}$ tel que :

$$\theta_{extract} = \frac{1}{2}(1 - \cos\ \theta_c)$$

ce qui correspond à un rendement d'environ 5% dans le cas d'une diode à base de ZnO (n = 2 pour $\lambda \approx$ 375 nm) et 4,5% dans le cas d'une LED GaN (n = 2,4 pour $\lambda \approx$ 365 nm). De nombreuses recherches portent actuellement sur l'amélioration de ce facteur (ruguosification de la surface, optimisation de la géométrie, intégration de micros réflecteurs, utilisation de structures type cristal photonique). La structuration d'indice à l'échelle nanométrique permet aussi d'extraire plus efficacement les photons de la couche émettrice.

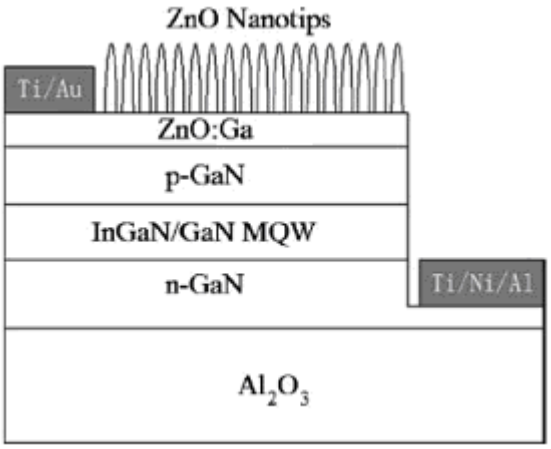

Figure 1.9 : Schéma d'une utilisation possible de nanocolonnes de ZnO dans le cas d'une LED à base de couche mince de $In_xGa_{1-x}N$. [12]

Le consortium *MONA* de la commission européenne, a publié une étude intitulée *«European Roadmap for Photonics and Nanotechnologies »* en 2008 [13] dans laquelle l'utilisation des LEDs a base de nanocolonnes de ZnO est désignée comme l'une des deux technologies clefs pour le futur de l'éclairage à base de LEDs. En effet, les propriétés spécifiques des nanostructures de ZnO permettent un contrôle unique de d'émission lumineuse. Ce domaine reste toutefois peu développé industriellement en raison notamment des difficultés rencontrées pour l'obtention du dopage p indispensable à la réalisation des dispositifs électroluminescents tout ZnO (homojonctions) [14]. Des alternatives existent comme la réalisation d'hétérojonctions électroluminescentes (p-GaN/n-ZnO). [15,16]

Un gain d'un facteur 4,8 en efficacité lumineuse a pu ainsi être démontré à l'aide de nanocônes [17]. Différentes conditions sur le diamètre de la base de la nanostructure (noté D) ont été définies :

D < 300 nm : Réflexions supprimées grâce à la fabrication d'un indice de réfraction gradué ;

D ≈ 400 nm : Réflexions diminuées ;

D ≈ 500 nm : Apparition de nombreux modes d'interférence.

Ce sujet est développé plus en détail dans les chapitres 2 et 4

1.4.2. Les cellules photovoltaïques

La figure suivante montre l'évolution de l'efficacité maximale des PVs produites en laboratoire pour différentes technologies. [18]

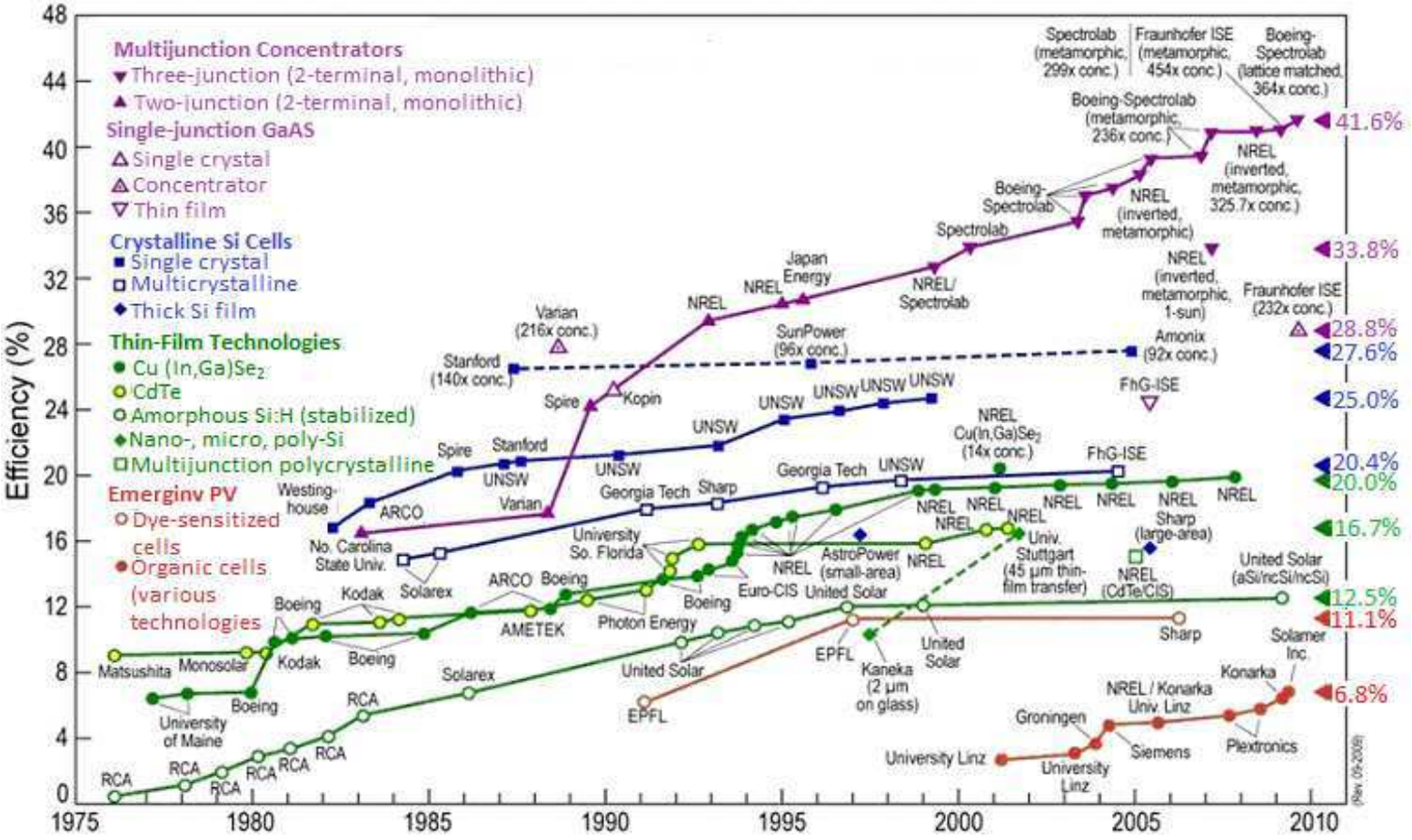

Figure 1.10 : Ce graphique représente les courbes d'évolution de l'efficacité en % des quatre grandes technologies des PVs entre 1975 et 2010. Les noms des universités ou entreprises sont associés à leurs résultats respectifs [18]. En violet sont représentés les PVs de type multi- et mono- jonctions qui, à l'heure actuelle, présentent les efficacités les plus importantes, comprises entre 28,8% (PVs monojonctions) et 41,6% (PVs multijonctions). En bleu sont représentées les PVs à base de Si cristallin qui présentent une efficacité comprise entre 20,4% (PVs à base de Si polycristallin) et 27,6% (PVs à base de Si monocristallin). En vert sont représentées les PVs utilisant les technologies couche-mince. Les efficacités varient de 12,5% (PVs à base de couche mince de CdTe) à 20,0% (PVs à base de couche mince de Cu $(In,Ga)Se_2$). En rouge les technologies émergentes sont représentées et ont démontré des efficacités variant de 6,8% (PVs organiques) à 11,1% (PVs électrochimiques).

Malgré l'efficacité relativement basse des PVs à base de silicium, celles-ci dominent le marché (cf. figure 1.11) [19].

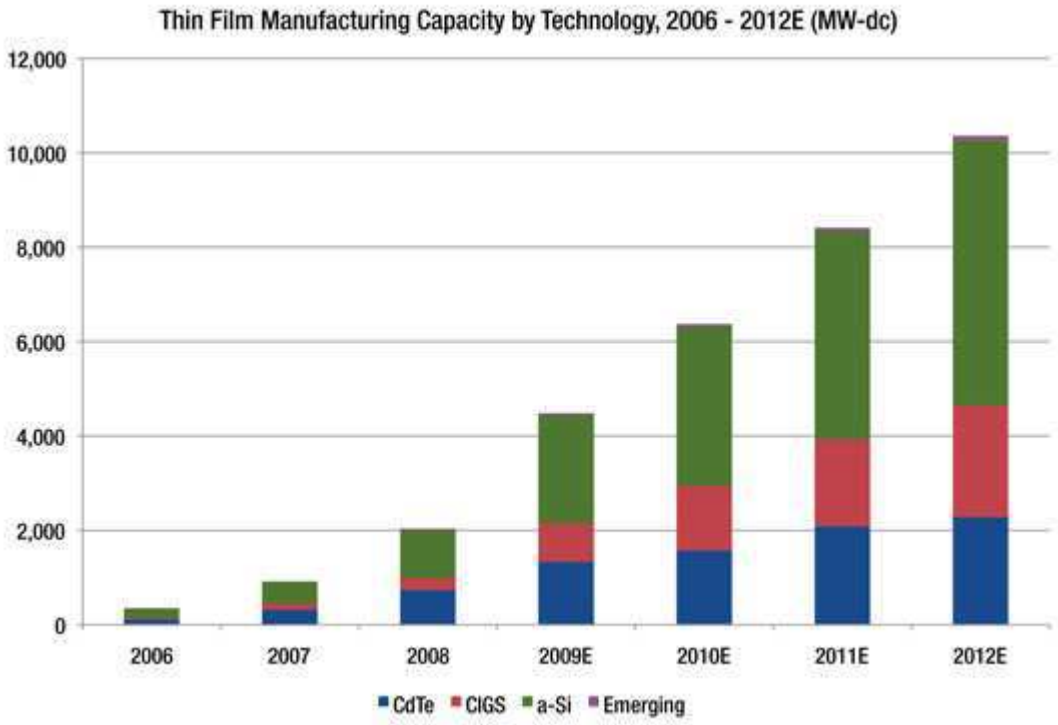

Figure 1.11 : Courbe comparant l'évolution des capacités de production de quatre technologies de PVs en MW en fonction des années. En bleu la technologie CdTe présente une évolution constante comparable à celle basé sur Cu (In,Ga)Se_2 (noté CIGS). Le silicium, représenté en vert, domine nettement le marché et les technologies émergentes en violet sont encore peu représentées. [19]

Aujourd'hui l'utilisation de silicium comme matériau de base pour les PVs est un frein à leur développement. En effet le prix de Si en tant que matière première est en hausse constante et l'énergie de bande interdite ne permet pas de couvrir l'ensemble du spectre visible, ce qui réduit d'autant plus leur efficacité. Pour diminuer le ratio prix/watt des PVs, il est nécessaire de trouver une alternative. L'utilisation des technologies multi-jonctions à base de couches minces pourrait peut-être offrir une réduction de ce ratio.

Comme décrit ci-dessus, les matériaux de type III-V (comme GaN) ont été abondamment utilisés dans les LEDs et ont montré des performances optiques et électriques exceptionnelles [20]. Si, à l'heure actuelle, l'utilisation de GaN dans les PVs, par contre, a attiré peu d'attention, elle présente un potentiel d'augmentation important dans la performance des PVs. [20] L'avantage principal des composés à base de GaN est la modularité de la bande interdite qui peut être ajustée entre 0,7 eV et 3,4 eV par l'introduction d'indium. Ceci en fait le matériau le mieux adapté actuellement au spectre

solaire (cf. figure 1.12) et permet de maximiser le rendement des PVs. Des cellules de ce type ont déjà montré un pic d'efficacité de 70% [21]. Le défi qui reste à relever est le développement de ce type de cellules sur des substrats peu onéreux : ce sujet est développé dans les chapitres 2 et 4.

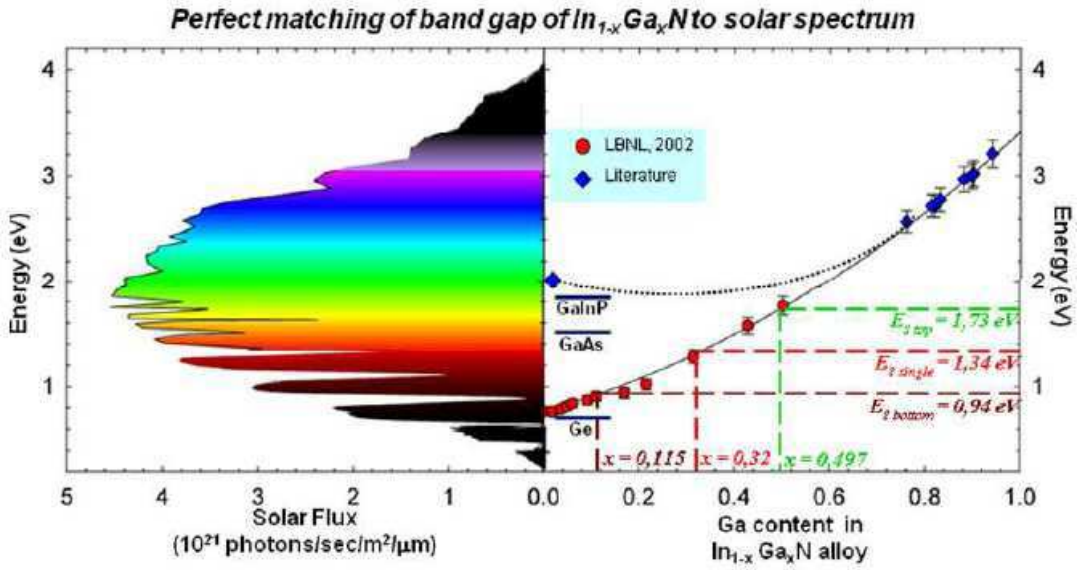

a) b)

Figure 1.12 : Courbe comparant l'énergie de la lumière en fonction du flux solaire (courbe a) et l'énergie de la bande interdite en fonction de la composition x de l'alliage $In_xGa_{1-x}N$ (courbe b). L'énergie de la bande interdite de $In_xGa_{1-x}N$ peut varier entre 0,7 eV et 3,4 eV en fonction de la quantité d'In. Cette particularité fait de ce matériau le mieux adapté au spectre solaire pour maximiser le rendement des PVs [22].

1.4.3 Oxydes conducteurs et transistors couches minces

ZnO comme oxyde conducteur transparent

Dans le domaine de l'électronique transparente, l'oxyde transparent conducteur (TCO) le plus utilisé est In_2O_3 dopé par Sn (ITO). Mais depuis quelques années la tendance est au remplacement d'ITO par ZnO et plus particulièrement ZnO dopé par l'aluminium (AZO). Il y a plusieurs raisons à cela : premièrement In est toxique, rare et coûteux. Deuxièmement, ZnO peut être fabriqué sous forme cristalline à relativement basse température comparé à ITO [23]. Troisièmement, ZnO est plus facilement utilisable dans la fabrication de composants. En effet, la gravure chimique est couramment utilisée dans l'industrie pour la mise en forme des composants et ZnO est facilement gravé par les acides et les alcalins. Quatrièmement, les propriétés de ZnO peuvent être modifiées par le dopage. Par exemple, le dopage par le fluor permet d'obtenir une transparence dans le spectre visible supérieure à tous les autres TCO. Et, finalement, les caractéristiques de mobilité et de conductivité des électrons se sont améliorées depuis quelques années, ce qui permet à AZO d'avoir des résistivités comparables à ITO [24]. Ces propriétés ont permis à ZnO d'être adopté pour de nombreuses applications qui nécessitent un conducteur transparent : couche transparente pour filtrer la lumière UV, contacts transparents utilisés dans les écrans plats, cellules solaires et LEDs. Ce sujet

est développé dans les chapitres 2 et 5.

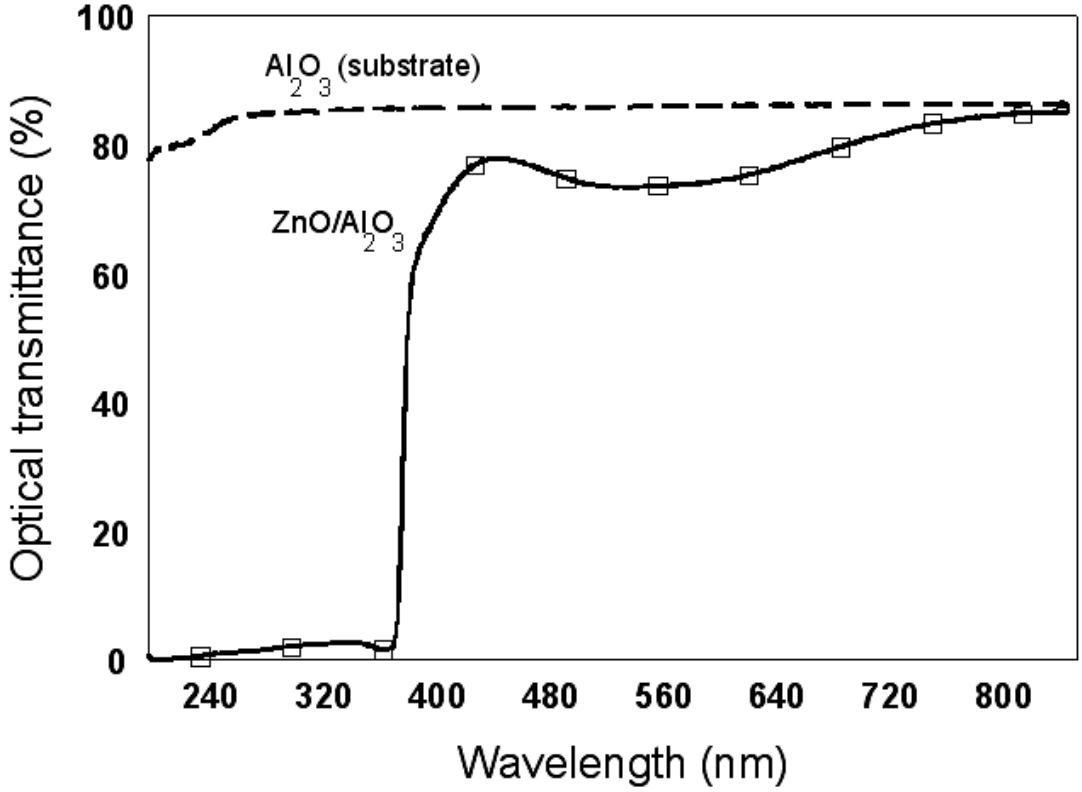

Figure 1.13 : Courbes de transmission à température ambiante d'un substrat Al_2O_3 et d'une couche mince de ZnO type n déposé par PLD sur Al_2O_3. Après le dépôt de ZnO la transmittance reste quasi constante dans le visible (~80%) puis diminue pour s'annuler à partir de 375 nm [25].

Transistor couche mince transparent à base de ZnO (TTFT)

Bien que le concept de TTFTs à base de ZnO ne soit pas nouveau, [26] il y a, depuis les premières publications en 2003, un intérêt croissant pour leur réalisation en vue d'applications aux écrans cristaux liquide à matrice active (AMLCD), au papier électronique et aux écrans flexibles à base de LEDs organique (OLEDs). Cette nouvelle génération de TTFTs présente un ratio on-off élevé ($>10^6$) et une mobilité dans le canal 10 fois plus élevée que ceux à base de Si, lesquels sont les plus couramment employés comme transistors pour les écrans LCD. Deux variantes de TTFTs à base de ZnO sont apparues, l'une utilisant ZnO de type würtzite, [27] et l'autre ZnO de type amorphe. [28] Ce sujet est développé dans les chapitres 2 et 5.

Références

[1] Optics Valley, *Les Marchés de l'optique-photonique : Eclairage affichage* (2004).
[2] Yole Développement, *Nouvelles technologies avancées pour la réalisation de LED blanches et leur impact sur le marché de l'éclairage*, Conférence Eclairage, Troyes (2008).
[3] Nanomarket.net, *New Reports from Nanomarket Foresees Continued Growth in the Zinc Oxide Electronics*.
http://nanomarkets.net/news/article/new_report_from_nanomarkets_foresees_continued_growth_in_the_zinc_oxide_ele/ (2009).
[4] Ü. Özgür, Ya. I. Alivov, C. Liu, A. Teke, M. A. Reshchikov, S. Doğan, V. Avrutin, S.-J. Cho, and H. Morkoç, J. Appl. Phy. **98**, 0413011–30 (2005).
[5] R. Triboullet, SPIE Proceedings **4412** R, 1 (2000).
[6] D. Rogers, F. Hosseini Teherani, and M. Razeghi, *Encyclopedia of Materials: Science and Technology, ZnO: From Transparent Conducting Oxide to Transparent Electronics,* pp. 1–5 ISBN: 978-0-0804-3152-9, Elsevier (2010).
[7] Y. Chen, D. Bagnall, and T. YaoChen, Materials Science and Engineering B, 75, 190 (2000).
[8] D. Bagnall, Y. F. Chen, Z. Zhu, T. Yao, M. Y. Shen, and T. Goto, Appl. Phys. Lett. **73**, 1038 (1998).
[9] http://www.nichia.co.jp/en/about_nichia/history.html
[10] OSRAM, Manufacturing LEDs for Lighting and Displays, EPIC/SPIE Europe Workshop, (Berlin Germany, 2007).
[11] M. Yamada, Y. Narukawa, and T. Mukai, J. of Appl. Phy. **41**, L246 (2002).
[12] J. Zhong, H. Chen, G. Saraf, Y. Lu, C. K. Choi, J. J. Song, D. M. Mackie, and H. Shen, Appl. Phy. Lett. **90**, 203515 (2007).
[13] www.ist-mona.org/pdf/MONA_v15_190308.pdf
[14] S. J. Choi, IEEE Transaction on Electron Devices **57**, 1 (2010).
[15] D. J. Rogers, F. Hosseini Teherani, A. Yasan, K. Minder, P. Kung, and M. Razeghi, Appl. Phy. Lett. **88**, 141918 (2006).
[16] C. Bayram, F. Hosseini Teherani, D. J. Rogers, and M. Razeghi, Appl. Phy. Lett. **93**, 081111 (2008).
[17] T. Kondo, A. Suzuki, F. Teramae, T. Kitano, Y. Kaneko, R. Kawai, K. Teshima, S. Maeda, S. Kamiyama, M. Iwaya, H. Amano, and I. Akasaki, Proceedings of SPIE, **7602**, 76021M-1(2010).
[18] National Renewable Energy Laboratory, National Center for photovoltaics, www.nrel.gov
www.nrel.gov/pv/thin_film/docs/kaz_best_research_cells.ppt
[19] http://www.greentechmedia.com/articles/read/the-future-of-thin-film-beyond-the-hype/
[20] Physics world, p. 27-31 (February 2011).
[21] E. Matioli, C. Neufeld, M. Iza, S. C. Cruz, A. A. Al-Heji, X. Chen, R. M. Farrell, S. Keller, S. DenBaars, U. Mishra, S. Nakamura, J. Speck, and C. Weisbuch, Appl. Phy. Lett. **98**, 021102 (2011).
[22] J. Wu, W. Walukiewicz, K. M. Yu, J. W. Ager, E. E. Haller, H. Lu, and W. J. Schaff, Appl. Phy. Lett. **80**, 4741 (2002).
[23] R. G. Gordon, MRS Bulletin **25**, 52–7 (2000).
[24] T. Minami Semicond. Sci. Technol. **20**, 35–44 (2005).

[25] D. J. Rogers & F. Hosseini Teherani Encyc. Mats. Sci. Technol., Elsevier, Oxford (2010) Pages 1-5
[26] G. F. Boesen and J. E. Jacobs, Proceeding Institute of Electrical and Electronics Engineers **56** (11), 2094–5 (1968).
[27] R. L. Hoffman, B. J. Norris, and J. F. Wager, Appl. Phy. Lett. **82**, 733–5 (2003).
[28] K .Nomura, H. Ohta, A. Takagi, T. Kamiya, M. Hirano, and H. Hosono, Nature **432**, 488–92 (2004).

II ZnO et ses applications en optoélectronique

Résumé

Ce chapitre est fondé sur un article analysant les différentes applications, dans le domaine de l'optoélectronique, réalisables avec ZnO déposé par PLD. Il analyse l'évolution croissante du nombre de publications dans ce domaine de recherche et discutes des futurs marchés importants.
Les applications décrites se focalisent d'une part sur ZnO sous forme de couches minces
- composants électroniques : LED verte, LED UV hybride, TTFT,
- procédés de fabrication de composants optoélectroniques à base de GaN : couche sacrificielle dans le cas des fabrications des LEDs ou couche tampon pour la fabrication de cellules photovoltaïques, d'autre part, sur les applications de ZnO nanostructuré
- couche anti-reflets pour les cellules photovoltaïques.

Les résultats présentés dans cet article sont expliqués de façon plus approfondie dans les chapitres suivants.
Ma contribution dans les travaux de recherches présentées dans cet article concerne la fabrication et la caractérisation du composant TFT. La fabrication a necessité la mise en place d'un procédé de photolithographie par gravure chimique. La figure suivante décris les étapes successives de la fabrication d'un composant via ce procédé.

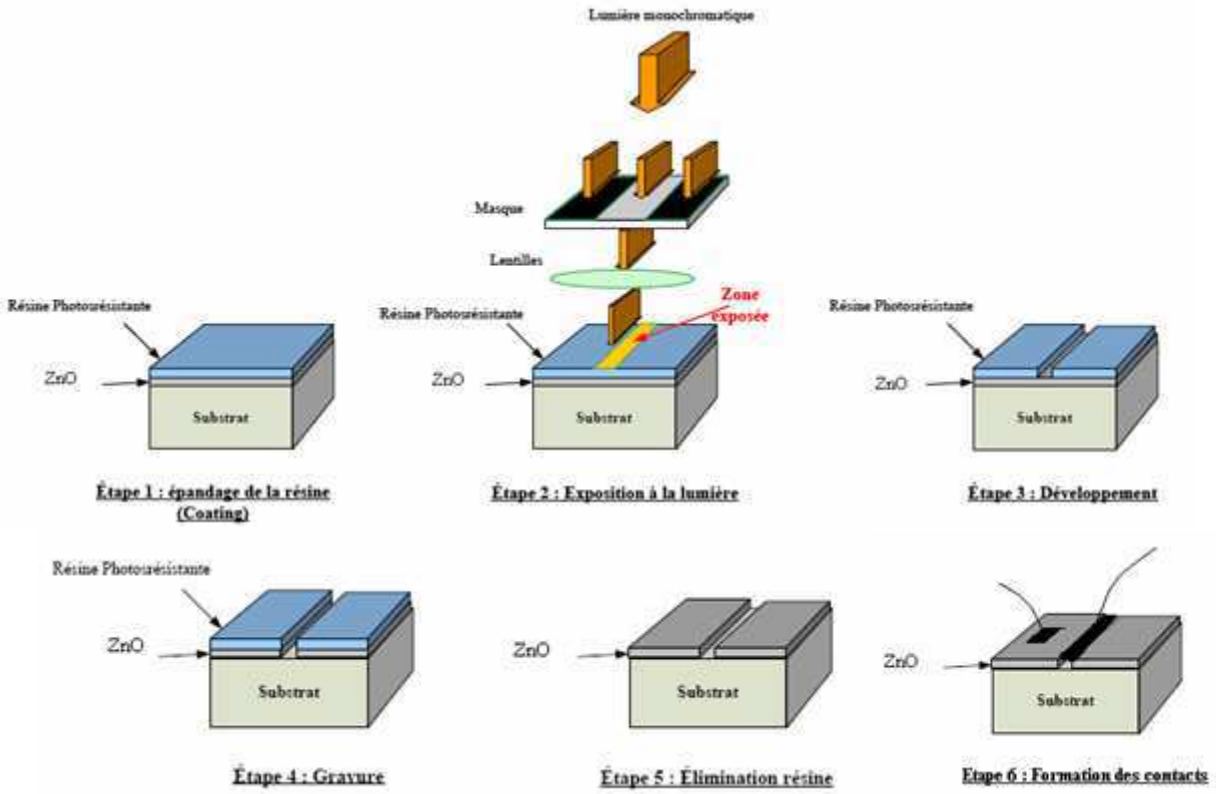

Figure 2.1 : Procédure mise en place pour la fabrication des composants.

Après dépôt de la couche de ZnO sur un substrat de type $Si_3N_4/SiO_2/Si$ (111) par ablation laser, une couche de résine (AZ®159) photorésistante de 100 µm est déposée par spin-coating (300 tours par minute) sur le substrat. Une exposition de 2 minutes sous une source UV à travers un masque métallique polymerise la résine. Les parties exposées aux rayons UV sont ensuite développées préférentiellement par attaque chimique avec de l'acétone. La gravure du ZnO est ensuite effectuée à l'aide d'acide chlorhydrique (0.1 mol/L), selon la réaction :

$$ZnO + 2\ HCl \Leftrightarrow ZN2+ + 2\ Cl- + H20$$

La résine photorésistante restante est ensuite enlevée avec de l'acétone. Pour finir, des contacts en In ont ensuite été déposés sur le silicium Si (111) ainsi que sur la source et le drain par pression.

Ce procédé a permis de réaliser le composant TFT suivant :

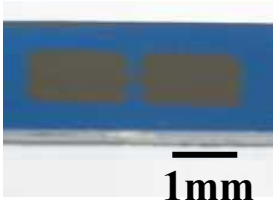

Figure 2.2 Photo du composant TFT fabriqué par photolithographie

Les composants finaux se présentent sous forme de deux rectangles de ZnO (la source et le drain) de ~ 1 mm² reliés par un canal de ZnO de 150 µm de long et dont la largeur varie de 75 µm à 700 µm selon le composant (cf.figure 2.2).

Les mesures électriques

Lorsque le composant a été réalisé il a fallut mettre en place des mesures électriques. Elles ont été réalisées avec un banc de mesure Karl Suss comme décrit dans la figure suivante.

Figure 2.3 : Photo du montage sur un banc Karl Suss pour les mesures électrique des composants.

Ce montage m'a permis de réaliser les caractérisations électriques du composant TFT. Le principe

repose sur les mesures de courant du drain en fonction de la tension entre la source et le drain pour des différentes tensions appliquées entre la source et la grille (« gate » en anglais). Les courbes ainsi obtenues sont présentées en figure 6 page 25.

ZnO Thin Films & Nanostructures for Emerging Optoelectronic Applications

D. J. Rogers et al. Proc. of SPIE Vol. 7605 76050K-1

D. J. Rogers[a], F. Hosseini Teherani[a], V. E. Sandana[a,b], & M. Razeghi[b]

[a]Nanovation SARL, 103b rue de Versailles, 91400 Orsay, France.
[b]Center for Quantum Devices, Northwestern University, Evanston, Illinois, USA.

1. INTRODUCTION

ZnO is a remarkable multifunctional material with a direct wide bandgap, intrinsically high transparency over the whole visible range and a resistivity that can be tuned from semi-insulating right through to semi-metallic by doping. Table 1 compares some key properties of ZnO and GaN (the next most industrially-important semiconductor after Si).

Materials	Crystal Structure	Lattice constants a (Å)	c(Å)	Band gap at RT (eV)	Cohesive energy (eV)	Melting point (K)	Exciton binding energy (meV)
ZnO	Wurtzite	3.249	5.207	3.37	1.89	2248	60
GaN	Wurtzite	3.189	5.185	3.39	2.24	1973	21

Table 1 Comparison of selected properties of ZnO and GaN (adapted from [1]).

The table reveals that ZnO and GaN are very similar materials, with the same wurtzite crystal structure, comparable lattice-constants/bandgaps and high cohesive-energies/melting points. Like GaN, ZnO is also a strongly polar material and it exhibits one of the highest piezoelectric responses of all semiconductors. There are some significant differences between ZnO and GaN, however. In particular, wet etching is possible for ZnO, with nearly all dilute acids and alkalis, whereas GaN requires HF or plasma etching. ZnO also shows a higher radiation resistance and is abundant (unlike Ga), so ZnO cost is low. Finally, ZnO is biocompatible. Indeed, it is one of the ingredients of vitamin pills. The distinctive property set has led to a number of industrial applications for ZnO-based electronics. A recent market study [2] identified the 4 main current uses as conductive & optical coatings, gas sensors, Surface Acoustic Wave (SAW) devices and varistors, amounting to an combined annual market of about half a billion dollars in 2009. Recently, there has been a surge of research activity focused on ZnO. Figure 1 shows the evolution over time of the number of publications per year in Applied Physics Letters for three direct wide bandgap materials: ZnO, GaN and SiC.

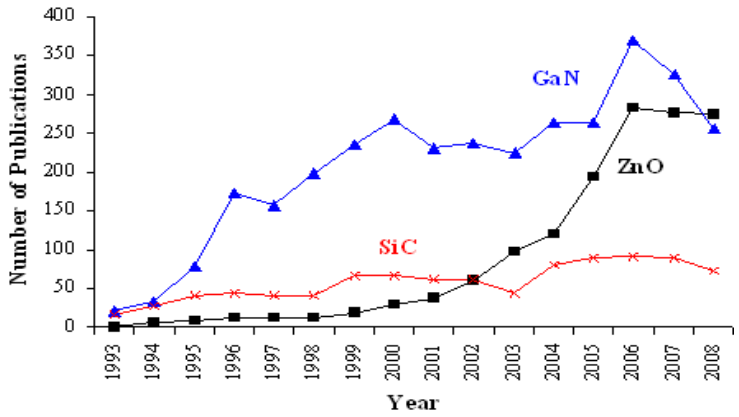

Figure 1. Number of publications/year in Applied Physics Letters for ZnO, GaN & SiC.

The graph reveals that the number of publications for ZnO has shown exponential growth since the mid 1990s and is now comparable with the number of publications for GaN. The number of publications for SiC, on the other hand, is much lower and has not progressed significantly over the same period. There are number of breakthroughs driving this, including the know-how for band gap engineering, studies of self forming laser cavities, availability of high quality ZnO substrates, suggestion that doped ZnO could be a Room Temperature (RT) ferromagnetic semiconductor, stimulated excitonic emission at temperatures over 550K, demonstration of schottky & ohmic contact know-how, high quality epitaxy, the development of novel ZnO-based Amorphous Oxide Semiconductors (AOS) with industrially relevant conductivities (σ)and mobilities (μ), reports of p-type doping, homojunction Light-Emitting Diodes (LEDs) & Laser Diodes (LDs), RT ultraviolet (UV) photonic crystal lasing, Transparent Thin Film Transistors (TTFT), a 2 dimensional electron gas & the fractional quantum Hall effect. A comprehensive overview of these developments is given by Ozgur et al. [3]

ZnO has also shown itself to be a very important nanomaterial. Figure 2 shows the evolution over time of the number of publications/year in Nanoletters for ZnO, GaN and carbon nanotubes (CNT).

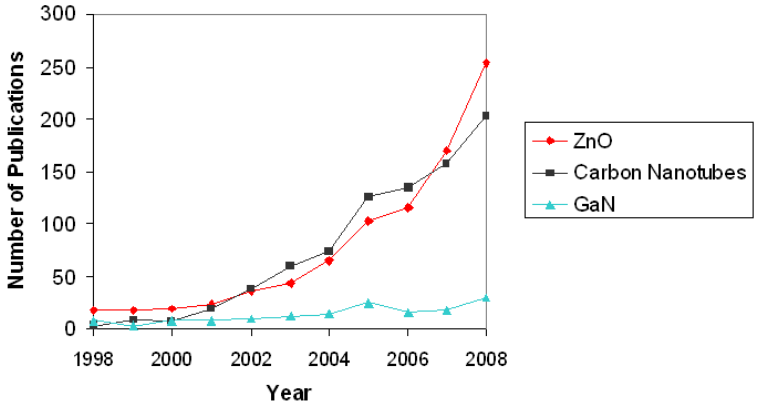

Figure 2. The evolution of the number of publications/year in Nanoletters for ZnO, GaN & CNT.

This graph shows that while there are far fewer publications on nanostructured GaN, there has been an exponential growth in publications on nanostructured ZnO, such that their number now exceeds

that for CNT. Indeed, a survey, by Thomson-Reuters, published in Physics World in 2009 recorded more publications dedicated to nano ZnO than dedicated to the whole of thin film semiconductors. There are many reasons for this, including the ease of fabricating ZnO nanostructures by various techniques and the large family of nanostructures that can be obtained. This remarkable propensity for miniaturization has led to claims that nanostructures of ZnO might even have a key role to play in beyond-lithography electronics [4].

Figure 4 shows a forecast of the ZnO-based electronics market, which came out in 2009 [2].

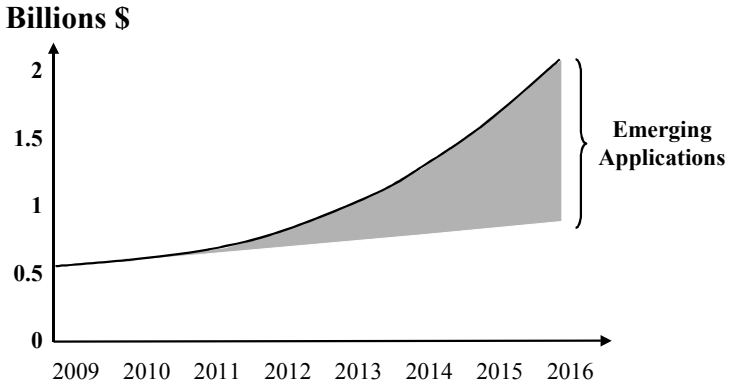

Figure 4. A forecast of the ZnO based electronics market.

The whole ZnO-based electronics market was estimated to be worth about 0.5 billion dollars in 2009 and predicted to grow to over 2 billion dollars by 2016. By 2016, 65% of the market is predicted to be made up of emerging applications.

Four key emerging applications were identified in the study: photovoltaics, displays, LEDs and sensors (Gas, UV & Bio). In this paper, we illustrate how ZnO-based thin films and nanostructures grown by Pulsed Laser Deposition (PLD) can respond to current issues in some of these applications.

2. EXPERIMENT

ZnO thin films and nanostructures were grown on various substrates by PLD, as described elsewhere [5, 6]. Scanning Electron Microscopy (SEM) was conducted using a Hitachi S4800 field emission system. TTFT electrical characteristics were studied using a dual-source dc power supply, a Fluke multimeter and a Keithley 2400 source-meter. Liquid crystal characteristics were tested using the following set-up:

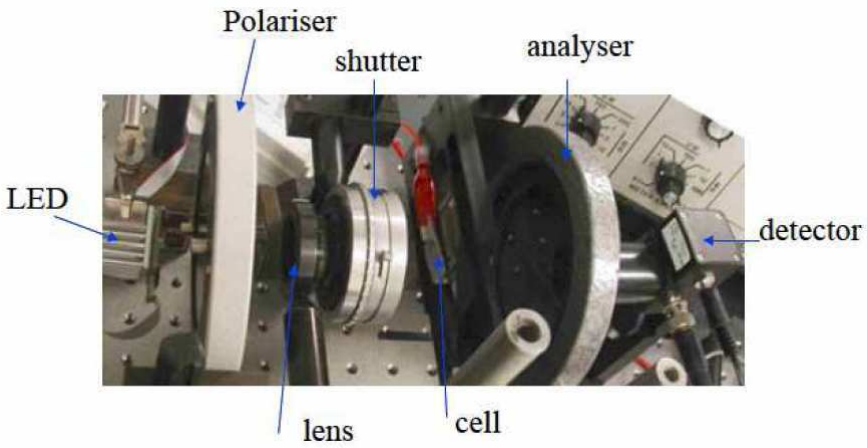

3. RESULTS & DISCUSSION

3.1 ZnO as a Transparent Conductive Oxide

Up till present, the most widely used Transparent Conducting Oxide (TCO) has been Sn-doped In_2O_3 (ITO). Recently, there has been a trend towards the substitution of wurtzite ZnO for ITO (particularly Al doped ZnO (AZO)). There are several reasons for this. Firstly, In is toxic, rare and costly, none of which apply to ZnO. Secondly, ZnO can be readily fabricated in crystalline form at relatively low temperatures compared with ITO [7]. Thirdly, ZnO is easier to process due to a greater amenability to chemical etching and a superior resistance to hydrogen plasmas than ITO. Fourthly, the properties of ZnO can be readily tuned by doping. For instance, doping with F gives ZnO the highest optical transparency and the lowest plasma frequency of all TCOs. Finally, both the μ and σ attainable with ZnO have improved considerably over recent years and AZO can now give resistivities comparable with ITO [8]. These properties have led to the adoption of ZnO for a number of TCO applications, such as transparent coatings for filtering of UV light and transparent contacts for use in flat panel displays, solar cells and LEDs. Figure 5 shows a schematic and the response of a liquid crystal with ZnO-based transparent contacts grown on glass substrates by PLD.

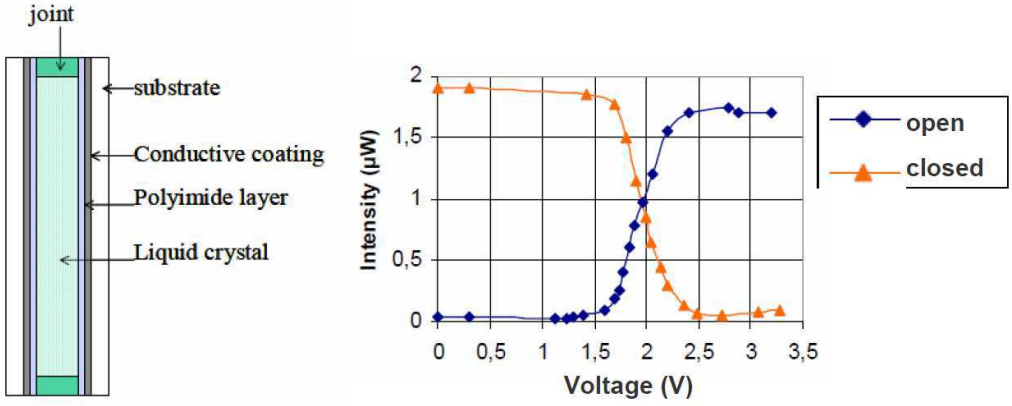

Figure 5. Schematic and open/closed transmissivity for a liquid crystal pixel activated via a ZnO TCO layer.

3.2 ZnO-Based Transparent Thin Film Transistors

Recently, there has been a surge of activity in the development of TTFT based on ZnO for use in applications such as Active Matrix Liquid Crystal Displays (AMLCD), electronic paper and flexible organic LED (OLED) panels. Although ZnO based TTFTs are not a new concept [9], the new generation exhibits a high on-off ratios (>106) and a higher channel μ than the Si-based devices, which are currently used as select transistor drivers in AMLCD and systems-on-glass. Two main ZnO TTFT variants, employing either wurtzite [10] or amorphous ZnO alloys [11] as channels, have emerged. Figure 6 shows a schematic plus transfer and output characteristics and for a staggered back-gate TFT with a wurtzite ZnO channel grown by PLD [12].

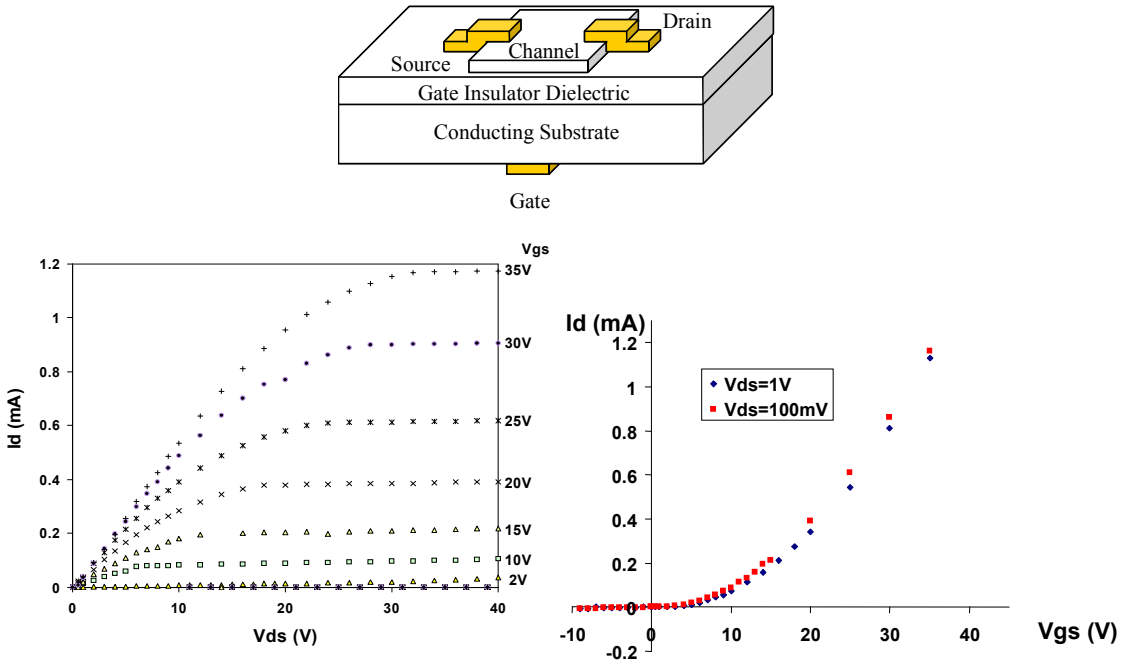

Figure 6. Schematic, transfer characteristic and output characteristics of a staggered back-gate TTFT [12].

The transfer characteristic (top) is rectifying, confirming transistor behaviour in the device. The VON is about 0V, which suggests that neither the electron nor the trap densities in the channel were too high. This device exhibited enhancement-mode behaviour, which is good for both energy efficiency (off-state is the power-down condition) and simplified circuit design. The lower (output) characteristics all showed "pinch-off" and "hard-saturation" (a plateauing of Id above a certain Vds), which suggests that the whole channel could be depleted of electrons. The Id is in the mA range, which is relatively large/good for a ZnO-based TFT. Such TFTs offer several advantages over incumbent Si-based devices. First of all, they are transparent, so that generally more light can be transmitted through each pixel, yielding a brighter, more efficient, display. This also means that the aperture ratio can be increased, so as to give smaller pixels. Next, state-of-the-art wurtzite ZnO and amorphous InGaNZnO (a-IGZO) TTFTs now exhibit channel μ as good as 250cm2/Vs and 12cm2/Vs, respectively, as compared with typical values of 100cm2/Vs and 1cm2/Vs for poly-Si and a-Si [13]. This gives faster device operation, which leads to a quicker response and an increased refresh rate. In addition, because of their wide bandgap, the ZnO based TTFTs have reduced sensitivity to light (ambient light has no significant effect on the current–voltage characteristics) and

less degradation on exposure to light compared with their a-Si counterparts. TTFTs made with a-IGZO are of particular significance because they give excellent performance when fabricated at RT, can be fabricated in large area format, are lighter and have better uniformity of properties (due, in part, to a lack of grain-boundaries). Moreover, their performance is stable and reproducible during and after repetitive bending, so they are compatibility with flexible substrates. This resolves the existing trade-off between processing temperature and device performance and allows fabrication on inexpensive heat-sensitive substrates such as transparent polymers or paper (poly-Si deposition temperature is too high for many flexible polymer substrates).

3.3 Use of ZnO in Photovoltaics

3.3.1 ZnO as an Adaptation Layer to Grow Novel InGaN-based Solar Cells on Cheap Substrates

Most commercial solar cells are based on amorphous Si (a-Si) and polycrystalline Si (poly-Si) and show relatively poor efficiencies (5-7 % and 13-15%, respectively). Recently, there has been a lot of work to try to develop solar cells with higher efficiencies. Multijunction cells employing alloys of InGaN currently present the highest theoretical efficiency. This is because of InGaN bandgap engineering know-how giving them superior capacity to absorb the solar spectrum. Indeed, efficiencies over 60% have already been demonstrated [14] and values over 70% are possible, theoretically. A key problem, however, is that InGaN does not crystallize readily on cheap substrates, so the cost of such cells is prohibitively high. PLD ZnO has proven to be much more crystallographically compliant to non-native substrates than MOCVD GaN. With a view to exploiting this, ZnO layers were used as buffer layers for MOVPE regrowth of InGaN. Figure 7 shows an SEM image of a fracture cross-section of an InGaN/GaN/ZnO/Si (111) sample with ~ 21.5% In [15].

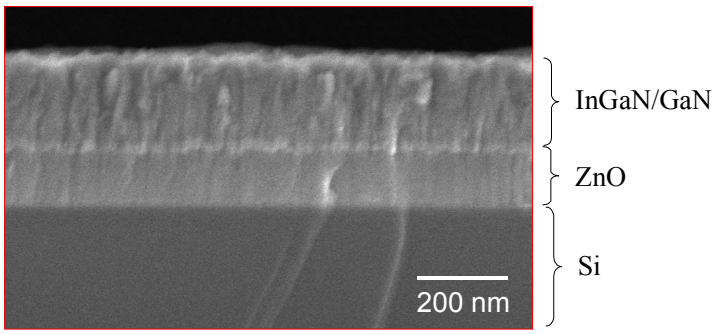

Figure 7. An SEM image of a fracture cross-section of an InGaN/GaN/ZnO/Si (111) sample.

The image reveals distinct InGaN/GaN and ZnO layers with a well-defined interface between the ZnO and InGaN/GaN. TEM [15] showed continuous lattice fringes across the interfaces with similar alignment and spacing in the InGaN/GaN and ZnO layers, suggesting that there had been epitaxial growth. Thus it was demonstrated that use of a PLD-grown ZnO buffer layer allows highly c-axis oriented wurtzite InGaN/GaN to be grown on Si substrates without removal of the amorphous SiO2 layer. Such an approach may open the way to the integration of InGaN based photovoltaics (and other devices) on cheap amorphous substrates, such as glass.

3.3.2 Nano ZnO as an Anti-Reflective (AR) Coating

Figure 8 shows SEM images of various self-forming ZnO nanostructures grown by PLD.

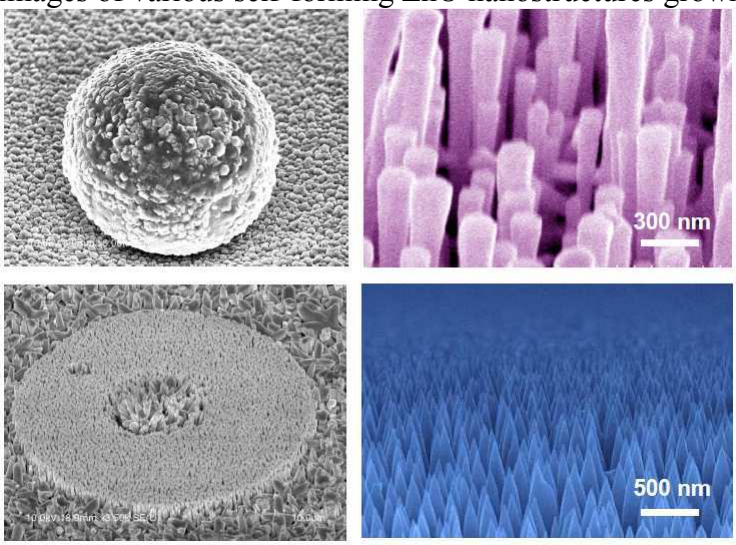

Figure 8 Examples of various self-forming ZnO nanostructures grown using PLD [16].

Figure 8 shows a microsphere assembly of nanocrystals, an annular microstructure made up of nanorods of different sizes, plus vertically aligned arrays of nanorods which either taper or broaden during growth. RT angular-dependent specular reflection measurements were conducted on the tapering "moth-eye type" version of these self-forming arrays, as shown in Figure 9 [17].

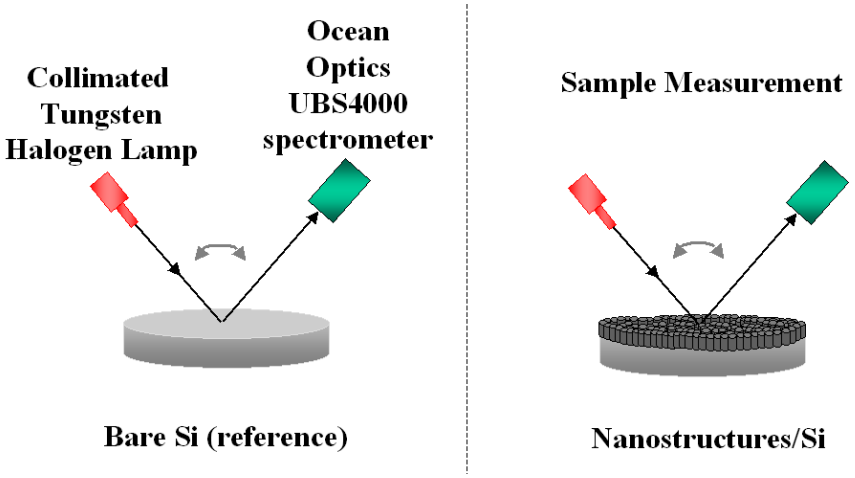

Figure 9. Schematics showing the angular-dependent specular reflection measurements set-up for a Si wafer with and without ZnO nanostructures on the surface.

These studies showed under 0.5% of reflected light between 450 nm to 800 nm for angles of incidence between 10 and 60 degrees. This indicates that the graded refractive index of such moth-eye type nanostructures could them to act as effective broad-band antireflection coatings for solar cells.

3.4 LEDs

3.4.1 ZnO Sacrificial Substrate Solution for GaN based LEDs

The future development of GaN based LEDs and LDs is being hampered by constraints imposed by non-native c-sapphire (c-Al_2O_3) and 6H-SiC substrates. ZnO substrates have a lower lattice mismatch than either of these substrates but have not been adopted industrially because they tend to dissociate in conventional GaN LED manufacturing process. Recently, the authors reported on a novel lower temperature approach to grow GaN on ZnO using MOVPE [18]. Figure 10 shows SEM image of MOVPE GaN grown on ZnO/c-Al_2O_3.

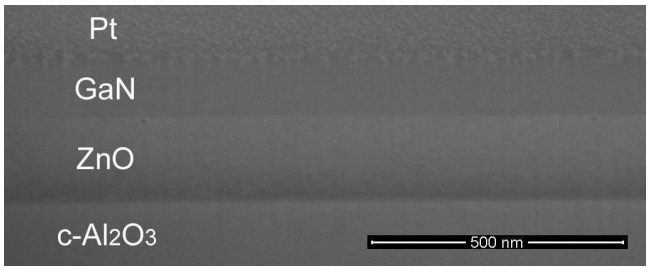

Figure 10. An SEM image of a fracture cross-section of MOVPE GaN grown on ZnO/c-Al_2O_3.

The image shows continuous GaN and ZnO with a smooth, well-defined interface. Since ZnO can be readily dissolved, subsequent lift-off of the GaN from insulating c-Al_2O_3 substrates was demonstrated through preferential chemical etching of ZnO. Such an approach opens up the possibility of wafer-bonding GaN LEDs onto electrically/thermally conducting substrates, as illustrated in Figure 11.

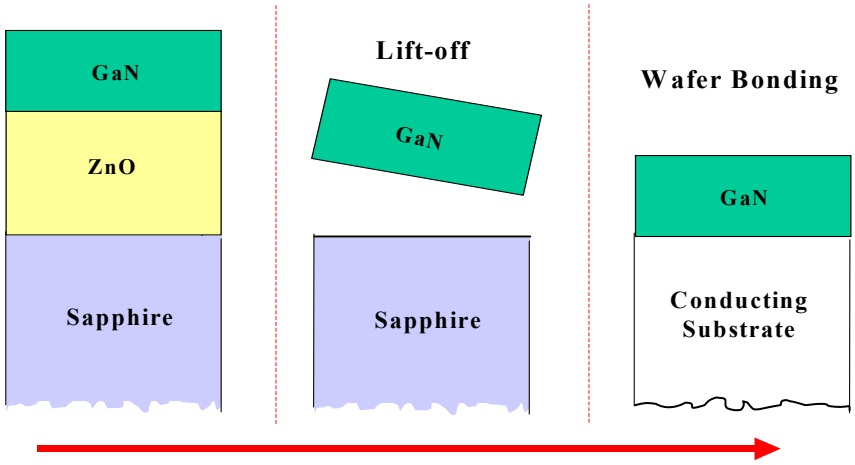

Figure 11. Schematic of GaN chemical lift-off via preferential chemical etching of ZnO followed by wafer bonding onto a conductive substrate.

Such an approach would allow vertical LED geometries with smaller footprints, improved heat dissipation, and reduced current crowding. These would, in turn, boost wafer yield and device performance in terms of efficiency, lifetime and brightness.

3.4.2 Hybrid UV LEDs

ZnO has been proposed as an active material for use in LEDs. One of the main driving forces for this is the superior stability of the ZnO free exciton (table 1 shows that ZnO has an exciton binding energy of 60 meV, vs. 21meV for GaN) [19]. A key roadblock, however, is the development of reliable p-type doping. Indeed, high levels of p-type doping, are hard to achieve in ZnO. This is because it has proven difficult to incorporate and activate sufficient acceptor concentrations in order to overcome the intrinsic n-type nature of ZnO. Indeed, native defects (O vacancies and Zn intersitials) and common background impurities (such as H, Al, and Ga) act as donors in ZnO and compensate the acceptors [20]. As an alternative to ZnO homojunctions, LEDs based on hybridization with p-GaN may profit from the ZnO exciton binding energy and the mature p-type doping know-how of GaN. Figure 12 shows a schematic of a n-ZnO/ p-GaN:Mg heterojunction LED plus the corresponding electroluminescence (EL) spectrum [21].

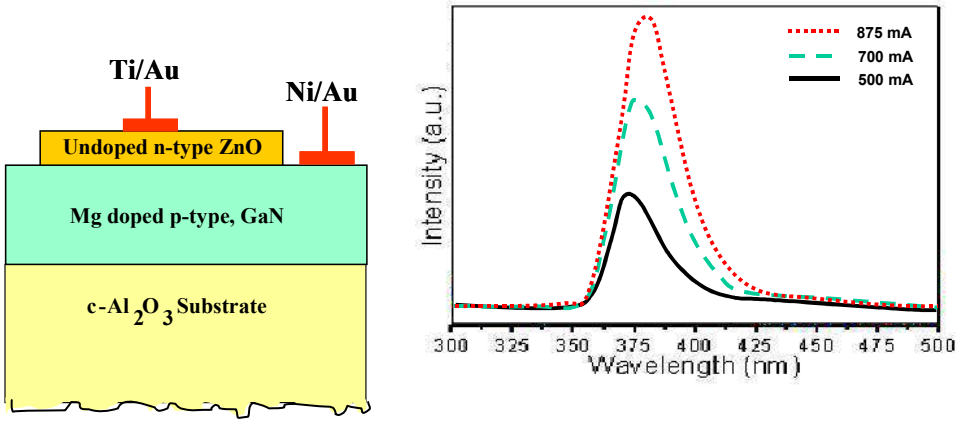

Figure 12, A schematic of the hybrid LED and the electroluminescence (EL) spectrum.

The spectrum exhibits a single peak in the near UV centred at around 375 nm. This is characteristic of Near Band Edge (NBE) emission from ZnO and indicates that there is radiative recombination in the ZnO layer. This implies that there was significant hole injection from the GaN:Mg into the ZnO and confirms that the EL in such hybrid devices may have the potential to profit from the elevated ZnO exciton binding energy.

3.4.3 Green Gap

AlInGaN-based LED performance is highly wavelength-dependent. In particular, the efficiency of LEDs drops off dramatically in the green: “the green gap” [22]. One of the main causes is that the elevated substrate temperature (Ts) necessary for the p-GaN causes In to leak out of the active layers in the InGaN/GaN multi-quantum-wells (MQWs). This severely compromises the brightness, efficiency, and lifetime of green LEDs. Figure 13 shows a schematic of a novel LED structure we developed to tackle this problem [23].

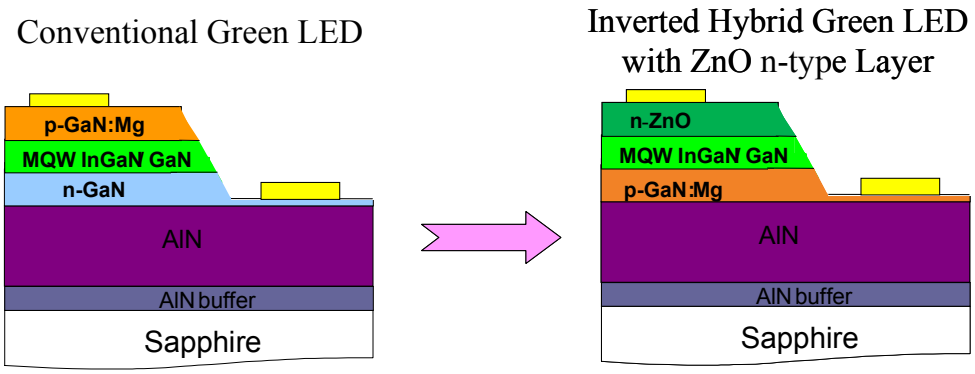

Figure 13. Schematic of inverted p-n junction green LED structure with n-ZnO substituted for n-GaN.

This LED has an inverted p-n structure, with n-type ZnO substituted for the n-type GaN. Through the use of PLD for the ZnO deposition, the top layer growth can be performed at significantly lower Ts. In this way, thermally induced degradation of the InGaN can be avoided and the integrity of the MQWs can be maintained. Prototype devices exhibited green EL peaked above 510 nm, as shown in Figure 14.

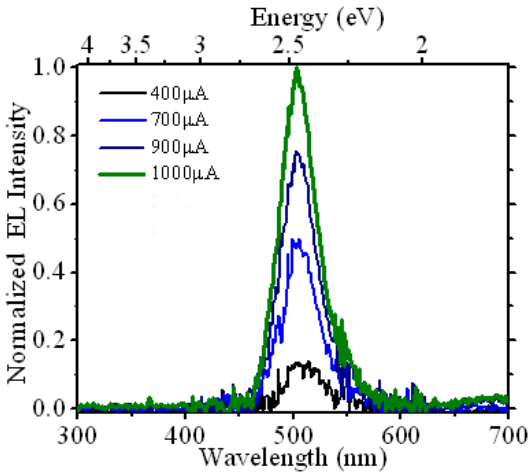

Figure 14. EL spectrum showing green emission from inverted hybrid heterojunction with PLD n-ZnO substituted for MOCVD n-GaN.

4. CONCLUSIONS

This paper illustrates how ZnO-based thin films and nanostructures grown by PLD can contribute to resolve issues in some key emerging optoelectronic applications. First of all, ZnO is currently displacing ITO for many TCO applications due to recent improvements in attainable AZO conductivity combined with processing, cost and toxicity advantages. Secondly, significant advances in the mobilities and Id on/off ratios which can be obtained with ZnO-based TTFTs have opened up the potential for replacing a-Si select FETs in future AM-OLED and LCD screens. Thirdly, reflection measurements of self-forming, moth-eye-like, nanostructure arrays revealed <0.5% reflectivity over the whole visible spectrum (for angles of incidence between 10 and 60 degrees). Such nanostructures may be useful for applications such as AR coatings on solar cells. Fourthly, PLD ZnO layers crystallise well on mismatched/amorphous substrates. Due to their similar crystal

structure, such ZnO films can be used as templates for epitaxial regrowth of GaN. This approach could be used to facilitate chemical lift-off of GaN-based LEDs from insulating sapphire substrates or allow the growth of InGaN-based solar cells on cheap substrates. Finally, LEDs based on the hybridisation of n-ZnO and p-GaN may be useful for the manufacture of UV and green LEDs. Simple n-ZnO/p-GaN heterojunction prototypes gave ZnO NBE UV EL peaked at around 375 nm. This suggests that there was significant hole injection into the ZnO and that such LEDs may profit from the relatively high exciton binding energy of ZnO. LEDs with an inverted p-n heterojunction (n-ZnO/InGaNMQW/p-GaN) were developed in order to combat the "green gap". Low Ts PLD growth of the top n-ZnO was employed in order to maintain the integrity of the InGaN/GaN MQWs. Prototypes gave green EL peaked at just over 510 nm.

ACKNOWLEDGEMENTS

The authors would like to thank the French "Association Nationale de la Recherche et de la Technologie" for financial support, Dr. G. Garry and co-workers at Thales Research and Technology for the liquid crystal tests, C. Bayram of Northwestern University for the green LED MOCVD work, Professor A. Ougazzaden and co-workers at the UMI CNRS/Georgia Tech Lorraine for the InGaN growth on ZnO, Professor J. Chapman and co-workers at the University of Glasgow for the SEM in Figure 10 plus Professor T. Monteiro and co-workers for the nanostructure reflectivity measurements.

REFERENCES

1. Chen et al. Mat. Sci. and Eng. B75 (2000) 190–198
2. www.nanomakets.com
3. Ozgur et al. J. Appl. Phys. 98, (2005) 0413011–30
4. Wang . *Scientific American*., Jan.(2008) 82-87
5. Rogers et al Proc. SPIE 5732, (2005) 412
6. Rogers et al. Proc. of SPIE Vol. 7217 (2009) 721708-1
7. Gordon. MRS Bull 25, (2000) 52–7
8. Minami Semicon. Sci. Technol. 20, (2005) 35–44
9. Boesen and Jacobs Proc. IEEE 56 (11), (1968) 2094–5
10. Hoffmann et al. Appl. Phys. Lett. 82, (2003) 733–5
11. Nomura et al Nature 432, (2004) 488–92
12. Rogers et al. Proc. of SPIE Vol. 7603 (2010) 760318-1
13. Nozawa Nikkei Electronics Asia November, (2007) 1024–30
14. Neufeld et al. Appl. Phys. Lett. 93, (2008) 143502
15. Ougazzaden et al. Proc. of SPIE Vol. 7603 (2010) 76031D-1
16. Sandana et al. J. Vac. Sci. Technol. B 27 (2009) 3
17. Peres et al. accepted for publication Physica Stat. Solidi (2010)
18. Rogers et al. Appl. Phys. Lett. 91,(2007) 071120
19. C. Klingshirn, Chem. Phys. Chem. 8 (2007) 782 – 803
20. Look Semicond. Sci. Technol. 20, (2005) 55–61
21. Rogers et al. Appl. Phys. Lett. 88, (2006) 141918
22. Peter, Compound Semiconductor, June (2008) 16-18
23. Bayram, Appl. Phys. Lett. 93, (2008) 081111.

Conclusion

AZO thin films are currently displacing ITO for many TCO applications due to recent improvements in attainable AZO conductivity combined with processing, cost and toxicity advantages. Advances in the channel mobilities and Id on/off ratios in ZnO-based TTFTs have opened up the potential for use as a replacement for a-Si in AM-OLED and AM-LCD screens. Angular-dependent specular reflection measurements of self-forming, moth-eye-like, nanostructure arrays grown by PLD were seen to have <0.5% reflectivity over the whole visible spectrum for angles of incidence between 10 and 60 degrees. Such nanostructures may be useful for applications such as AR coatings on solar cells. Compliant ZnO layers on mismatched/amorphous substrates were shown to have potential for MOVPE regrowth of GaN. This approach could be used as a means to facilitate lift-off of GaN-based LEDs from insulating sapphire substrates and could allow the growth of InGaN-based solar cells on cheap substrates. The green gap in InGaN-based LEDs was combated by substituting low Ts PLD n-ZnO for MOCVD n-GaN in inverted hybrid heterojunctions. This approach maintained the integrity of the InGaN MQWs and gave LEDs with green emission at just over 510 nm. Hybrid n-ZnO/p-GaN heterojunctions were also seen to have the potential for UV (375 nm) EL, characteristic of ZnO NBE emission. This suggests that there was significant hole injection into the ZnO and that such LEDs could profit from the relatively high exciton binding energy of ZnO.

III Mise en place d'une approche pour la fabrication de ZnO nanostructuré

Résumé

Comme decrit dans l'introduction, le premier grand objectif de cette these était de mettre au point la fabrication de nanostructures de ZnO et, ainsi, d'ajouter (à fabrication, existant, de couches minces par PLD) une platforme pour une nouvelle gamme de produits à base de nanostructures, comme schématise dans la figure 3.1.

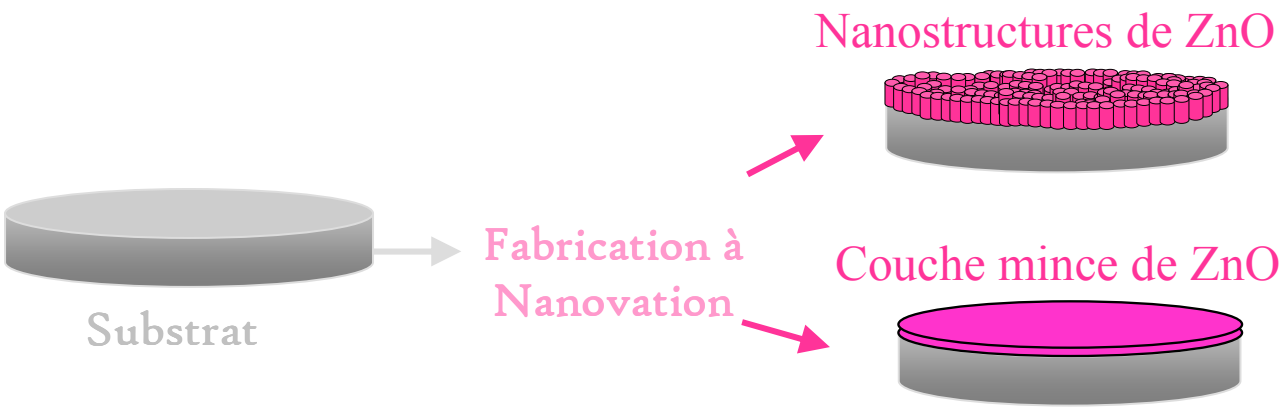

Figure III.1 Schéma de la fabrication des plaquettes de couches minces et des nanostructures de ZnO.

Ce chapitre présente, donc, deux articles dont l'objectif est de déterminer quel procédé de fabrication est le mieux adapté pour la croissance de nano ZnO dans le cadre des applications optoélectroniques visées (cf. p. 6). Il existe deux approches permettant de fabriquer des nanostructures :
-Bottom-up : Ce terme « de bas en haut » décrit un processus dans lequel chacune des étapes technologique successives apporte un élément nouveau et fondamental pour la structure finale ;
-Top-down : Ce terme « de haut en bas » caractérise un procédé technologique au cours duquel une partie ou l'ensemble des éléments intermédiaires sont enlevés pour parvenir à la structure finale.
L'approche choisie dans cette étude est la formation de type bottom up. Ce sujet est développé dans ce chapitre.

Croissance de type VLS

La croissance de nanocolonnes unidimensionnelles a été démontrée en 1960 par Wagner et al. [1] Une théorie correspondant à ce processus fut développée : le mécanisme gaz-liquide-solide (en anglais VLS : Vapor-Liquid-Solid) qui peut être décrit en deux grandes étapes illustrées sur la figure suivante :

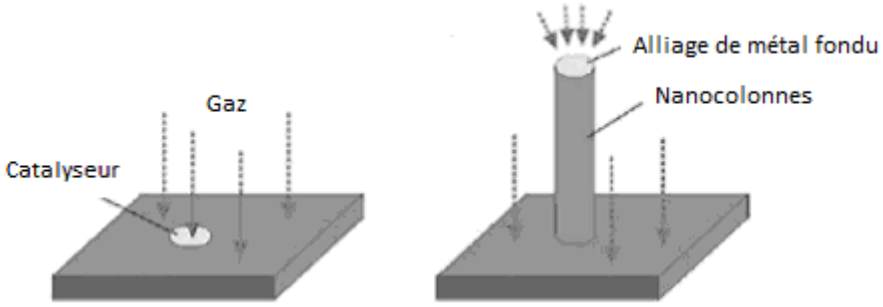

a) b)

Figure 3.2 : Schéma du principe de mécanisme de croissance par PVT.

a) Le catalyseur sous forme liquide est en contact avec le gaz qui amène le matériau à déposer sous forme vapeur ; b) Formation d'une gouttelette d'alliage liquide entre le catalyseur et le matériau amené par le gaz. Lorsque cet alliage arrive à saturation, il y a diffusion du matériau à déposer à travers la gouttelette puis formation d'une nanocolonne sous celle-ci.

Dans un premier temps se forment des catalyseurs (des métaux) en phase liquide (cf. figure 3.2 a). Dans un second temps, le gaz amène sous forme vapeur le matériau que l'on souhaite faire croître sous forme de nanocolonnes, ce qui permet la nucléation et la croissance de nanocolonnes (cf. figure 3.2 b). La croissance a lieu sur une partie de la surface du substrat. Généralement les substrats utilisés sont des semi-conducteurs, mais l'utilisation de saphir ou de verre est possible.

Le premier article se focalise sur l'utilisation de catalyseur métallique, dans le cas présent Au, pour permettre la croissance de nanostructures ordonnées de ZnO et ce sur deux substrats : Si (111) et c-Al_2O_3. Le procédé de croissance utilisé est la MOCVD. L'étude porte sur l'aspect morphologique des couches d'or après recuit et de ZnO après dépôt par MOCVD. Sous des conditions optimisées, une distribution relativement homogène de nano-gouttelettes d'or a été obtenue. Les images réalisées par microscopie électronique à balayage (MEB) ont permis d'observer une grande variété de nanostructures : des nanopointes, des nanocolonnes et des nanotubes. Mais de nouvelles structures ont aussi pu être observées tel que des nanocolonnes multifacettées.

Le second article compare trois procédés de croissance pour les nanostrucutres de ZnO : PVT, PLD et MOCVD. Il permet de déterminer quel est le procédé le mieux adapté aux exigences recherchées pour la fabrication de composants optoélectroniques. Les formes et les propriétés des nanostructures déposées sur Si(111) et c-Al_2O_3 ont été comparées en fonction de leurs procédés de croissance. Une grande variété de nanostructures a été observée : nanocolonnes, nanopointes, nanopeignes et de nouvelles structures comme des nanocolonnes multifacettées. La croissance par PVT donne la plus grande variété de formes de structures. La PLD produit une forte densité de nanocolonnes de formes et tailles homogènes et perpendiculaires aux substrats, et ce sans l'utilisation de catalyseur. L'étude par diffraction X (XRD) confirme que les nanostructures réalisées par PLD sont mieux cristallisées et plus orientées (selon l'axe c) que celles préparées par PVT ou MOCVD.

Après étude de ces différents procédés, il a pu être déterminé que la PLD est le procédé le mieux adapté à la fabrication des nanostructures de ZnO : nanostructures autoformées,

alignées, verticales, présentant un indice de réfraction gradué et des températures de déposition relativement basses.

Mon travail dans cette étude a consisté dans un premier temps à mettre en place un bati d'évaporation thermique pour pouvoir déposer des couches minces d'or sur des substrats comme présenté dans les images de la figure 3.3 et 3.4 Le principe de l'évaporation thermique sous vide est une technique par voie physique qui permet de produire des vapeurs de divers métaux. Le métal solide est placé dans creuset puis porté à une température supérieure à sa température de fusion par effet Joule et s'évapore sur le substrat.

Chambre

Électrodes

Porte-Echantillon Rotatif

Figure 3.3 : Photos des éléments réalisés pour le montage du bâti d'évaporation thermique.

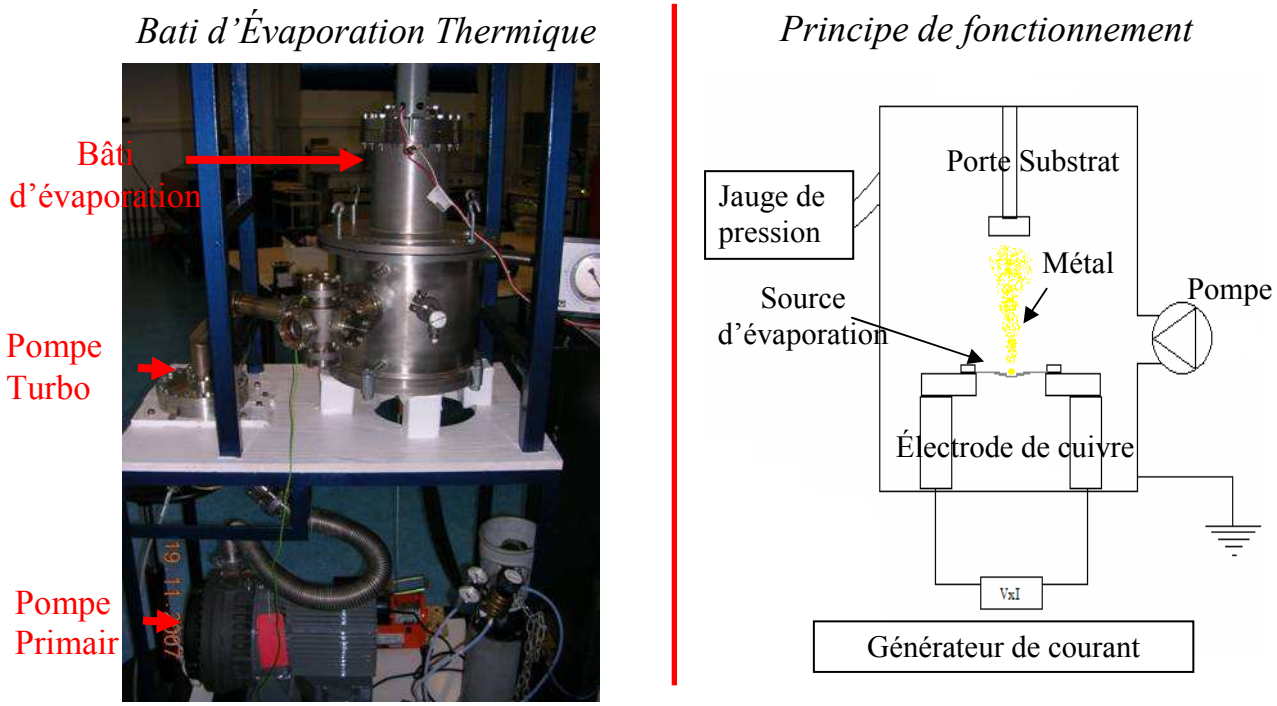

Figure 3.4 : Photo du montage final du bâti d'évaporation thermique et schéma du principe de fonctionnement.

Ensuite il a fallu déterminer les conditions optimales de recuit de ces couches pour obtenir des gouttelettes d'or de taille et forme homogène. J'ai effectué l'ensemble des caractérisations de photoluminescences et des images MEB présentées dans ce chapitre. Les images ont permis l'analyse via le logiciel *image J* de la distribution des gouttelettes d'or et leur homogénéité en fonction des condition de recuit (température et durée). La croissance de nanostructures de ZnO par MOCVD a été réalisée en collaboration avec le laboratoire GeMAC auquel j'ai fourni des substrats recouverts de gouttellette d'or. J'ai mis en place le procédé de croissance par PVT et déterminé les conditions de croissance des nanostructures de ZnO par PVT et PLD.

Référence

[1] R. S Wagner and W. C. Ellis, Appl. Phys. Lett. **4** (5), 89 (1964).

3.1 *MOCVD Growth of ZnO Nanowires Using Au Droplets as Catalysts*

V. E. Sandana et al. Proc. SPIE, 6895, (2008). 68950Z-68950Z-6

V. E. Sandana[a,b,c], D. J. Rogers[a], F. H. Teherani[a], R. McClintock[b],
M. Razeghi[b], H.-J. Drouhin[c], M.C. Clochard[c], V. Sallet[d], G. Garry[e], F. Falyouni[d].
[a]Nanovation, 103B Rue de Versailles, 91400 Orsay, France.
[b]Center for Quantum Devices, Northwestern University, Evanston, Il 60208, USA;
[c]Department of Irradiated Solids, École Polytechnique, 91128 Palaiseau, France.
[d]GEMAC, 45 avenue des États-Unis, 78035 Versailles, France.
[e]Thales Research & Technology, Route Départementale 128, F-91767 Palaiseau, France.

1. INTRODUCTION

ZnO is a remarkable multifunctional material with a distinctive set of properties including a direct bandgap of ~3.37eV, high transparency over the visible spectrum, a very wide range of obtainable conductivities and a remarkably high piezoelectric response. Thus ZnO has many established and emerging applications including varistors, contacts, light emitting diodes [1] and surface acoustic wave devices [2]. Unidimensional ZnO structures, such as nanowires and nanoneedles, also have many potential applications based on this same property set augmented with quantum phenomena of the nanoworld [3].
ZnO nanowires are often synthesised by vapor transport based on a vapor–liquid–solid (VLS) growth mechanism using a metal catalyst such as Au or Cu droplets [4,5,6]. In this case, the metal catalyst can act to both promote alignment of the ZnO nanostructures and to provide a template for their size and distribution [3]. Thus a method for obtention of a regular array of metallic nanodroplets of homogeneous form/size is required. However, recent studies show that well-aligned ZnO nanorods can be grown by Metal Organic Vapor Deposition (MOCVD) without using a metal catalyst [6].
This work reports on preliminary studies into the preparation and use of self-forming Au droplets as catalysts for the MOCVD growth of ZnO nanostructures.

2. EXPERIMENT

5 nm thick Au layers were deposited on 1cm x 1cm Si (100) and c-Al_2O_3 substrates using thermal evaporation. Thermal annealing was employed in order to promote the formation of Au nanodroplets. The anneals were conducted at atmospheric pressure in air using a horizontal tubular furnace. The impact of annealing on the Au layer was studied as a function of annealing time (from 30s to 5 min) and temperature (from 300°C to 800°C).
ZnO was deposited by MOCVD in a water-cooled vertical quartz reactor with an inner diameter of 40mm in the growth zone. Dimethyl zinc triethylamine ($(CH_3)_2Zn\text{-}N(CH_2CH_3)_3$) was used as the Zn source and N_2O gas was used as the as an O source. The carrier gas was N_2 and the flow rate was

500 sccm. The substrate was placed in the middle of the reactor on a graphite susceptor, which was inclined at 45° to the vertical. The susceptor was heated to 800°C during film growth using a radio frequency (rf) spire.
The sample morphology was studied using a Hitachi S4800 Field Emission-Scanning Electron Microscope (FE-SEM). The local composition was investigated in situ in the SEM using an Energy Dispersive X-ray (EDX) micro fluorescence system. "IMAGE-J" software was used in order to do statistical analysis of the Au droplet distribution [7].

3. RESULTS

3.1 Annealing of the Au-Coating

Figure 1 shows SEM pictures of Au-coated Si (100) as a function of annealing temperature from 300°C to 800°C for an annealing time fixed at 5 minutes.

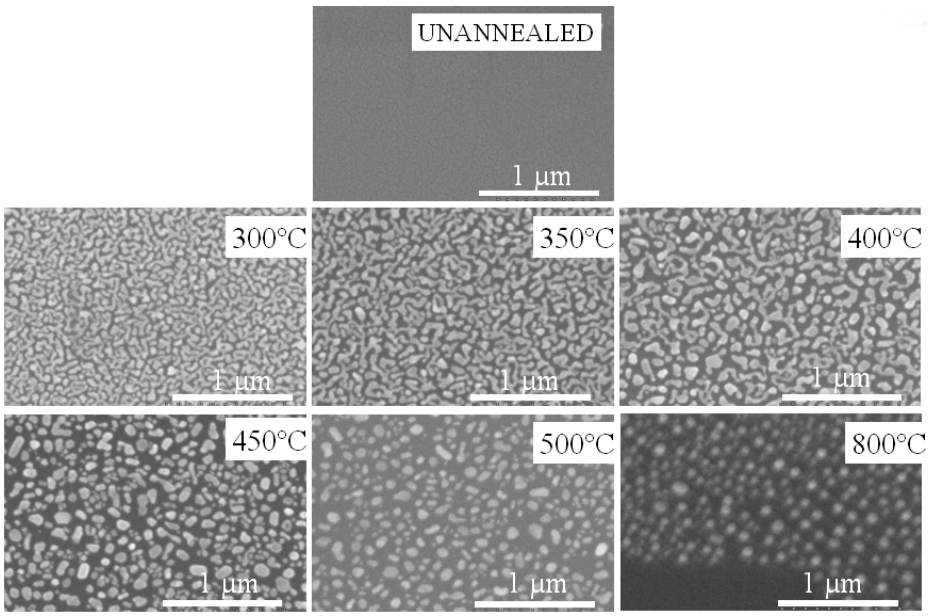

Figure 1. Morphological evolution of the Au layer as a function of annealing temperature.

Figure 2 shows the mean size (top-down cross-sectional area as calculated by "IMAGE J" software) of the Au nanodroplets as a function of annealing temperature.

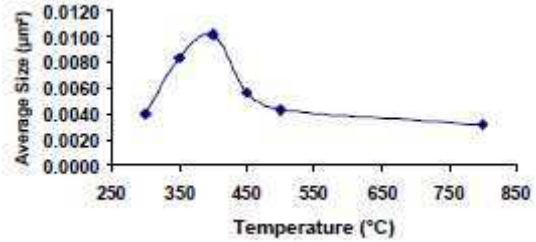

Figure 2. Mean size of the Au nanodroplets as a function of annealing temperature

The average size of the nanodroplets increases with annealing temperature between 300°C and 400°C. The corresponding SEM images (Figure 1) show that this corresponds to the Au film progressively breaking up into discrete Au droplets. Above 400°C the average size of the Au droplets drops off rapidly with increasing annealing temperature up to about 475°C then falls off much more slowly with increasing temperature up to 800°C. This process can be explained as the result of Au droplet surface energy minimisation considerations dominating over the sticking coefficient with the substrate. The associated standard deviations in droplet size decreased gradually with increasing anneal temperature, as might be expected for Ostwald ripening [8]. Thus 800°C was chosen as the best temperature for obtention of the finest and most regular distribution of nanodroplets.
Figure 3 shows SEM pictures of the Au-coated Si (100) as a function of annealing time for an annealing temperature of 800°C.

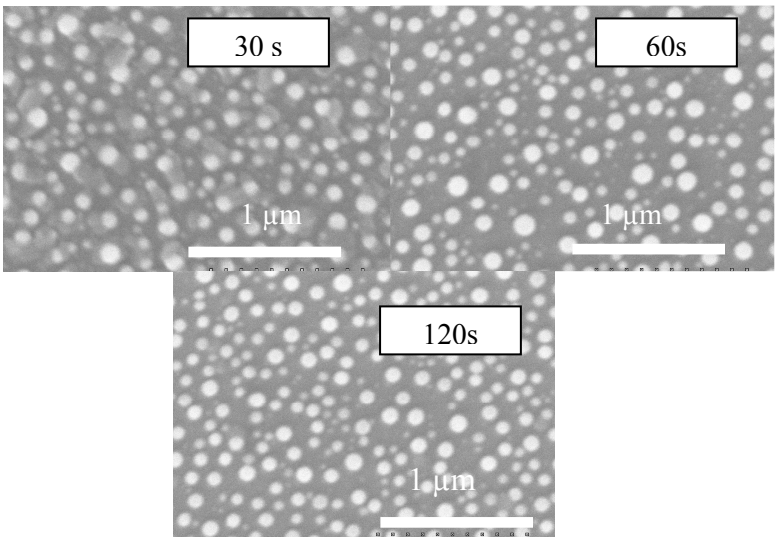

Figure 3. SEM pictures of the morphology of an Au-coated Si (100) substrate for annealing times from 30s to 120s.

Figure 4 shows the evolution of island size with annealing time. After 60s of annealing the average size of the nanoislands remained the same.

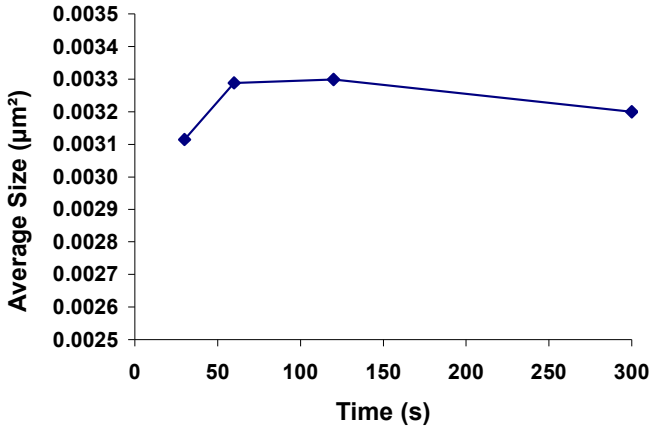

Figure 4. Mean size of the Au nanoislands as a function of annealing time.

Between 60s and 300s, annealing time does not appear to strongly influence the average nanodroplet size. The standard deviation in droplet size occurred at 60s, however, so an anneal of 60s at 800°C was adopted.

3.2 ZnO Deposition by MOCVD

The second step of the process was to grow ZnO by MOCVD. A growth temperature of 800°C was chosen based on previous experience. Three different substrates were used for the MOCVD deposition process:
1) Au-coated c-Al_2O_3 which was not pre-annealed
2) Au-coated Si (100) which was not pre-annealed
3) Au-coated Si (100) which was pre-annealed at 800°C for 1 minute.

3.2.1 MOCVD Growth at 800°C of ZnO on Au-coated Al_2O_3 (without pre-annealing)

Figure 5 shows an SEM image of some ZnO nanostructures obtained on the Au-coated c-Al_2O_3 which was not pre-annealed.

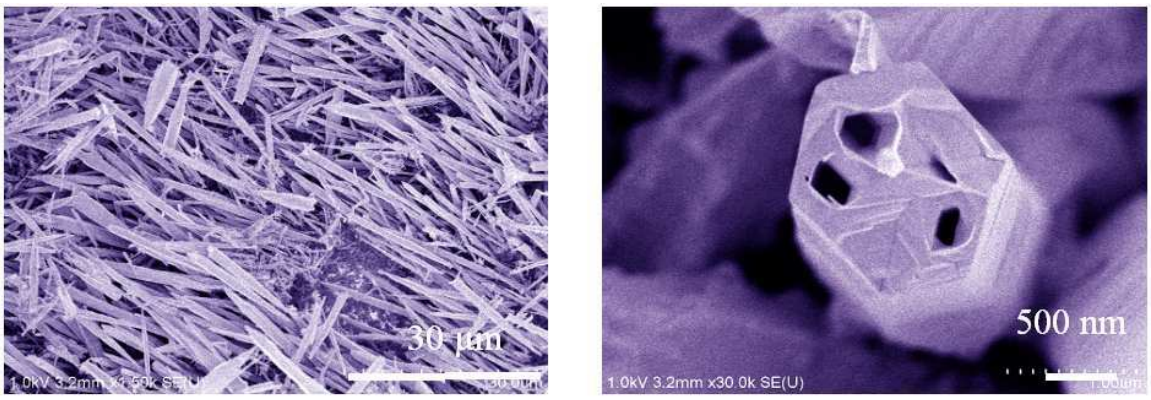

Figure 5. SEM Pictures of ZnO on Au-coated c-Al_2O_3 which was not pre-annealed.

In the image on the left hand side of Figure 5 we can see a forest of nanocolumns/wires of rather uniform diameter and length (typically 1.5 and 30 μm respectively). The majority of the columns appear to have a preferred orientation perpendicular to the substrate plane. The higher magnification image on the right side reveals that some of these nanostructures are partially-hollowed such that the best description of their form might be hexagonally-faceted nanotubes. The origin of this hollowing is unclear.
EDX analysis of these nanotubes revealed strong Zn and O signals and a trace amount of Al but no trace of Au. Thus the location and the role of the Au is also unclear.

3.2.2 MOCVD Growth at 800°C ZnO on Au-coated Si (without pre-annealing).

A variety of different nanostructures was observed on this sample. Figure 6 shows some representative SEM images.

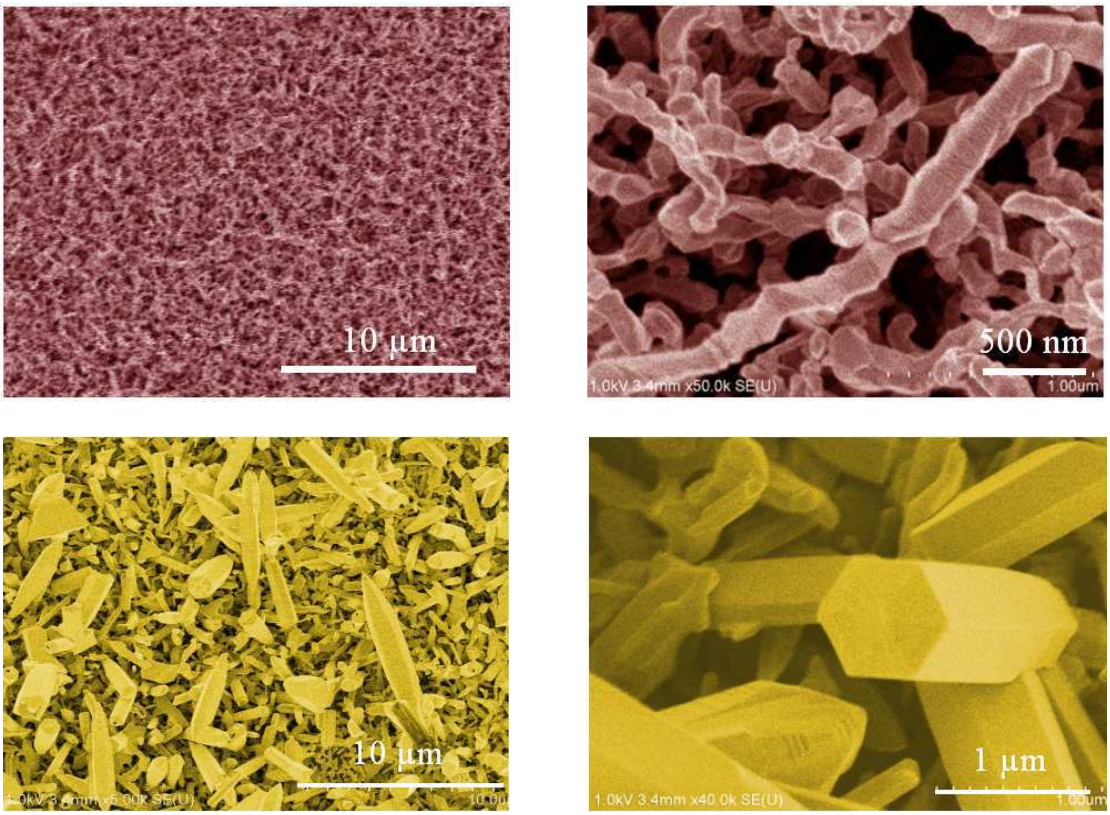

Figure 6. SEM pictures of ZnO nanostructures grown by MOCVD on Au-coated Si without pre-annealing

The nanostructures in the upper part of Figure 6 were observed at the centre of the sample while those in the lower part were observed near the edge of the sample. The nanostructures in the centre of the sample resemble interwoven jointed twisted-cords (they might also be described as twist-pastry-like). They have no obvious preferred orientation and they are relatively long, although their

length is difficult to estimate. Their diameter is quite homogeneous, between approximately 100 and 200nm.
The nanostructures from near the edge of the sample are hexagonally faceted and resemble nano-needles or nanocolumns/rods. They are of various lengths and diameters (up to 10 microns and 1.5 microns respectively) and appear to have random orientation.
As well and Zn, O and Si, EDX analysis of these nanostructures showed traces of Au. It is not possible to deduce where it is located but the signal indicates that the Au does not evaporate under these growth conditions.

3.2.3 MOCVD Growth of ZnO at 800°C on pre-annealed Au-coated Si (100)

Figure 7 shows SEM pictures of the ZnO nanostructure obtained on top of the Au-coated Si substrate which was pre-annealed at 800°C for 1 minute prior the MOCVD process.

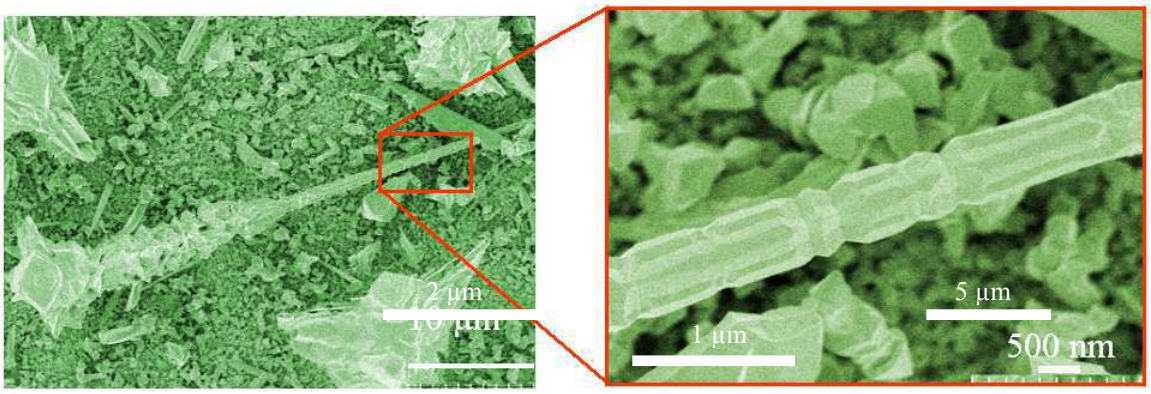

Figure 7. SEM images of ZnO grown on pre-annealed Au-coated Si

A wide range of nanostructures, of varying form and size, was observed in this sample. Of particular note was a region expanded in Figure 7 which showed a remarkable nanorod with 12 fold faceting and a bevelling which resembles a table leg. EDX revealed Zn, O and Si plus trace amounts of Au.

4. CONCLUSIONS

The influence of air annealing on 5nm thick Au films on Si (100) and c-Al_2O_3 substrates was studied as a function of temperature and duration. Au nanodroplets formed and grew spontaneously. The finest droplets and most regular distribution were obtained for an anneal of 60s at 800°C.
ZnO nanostructures were grown on the Au-coated Si (100) and c-Al_2O_3 by MOCVD. Even after pre-annealing, a regular distribution of preferentially oriented ZnO nanocolumns was not obtained. A myriad of other nanostructures was observed, however, including well-known ZnO nanostructures such as hexagonal nanorods, nanoneedles and nanotubes. Some novel ZnO nanostructures were also observed, including beveled & faceted table-leg-like structures and twist pastry like structures.
EDX analysis showed that the Au was still present after the MOCVD ZnO growth but it could not be localized. It is not clear whether or not the Au plays the role of a catalyst or not in these ZnO growths. Further investigations are underway.

REFERENCES

1. D. J. Rogers, F. H. Teherani, Appl. Phys. Lett. **91**, 071120 (2007)
2. M. Zerdali, S. Hamzaoui, F.H. Teherani and D. Rogers, Materials Letters 60:44, 504-508, (2006)
3. G. Zhang, A. Nakamura, T. Aoki et al., Appl. Phys. Lett. **90**, 203515 (2007)
4. S.Y. Li, P. Lin, C.Y. Lee, et al., , J. Appl. Phys. 95 (2004) 3711.
5. S.Y. Li, P. Lin, C.Y. Lee, et al., J. Cryst. Growth 247 (2003) 357.
6. M.H. Huang, Y. Wu, H. Feick, et al., Adv. Mater. 13 (2001) 113.
7. National Center for Biotechnology Information, http://rsb.info.nih.gov/ij/
8. J. B. Hannon, S. Kodambaka, F. M. Ross et al., NaturesVol 440|2 March 2006

3.2 *Comparison of ZnO nanostructures grown using pulsed laser deposition, metal organic chemical vapor deposition, and physical vapour transport*

V.E. Sandana et al. J. Vac. Sci. Technol. B 27(3), May/Jun 2009

V. E. Sandana
Nanovation, 103B Rue de Versailles, 91400 Orsay, France; Center for Quantum Devices, Northwestern University, Evanston, Illinois 60208; and Department of Irradiated Solids, Ecole Polytechnique, 91128 Palaiseau, France
D. J. Rogers and F. Hosseini Teherani
Nanovation, 103B Rue de Versailles, 91400 Orsay, France
R. McClintock, C. Bayram, and M. Razeghi
Center for Quantum Devices, Northwestern University, Evanston, Illinois 60208
H.-J. Drouhin and M. C. Clochard
Department of Irradiated Solids, Ecole Polytechnique, 91128 Palaiseau, France
V. Sallet
GEMAC, 45 avenue des Etats-Unis, 78035 Versailles, France
G. Garry
Thales Research & Technology, Route Départementale 128, F-91767 Palaiseau, France
F. Falyouni
GEMAC, 45 avenue des Etats-Unis, 78035 Versailles, France

I. INTRODUCTION

ZnO is a remarkable multifunctional material with a distinctive set of properties, including a direct bandgap of ≈ 3.37 eV, high transparency over the visible spectrum, a very wide range of possible conductivities, and a strong piezoelectric response. Thus ZnO has many established and emerging applications including varistors, light emitting diodes[1] (LEDs) and surface acoustic wave devices.[2] Nanostructuration of ZnO[3] further extends the range of potential applications by augmenting the basic property set with phenomena unique to the quantum world. .[4] Indeed, nanostructured ZnO has become a huge research topic with more publications in 2008 than even carbon nanotubes.[5] There are many reasons driving this interest, including the unique property set of ZnO, .[6] the ease of fabrication of ZnO nanostructures with a wide range of techniques, .[7] the wide range of emerging and potential applications,[8] the biocompatibility of ZnO,[9] and the enormous family of nanostructures exhibited by ZnO (probably the largest of any nanomaterial [6,10]). Although ZnO has been grown with a vast range of different techniques, direct comparison of the properties of nanostructures grown with different methods is lacking in the literature. This article compares the forms, crystallographic properties, and optical properties of ZnO nanostructures prepared using three common growth processes: metal organic chemical vapor deposition (MOCVD), pulsed laser deposition (PLD), and physical vapor transport (PVT). Three different techniques were employed in order to facilitate exploration of the relative merits of each approach.

II. EXPERIMENT

Both Si (111) and c-plane sapphire (c-Al_2O_3) were used as substrates for the three growth processes

A. MOCVD

ZnO was deposited by MOCVD [Fig. 1(a)] in a watercooled vertical quartz reactor with an inner diameter of 40 mm in the growth zone. The Zn source was dimethyl zinc triethylamine (DZT) [$(CH_3)_2Zn\text{-}N(CH_2CH_3)_3$] and the carrier gas was N_2. The flow rate was 500 SCCM (SCCM denotes cubic centimeter per minute at STP) for the carrier gasand the DZT combined. N_2O gas was used as the O source and its flow rate was also 500 SCCM. The substrate was placed in the middle of the reactor on a graphite susceptor, which was inclined at 45° to the vertical. The susceptor was heated to 800 °C during film growth using a radio frequency (rf) coil.

B. PVT

ZnO was deposited by carbothermal evaporation in a tubular furnace with an inner diameter of 30 mm [Fig. 1(b)]. A 2g (1:1 mass ratio) mix of ZnO and graphite powders was used for the growth and covered a 1 cm^2 surface. N_2 was used as the carrier gas at 80 SCCM gas flow rate. Both outlets of the furnace were kept open to ambient air. A ceramic holder with the powder was inserted into the quartz tube when the furnace temperature stabilized at 1100 °C. The c-Al_2O_3 and Si (111) substrates were placed with a distance of 5 cm from the end of the powder boat to the beginning of the substrate. The reaction time was 30 min.

C. PLD

ZnO nanostructures were grown from a 99.99% pure ZnO target by PLD [Fig. 1(c)] using a KrF excimer laser (248 nm) as described elsewhere.[11,12]

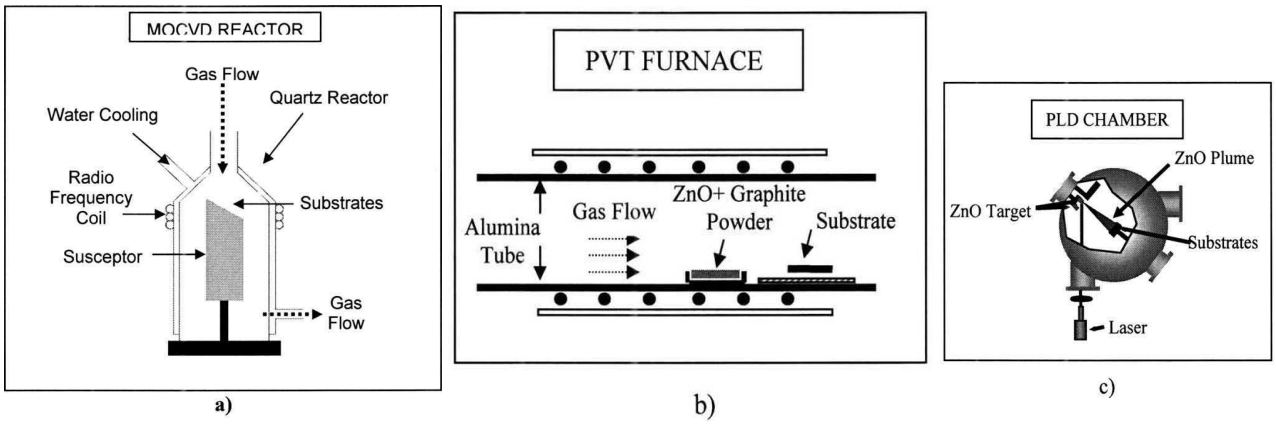

FIG. 1. Growth process schematics of a) MOCVD, b) PVT, and c) PLD.

III. CHARACTERIZATIONS

The sample morphology was studied using a Hitachi S4800 field emission-scanning electron microscope (SEM). The crystal quality of the nanostructures was investigated using x-ray diffraction (XRD) performed in a Panalytical MRD Pro system using Cu Kα radiation. The x-ray optics and spot size were kept the same for all samples. Optical properties were studied via room temperature

photoluminescence (PL) with a continuous-wave frequency-doubled argon ion laser (244 nm, power of 30 mW)

IV. RESULTS
A. SEM investigations

1. SEM images for MOCVD growth of ZnO

SEM images for MOCVD growth of ZnO on c-Al_2O_3. Figure 2(a) is a SEM image for a MOCVD growth on c-Al_2O_3. The image shows a forest of microcolumns/wires of rather uniform diameter and length (typically 1.5 and 30 μm, respectively). The majority of the columns have a preferred orientation perpendicular to the substrate plane. The higher magnification image shown in Fig. 2(b) reveals that some of these microstructures are partially hollowed, such that the best description of their form might be hexagonally faceted nanotubes. The origin of this hollowing is still under consideration.

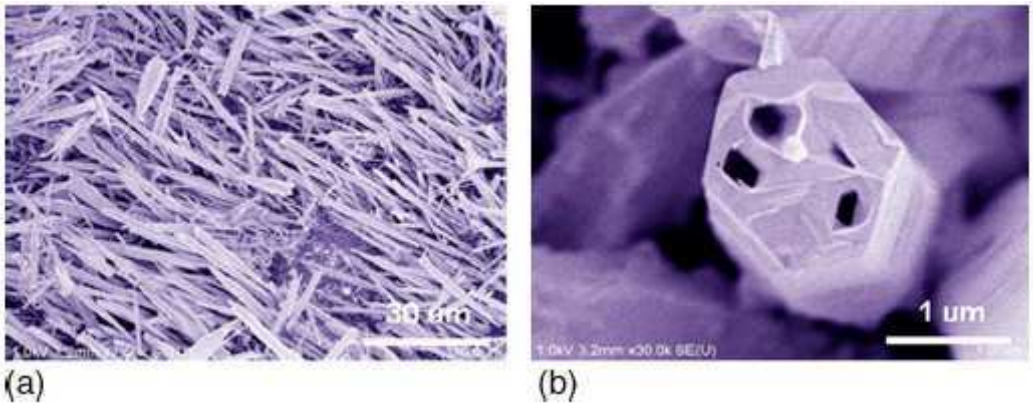

FIG. 2. SEM images of ZnO on c-Al_2O_3 grown by MOCVD.

For growth on Si (111), a wide range of microstructures of varying form and size was obtained. For one particular region expanded in Fig. 3(b), an unusual microrod structure with 12 facets and a structure which resembles bevelling of a table leg were observed. The presence of this atypical microstructure could be related to an effect of the Si substrate, since microstructures on c-sapphire did not show this form or symmetry. A suggested growth process for similar structures reported in the literature [13,14] proposes (a) that such faceting can result from preferential lateral growth along the (01-10) (11- 00), and (1-010) directions to give the faceted crystallitesand (b) that the bevelling can be the interfaces between many independently formed crystallites which combine along the axis of the rod.

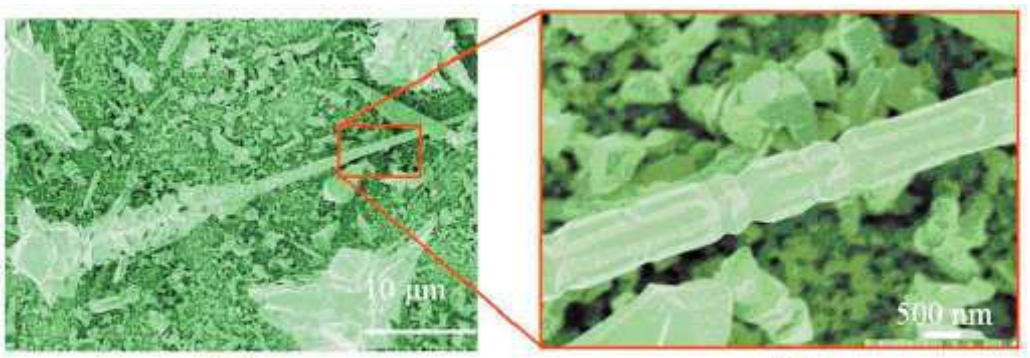

FIG. 3. SEM images of ZnO grown on Si (111) by MOCVD.

2. SEM images for PVT growth of ZnO

SEM images for PVT growth of ZnO on c-Al_2O_3. A very wide range of ZnO nanostructures, of varying form and size, were observed for samples grown by PVT on c-Al_2O_3. No preferred orientation was observed. Figure 4(a) shows pyramidal, faceted structures. Figure 4(b) shows typical nanowire type structures for which a suggested growth mechanism has been proposed elsewhere: [15,16] the reaction of Zn vapor and O form a hexagonal columnar base on the substrate [Figure 4(a)]. On top of this hexagonal base [the (0001) plane], a nucleation of ZnO particles can occur, leading to a full ZnO hexagonal columnar pin [Fig. 4(b)]. SEM images for PVT growth of ZnO on Si (111).

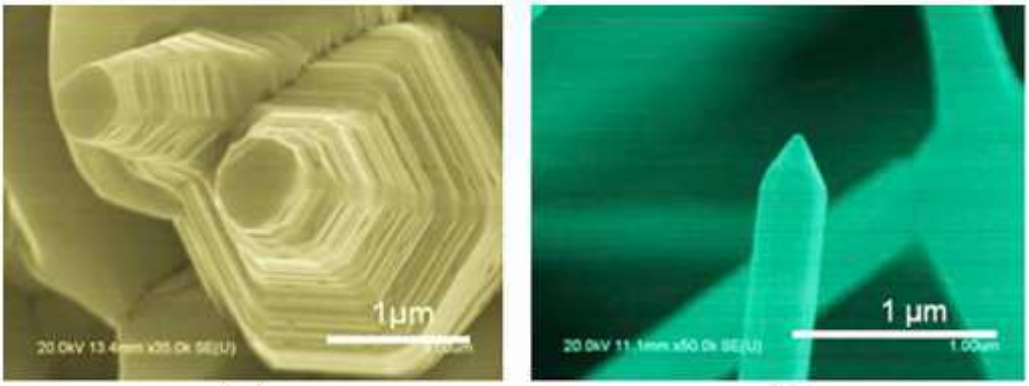

FIG. 4. SEM images of ZnO nanostructures on c-Al_2O_3 grown by PVT.

The growth of ZnO on Si (111) by PVT also presented a very wide range of nanostructures of varying form, size, and orientation. Of particular note was a region, expanded in the SEM image in Fig. 5(a), which showed a remarkable ZnOnanocomb- like structure. A possible growth process for such structures has also been proposed in the literature: [17] at the initial stages of growth, Zn and O combine on the substrate to form a microwire. During subsequent growth, the combined effect of diffusion gradients, different relative growth rates, and thermal perturbations cause inhomogeneous nuclei to form on the surface of the microwire. Nanowires then grow on these nuclei to form the nanocomblike structure. Commonly observed, hexagonally faceted, nanowires were also visible in the same sample [Fig. 5(b)].

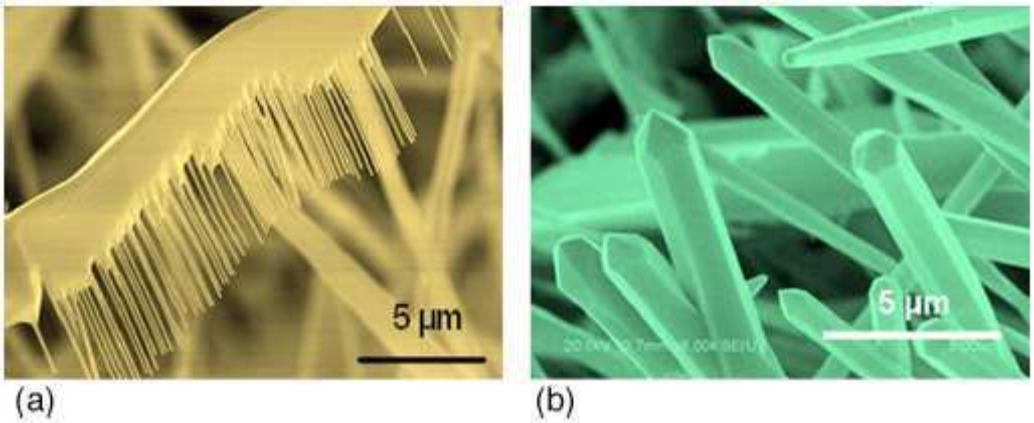

FIG. 5. SEM images of ZnO nanostructures on Si(111) grown by PVT.

3. SEM images for PLD growth of ZnO

Figure 6(a) shows a typical region of sample for the ZnO nanostructures grown on c-Al_2O_3 by PLD. The image shows a high density array of nanostructures of rather similar shape with a strong preferred orientation perpendicular to the substrate plane. The higher magnification image in Fig. 6(b) reveals that some of these nanostructures look something like incomplete nanotubes. The growth process for such nanostructures is unclear but the structures indicate a preferential growth along both the c-axis and one basal plane axis.[16] SEM images for PLD growth of ZnO on Si (111).

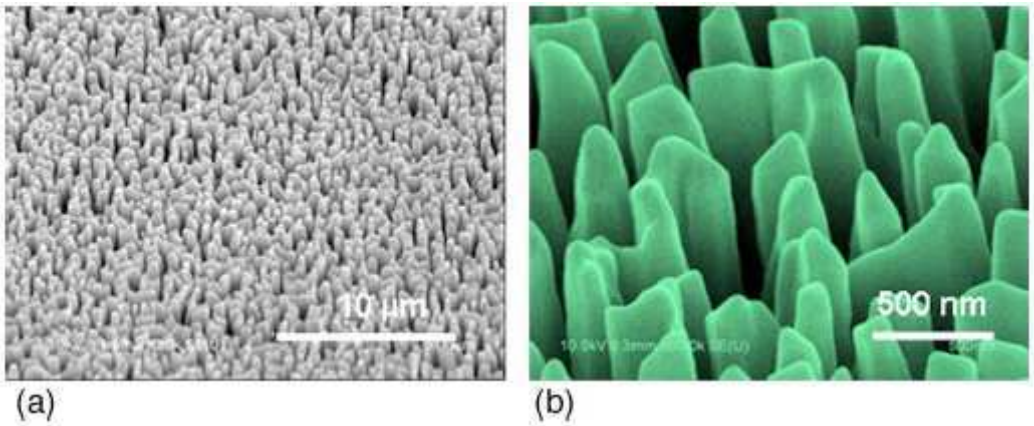

FIG. 6. SEM images of ZnO nanostructures grown by PLD on c-Al_2O_3.

In the SEM image shown in Fig. 7(a), an array with a very high density of nanostructures can be seen. The higher magnification image of Fig. 7(b) reveals nanorods of rather uniform shape, typically 200 nm in diameter and 3 μm long. The vast majority of the columns is strongly aligned along the perpendicular to the substrate plane. It has been suggested that the shape of such nanostructures could be explained by a preferential hexagonal growth along the c-axis plus a secondary preferential growth along the (1011) axis related to different relative cyrstal growth rates [16]. The relatively homogeneous array of vertically aligned nanorods could be useful for many potential applications such as improved light extraction in LEDs or directional sensitive detectors.

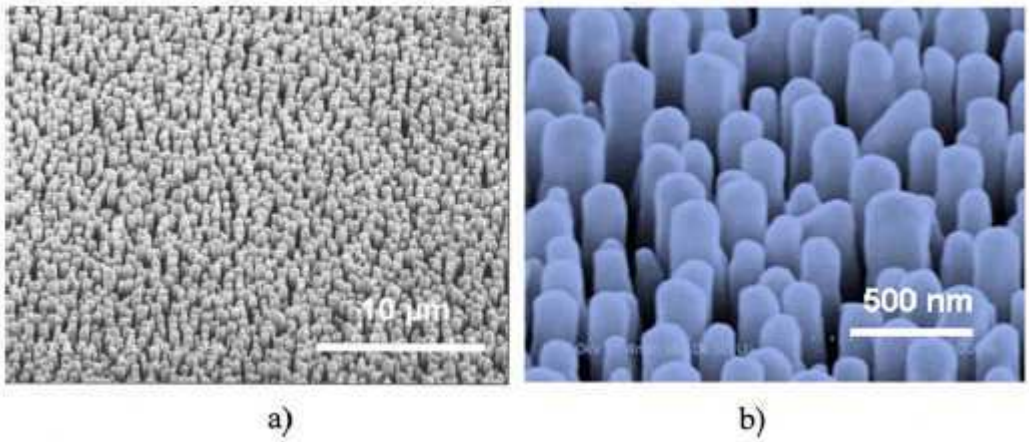

FIG. 7. SEM images of ZnO nanostructures grown by PLD on Si (111).

B. XRD investigations

Strong ZnO (0002) reflections corresponding to a c-axis oriented wurtzite phase were observed for the samples grown on c-Al_2O_3 by all three growth process (Figs. 8-10). The intensity of the XRD peak for the nano-ZnO grown by PLD (Tables I and II) is more than three orders of magnitude higher than those for the structures grown by MOCVD and PVT. Although direct comparison of XRD peak intensity cannot be absolute, SEM study suggested that the volume of ZnO was comparable for all the samples, so the PLD samples appear to be much better crystallized. The rocking curve full width at half maximum (FWHM) was smallest for the nanostructures grown by PLD and largest for those grown by MOCVD. For the Si (111) substrate, only the nanostructures grown by PLD gave a response in the XRD analysis (Fig. 10 and Table II). This indicates a relatively poor crystallization on Si (111) compared with that on c-Al_2O_3. The c-axis lattice constants of the nanostructures were determined from the ZnO (0002) peak position and found to be similar for all the nanostructures (from 5.205 to 5.206 Å) and close to that for relaxed wurtzite ZnO.[18] In summary, the nanostructures grown by PLD appeared to be better crystallized and have less dispersion in crystallographic orientation than the other nanostructures.

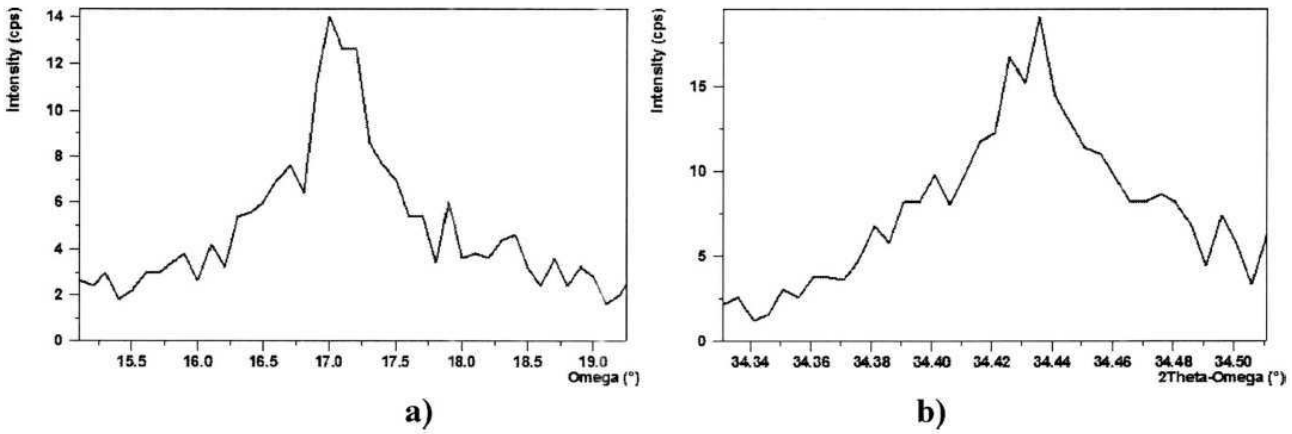

FIG. 8. a) Omega scans and b) two theta omega scans for ZnO nanostructures grown by MOCVD on c-Al_2O_3.

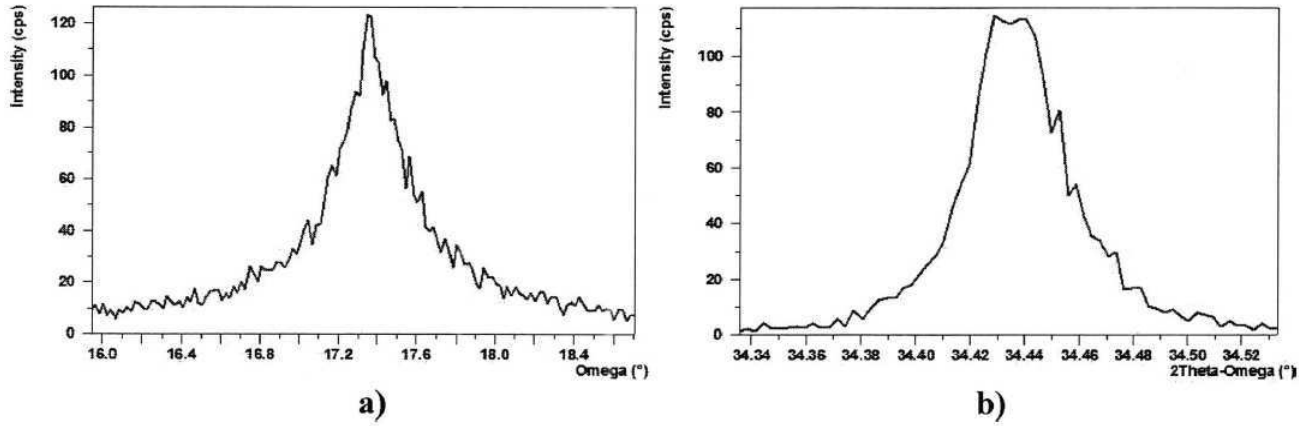

FIG. 9. a) Omega scans and b) two theta omega scans for ZnO nanostructures grown by PVT on c-Al_2O_3.

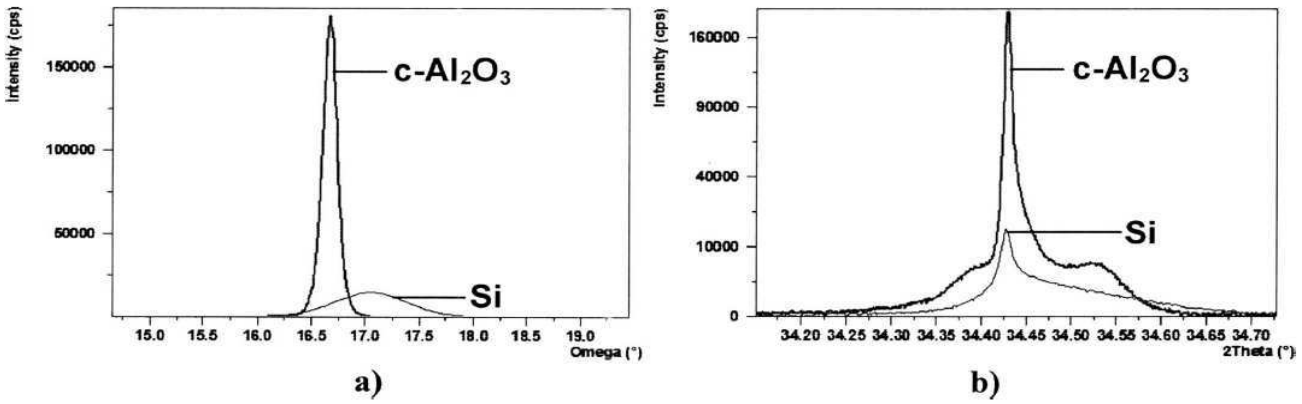

FIG. 10. a) Omega scans and b) two theta omega scans for ZnO nanostructures grown by PLD on c-Al_2O_3 and Si(111).

Sample	Intensity (counts/s) (cps)	ω rocking curve FWHM (deg)
MOCVD ZnO/c-Al_2O_2	13	0.56
PVT ZnO/c-Al_2O_3	107	0.41
PLD ZnO/c-Al_2O_3	180 974	0.16

TABLE I. Comparison of XRD scans intensities and FWHM for ZnO nanostructures grown on c-Al_2O_3

Sample	Intensity (counts/s) (cps)	ω rocking curve FWHM (deg)
MOCVD ZnO/Si (111)	No peak	No peak
PVT ZnO/Si (111)	No peak	No peak
PLD ZnO/Si (111)	15 047	0.79

TABLE II. Comparison of XRD scans intensities and FWHM for ZnO nanostructures grown on Si(111).

C. PL investigations

PL spectra for all samples (Figs. 11 and 12 and Tables III and IV) showed an ultraviolet UV band and a green band [N.B. there is a gap in all spectra at around 488 nm due to the second harmonic peak of the UV laser (244 nm) used for this experiment]. The UV emission was indexed as ZnO near band edge (NBE) emission19 and the green emission was attributed to defects in the ZnO.[20] The NBE emission wavelength and FWHM were lower for the structures grown on Si substrates than for those grown on c-Al_2O_3. The NBE emission wavelengths max were also observed to depend on growth technique. The structures grown by PLD had the shortest NBE max 380.0 nm on Si and 380.3 nm on c-Al_2O_3 and the structures grown by PVT had the longest max 387.5 nm on Si and 391.5 nm on c-Al_2O_3. Structures grown by MOCVD had NBE max at 382.3 nm on Si and 383.5 nm on c-Al_2O_3. The intensity of the PL peak for the nano-ZnO grown on c-Al_2O_3 and by MOCVD (Table IV) is more than an order of magnitude higher than those for the structures grown by PLD and PVT. The lower NBE max and smaller FWHM for structures grown on Si compared to those grown on c-Al_2O_3 could be related to Al diffusion from the c-Al_2O_3 substrate, which the authors have observed by secondary ion mass spectroscopy in ZnO thin films grown at similar temperatures.[21]

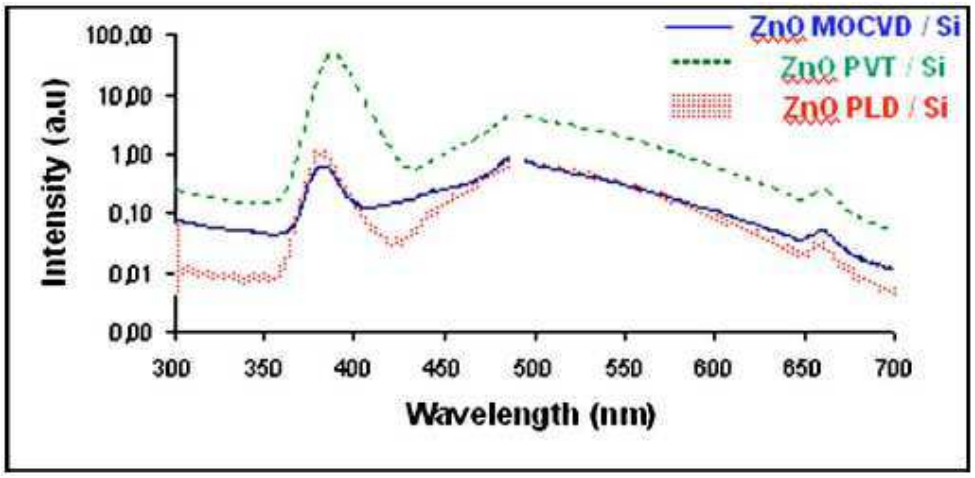

FIG. 11. PL spectra for ZnO nanostructures grown on Si (111).

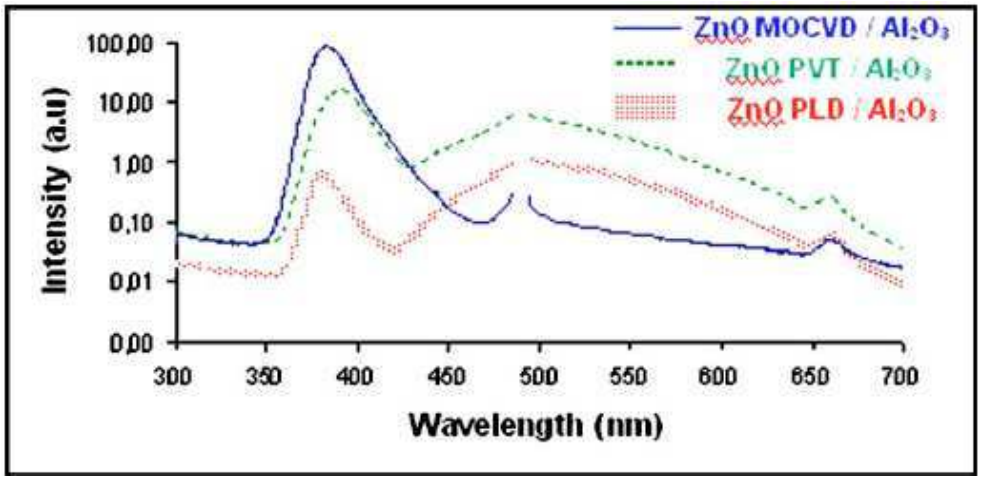

FIG. 12. PL spectra for ZnO nanostructures grown on c-Al_2O_3.

Sample	λ (nm)	FWHM (nm)	Intensity (a.u.)
PLD ZnO/Si (111)	380.0	13.0	1.1
MOCVD ZnO/Si (111)	382.3	15.8	0.6
PVT ZnO/Si (111)	387.3	15.3	49.1

TABLE III. Comparison of PL spectra, main peak wavelength , FWHM, and intensity for ZnO nanostructures grown on Si (111).

Sample	λ (nm)	FWHM (nm)	Intensity (a.u.)
PLD ZnO/*c*-Al_2O_3	380.3	14.5	0.7
MOCVD ZnO/*c*-Al_2O_3	383.5	18.3	81.0
PVT ZnO/*c*-Al_2O_3	391.5	22.5	16.2

TABLE IV. Comparison of PL spectra, main peak wavelength, FWHM, and intensity for ZnO nanostructures grown on c-Al_2O_3.

V. CONCLUSION

ZnO nanostructures were grown on Si (111) and c-Al_2O_3 substrates by MOCVD, PVT, and PLD. The comparison of nanostructures grown with these three different techniques was complicated by the fact that they gave structures with different forms and scales. Indeed, SEM revealed a myriad of ZnO nanostructures such as hexagonal nanorods, nanoneedles, and nanotubes along with novel bevelled structures with 12 facets. PVT growth gave the biggest family of nanostructures. A dense array of regular nanorods with a preferred orientation perpendicular to the substrate plane was obtained on both Si and c-Al_2O_3, by PLD, without the use of a catalyst. XRD did not reveal peaks for the structures grown on Si by MOCVD and PVT. XRD scans for the PLD nanostructures grown on c-Al_2O_3 gave a much more intense (0002) peak and the smallest rocking curve FWHM, suggesting that the PLD structures were very well crystallized and the most highly oriented. PL spectra showed that the nanostructures grown by PLD had the lowest max and the smallest FWHM. This is consistent with MOCVD having higher impurity doping levels than the PLD. Structures grown on Si had lower max and smaller FWHM than those grown on c-Al_2O_3. This redshift and peak broadening on c-Al_2O_3 may be related to Al diffusing into the ZnO from the substrate.

REFERENCES

[1] D. J. Rogers et al., Appl. Phys. Lett. 91, 071120 (2007).
[2] M. Zerdali, S. Hamzaoui, F. Hosseini Teherani, and D. Rogers, Mater.Lett. 60, 504 (2006).
[3] V. E. Sandana et al., Proc. SPIE 6895, 29 (2008).
[4] J. Zhong, H. Chen, G. Saraf, Y. Lu, C. K. Choi, and J. J. Song, Appl.Phys. Lett. 90, 203515

(2007).
[5] T. Reuters, Phys. World 21, 36 (2008).
[6] Ü. Özgür, Ya. I. Alivov, C. Liu, A. Teke, M. A. Reshchikov, S. Doğan, V. Avrutin, S.-J. Cho, and H. Morkoç, J. Appl. Phys. 98, 041301 (2005).
[7] H. J. Fan, P. Werner, and M. Zacharias, Biophys. J. 2, 700 (2006).
[8] Z. L. Wang, J. Phys.: Condens. Matter 16, R829 (2004).
[9] Z. Li, R. Yang, M. Yu, F. Bai, C. Li, and Z. L. Wang, J. Phys. Chem. C 112, 20114 (2008).
[10] X. Y. Kong and Z. L. Wang, Nano Lett. 3, 1625 (2003).
[11] D. J. Rogers et al., Phys. Status Solidi C 5, 3084 (2008).
[12] R. Nishimura, T. Sakano, T. Okato, T. Saiki, and M. Obara, Jpn. J. Appl. Phys. 47, 4799 (2008).
[13] V. A. Coleman, J. E. Bradby, C. Jagadish, and M. R. Phillips, Appl. Phys. Lett. 89, 082102 (2006).
[14] Z. Li, F. Xu, X. Sun, and W. Zhang, Cryst. Growth Des. 8, 805 (2008).
[15] H. Hou, Y. Xiong, Y. Xie, Q. Li, J. Zhang, and X. Tian, J. Solid State Chem. 177, 176 (2004).
[16] G. Z. Wang, Y. Wang, M. Y. Yau, C. Y. To, C. J. Deng, and D. H. L. Ng.,Mater. Lett. 59, 3870 (2005).
[17] X. Tian, F. Pe, J. Fe, C. Yang, H. Luo, D. Luo, and Z. Pi, Physica E 31, 213 (2006).
[18] H. Karzel et al., Phys. Rev. B 53, 11425 (1996).
[19] Y. C. Kong, D. P. Yu, B. Zhang, W. Fang, and S. Q. Feng, Appl. Phys. Lett. 78, 407 _2001_.
[20] S. A. Studenikim, N. Golego, and M. Cocivera, J. Appl. Phys. 84, 2287 (1998).
[21] D. J. Rogers et al., Proc. SPIE 7217, 72170F (2009).

Conclusion

MOCVD Growth of ZnO Nanowires Using Au Droplets as Catalysts.
ZnO nanostructures were synthesised by Metal Organic Chemical Vapor Deposition growth on Si (100) and c-Al_2O_3 substrates coated with a 5nm thick layer of Au. The Au coated substrates were annealed in air prior to deposition of ZnO so as to promote formation of Au nanodroplets. The development of the nanodroplets was studied as a function of annealing duration and temperature. Under optimised conditions, a relatively homogeneous distribution of regular Au nanodroplets was obtained. Using the Au nanodroplets as a catalyst, MOCVD growth of ZnO nanostructures was studied. Scanning electron microscopy revealed nanostructures with various forms including commonly observed structures such as nanorods, nanoneedles and nanotubes. Some novel nanostructures were also observed, however, which resembled twist pastries and bevelled-multifaceted table legs.

Comparison of ZnO nanostructures grown using pulsed laser deposition, metal organic chemical vapor deposition, and physical vapour transport.
The forms and properties of ZnO nanostructures grown on Si(111) and c-plane sapphire (c-Al_2O_3) substrates was compared, using three different growth processes: MOCVD, PLD, PVT. A very wide range of ZnO nanostructures was observed, including nanorods, nanoneedles, nanocombs, and some novel structures resembelling “bevelled” nanowires. PVT gave the widest family of nanostructures. PLD gave dense regular arrays of nanorods with a preferred orientation perpendicular to the substrate plane on both Si and c-Al_2O_3 substrates, without the use of a catalyst. XRD studies confirmed that nanostructures grown by PLD were better crystallized and more highly oriented than those grown by PVT and MOCVD. Samples grown on Si showed relatively poor XRD response but lower wavelength emission and narrower linewidths in PL studies.

IV Dépôts de ZnO par PLD pour la fabrication de LEDs et de PVs

Résumé

Ce chapitre traite de la croissance de nano ZnO par PLD, le procédé le mieux adapté à la fabrication de nanostructures de ZnO sans catalyseur pour les applications que nous considérons (cf. p. 6) : nanostructures autoformées, alignées, verticales, présentant un indice de réfraction gradué et une température de dépôt relativement basse. L'étude s'est poursuivie selon quatre axes correspondant aux quatre articles suivants.

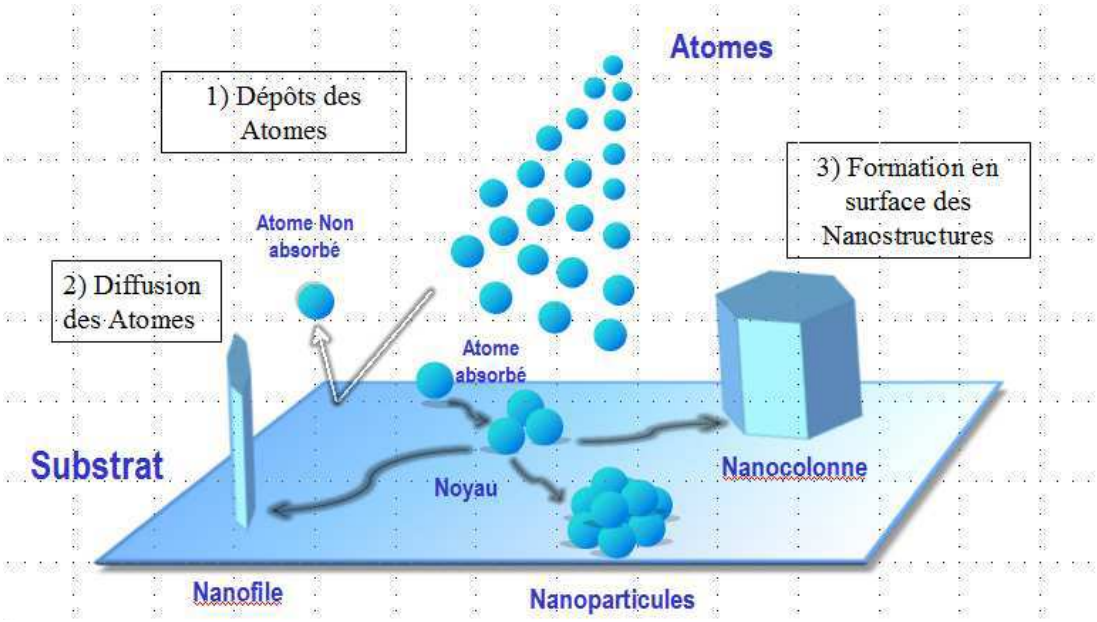

Figure IV.1 : Schéma du principe de croissance de nanostructures sans catalyseur par PLD.

Le premier article se concentre sur la réalisation d'un composant nano-LED à l'aide d'une hétérojonction n-ZnO/p-Si car des composants électroluminescents à base de couches minces de ZnO ont déjà été réalisés (Annexe V, *Hybrid Ultraviolet Light Emitting Diodes,* pages 117 à 119). Des nanostructures de ZnO ont été réalisées sur des substrats de Si(111) par PLD. L'impact de la température et de la pression en Ar sur la morphologie, la structure cristalline et la photoluminescence ont été étudiés. Différents types de nanostructures de ZnO ont été obtenues. Les structures de type nanocônes ont été choisies pour réaliser une nano-LED. Leur indice de réfraction gradué permet de faciliter l'extraction de photons à l'interface LED/air. Ces nanocônes ont été déposés par PLD sur un substrat de Si (111) de type p afin de former une LED à base d'hétérojonction nanostructurée. La nano-LED donne une caractéristique I/V rectifiante et une électroluminescence bleue-blanche observable à l'œil nu.

Le deuxième article fait le lien entre les caractéristiques morphologiques des nanostructures déposées sur Si (111) et c-Al_2O_3 et leurs propriétés optiques pour des applications en tant que couches antireflets dans les cellules photovoltaïques. Des caractérisations optiques de nanostructures autoformées et alignées verticalement de ZnO obtenues par PLD ont été effectuées. Les substrats utilisés ont été c-Al_2O_3 et Si (111) (de types p et n). Les mesures de PL à basse température indiquent que les nanocolonnes de ZnO, sur les substrats c-Al_2O_3 et Si (111) de type n, présentent une émission similaire à celles observées dans le cas de cristaux massifs de ZnO [dominante de l'émission de recombinaison par exciton lié (~ 3,36 eV)] et une bande d'émission dans le vert. L'intensité du spectre PL des nanocônes de ZnO sur Si (111) de type n est la mesure la plus élevée au cours de cette étude, de plus d'autres émissions ont été observées à 3,12, 3,02 et 2,92 eV. Les mesures de réflectivité à température ambiante ont montré que toutes les structures agissent comme des couches antireflets (absorption > 95%) sur une large gamme spectrale (de 450 à 750 nm).

Le troisième article détaille la croissance de nanocônes de ZnO sur quatre substrats ayants des propriétés optiques, électriques et cristallines différentes : Si (111), c-Al_2O_3, cristaux massif de ZnO et acier austénitique. Des nanocônes de ZnO autoformés, alignés et verticaux ont été déposés par PLD sur ces quatre substrats. La XRD indique que les nanostructures de ZnO sont de type würtzite et possèdent un axe cristallographique préférentiel selon l'axe c et ceci sur tous les substrats étudiés. La CL montre systématiquement une émission de bord de bande caractéristique de ZnO. Ces résultats prouvent que les nanostructures de ZnO peuvent être déposées sur des substrats très variés, ce qui pourrait faciliter la reprise de croissance de GaN sur ZnO sur des substrats sur lesquels il est habituellement difficile de faire croître GaN directement.

Un dépôt InGaN/GaN par MOVPE, sur de couches minces de ZnO obtenues par PLD sur un substrat de Si, a déjà été démontré (Annexe II). Ceci permet d'introduire le quatrième article de ce chapitre. Il traite de la reprise de croissance de GaN par MOVPE sur des nanocônes de ZnO déposés par PLD sur substrat Si (111). L'objectif est de confirmer la faisabilité de nouveaux composants. Des nanocônes de ZnO ont été déposés par PLD sur un substrat de Si(111). Les spectres XRD ont indiqué que les nanocônes présentent une structure cristalline de type würtzite avec une orientation cristallographique selon l'axe c (correspondant aussi à l'axe de croissance). Les spectres de CL montrent une émission caractéristique de bord de bande de ZnO. Les nanostructures sur Si ont été utilisées comme « moule » pour la reprise de croissance de GaN par MOVPE. Les outils de XRD, MEB et CL ont tous indiqué que les nanocônes de ZnO ont été encapsulés par GaN. Les mesures de réflectivité à température ambiante ont établi que les nanostructures de GaN/ZnO agissent comme des couches antireflets efficaces sur une large gamme spectrale (de 450 à 750 nm)

Une grande variété de formes de structures a été obtenue par PLD. On obtient ainsi des colonnes et cônes dont les qualités structurales sont excellentes y compris sur des substrats avec lesquels ZnO n'a pas un bon accord paramétrique. Leurs propriétés d'émission sont aussi excellentes avec des bandes de défauts, observables en PL, relativement faibles. La faisabilité de composants à base de nano ZnO a été démontrée grâce à la réalisation d'une nanoLED de type n-nanoZnO/ p-Si et à la reprise de croissance de GaN par MOVPE sur des nanocônes de ZnO/Si.

Dans l'étude de la fabrication de la nanoLED, j'ai étudié les conditions de déposition de nanocônes de ZnO sur Si (111) de type p et j'ai fabriqué le composant LED. J'ai réalisé les caractérisations MEB (figure 1 page 55), les spectres de photoluminescence (figure 3 page 58) et les mesures électriques (figure 6 page 61) à l'aide d'un banc Karl Suss (cf chapitre 2)

Dans l'étude de la réflectivité des nanocônes de ZnO j'ai fourni à l'université d'Aveiro (Portugal) des échantillons dont on peut voir mes images MEB figure 1 page 63.

Concernant l'étude de la croissance de nanocônes de ZnO sur différents substrats j'ai déterminé les conditions de croissance et réalisé l'ensemble des images MEB présentées. La cathodoluminescence a été faite en collaboration avec le laboratoire LMEN de l'université de Reims.

Enfin dans l'étude de la reprise de croissance de GaN par MOVPE sur des nanocône de ZnO j'ai fourni des échantillons au laboratoire de Georgia Tech-Lorraine.

4.1 Fabrication of Nanostructured Heterojunction LEDs Using Self-Forming "Moth-Eye" Type Arrays of n-ZnO Nanocones Grown on p-Si (111) Substrates by Pulsed Laser Deposition

D. J. Rogers et al. Proc. of SPIE Vol. 7217, 721708

D. J. Rogers[1], V. E. Sandana[1,2,3], F. Hosseini Teherani[1], M. Razeghi[2] and H.-J. Drouhin[3]

[1]*Nanovation, 103B Rue de Versailles, 91400 Orsay, France.*
[2]*Center for Quantum Devices, Northwestern University, Evanston, Il 60208, USA.*
[3]*Department of Irradiated Solids, École Polytechnique, 91128 Palaiseau, France.*

1. INTRODUCTION

ZnO is a remarkable multifunctional material with a distinctive set of properties including a direct bandgap of ~3.4eV and an exciton binding energy of ~60meV. It also has a high transparency over the visible spectrum, a strong piezoelectric response, a very wide range of tuneable conductivities (varying from semi-insulating to semi-metallic) and good bio-compatibility. As a result, ZnO has many established and emerging applications spanning from use as an ultra-violet filter in sun cream to varistor, light emitting diode (LED) [1] and surface acoustic wave applications [2]. ZnO also exhibits one of the largest families of nanostructures of all materials systems with a huge range of potential applications opening up as a result of the nanostructuring. Indeed, ZnO nanowires were recently identified by Thomson-Reuters as the most researched nanomaterial in 2008 [3].
In previous work [4,5] it was established that Pulsed Laser Deposition (PLD) gave nanostructures with superior crystallinity compared with those prepared using Metal Organic Chemical Vapor Deposition or Physical Vapour Transport. This paper compares the forms and properties of ZnO nanostructures prepared using PLD on Si (111) substrates under various growth conditions. The paper then considers the optimum structure for LED light extraction and describes the fabrication of heterojunction LEDs employing n-type ZnO nanostructures as active components [6,7].

2. EXPERIMENT

ZnO nanostructures were grown by PLD from a 99.99% pure sintered ZnO target using a KrF excimer laser (248 nm) at a frequency of 10 Hz. The vacuum chamber was evacuated using a turbo-molecular pump to a pressure of about 1×10^{-6} Torr. The impact of growth conditions was investigated as a function of both Ar partial pressure (P_{Ar}) and growth temperature (Ts). Si (111) was chosen as the substrate and growths were all made for a duration of about 10 minutes.
Sample morphology was studied using a Hitachi S4800 Field Emission-Scanning Electron Microscope (FE-SEM). The crystal quality of the nanostructures was investigated using X-Ray Diffraction (XRD) performed in a Panalytical MRD Pro system using Cu Kα radiation. Optical properties were studied via Room Temperature (RT) PhotoLuminescence (PL) with a continuous-wave, frequency-doubled, argon-ion laser (244 nm, power of 30mW). Heterojunction LEDs were

made by growing n-type ZnO nanostructures on p-type Si (111) substrates. Device I/V characteristics and electroluminescence (EL) were investigated using a Karl-Suss probe station, a Keithley 2400 Source-Meter and an Olympus digital camera.

3. RESULTS & DISCUSSION

3.1 The Dependence of the Nanostructures on Growth Conditions

Figure 1 shows SEM images of samples obtained under various growth conditions. The lower and intermediate Ts gave films with a relatively high surface roughness but no distinct nanostructures. Samples grown at higher Ts showed dense arrays of vertically-aligned nanostructures. Growths at higher P_{Ar} gave nanorods about 200 nm in diameter and 3 microns in length, which were rounded at the tips. Samples grown at lower P_{Ar} gave a "moth-eye" type array of nanocones [8,9], which were about 3 microns in length and 200 nm in diameter at the base.

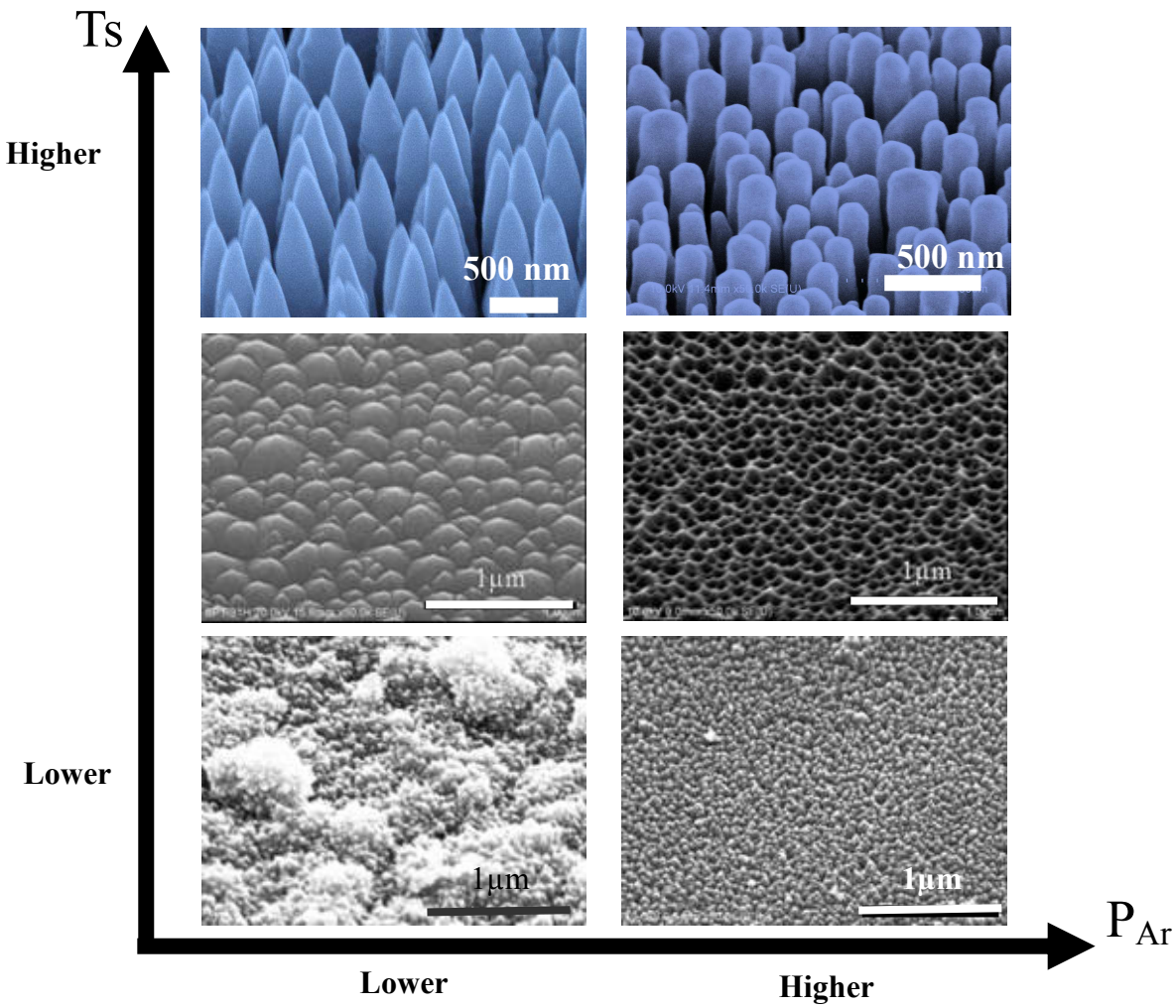

Figure 1: SEM images of ZnO nanostructures grown by PLD on Si (111) from low to high P_{Ar} / Ts.

Figure 2 shows the XRD scans for the (0002) peaks of the nanostructures grown at higher Ts. The main peak position in the 2θ/Ω scans is similar for both samples, corresponding to c lattice parameters of 5.205 and 5.206 Å for the lower and higher P_{Ar} samples, respectively. This is what would be expected for relaxed wurtzite ZnO. Both 2θ/Ω peaks also show a higher-angle broadening at the base of the 2θ/Ω peak, indicative of contribution of a region with a smaller c lattice parameter. This could be due to disorder at the start of nanostructure growth creating a less dense a-b plane at the base of the columns/cones (and thus a larger a lattice parameter). The 2θ/Ω scan for the sample grown at lower P_{Ar} presented a significantly more intense peak than that for the nanostructures grown under higher P_{Ar}. This suggests that the sample grown at lower P_{Ar} was better crystallised. It should be noted, however, that although the samples were analysed using the same XRD configuration, it is difficult to make direct comparison of peak intensity because of possible differences in growth rates. The Full Wave Half Maxima (FWHM) for the two samples were similar at 0.015 and 0.014 for lower and higher P_{Ar}, respectively.

The Ω scan for the sample grown at lower P_{Ar} showed a smaller FWHM than that for the sample grown at higher P_{Ar} (0.64° vs 0.79°). This suggests that the lower P_{Ar} sample was more highly c-axis oriented.

(a)

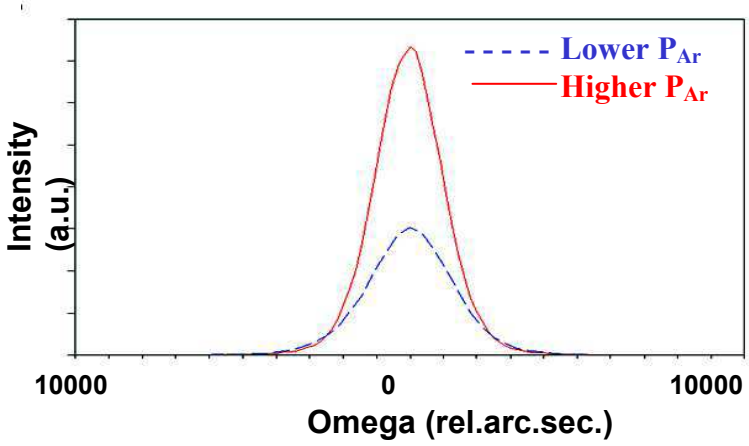

(b)

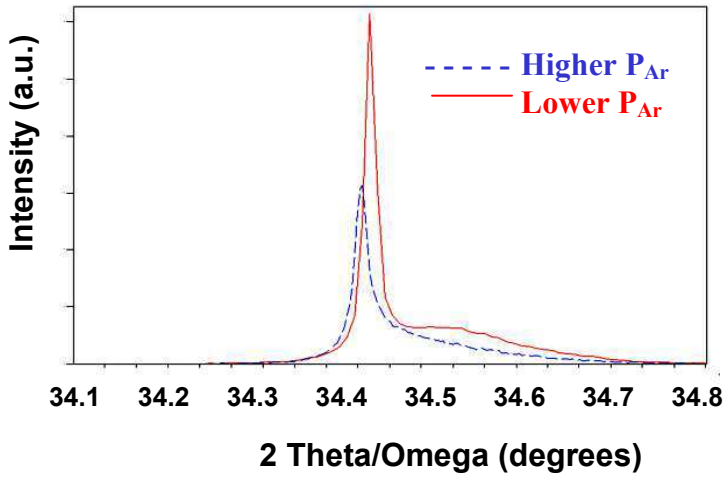

Figure 2 : (a) XRD 2 θ/Ω & (b) Ω scans for the (0002) peak of the nanostructured ZnO grown on Si (111) at higher Ts as a function of P_{Ar}

RT PL for the samples grown at higher Ts are shown in Figure 3. The spectra for both P_{Ar} showed low green signals and strong main peaks with FWHM of about 51 nm and main emission wavelengths (λMAX) of about 390.5 nm, which is typical for Near Band Edge (NBE) emission from wurtzite ZnO. This indicates that the nanostructures had good crystal quality with a relatively low defect density. The spectrum for the nanostructures grown under higher P_{Ar} had a significantly more intense peak than that for the nanostructures grown under lower P_{Ar}. This could indicate that the higher P_{Ar} nanostructures present a better cristallinity. It should be noted, however, that although the

spectra were acquired under the same conditions, it is possible that differences in growth rates or other factors (such as beam scattering variations) may invalidate such direct comparison of peak intensity.

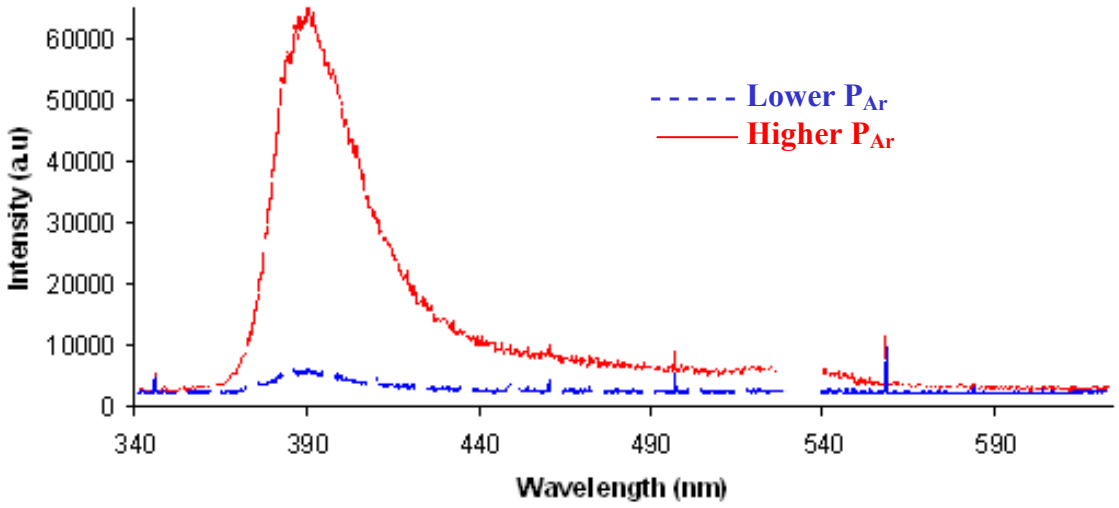

Figure 3: (a) PL spectra of the nanostructured ZnO on Si (111) grown under higher and lower P_{Ar}

3.2 Device Fabrication and Characterisation

The "moth-eye" type nanostructures, grown at lower P_{Ar}, were chosen for use in the LED because they represent a graded effective refractive index (Figure 4) at the LED/air interface, which could promote improved light extraction [10].

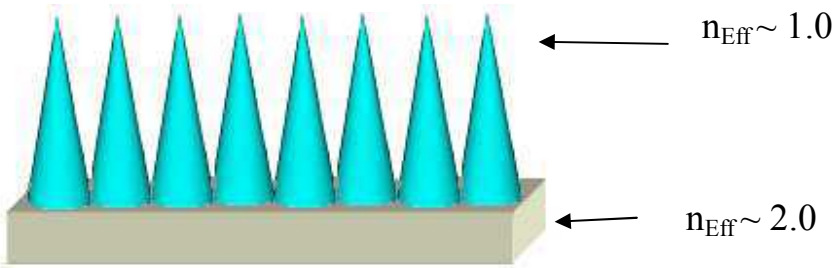

Figure 4: Schematic illustrating the graded effective refractive index of the nanocone type structures

A schematic of the device structure grown using these nanocones is shown in Figure 5. Metallic contacts were applied to the nanostructures surface and the backside of the substrate.

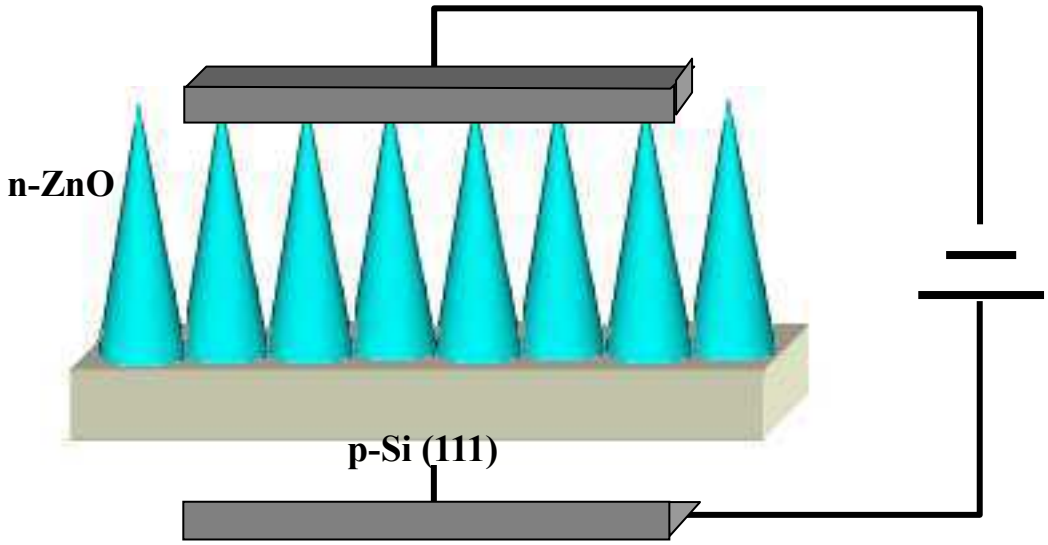

Figure 5: Schematic diagram of the nanostructured n-ZnO/p-Si(111) heterojunction LED.

The I/V characteristics for the device and the contacts are shown in Figure 6.

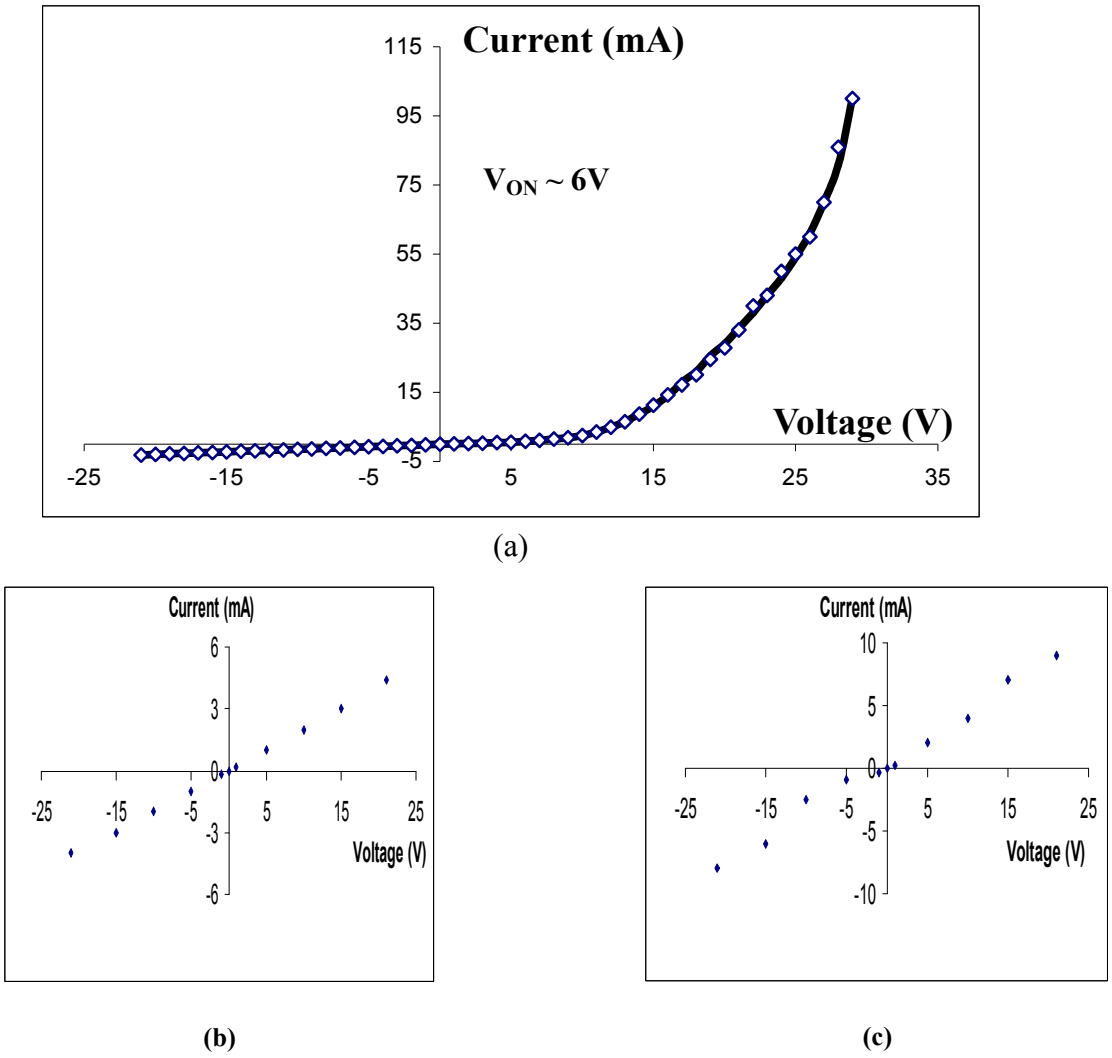

Figure 6 (a) I/V characteristic for the n-ZnO nanocone / p-Si (111) heterojunction (b) I/V characteristic for the p-to-p contact, (c) I/V characteristic for the n-to-n contact.

The I-V curves revealed a turn-on voltage of approximately 6V, a series resistance of about 500 ohms and a leakage current of about 2.5 mA at –15V. The I/V characteristic for the p-to-p contact showed very good linearity, indicating that the contacts seemed ohmic, while the I/V characteristic for the n-to-n contact deviated slightly from linearity. This may be due to parallel conduction of the current flow through the p-Si substrate as illustrated in figure 7.

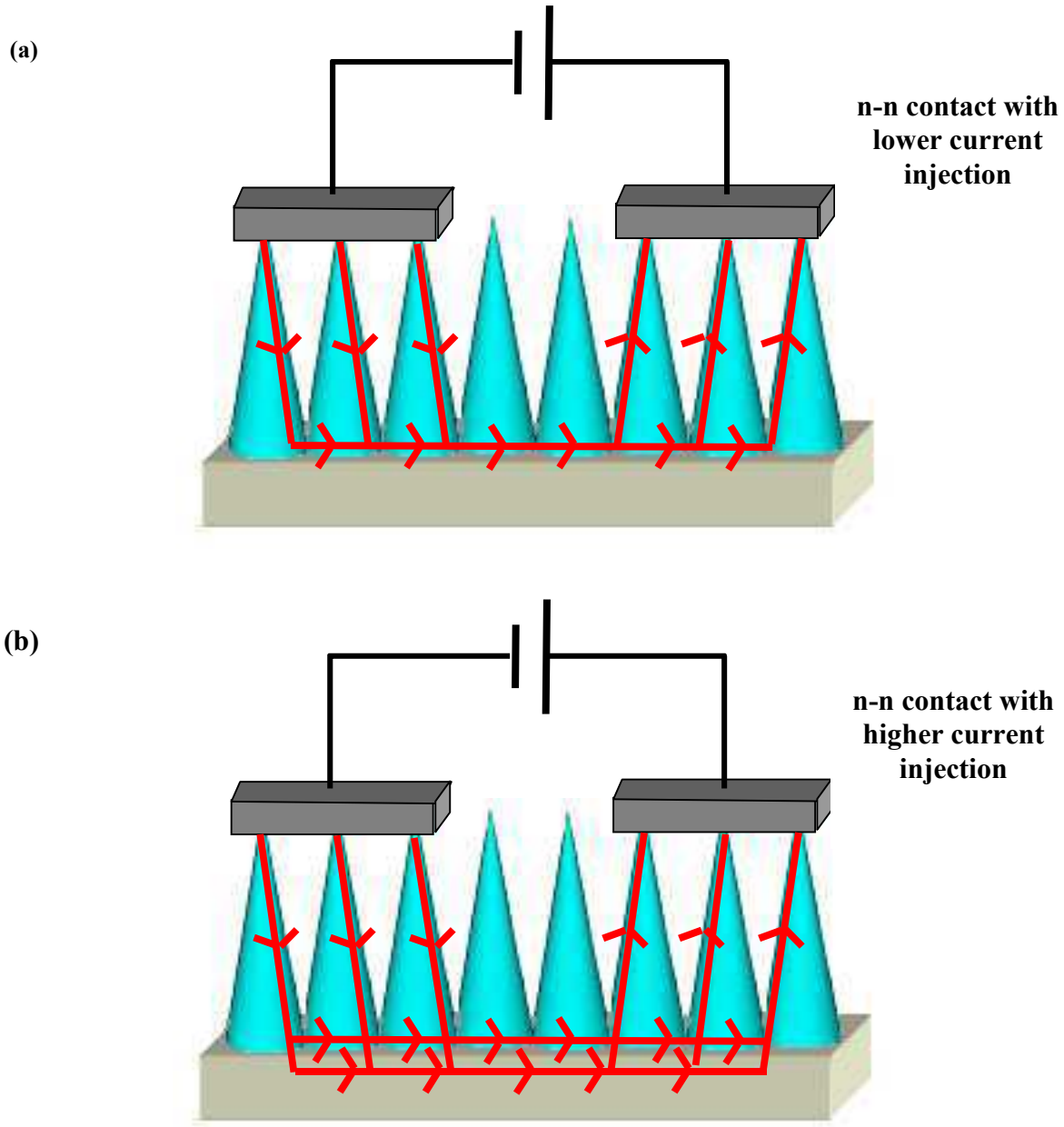

Figure 7: Schematic of the n-to-n contact current flow in the n-ZnO/p-Si LED device with (a) lower and (b) higher current injection.

The device showed a blueish-white EL which was clearly visible to the naked eye for currents over about 25mA. Photographs of the EL are shown in Figure 8. Investigation of the EL spectrum with an integrating sphere is in progress.

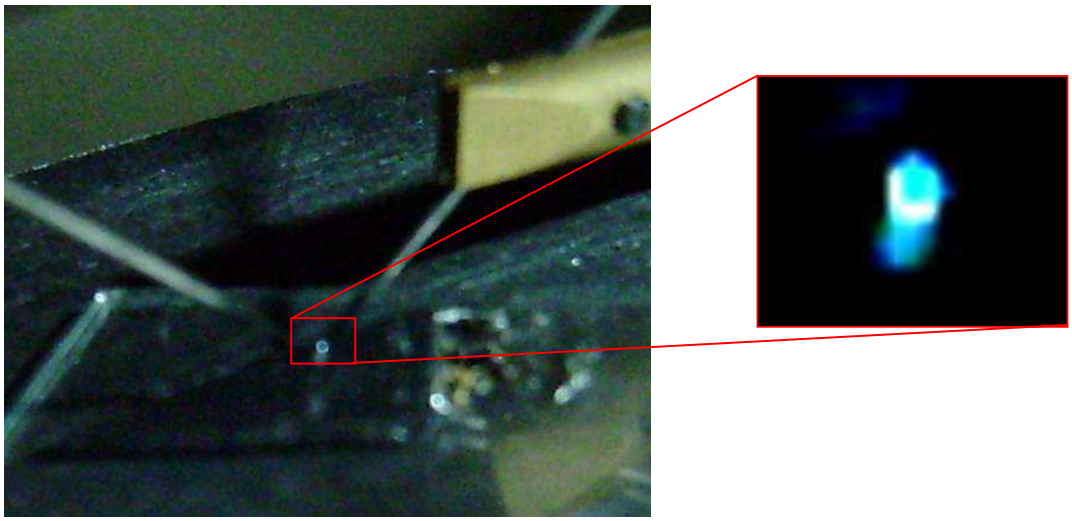

Figure 8: Photographs showing the blueish-white EL emanating from the device for a forward current of about 50mA.

6. CONCLUSIONS

Nanostructures were grown on Si (111) substrates using catalyst-free PLD. The impact of Ts and P_{Ar} on the sample morphology and properties was investigated. Self-forming, vertically-aligned nanostructures were obtained for growths at higher Ts. Growths at higher P_{Ar} gave arrays of nanorods, while those at lower P_{Ar} gave "moth-eye" type arrays of nanocones. XRD and RT PL studies indicated that the nanostrucutures grown at higher Ts were highly c-axis oriented wurtzite ZnO with strong NBE emission and relatively low defect density. The moth-eye nanostructures were chosen for LED fabrication because of their graded effective refractive index, which may improve light extraction. Heterojunction LEDs were fabricated by growing n-ZnO nanocones on p-Si (111). The devices showed rectifying I/V characteristics and blueish-white EL, which was clearly visible to the naked eye.

ACKNOWLEDGEMENTS

The authors would like to thank the French "Agence National de la Recherche" for financial support.

REFERENCES

[1] D. J. Rogers et al. Appl. Phys. Lett. 91, (2007), 071120
[2] M. Zerdali et al. Materials Letters 60, (2006), 504-508
[3] Thomson-Reuters in Physics World, Oct. (2008) 36-37
[4] V. E. Sandana et al. Proc. SPIE, 6895, (2008). 68950Z-68950Z-6

[5] V. E. Sandana et al. submitted to J. Vac. Sci Tech. (2009)
[6] Y.F. Gu et al. Solid State Communications 143 (2007) 421–424
[7] D.C. Kim et al. Appl. Phys Lett. **91**, (2007) 231901 [8] H.Hou et al J. Sol. State Chem.177 (2004) 176
[9] G.Z.Wang et al. Mat. Letts 59, (2005) 3870
[10] W.J. Zhong Appl. Phys. Lett., 90, (2007) 203515

4.2 Morphological and optical studies of self-forming ZnO nanocolumn and nanocone arrays grown by PLD on various substrates

M. Peres et al. Phys. Status Solidi A, 1–4 (2010) pssb.200983685

M. Peres[1], M. J. Soares[1], A. J. Neves[1], T. Monteiro[1], V. E. Sandana[2,3,4], F. Teherani[2], and D. J. Rogers[2]
1 Departamento de F1´sica/I3N, Universidade de Aveiro, 3810-193 Aveiro, Portugal
2 Nanovation, 103 bis rue de Versailles, Orsay 91400, France
3 Center for Quantum Devices, Northwestern University, Evanston, IL 60208, USA
4 Department of Irradiated Solids, E ´ cole Polytechnique, 91128 Palaiseau, France

1 Introduction

During the last decade, zinc oxide nanostructures have been extensively studied due to their potential relevance in optoelectronics, spintronics and bioapplications [1]. Pulsed laser deposition (PLD) is recognized as one of the most powerful techniques for the growth of ZnO-based thin films and it has recently shown a tendency for the growth of self-organizing ZnO-based nanostructures arrays [1–3]. In previous studies [4], it was found that self forming arrays of vertically aligned nanocolumns and nanocones can be grown by PLD under optimized growth conditions. It was proposed that such arrays of nanostructures could be useful for enhancing light extraction and/or absorption in optical devices. Indeed, simple p–n heterojunction LEDs made with such n-type ZnO nanocone arrays grown on p-type Si were found to give rectifying characteristics and blueish–white electroluminescence which was visible to the naked eye [5]. The purpose of the present work is to examine the morphological and optical properties of these PLD grown ZnO nanostructure arrays by scanning electron microscopy (SEM), photoluminescence (PL) and angle resolved reflectivity (ARS). The sample optical properties will then be discussed and correlated with their morphological and structural properties.

2 Experimental

Substrates of Si (111) and c-plane sapphire (c-Al_2O_3) were used for the growth of the ZnO nanostructures. The samples were grown by PLD from a 99.99% pure ZnO target using a KrF excimer laser (248 nm) as described elsewhere [3–5]. The sample morphology was studied using a Hitachi S4800 field emission-SEM. X-ray diffraction (XRD) was carried out in a Panalytical MRD Pro system in order to investigate the crystal structure of the samples.

Optical properties were assessed by PL and reflection. For the PL measurements, the samples were mounted on a cold finger in a continuous flow cryostat permitting temperature control in 14K to room temperature (RT) range. A He–Cd laser (0.6W/cm2) was used as the excitation source. The sample emission was dispersed using a SPEX1704 spectrometer and detected using a cooled photomultiplier. RT reflection measurements were performed using an Ocean Optics UBS4000 spectrometer and computer-controlled rotation stages. The sample was illuminated with a collimated beam of a tungsten/halogen lamp. The rotation stages and the spectra acquisition were piloted with

homemade software.

3 Results and discussion

Figure 1 shows typical SEM images of the two kinds of nanostructure arrays observed in the samples. Figure 1(a) reveals nanocolumns of rather uniform shape, aligned preferentially along the perpendicular to the Si (111) substrate plane. They are averaged 200 nm in diameter and about 3mm in length. Figure 1(b) shows the 'moth-eye' type array of nanocones, which was obtained on the same substrate by changing the growth conditions [4, 5]. The nanocones are also aligned preferentially along the perpendicular to the substrate plane and are typically 3 μm in length with an average diameter of about 200 nm at the base. Five samples were selected for studies: nanocolumns/c-Al_2O_3, nanocolumns/n-Si (111), nanocones/c-Al_2O_3, nanocones/n-Si (111) and nanocones/p-Si (111).

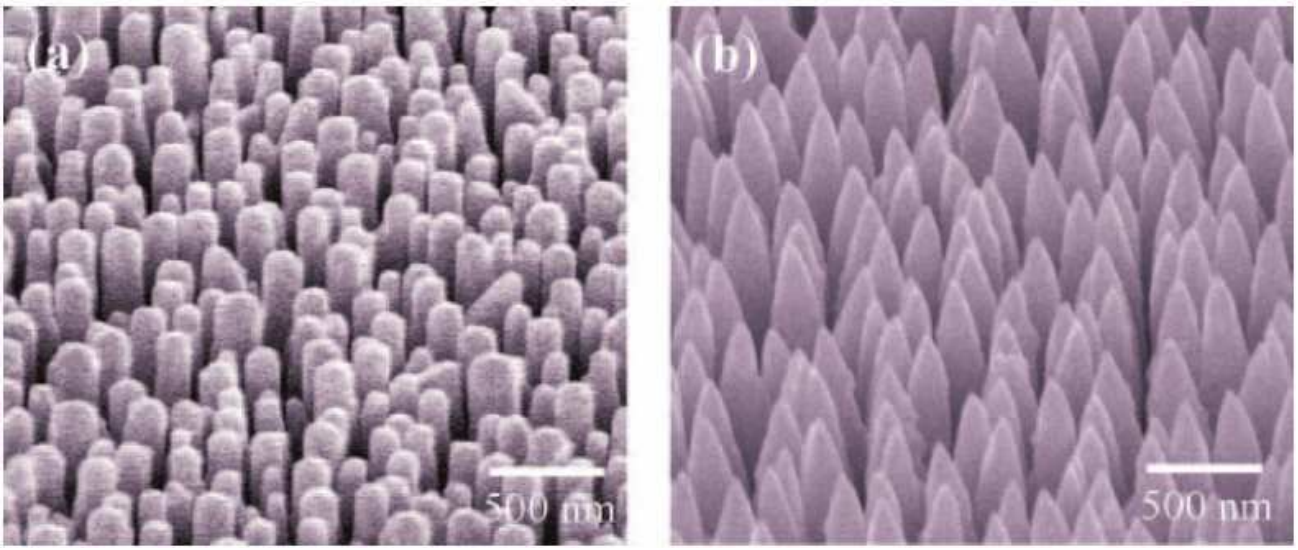

Figure 1 SEM images of the two kinds of morphologies observed in samples: (a) ZnO nanocolumns/ Si (111) and (b) ZnO nanocones/Si(111).

XRD measurements indicated that all the samples had single-phase wurtzite structure with c-axis highly oriented along the growth direction, as discussed elsewhere [4, 5].
Low temperature PL spectra of the analysed samples are shown in Fig. 2. Besides the ultraviolet recombination due to free and bound-excitons (Ii lines) and the donor–acceptor pair transitions (DAP) [6–8] the structured and unstructured green-emission band [9, 10] is also present in these samples, as is observed for some ZnO bulk samples.

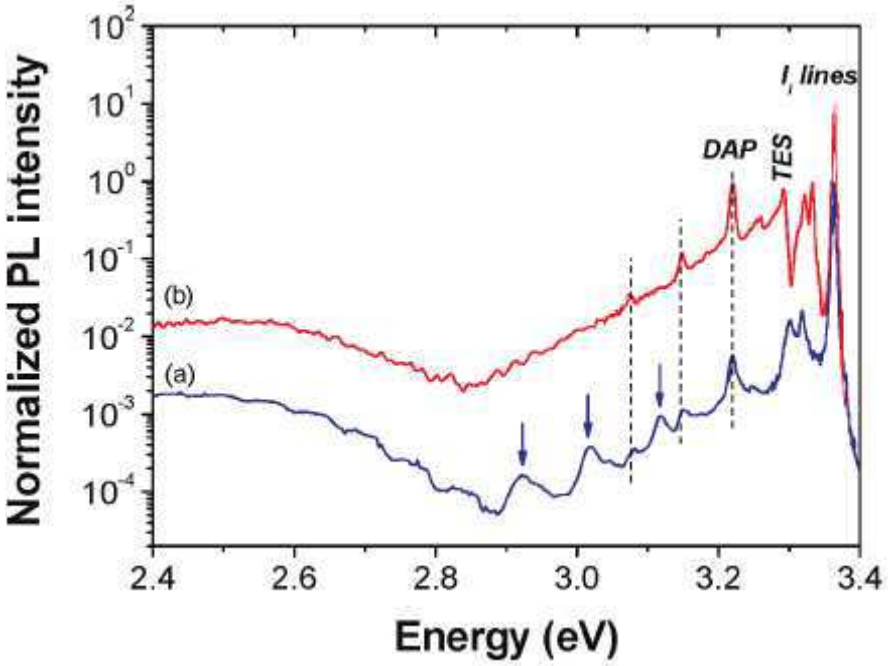

Figure 3 14K PLspectra of the (a) PLDgrownZnOnanocones/n-Si (111) and (b) a typical bulk ZnO sample.

A closer inspection of the PL spectrum for the ZnO nanocones/n-Si (111) sample reveals additional features to the ones observed in bulk samples as indicated by arrows in Fig. 3. The lines at 2.92, 3.02 and 3.12 eV have a constant energy separation of 100 meV, suggesting a vibronic progression. The same features were not detected in the PL spectra of the other PLD grown nanostructures suggesting an additional optical active defect in this sample.

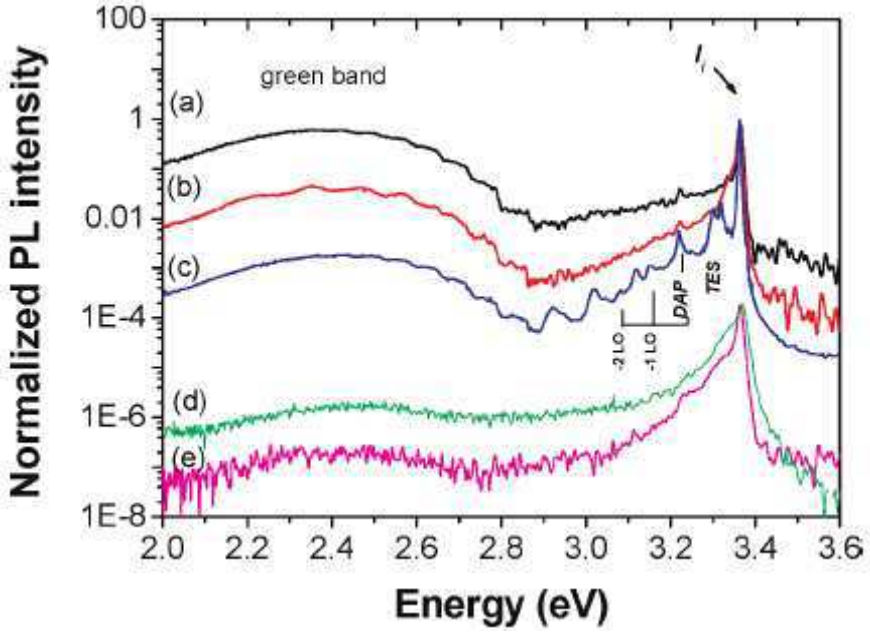

Figure 2 14K PL spectra of the PLD grown ZnO (a) nanocolumns/c-sapphire, (b) nanocolumns/n-Si(111), (c) nanocones/n-Si (111), (d) nanocones/p-Si (111) and (e) nanocones/c-sapphire. The (d) and (e) spectra were vertically shifted.

To investigate the characteristics of the ZnO 'moth-eye' nanostructures [5], antireflection RT specular reflection measurements were performed as a function of wavelength in the range 450–720 nm and for angles of incidence between 10 and 60°. Figure 4 shows the RT reflection of the (a) nanocolumns/n-Si (111), (b) nanocones/n-Si (111) and (c) nanocones/p-Si (111), normalized to the reflection from the silicon substrate reference. As observed in Fig. 4(b) for the ZnO nanocones/n-Si a periodic pattern was found which is likely due to an unwanted oxide layer or related to morphological aspects (length and tapering of the nanorods tips).

From Fig. 4 (a, b and c) the reflection from the nanostructured surfaces at 650 nm was _1.5 and 0.5%, over almost the whole range of measured angles. These measurements indicate that the ZnO nanostructures act as broadband antireflection coatings. The use of silicon substrates precluded transmission measurements at visible wavelengths, so the effect of the light scattering by the nanostructures on the reduction of the reflection was not determined. Measurements to understand whether this reduced reflection occurs due to an enhanced absorption in the antireflection coating and/or to refractive index matching to the substrate are underway.

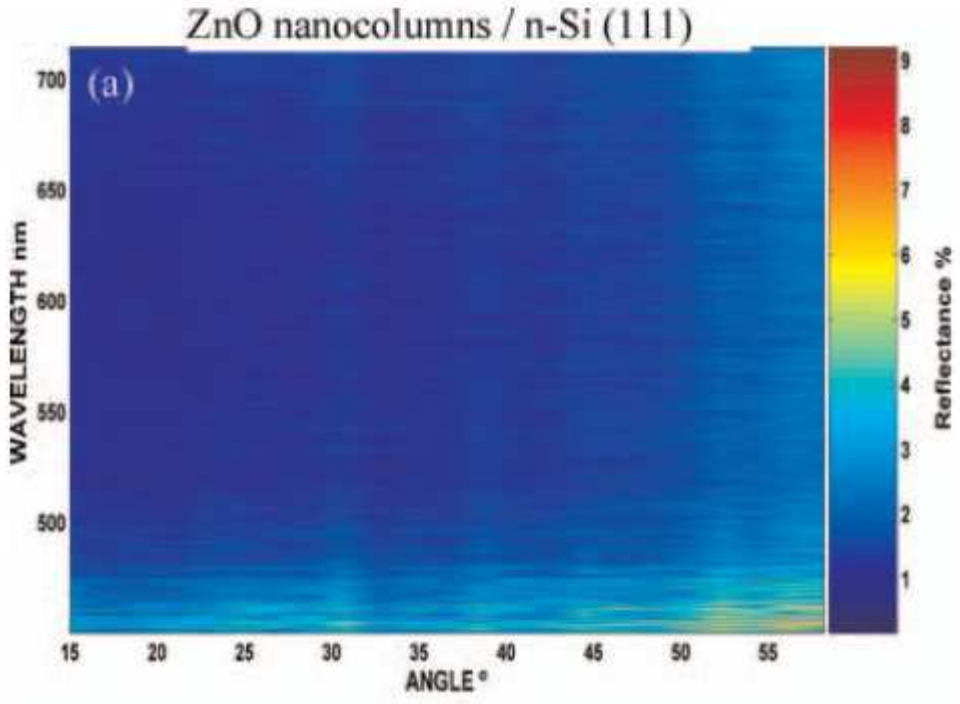

(a)

Figure 4 (a) RT reflection of the ZnO nanostructures normalized to the reflection of the silicon reference. ZnO nanocolumns/n-Si (111),

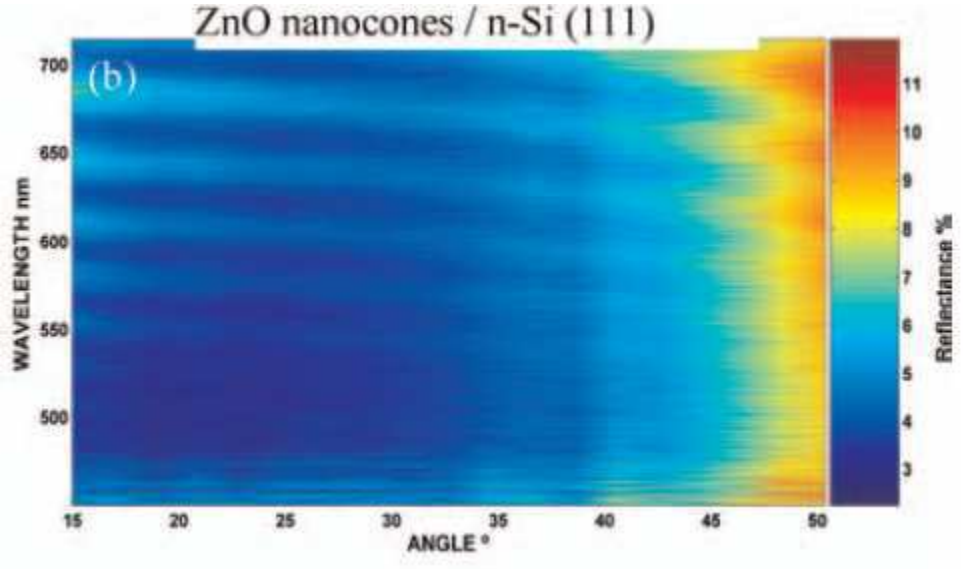

(b)

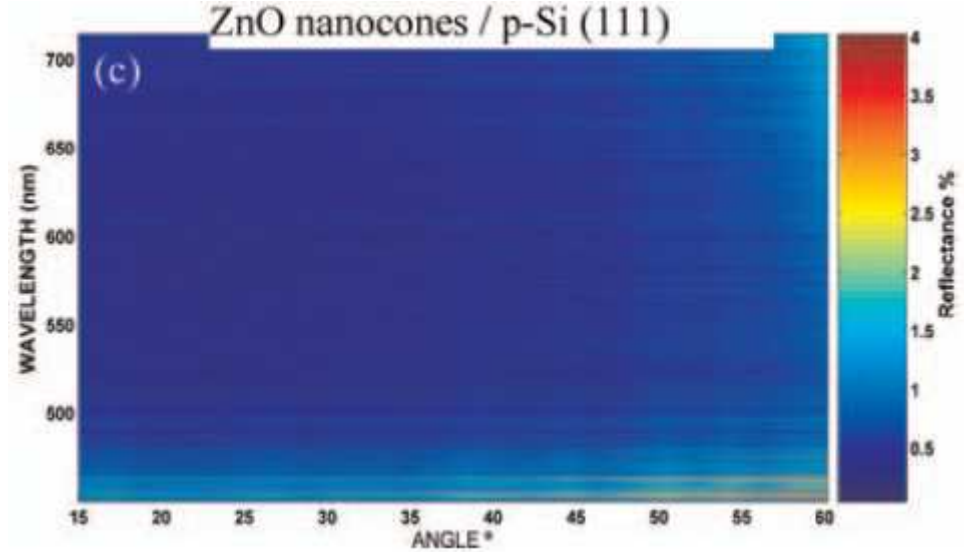

(c)

Figure 4 RT reflection of the ZnO nanostructures normalized to the reflection of the silicon reference. (b) ZnO nanocones/ n-Si (111) and (c) ZnO nanocones/p-Si (111).

4 Conclusions

The morphological and optical propertiesof ZnO nanostructures grown by PLD on c-sapphire and Si (111) were assessed by SEM, PL and wavelength and angle dependence reflection. SEM images showed two main kinds of morphology: high-density nanocolumn and nanocone arrays with preferential orientation perpendicular to the substrate plane. Low temperature luminescence observed upon bandgap excitation revealed optical active centres similar to those observed for bulk samples for the different analysed nanostructures, including near band edge recombination and the

green band. For the ZnO nanocone-type nanostructures grown on n-Si, however, additional features with a periodic spacing of 100 meV were found. The nature and characterization of these lines is the subject of ongoing research. In order to analyse the antireflective properties of the PLD grown nanostructures RT wavelength and RT angle dependence reflection measurements were performed. The preliminary results suggest that the nanostructures act as highly effective broadband antireflection coatings.

Acknowledgements

We acknowledge the support of FCT,
Portugal (PTDC/FIS/66262/2006). M. Peres thanks the FCT for its
Grant (SFRH/BD/45774/2008).

References

[1] M. Willander, O. Nur, Q. X. Zhao, L. L. Yang, M. Lorenz, B. Q. Cao, J. Zu´n˜iga Pe´rez, C. Czekalla, G. Zimmermann, M. Grundmann, A. Bakin, A. Behrends, M. Al-Suleiman, A. El-Shaer, A. Che Mofor, B. Postels, A. Waag, N. Boukos, A. Travlos, H. Kwack, S. Guinard, J. Le Si, and D. Dang, Nanotechnology 20, 33201 (2009).
[2] R. Nishimura, T. Sakano, T. Okato, T. Saiki, and M. Obara, Jpn. J. Appl. Phys. 47, 4799 (2008).
[3] D. J. Rogers, D. C. Look, F. Hosseini Teherani, K.Minder, M. Razeghi, A. Largeteau, G. Demazeau, J. Morrod, K. A. Prior, A. Lusson, and S. Hassani, Phys. Status Solidi C 5, 3084 (2008).
[4] V. E. Sandana, D. J. Rogers, F. Hosseini Teherani, R. McClintock, C. Bayram, M. Razeghi, H.-J. Drouhin, M. C.
Clochard, V. Sallet, G. Garry, and F. Falyouni, J. Vac. Sci. Technol. B 27, 1678 (2009). [5] D. J. Rogers, V. E. Sandana, F. Hosseini Teherani, M. Razeghi, and H.-J. Drouhin, Proc. SPIE 7217, 721708 (2009).
[6] B. K. Meyer, H. Alves, D. M. Hofmann, W. Kriegseis, D. Forster, F. Bertram, J. Christen, A. Hoffmann, M. Straßburg, M. Dworzak, U. Haboeck, and A. V. Rodina, Phys. Status Solidi B 241, 231 (2004), and references therein.
[7] K. Thonke, Th. Gruber, N. Teofilov, R. Schonfelder, A. Waag, and R. Sauer, Physica B 308, 945 (2001).
[8] T. Monteiro, A. J. Neves, M. C. Carmo, M. J. Soares, M Peres, J. Wang, E. Alves, E. Rita, and U. Wahl, J. Appl. Phys. 98, 13502 (2005).
[9] Ch. Solbrig and E. Mollwo, Solid State Commun. 5, 625 (1967).
[10] R. Dingle, Phys. Rev. Lett. 23, 579 (1969).

4.3 Growth of "moth-eye" ZnO nanostructures on Si (111), c-Al_2O_3, ZnO and steel substrates by PLD

To Be Submitted to Journal of Crystal Growth (2011)

V. E. Sandana [1,2,3], D. J. Rogers[1], F. Hosseini Teherani[1], M. Molinari[4], M. Troyon[4], A. Largeteau[8], G. Demazeau[8], H.-J. Drouhin[3], C. Scott[9] & M. Razeghi[2]

[1]Nanovation, Orsay, France,
[2]Center for Quantum Devices, Northwestern University, Evanston, USA
[3]Dept. of Irradiated Solids, École Polytechnique, Palaiseau, France
[4]LMEN, Université de Reims Champagne Ardennes, France,
[5]ICMCB, Université de Bordeaux, France.
[6]Arcelor-Mittal, Metz, France.

1. INTRODUCTION

ZnO is a remarkable multifunctional material with a distinctive set of properties including a direct bandgap of ~3.4eV and an exciton binding energy of ~60meV. It also has a high transparency over the visible spectrum, a strong piezoelectric response, a very wide range of tuneable conductivities (varying from semi-insulating to semi-metallic) and good biocompatibility [1]. In previous work [2,3] it was shown that Pulsed Laser Deposition (PLD) could be used to give self-forming arrays of vertically aligned nanostructures on Si and sapphire substrates. In particular, moth-eye-type nanostructures were shown to exhibit blackbody-like properties over the whole visible spectrum [4], which suggested that they could be used, for instance, as anti-reflection coatings on solar cells [5] or for enhanced extraction in LEDs [6]. Such nanocones were also used as an active layer in n-ZnO/p-Si heterojunction LEDs [7]. This paper reports on the development of similar ZnO structures on ZnO and high manganese austenitic steel substrates by PLD and compares them with those obtained on Si (111) and c-Al_2O_3.

2. EXPERIMENT

ZnO moth-eye nanostructures were grown by PLD on Si (111), c-Al2O3, hydrothermal ZnO [8] and austenitic steel substrates, using growth conditions described previously [9]. The growth times were similar for all substrates. Sample morphology was studied using a Hitachi S4800 Field Emission-Scanning Electron Microscope (FE-SEM). The crystal quality of the nanostructures was investigated using high resolution X-Ray Diffraction (XRD) performed in a Panalytical MRD Pro system using Cu Kα radiation. Optical properties were studied using room temperature cathodoluminescence (CL) performed with a home made system in an SEM [10].

3. RESULTS & DISCUSSION

3.1 PLD Growth of ZnO Nanostructures on Si(111), c-Al_2O_3 , ZnO and high manganese austenitic steel

3.1.1 FE-SEM images

Figure 1 shows SEM images of samples of ZnO nanocones obtained on the 4 different substrates. The structures on all the substrates exhibit dense, self-forming, arrays of vertically-aligned cone-like "moth-eye" nanostructures.

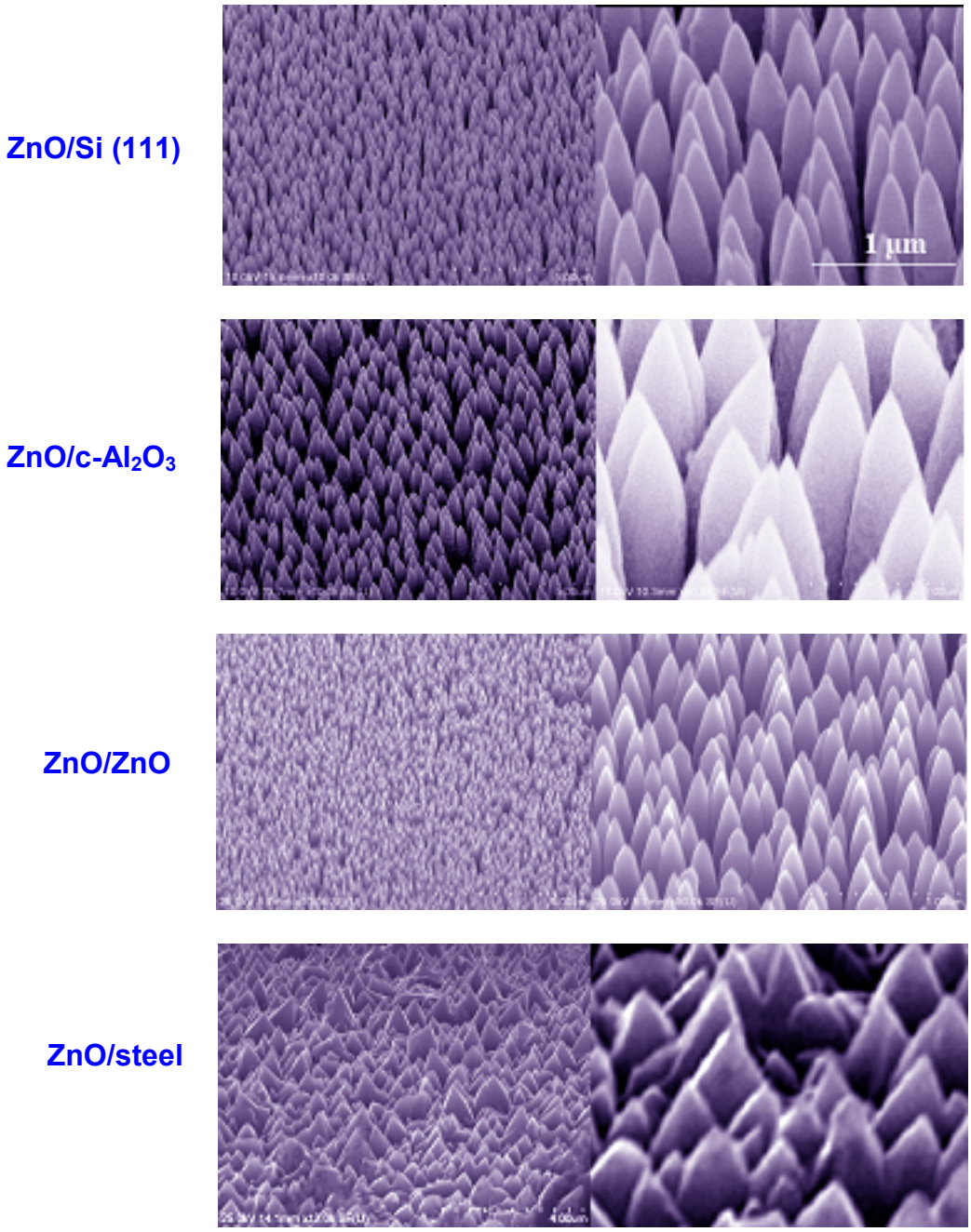

Figure 1: SEM images of ZnO nanostructures grown by PLD on (a) Si (111), (b) c-Al_2O_3, (c) ZnO and (d) high manganese austenitic steel. The images on the right are zooms of the images on the left. The scales for the images on the right are similar for all substrates.

Laudise et Ballman. [11] suggest that such tapered nanorods develop as a result of the relative growth rates of the different crystal facets of ZnO (growth rates are higher for directions orthogonal to closer spaced lattice planes). For wurtzite ZnO, the maximum growth rate is in the [0001] direction and it should be about twice as fast as that in the [10-10] direction, while the growth rate along [10-11] should be intermediate. Figure 2 shows a top view of ZnO nanocones on a Si (111) substrate.

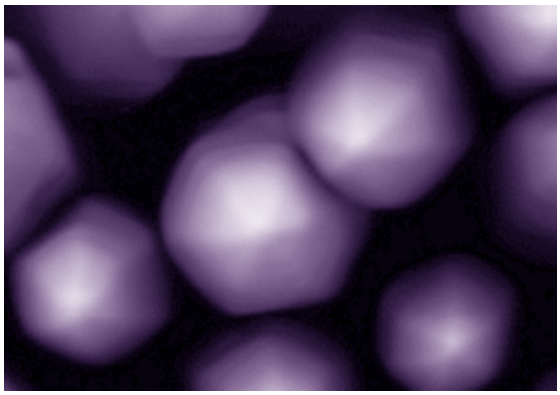

Figure 2: SEM top view of ZnO nanocones grown on Si (111).

In this figure the characteristic, six-fold, faceting of the wurtzite ZnO structure can clearly be discerned. Such faceting is well pronounced at the initial stages of growth. Under the deposition conditions used in this study, however, the facets become more indistinct as growth proceeds, until the side-walls of the nanotips take on the smoothed, nanocone-like appearance observed in Figure 1.

3.1.2 XRD Investigations

Figure 3 shows the XRD 2θ/ω scans for the (0002) peaks of the nanostructures grown on the different substrates. Strong ZnO (0002) reflections corresponding to a c-axis oriented wurtzite phase were observed for all the samples. The Full Width at Half Maximum (FWHM) for the samples (see Table 1) vary from 0.011° for the nanocones grown on ZnO up to 0.019 on Si, 0.06° on c-Al2O3 and 0.34° on steel. This suggests that, apart from the ZnO on steel, the nanostructures have relatively small variation in lattice parameter relative to that observed for ZnO thin films on similar substrates. These results indicate that the sample grown on ZnO bulk was more perfectly crystallized than the others.

Table 1 also shows that the main peak position in the 2θ/ω scans is similar for the Si, c-Al_2O_3 and ZnO substrates, corresponding to c lattice parameters of 5.202 - 5.203 Å. This is very close to what would be expected for relaxed wurtzite ZnO (5.204 – 5.206 Å). The c lattice parameter corresponding to the peak maximum for the nano ZnO on high manganese austenitic steel, however, is significantly larger, at 5.225 Å, which corresponds to ZnO under compressive strain (the lattice parameter of the steel is 3.6137 Å). Closer inspection reveals that the peak seems to be made up of multiple peaks, which could be related to relaxation during film growth.

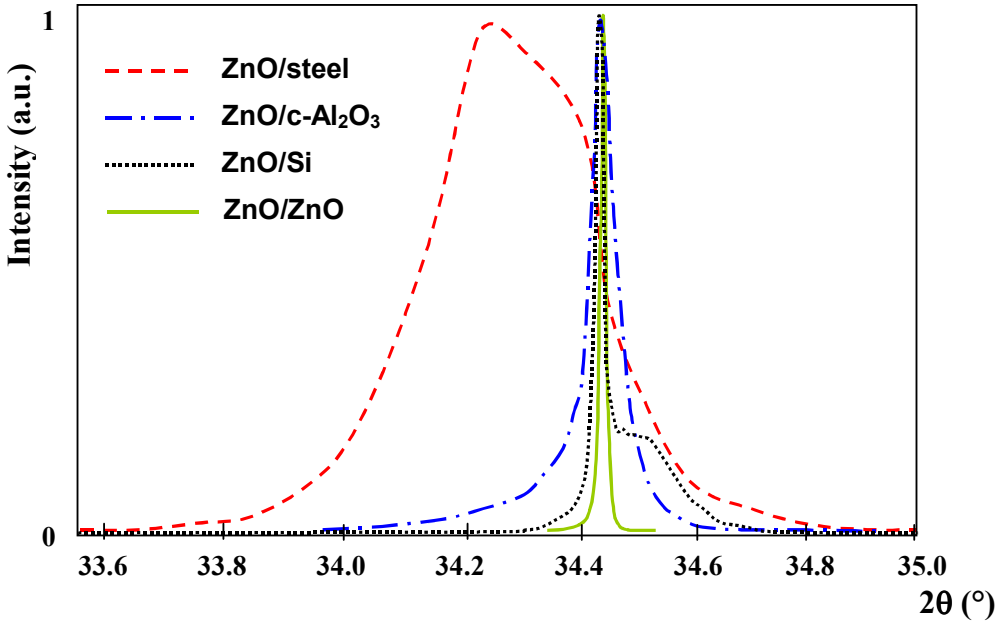

Figure 3. Normalised XRD 2θ/ω scans (linear intensity scale) for the (0002) peaks of the nanostructured ZnO grown on various substrates.

The nano ZnO/Si (111) shows broadening on the higher-angle side at the base of the peak, signifying a region with a smaller c lattice parameter. This could be due to disorder at the start of growth creating a less dense a-b plane at the base of the nanocones (and thus a larger a lattice parameter). Figure 4 shows an SEM side-view image, which confirms that crystallographic disorder does indeed exist at the base of the cones.

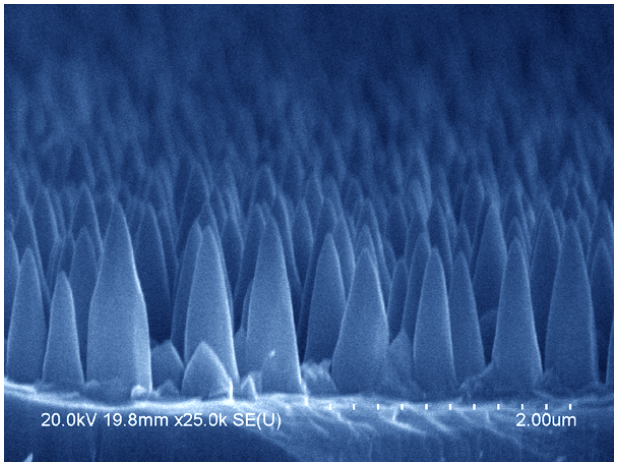

Figure 4: SEM side view of ZnO nanocones grown on Si (111).

The XRD ω rocking curves (open detector configuration) are shown in Figure 5.

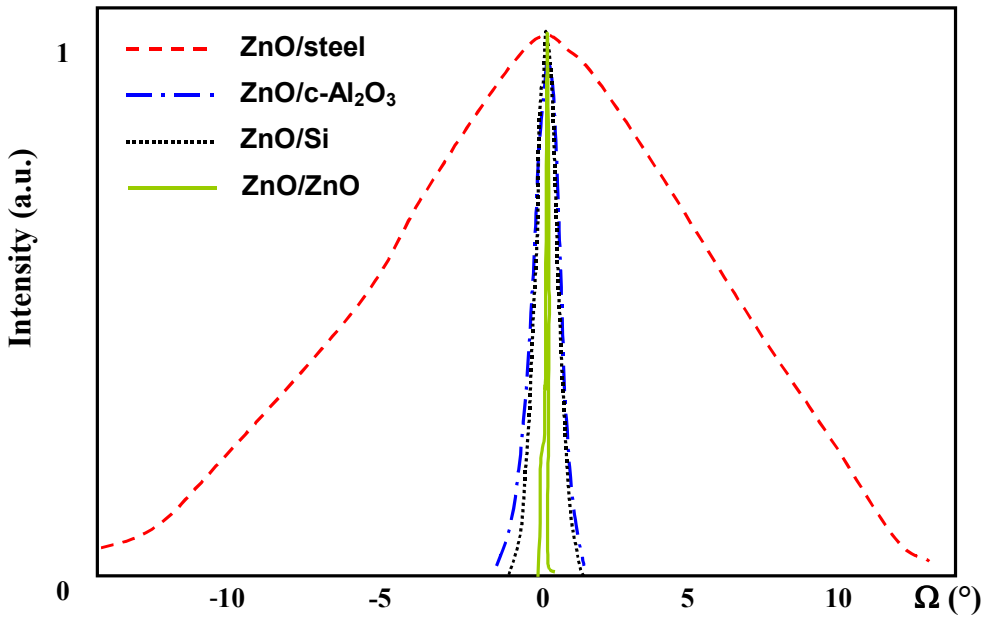

Figure 5. Normalised XRD ω scan rocking curves (linear intensity scale) for the (0002) peaks of the nanostructured ZnO grown on various substrates.

The FWHM is significantly larger for the sample on steel and is narrowest for the sample on ZnO (a lower FWHM corresponds to a smaller dispersion in the crystallographic orientation). The ZnO on sapphire is larger than would typically be observed for equivalent thin films whereas that for Si is comparable or smaller.

SUBSTRATE	ω Scan INTENSITY (cps)	ω ROCKING CURVE FWHM (°)	2θ/ω FWHM (°)	c LATTICE PARAMETER (Å)
Si (111)	~1000	0.85	0.019	5.203
c-Al_2O_3	~500	0.94	0.06	5.202
Bulk ZnO	~100000	0.028	0.011	5.202
Austenitic Steel	~100	11.7	0.34	5.225

TABLE 1. Comparison of XRD scan intensities and FWHM for ZnO nanocones grown on Si (111), *c*-Al_2O_3 , ZnO and high Mn austenitic steel.

3.1.3 CL Investigations

RT CL spectra of the nanostructured ZnO on various substrates are shown in Figure 6 and Table 2.

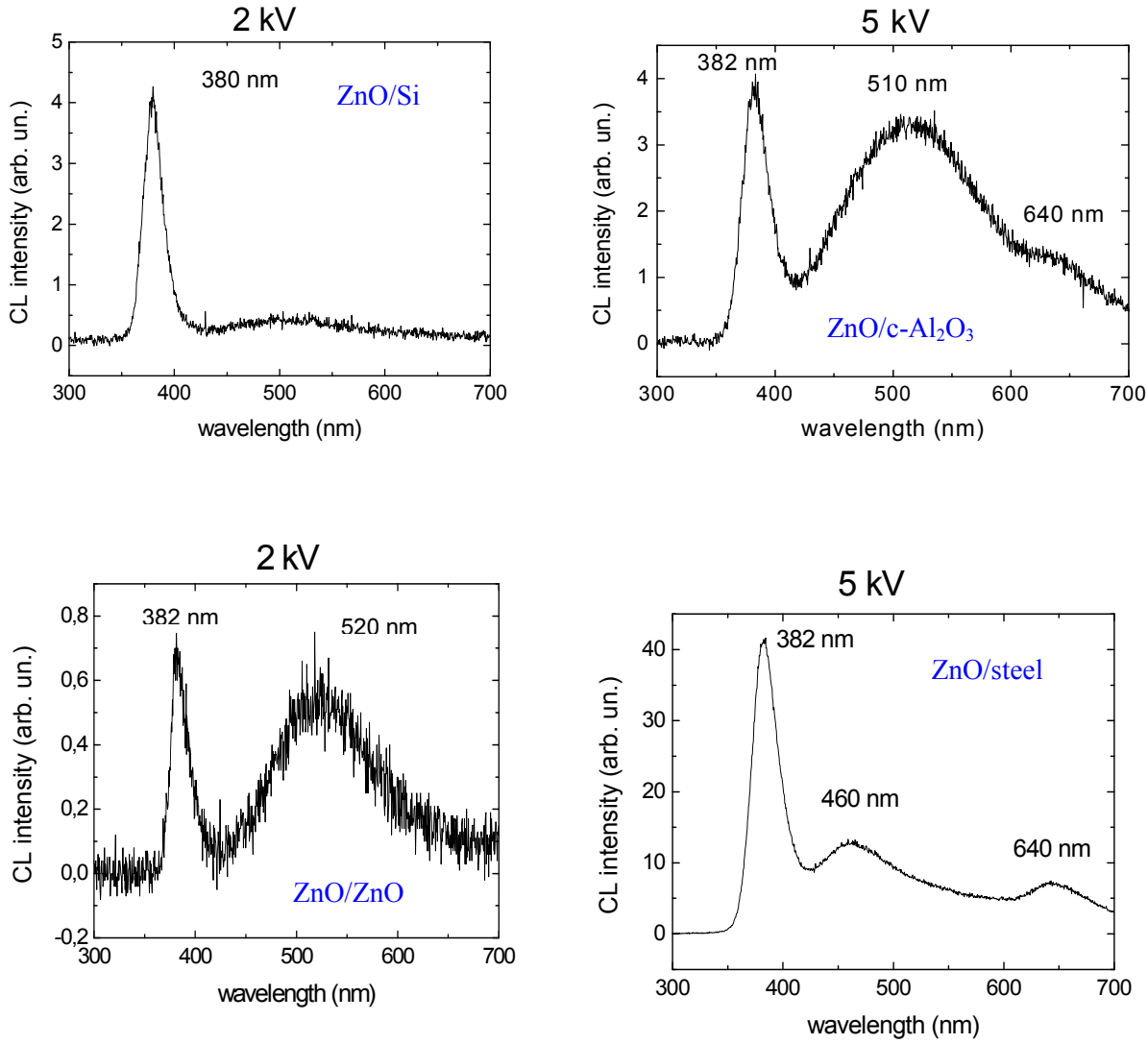

Figure 6. CL spectra of the nanostructured ZnO on various substrates.

The spectra all show an ultraviolet (UV) band (at around 380-382 nm), which is characteristic of Near Band Edge (NBE) emission from wurtzite ZnO [12]. The NBE emission wavelength and the FWHM were slightly lower for the structures grown on the Si (111) substrates than for those grown on the c-Al_2O_3, ZnO and austenitic steel. Green bands visible in the spectra for the growths on c-Al_2O_3 and Si (111) (at wavelengths of 510 and 520 nm, respectively) were attributed to defects in the ZnO [13]. A red peak at 640nm, present in the spectra for the growths on c-Al_2O_3 and steel, could be related to Al and Fe from the substrates diffusing into the ZnO. An additional blue (460 nm) peak was observed in the spectrum for the sample on steel. Although the origin is not yet clear, a similar band has been reported elsewhere for ZnO films [14] and nanorods [15]. Jin et al. [16] considered that it might be due to the existence of oxygen-depleted interface traps. Of particular note, is the absence of green, red or blue bands in the CL spectra of the ZnO nanocones grown on Si (111), plus the relatively intense peak of the NBE. These indicate that the nanostructures on Si had particularly good crystal quality and a relatively low defect density.

SUBSTRATE	1st Peak position (nm)	1st Peak FWHM (nm)	2nd Peak position (nm)	3rd Peak position (nm)
Si (111)	380	22	None	None
c-Al_2O_3	382	23	510	640
Bulk ZnO	382	22	520	None
Austenitic Steel	382	28	460	640

TABLE 2. Comparison of CL spectra, main peak, FWHM, and intensity for ZnO nanostructures grown on Si(111), c-Al_2O_3, ZnO and high Mn austenitic steel.

6. CONCLUSIONS

Nanostructures were grown on Si (111), c-Al_2O_3, ZnO and high Mn austenitic steel substrates using catalyst-free PLD. The impact of substrates on the sample morphology and crystallographic and optical properties was investigated. Self-forming, vertically-aligned, arrays of moth-eye-like nanocones were obtained on all substrates. XRD and RT CL studies indicated that the nanostructures grown on all substrates were highly c-axis oriented wurtzite ZnO with strong NBE emission. Of particular note was the fact that the ZnO crystallized well on all substrates (including steel) and that the moth-eye structures on Si (111) showed very good crystallographic and optical characteristics compared with equivalent thin films grown on Si.

Such moth-eye nanostructures have a graded effective refractive index and exhibit black-body characteristics. In photovoltaic applications they may, therefore, have potential for use as anti-reflective coatings[4], light trapping layers and nanostructured template back-electrodes[17]. In LED applications they may have potential for use as coatings for enhancement of light extraction[6], as active ZnO layers for light emission[9] or as nanostructured templates for (In)GaN regrowth[18]. Indeed, since ZnO nanostructures can be grown readily on a wide range of substrates such an approach could facilitate growth of GaN-based devices and nanostructures on mismatched and/or technologically important substrates, which may have been inaccessible till present, including steel.

ACKNOWLEDGEMENTS

The authors would like to thank the French "Association Nationale de la Recherche et de la Technologie" for financial support and Professor Ryan McClintock of Northwestern University for useful discussions.

REFERENCES

(1) Look D. C. in "Zinc Oxide: A Material for Micro- and Optoelectronic Applications", ed. by Nickel N. H. eNATO Science series II : Mathematics, physics & chemistry, **2005**, 194, 37
(2) Sandana V. E.; Rogers, D. J.; Teherani, F. H.; McClintock, R.; Razeghi, M.; Drouhin, H.-J.; Clochard, M.C.; Sallet, V.; Garry, G.; Fayoud, F. Proc. SPIE, **2008**, 6895, 68950Z
(3) Sandana, V. E.; Rogers, D. J.; Hosseini Teherani, F.; McClintock, R.; Bayram, C.; Razeghi M.; Drouhin H.-J.; Clochard, M. C.; Sallet, V.; Garry, G.; Falyouni F. J. Vac. Sci. Technol. B

2009, 27, 31678-1683
(4) Peres, M.; Soares, M. J.; Neves, A. J.; Monteiro, T.; Sandana, V. E. Teherani, F.; Rogers, D. J. Phys. Status Solidi A, **2010** 1–4
(5) Tsakalakos, L. Mater. Sci. and Eng. R **2008**, 62, 175–189
(6) Zhong, J.; Chen, H.; Saraf, G.; Lu, Y.; Choi, C. K.; Song, J. J. Appl. Phys. Lett. **2007**, 90, 203515
(7) Pau, J-L; Piqueras, J.; Rogers, D. J.; Hosseini Teherani, F.; Minder, K.; McClintock, R.; Razeghi, M. J. Appl. Phys. **2010**, 107, 033719
(8) Rogers D. J.; Hosseini Teherani, F; Largeteau, A.; Demazeau, G.; Moisson, C.; Turover, D.; Nause, J.; Garry, G.; Kling, R., Gruber, T.; Waag, A., Jomard, F.; Galtier, P.; Lusson, A.; Monteiro, T.; Soares, M. J., Neves, A.; Carmo, M. C.; Peres, M.; Lerondel, G.; Hubert, C, Appl. Phys. A, **2007**, 88, 49-56
(9) Rogers D. J.; Sandana, V. E.; Hosseini Teherani, F.; Razeghi, M.; Drouhin, H.-J. Proc. SPIE, **2009**, 7217, 721708
(10) Troyon M.; Pastré, D.; Jouart, J. P.; Beaudoin, J. L. Ultramicroscopy **1998**, 75, 15
(11) Laudies, R. A.; Ballman, A. A. J. Phys. Chem. **1960**, 64, 688
(12) Kong Y. C.; Yu, D. P.; Zhang, B.; Fang, W.; Feng, S. Q. Appl. Phys. Lett. **2001**, 78, 407
(13) Studenikim, S. A.; Golego, N.; Cocivera, M. J. Appl. Phys., **1998**, 84, 2287
(14) Fu, Z.; Lin, B.; Liao, G.; *Z*. Wu J. Cryst. Growth **1998** 193, 316.
(15) Wu, J.-J. ; Liu, S.C. Adv. Mater. **2002** 14, 215.
(16) Jin, B. J.; S. Im; Lee, S.Y. Thin Solid Films **2000**, 366, 107
(17) Söderström, T.; Dominé, D.; Feltrin, A.; Despeisse, M.; Meillaud, F.; Bugnon, G.; Boccard, M.; Cuony, P.; Haug, F.-J.; Faÿ S.; Nicolay S.; Ballif C. Proc. SPIE, **2010**, 7603
(18) Rogers, D. J.; Sandana, V. E.; Hosseini Teherani, F.; Orsal,G.; Molinari, M.; Troyon, M.; Gautier, G.; Moudakir, T.; Abid, M.; Ougazzaden,A.; Peres, M.; Soares, M. J.; Neves, A. J.; Monteiro,T.; Drouhin H.-J.; Razeghi, M. submitted to Adv. Mater. **2011**

4.4 Use of "moth-eye" ZnO nanostructures on Si (111) as templates for MOVPE growth of GaN

To be submitted to Applied Physics Letters in 2011

D. J. Rogers[1], V. E. Sandana [1,2,3], F. Hosseini Teherani[1], G. Orsal[4], M. Molinari[5], M. Troyon[5], S. Gautier[4], T. Moudakir[6], M. Abid[7], A. Ougazzaden[7], M. Peres[8], M. J. Soares[8], A. J. Neves[8], T. Monteiro[8],H.-J. Drouhin[3] & M. Razeghi[2]

[1]Nanovation, Orsay, France
[2]Center for Quantum Devices, Northwestern University, Evanston, USA
3Dept. of Irradiated Solids, École Polytechnique, Palaiseau, France
[4]LMOPS Université de Metz Metz, France
[5]LMEN, Université de Reims Champagne Ardennes, France
[6]Supelec, Metz, France
[7]UMI Georgia Tech Lorraine & CNRS, Metz, France
[8]Departamento de Física/I3N, Universidade de Aveiro, 3810-193 Aveiro, Portugal

INTRODUCTION

Wurtzite ZnO is a remarkable multifunctional material with a distinctive set of properties including a direct bandgap of ~3.4eV and an exciton binding energy of ~60meV. It also has a high transparency over the visible spectrum, a strong piezoelectric response, a very wide range of tuneable conductivities (varying from semi-insulating to semi-metallic) and good biocompatibility[1]. In previous work[2,3] it was shown that Pulsed Laser Deposition (PLD) could be used to give self-forming arrays of vertically aligned nanostructures on Si and sapphire substrates. In particular, moth-eye-type nanostructures were shown to exhibit blackbody-like properties over the whole visible spectrum[4], which suggested that they could be used, for instance, as non-reflective coatings on solar cells[5] or for enhanced extraction in LEDs[6]. Such nanocones were also used as an active layer in n-ZnO/p-Si heterojunction LEDs[7]. This paper reports on the use of such nanostructure arrays as templates for the growth of GaN by MOVPE.

1 EXPERIMENT

ZnO moth-eye nanostructures were grown by PLD on Si (111)[8] as described previously[9]. Sample morphology was studied using a Hitachi S4800 Field Emission-Scanning Electron Microscope (FE-SEM). The crystal quality of the nanostructures was investigated using high resolution X-Ray Diffraction (XRD) performed in a Panalytical MRD Pro system using Cu Kα radiation. Optical properties were studied using room temperature cathodoluminescence (CL) performed with a home made system in an SEM[8] 140 nm of GaN was deposited on the ZnO/Si(111) nanostructures using a low pressure MOVPE T-shaped reactor[9] with Trimethylgallium (TMG) as the Ga source and Trimethylindium (TMIn) as the In source. A combination of NH_3 and Dimethylhydrazine (DMHY) was used as a source of atomic nitrogen. DMHY was added because of a low decomposition temperature, which enhances the concentration

of atomic nitrogen in the gas phase compared to NH_3 alone. This allowed GaN growth at lower initial growth temperatures than those used in conventional MOVPE deposition in order to avoid back-etching of ZnO. Nitrogen was employed as a carrier gas[10] during the whole growth process, in order to avoid hydrogen use, which can also promote back-etching of the ZnO surface at elevated temperatures[11]. RT specular reflection measurements were performed as a function of scattering angle and wavelength (in the range 450–720 nm) with an incidence angle fixed at 45º as shown in Figure 1.

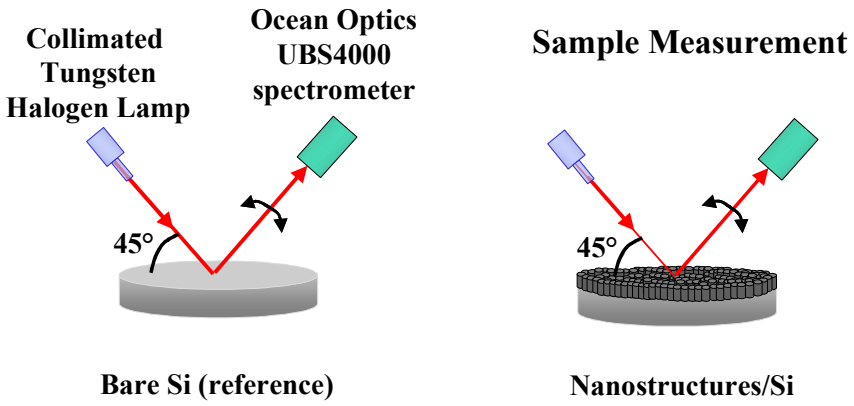

Figure 1: Experimental set-up used for RT specular reflection measurements.

An Ocean Optics UBS4000 spectrometer and computer-controlled rotation stages were employed. The sample was illuminated with a collimated beam of a tungsten/halogen lamp. The rotation stages and the spectra acquisition were piloted with homemade software.

2. RESULTS & DISCUSSION

2.1 SEM

Figure 2 shows SEM images of an ZnO/Si(111) sample before and after MOVPE growth of GaN.

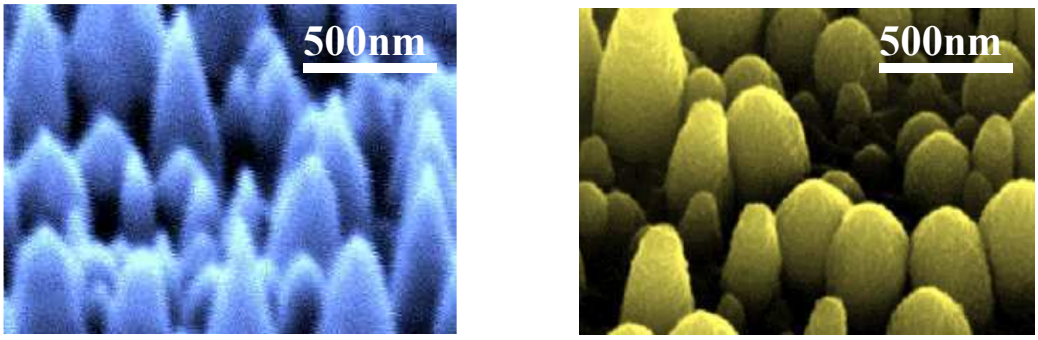

Figure 2. SEM images of a nano ZnO/Si sample before and after MOVPE overgrowth of GaN.

In this figure it can be seen that the nanocones thicken and become more rounded after the GaN growth, which is coherent with GaN having encapsulated the ZnO nanocones.

2.2 XRD Investigations

Figure 3 shows normalized XRD 2θ/ω scans for the wurtzite (0002) peak before and after MOVPE growth of GaN.

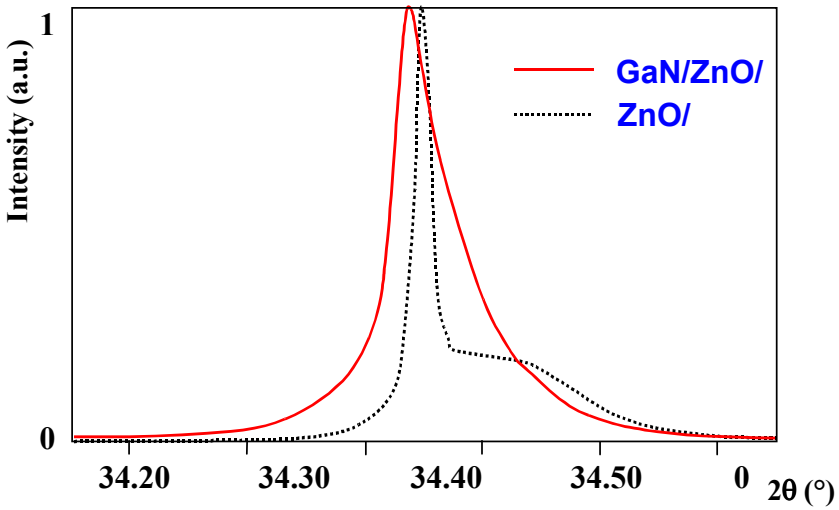

Figure 3. Normalised XRD 2θ/ω scans around the (0002) peak of the nanostructured ZnO on Si (111) before and after MOVPE GaN overgrowth.

A strong (0002) reflection is observed before and after GaN growth, which suggests that the preferential c-axis orientation has been maintained. The nano ZnO/Si (111) shows broadening on the higher-angle side at the base of the peak, signifying a region with a smaller c lattice parameter. This could be due to disorder at the start of growth creating a less dense a-b plane at the base of the nanocones (and thus a larger a lattice parameter). The peak is broader after the GaN growth (FWHM of 0.061° vs a value of 0.019° before GaN growth), which is what might be expected for epitaxy of a thin layer of GaN. The main peak position in the 2θ/ω scans after GaN growth has a c lattice parameter of 5.204 Å as compared to the value of 5.203 Å for the ZnO/Si (111) prior to GaN growth. This is a negligible difference under these measurement conditions and both of these values are very close to what would be expected for relaxed wurtzite ZnO (5.204 – 5.207 Å).

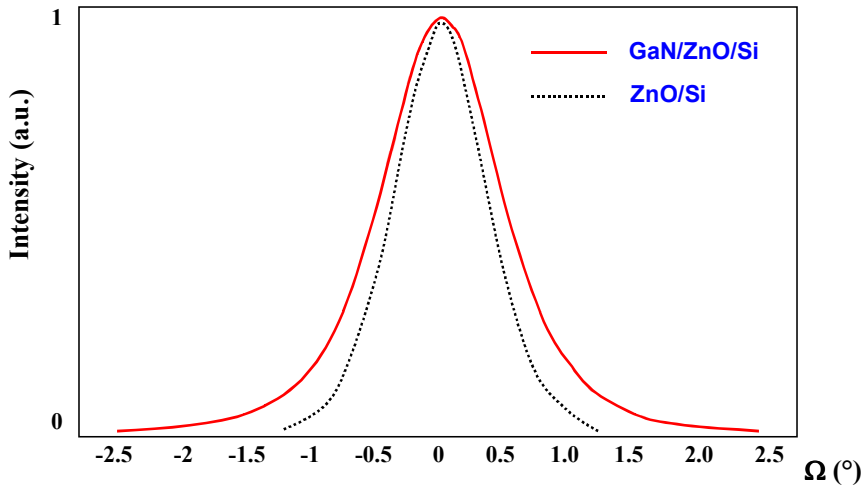

Figure 4. Normalised XRD ω scans around the (0002) peak of the nanostructured ZnO on Si (111) before and after MOVPE GaN overgrowth.

The figure shows that the rocking curve FWHM increased from 0.85° to 1.07° after GaN growth. This indicates that there is slightly more dispersion in the crystallographic orientation about the c-axis after the GaN growth.

2.3 CL Investigations

Figure 5 shows the CL spectrum for the sample after GaN growth.

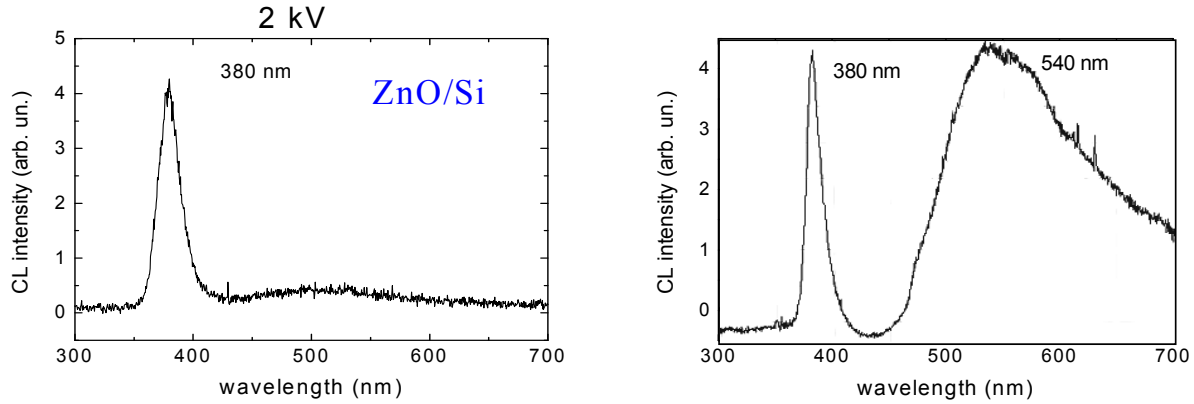

Figure 5: CL spectrum for a sample of moth-eye ZnO/Si (111) before and after growth of GaN by MOVPE.

The spectra both show an ultraviolet (UV) band (at around 380-382 nm), which is characteristic Edge (NBE) emission from wurtzite ZnO[12]. The CL spectrum for the ZnO nanocones on Si (111) has a relatively low green emission compared with the NBE emission which indicates that the nanostructures had particularly good crystal quality and a relatively low defect density.
After GaN growth, a strong yellow/green band peaked at about 540 nm appeared. This yellow/green band was observed in previous studies of GaN films grown on 2D ZnO buffer layers and it was

suggested that it could be associated with defects in the wurtzite GaN structure[13].

2.4 RT specular reflection measurements

Figure 5 shows the results of RT reflection measurements were for (a) the Si (111) substrate and (b) the moth-eye GaN/ZnO/Si (111) with intensity expressed relative to the maximum reflectance for the Si (111) substrate.
The plots show that the relative reflectance from the moth-eye nanostructures show less than 1% of the reflection for the substrate over the whole visible range at all scattering angles. Furthermore, the change in the intensity of specular reflection relative to the diffuse reflection is abrupt for the substrate and gradual for the nanostructures. This indicates that the diffuse radiation is higher for the surface with nanorods. The reflection in the region ($\lambda < 550$ nm) seems to be more suppressed. This may be due to the features being subwavelength, combined with absorption in the GaN.

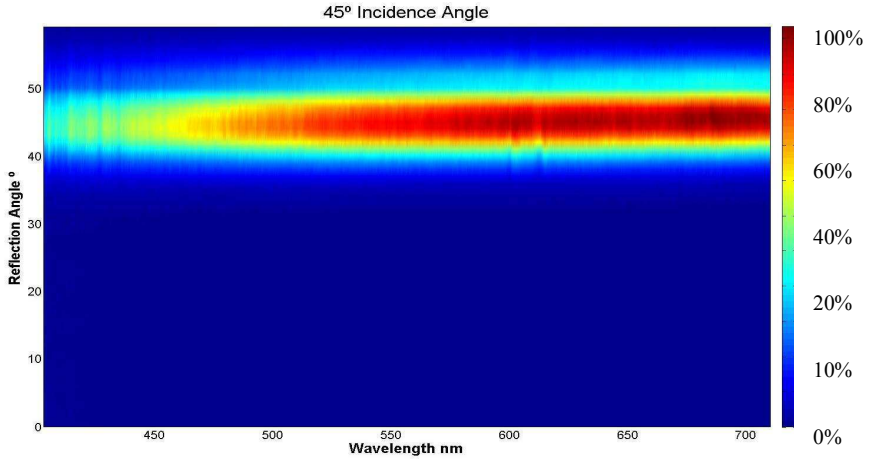

(a)

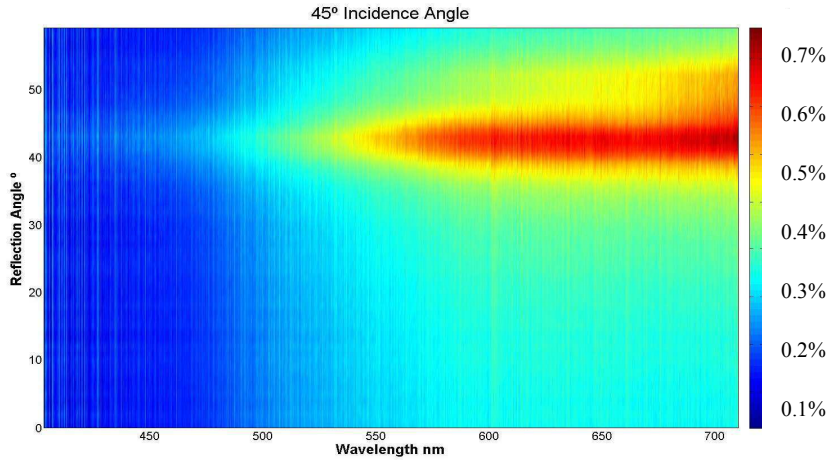

(b)

Figure 5: optical reflectance as a function of scattering angle and wavelength for (a) the Si (111) substrate and (b) the moth-eye GaN/ZnO/Si (111), with the incident beam held at an angle of 45 degrees from the normal to the sample surface.

4. CONCLUSIONS

Self-forming, vertically-aligned, arrays of moth-eye like nanocones were grown by catalyst-free PLD on Si (111) substrates. Such moth-eye nanostructures have a graded effective refractive index and exhibit black-body characteristics. Thus they may have potential for use as anti-reflective coatings on photovoltaics or for light extraction in LEDs.

XRD and RT CL studies indicated that nanostructures were highly c-axis oriented wurtzite ZnO with strong NBE emission and very good crystallographic and optical characteristics compared with equivalent thin films grown on Si (111)[13].

The nanostructures on Si (111) were adopted for use as templates for the overgrowth of GaN by MOVPE. XRD, scanning electron microscopy, EDX and CL revealed that the ZnO nanocones were encapsulated with GaN, without evidence of ZnO back-etching. Since ZnO nanostructures can be grown readily on nearly all substrates[14], such an approach could facilitate growth of GaN based nanostructures, thin films and devices on mismatched and/or technologically important substrates, which may have been inaccessible till present. RT angular-dependent specular reflection measurements indicated that the GaN/ZnO nanostructures acted as highly effective broadband antireflection coatings. The reflection in the region ($\lambda < 550$ nm) was greatly reduced. This may be due to subwavelength structured features and/or absorption in the GaN.

In fact, the reduction behaviour in specular reflection from GaN/ZnO could be explained by multiple scattering because of the surface areas increased remarkably compared to the wafer surface. The high surface area of the GaN/ZnO density causes the multiple scattering of light between nanostructures to enhance light trapping. Thereby, better antireflection characteristics (with an average reflection of less than 1%) were observed in a GaN/ZnO/Si in the wavelength range of 400 – 720 nm. From the viewpoint of the graded refractive index effect, the GaN/ZnO array is explained to act as a buffer layer to intervene the difference in refractive indexes between air and the Si substrate.

ACKNOWLEDGEMENTS

The authors would like to thank the French "Association Nationale de la Recherche et de la Technologie" for financial support and Professor Ryan McClintock of Northwestern University for useful discussions.

REFERENCES

[1] D. J. Rogers and F. Hosseini Teherani, Encyclopedia of Materials: Science and Technology, Elsevier, Oxford **2010**, 1-5.

[2] V. E. Sandana, D. J. Rogers, F. H. Teherani, R. McClintock, M. Razeghi, H.-J. Drouhin, M. C. Clochard, V. Sallet, G. Garry, F. Fayoud, Proc. SPIE, **2008**, 6895, 68950Z

[3] V. E. Sandana, D. J. Rogers, F. H. Teherani, R. McClintock, C. Bayram, M. Razeghi, H.-J. Drouhin, M.C. Clochard, V. Sallet, G. Garry, F. Falyouni, J. Vac. Sci. Technol. B, **2009**, 27, 3, 1678-1683

[4] M. Peres, M. J. Soares, A. J. Neves, T. Monteiro, V. E. Sandana, F. Teherani, and D. J. Rogers, Phys. Stat. Sol B **2010**, 247, 1695-1698

[5] L. Tsakalakos Mater. Sci. and Eng. **2008**, R 62, 175–189

[6] J. Zhong, H. Chen, G. Saraf, Y. Lu, C. K. Choi, J. J. Song, Appl. Phys. Lett. **2007**, 90, 203515
[7] D. J. Rogers, V. E. Sandana, F. Hosseini Teherani, M. Razeghi and H.-J. Drouhin, Proc. SPIE, **2009**, 7217, 721708
[8] M. Troyon, D. Pastré, J. P. Jouart, J. L. Beaudoin, Ultramicroscopy **1998**, 75, 15
[9] A. Mircea, A. Ougazzaden, R. Mellet, Prog. in Cryst. Growth Charac. **1989**, 19, 39
[10] S. Gautier, J. Ould-Saad, A. Martin, A. Sirenko, A. Ougazzaden, J. Cryst. Growth **2007**, 298, 428
[11] F. Scholz, V. Harle, F. Steuber, *H.* Bolay, A. Dornen, B. Kaufmann, V. Syganow, A. Hangleiter, J. Cryst. Growth **1997** 170, 321
[12] Y. C. Kong, D. P. Yu, B. Zhang, W. Fang, S. Q. Feng, Appl. Phys. Lett. **2001**, 78, 407
[13] A. Ougazzaden, D. J. Rogers, F. Hosseini Teherani, G. Orsal, T. Moudakir, S. Gautier, V. E. Sandana, F. Jomard, M. Abid, M. Molinari, M. Troyon, P. L. Voss, D. McGrouther and J. N. Chapman, Proc. of SPIE, **2010**, 7603, 76031D-1
[14] D. J. Rogers, F. Hosseini Teherani, V. E. Sandana and M. Razeghi, Proc. of SPIE, **2010**, 7605, 76050K-1

Conclusion

Fabrication of Nanostructured Heterojunction LEDs Using Self-Forming "Moth-Eye" Type Arrays of n-ZnO Nanocones Grown on p-Si (111) Substrates by Pulsed Laser Deposition.
ZnO nanostructures were grown on Si (111) substrates using Pulsed Laser Deposition. The impact of growth temperature and Ar pressure on the morphology, crystal structure and photoluminescence was investigated. Various types of ZnO nanostructures were obtained. Self-forming arrays of vertically-aligned nanorods and nanocones with strong c-axis crystallographic orientation and good optical response were obtained at higher Ts. The nanocone, or "moth-eye" type structures were selected for LED development because of their graded effective refractive index, which could facilitate improved light extraction at the LED/air interface. Such moth-eye arrays were grown on p-type Si (111) substrates to form heterojunction LEDs with the n-type ZnO nanocones acting as an active component of the device. These nanostructured LEDs gave rectifying I/V characteristics with a threshold voltage of about 6V and a blueish-white electroluminescence, which was clearly visible to the naked eye.

Morphological and optical studies of self-forming ZnO nanocolumn and nanocone arrays grown by PLD on various substrates.
ZnO nanostructures were grown by pulsed laser deposition on c-sapphire, Si (111) (n-type and p-type) and analysed using morphological and optical techniques. Under optimized growth conditions, self-forming arrays of vertically aligned nanostructures were obtained. Scanning electron microscopy studies revealed two main structures: nanocolumns and a 'moth-eye type' array of nanocones, which gave a graded effective refractive index. X-ray diffraction measurements indicate that both types of structures are highly oriented along the c-axis. The optical properties were investigated using low temperature photoluminescence (PL) and room temperature (RT) reflection measurements. Low temperature PL spectra for nanocolumns grown on sapphire and n-type Si showed an emission which is similar to that observed for bulk ZnO with a spectrum dominated by donor bound exciton recombination at ≈3.36 eV and a structured green band. The PL intensity was particularly enhanced for nanocone structures grown on cubic Si substrates. For these samples, additional features, which are not observed for bulk ZnO were observed at 3.12, 3.02 and 2.92 eV following a vibronic progression of 100 meV. RT angular-dependent specular reflection measurements indicated that all the nanostructures act as highly effective broadband antireflection coatings.

Growth of "moth-eye" ZnO nanostructures on Si (111), c-Al_2O_3, ZnO and steel substrates by PLD.
Self-forming, vertically-aligned, arrays of black-body-like ZnO moth-eye nanostructures were grown on Si (111), c-Al_2O_3, ZnO and high manganese austenitic steel substrates using Pulsed Laser Deposition. X-ray diffraction (XRD) revealed the nanostructures to be well-crystallised wurtzite ZnO with strong preferential c-axis crystallographic orientation along the growth direction for all the substrates. Cathodoluminescence (CL) studies revealed emission characteristic of the ZnO near band edge for all substrates. Such moth-eye nanostructures have a graded effective refractive index and exhibit black-body characteristics. Coatings with these features may offer improvements in photovoltaic and LED performance. Moreover, since ZnO nanostructures can be grown readily on a wide range of substrates it is suggested that such an approach could facilitate growth of GaN-based

devices on mismatched and/or technologically important substrates, which may have been inaccessible till present.

Use of "moth-eye" ZnO nanostructures on Si (111) as templates for MOVPE growth of GaN.
Self-forming, vertically-aligned, arrays of black-body-like ZnO moth-eye nanostructures were grown on Si (111) using Pulsed Laser Deposition. X-ray diffraction (XRD) revealed the nanostructures to be well-crystallised wurtzite ZnO with strong preferential c-axis crystallographic orientation along the growth direction for all the substrates. Cathodoluminescence (CL) studies revealed emission characteristic of the ZnO near band edge. The nanostructures on Si were used as templates for the overgrowth of GaN by metal organic vapor phase epitaxy. XRD, scanning electron microscopy and CL revealed that the ZnO nanocones were encapsulated with GaN, without evidence of ZnO back-etching. Since ZnO nanostructures can be grown readily on nearly all substrates, such an approach could facilitate growth of GaN based devices and nanostructures on mismatched and/or technologically important substrates, which may have been inaccessible till present. RT angular-dependent specular reflection measurements indicated that the GaN/ZnO nanostructures acted as highly effective broadband antireflection coatings.

VI Dépôts de ZnO par PLD pour la fabrication de TFT et TCO

Résumé

Les deux articles qui constituent ce chapitre décrivent l'utilisation de ZnO déposé par PLD pour la fabrication de TFT et de TCO.

Dans le premier article l'étude porte sur un TFT à base de dépôt de ZnO sur une structure de type $Si_3N_4/SiO_2/Si$ (111) et présente les caractéristiques cristallographiques, électriques et optiques (transmission de la lumière visible) de ce composant. Les spectres de XRD et les images MEB montrent que dans les conditions expérimentales utilisés ZnO présente une structure würtzite polycristalline, une qualité cristallographique relativement bonne, le scan XRD « $2\theta/\omega$ » (cf. annexe I.3) présente une largeur à mi-hauteur de 0.11º et une position du pic correspondant à une valeur du paramètre de maille c de 5.189 Å. Le scan XRD « ω » (cf. annexe I.3) indique une orientation préférentielle selon l'axe c. Des dépôts de ZnO sur du verre dans les mêmes conditions ont été réalisés afin de pouvoir étudier les spectres de transmission. Les résultats ont indiqué une transmission élevée sur tout le spectre visible. Un composant FET à géométrie « back-gate » a été fabriqué. Dans cette configuration le drain et la source sont situés sur la même surface alors que la grille est située sur la surface opposée. Les mesures électriques montrent une amélioration de la réponse du composant pour une tension d'allumage de ~ 0 V et un courant proche de du courant de fuite. Réduit en taille, ce composant TFT pourrait être utilisé dans des applications hautes fréquences.

Dans le second article, l'étude porte sur les applications pour l'électronique sur support souple. ZnO est, dans ce, déposé sur du papier afin d'étudier la possibilité de fabriquer des composants électroniques sur des substrats souples à l'aide d'un dépôt par PLD à basse température. Les caractéristiques cristallographiques et optiques sont présentées. Néanmoins, à l'heure actuelle, une étape de recuit post-déposition de ZnO, à une température d'au moins 200°C est nécessaire pour obtenir des propriétés électriques et optiques satisfaisantes (cf. p. 6). L'expérience menée a démontré la possibilité de déposer ZnO amorphe par PLD à température ambiante, directement sur du papier et du mylar. La réstivité mesurée à température ambiante est de 13 ± 9 Ω.cm.

Un composant TFT a été réalisé et ZnO a été déposé sur des substrats souples (mylar et papier) par PLD à basse température et a permis de rendre ces substrats conducteurs.

Dans l'étude du TFT, mon travail a consisté a mettre en place un procédé de fabrication du composant par photolithographie (cf. chapitre 2). Dans l'étude de la déposition de ZnO sur substrat souple, j'ai déterminé les conditions de croissance. Pour l'ensemble de ces travaux j'ai réalisé les images MEB, les spectres d'EDX et les mesures électriques.

5.1 Thin film transistors with wurtzite ZnO channels grown on $Si_3N_4/SiO_2/Si$ (111) substrates by pulsed laser deposition

D.J. Rogers Proc. of SPIE 2010 Vol. 7603 760318-1

D. J. Rogers[a], V. E. Sandana[a,b,c], F. Hosseini Teherani[a] & M. Razeghi[b]

[a]Nanovation SARL, 103b rue de Versailles, 91400 Orsay, France
[b]Center for Quantum Devices, Northwestern University, Evanston, Illinois, USA
[c]Department of Irradiated Solids, École Polytechnique, 91128 Palaiseau, France.

1. INTRODUCTION

Wurtzite Zinc Oxide (ZnO) is a remarkable multifunctional material with a distinctive property set and a huge range of existing and emerging applications [1]. In particular, it is a direct wide bandgap semiconductor (Eg ~ 3.4eV) with intrinsically high transparency over the whole visible range and a resistivity that can be tuned from semi-insulating right through to semi-metallic by doping. Recently, there has been a surge in interest for Metal Insulator Semiconductor Field Effect Transistors (MISFETs) employing n-type ZnO-based channel layers. Although these Transparent Thin Film Transistors (TTFTs) are not a new concept [2,3], the new generation exhibits a high on-off ratio ($>10^6$) and a higher channel mobility (μ) than current Si-based TFTs. Two main ZnO TTFT variants, employing either wurtzite [4-8] or amorphous [9] ZnO-based alloys as channels, have emerged. The Amorphous Oxide Semiconductor (AOS) variants are being put forward as an alternative to amorphous Si for use in applications such as select transistors in Liquid Crystal Displays (LCD) and Organic Light Emitting Diode (OLED) displays [10]. TFTs with wurtzite ZnO channels, on the other hand, have exhibited GHz range power cut-off frequencies [11] and it has been suggested, therefore, that they may have potential as high frequency devices and thus add increased functionality to future Si integrated circuits.

2. EXPERIMENT

Back gate MISFET structures were made by growing a layer of ZnO by Pulsed Laser Deposition (PLD) on Si (111) substrates [12] coated with 4.5nm of amorphous Si_3N_4, as shown in Figure 1.

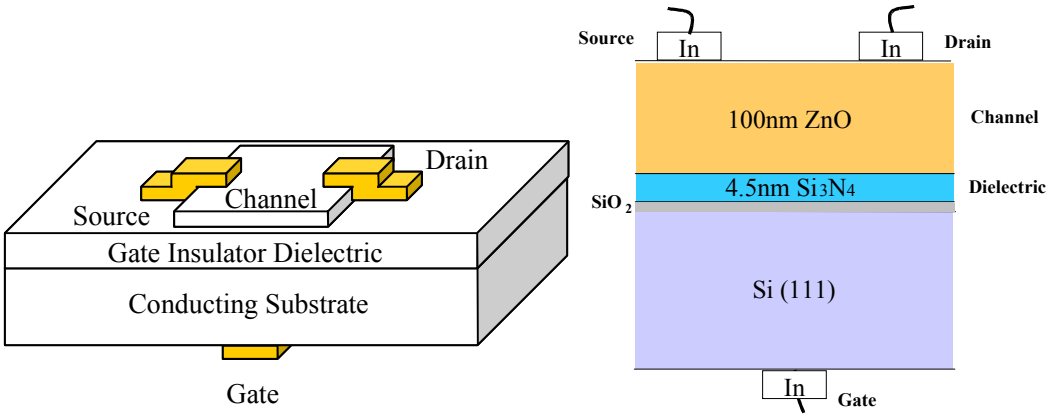

Figure 1. Schematic cross-section and layer detail for the staggered, bottom gate ZnO/Si_3N_4/SiO_2/Si (111) TFT structure employed in this study.

Si_3N_4 was chosen as the dielectric insulator because of its' relatively high dielectric constant (~7.5) and resistivity (10^{14} Ω.cm). TFTs with a gate length (L) of 150 μm and gate widths (W) of 75, 150, 350 and 700 μm were fabricated using photolithography. X-ray diffraction (XRD) studies were conducted with a 4-circle Philips X-Pert MRD PRO system. Images of fracture cross-sectional samples were obtained using a Hitachi S-4800 field-emission scanning electron microscope (SEM). Electrical characteristics were made using a dual-source dc power supply, a Fluke multimeter and a Keithley 2400 source-meter. Resistivity was measured using a four-point system. Transmittance spectra were acquired for a ZnO layer grown on a Corning glass substrate using similar growth conditions to the ZnO/Si_3N_4/SiO_2/Si (111).

3. RESULTS & DISCUSSION

Figure 2 shows an SEM image of a fracture cross-section of the ZnO/Si_3N_4/SiO_2/Si (111).

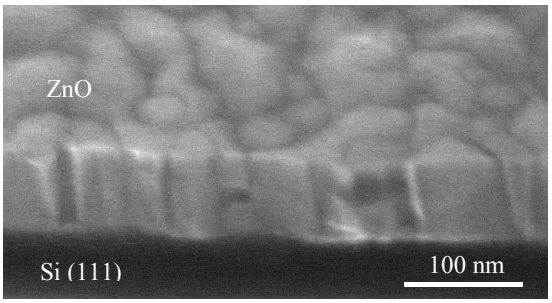

Figure 2. An SEM image of a fracture cross-section of the ZnO/Si_3N_4/SiO_2/Si (111).

The image shows that the film thickness was about 100 nm and indicates that the average grain size was about 50 nm. Figure 3 shows the (0002) peak XRD 2θ/ω and ω rocking curve scans for the ZnO/Si_3N_4/SiO_2/Si (111).

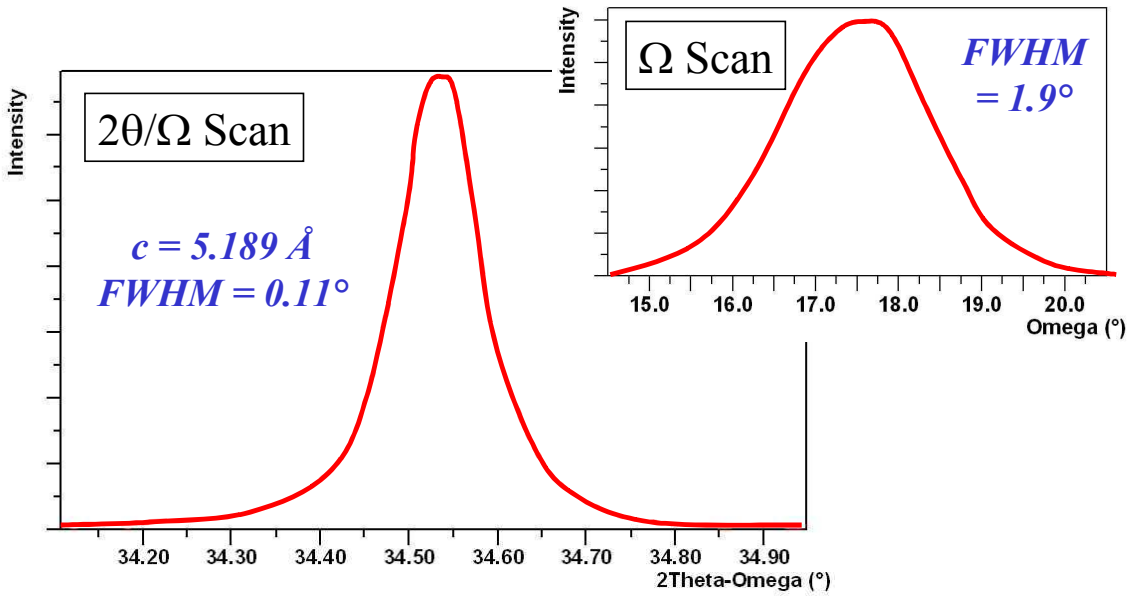

Figure 3. XRD 2θ/ω and ω scans for the (0002) peak of the ZnO/Si_3N_4/SiO_2/Si (111).

XRD revealed a wurtzite crystal structure for the ZnO with a preferential c-axis orientation along the growth direction. The 2θ/ω scan had a Full Wave Half Maximum (FWHM) of 0.11º and a peak position corresponding to a c lattice parameter of 5.189 Å, which is a little smaller than would be expected for relaxed wurtzite ZnO. This implies that the layer was under tensile strain in the film plane. The ω scan FWHM was 1.9º. Thus, although the ZnO film grown had preferential c-axis orientation, there was more dispersion than typically observed for films grown on c-sapphire substrates [13].

Figure 4 shows the optical transmission spectrum for the ZnO/glass sample grown under similar conditions to the ZnO/Si_3N_4/SiO_2/Si (111).

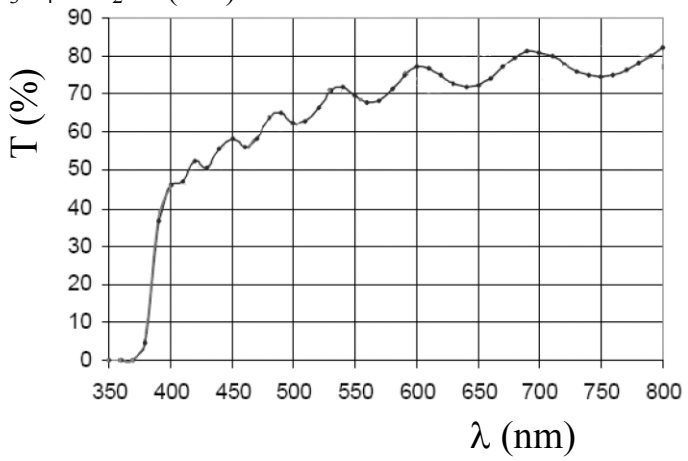

Figure 4. Optical transmission spectrum for a ZnO/glass sample.

The spectrum shows a transmittance, for the ZnO plus the glass substrate, over 70% for visible wavelengths above about 500 nm.

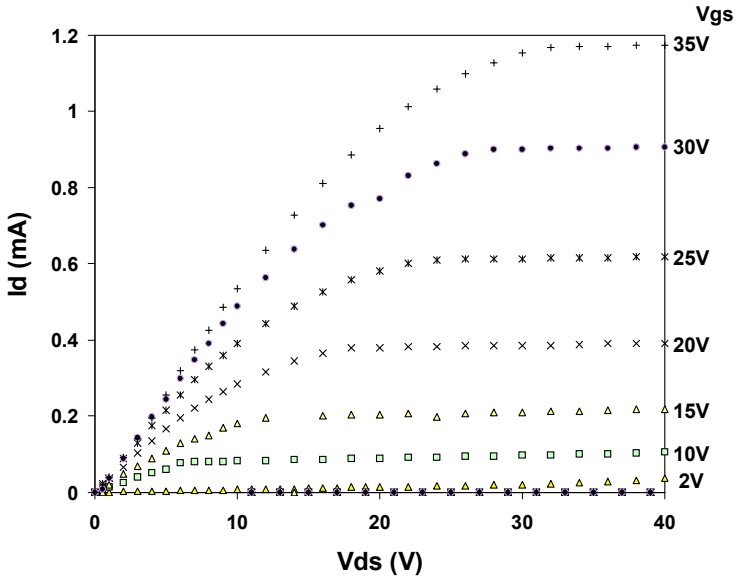

Figure 5: Output characteristic of an ZnO/Si_3N_4/SiO_2/Si (111) TFT with L =150μm & W = 700μm.

Four point electrical resistance measurements of the ZnO gave an estimate of the film resistivity at about 0.08 Ω.cm. In contacts gave a good ohmic response. Figure 5 shows the output characteristic for a MISFET structure with an L of 150 μm and a W of 700 μm, for various Vgs.

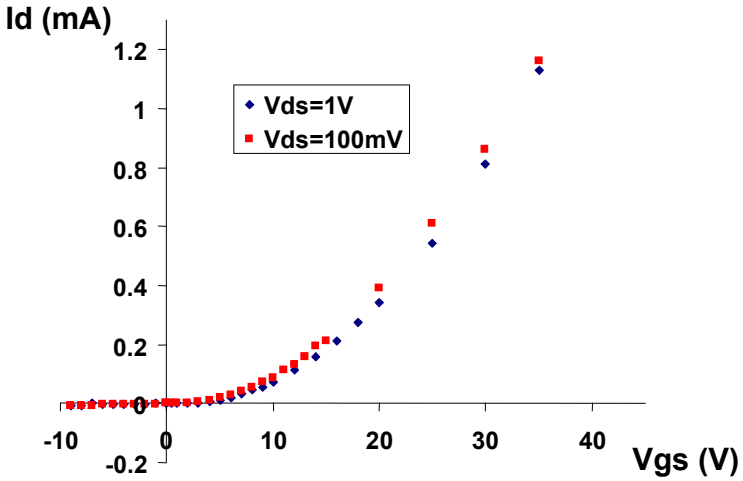

Figure 6. Transfer characteristic of ZnO/Si_3N_4/SiO_2/Si (111) TFT.

The devices exhibited enhancement-mode TFT behaviour. This is preferable to the depletion mode alternative, since the off-state is the power-down condition, which is good for both energy efficiency and simplified circuit design. The characteristics all showed "pinch-off" and "hard-saturation" (a plateauing of Id above a certain Vds), which suggests that the whole channel could be depleted of electrons. Finally, the Id was in the mA range, which is relatively large/good for a ZnO-based TFT. Figure 6 shows transfer characteristics, of the same TFT as shown in Figure 5, for Vds of 100mV

and 1V.

The transfer characteristics are rectifying, confirming transistor behaviour in the device. The V_{ON} is about 0V, which suggests that neither the electron nor the trap densities in the channel were too high. The characteristics for the two different Vds are similar. The gate leakage current could not be measured because the detection limit of the ammeter was insufficient and I_{ON}/I_{OFF} could not be calculated.

4. CONCLUSION

Thin Film Transistors (TFT) structures were made by growing n-type ZnO on $Si_3N_4/SiO_2/Si$ (111) by PLD. XRD and SEM studies indicated that the ZnO layers had a polycrystalline wurtzite structure, a smooth surface and a strong preferential c-axis orientation. Optical transmission studies of similar ZnO layers on glass substrates showed good transparency over the whole visible spectrum. Electrical measurements of a back gate $ZnO/Si_3N_4/SiO_2/Si$ (111) FET with ohmic In contacts, revealed rectifying transfer characteristics, with a V_{ON} ~0V, and enhancement-mode output characteristics showing hard saturation and a mA range Id. When scaled down, TFT devices based on such structures may be of interest for high frequency applications.

ACKNOWLEDGEMENTS

The authors would like to thank G. Garry of Thales Research and Technology for the optical transmittance measurements.

REFERENCES

[1]. D. C. Look J. Elec. Mater. 35 (6) (2006) 1299–305
[2]. G. F. Boesen and J. E. Jacobs Proc. IEEE 56 (11) (1968) 2094–5
[3]. Y. Ohya et al.. Jpn. J. Appl. Phys. Part 1 40 (2001) 297–8
[4]. P. F. Carcia et al. Appl. Phys. Lett. 82 (2003) 1117–9
[5]. R. L. Hoffmann et al. Appl. Phys. Lett. 82 (2003) 733–5
[6]. M. Masuda et al. J. Appl. Phys. 93 (2003) 3
[7]. K. Nomura et al. Science 300, (2003) 1269–72
[8]. J. F. Wager J F Science 300 (2003) 1245–6
[9]. K. Nomura et al. Nature 432 (2004) 488–92
[10]. D.J. Rogers & F. Hosseini Teherani, Encyclopedia of Materials: Science & Technology, Elsevier, Oxford (2010) 1-5.
[11]. B. Bayraktaroglu et al. IEEE Elec. Device Letts. (2009) 1-3
[12]. M. Zerdali et al. Materials Letts. 60 (2006) 504–508
[13]. D. J. Rogers Proc. of SPIE Vol. 5732 (2005) 412-416

5.2 Amorphous ZnO Films Grown by Room Temperature Pulsed Laser Deposition on Paper and Mylar for Transparent Electronics Applications

D. J. Rogers et al. Proc of SPIE 2011 vol 7940-53

D. J. Rogers[a], V. E. Sandana[a,b,c], F. Hosseini Teherani[a], R. McClintock[b], M. Razeghi[b] & H-J Drouhin[c]

[a]Nanovation SARL, 103b rue de Versailles, 91400 Orsay, France
[b]Center for Quantum Devices, Northwestern University, Evanston, IL60208, USA
[c]Department of Irradiated Solids, École Polytechnique, 91128 Palaiseau, France.

1. INTRODUCTION

Wurtzite Zinc Oxide (ZnO) is a remarkable multifunctional material with a distinctive property set and a huge range of existing and emerging applications [1]. In particular, it is a direct wide bandgap semiconductor (Eg ~ 3.4eV) with intrinsically high transparency over the whole visible range (Fig. 1) and a resistivity that can be tuned from semi-insulating right through to semi-metallic by doping [2].

In the latter case, ZnO can be considered as belonging to a class of materials termed "Transparent Conducting Oxides" (TCO). TCOs are degenerate n-type semiconductors with resistivities under about 10^{-3} ohm.cm, free-electron concentrations of the order of 10^{20} cm^{-3}, an Eg > 3.1 eV and average transmittance > 80% for the whole visible range.

Although many new TCO materials have been developed in recent years, most practical TCO applications employ doped oxides of Indium (In), Tin (Sn) and Zn. These are passive applications including window defrosting, filtering of ultra-violet and/or infra-red light, electromagnetic shielding, transparent wiring, touch-sensitive panels and transparent contacts for use in flat panel displays, solar cells and Light Emitting Diodes [3]. Most of these applications need as conductive and transparent a TCO as possible.

Recently, a new kind of ZnO-based TCO has emerged. These are Amorphous Oxide Semiconductors (AOS) [4]. Compared to wurtzite ZnO, amorphous ZnO-based alloys have lower processing temperatures, are cheaper to fabricate, are lighter and have better uniformity of properties (due, in part, to a lack of grain-boundary-related issues). Moreover, their performance is stable and reproducible during and after repetitive bending, so they are compatible with flexible substrates.

Although AOS are not a new class of materials [5] the new generation of ZnO-based AOS exhibits enhanced electron mobility (μ), superior capacity for processability in air and improved thermodynamic stability compared with conventional Covalent Amorphous Semiconductors (CAS) and existing AOS [6].

Nomura *et al.* [6] proposed, that the improved μ are obtained because of differences in the intrinsic nature of the chemical bonding between AOS and CAS. In CAS the hybridized *sp*3 orbital overlap is highly directive. Therefore, any bond angle fluctuations significantly alter the electronic levels, and

carrier transport is thus controlled by hopping between localized tail-states rather than band conduction. Hence structural randomness can greatly degrade the carrier mobility. AOS, in contrast, have higher ionicity and the bottom of the conduction band has extended, spherical s orbitals associated with the metal ion. These electronic levels have an overlap which is relatively insensitive to distortion of the metal–oxygen–metal chemical bonds. Thus strain and disorder within the material do not strongly impact the conduction such that AOS materials can show degenerate band conduction and superior electron μ compared with CAS, even though they are formed at room temperature. Indeed, amorphous $InGaZnO_4$ (a-IGZO) [7], can have a Hall μ > 12cm^2/Vs [8] compared with a typical μ of < 1 cm^2/Vs for hydrogenated amorphous Silicon (a-Si) and it is reported to be stable up to 500°C in air [6]. Amorphous InZnO (a-IZO) can have even higher μ (> 100cm^2/Vs: [9]) plus a transparency and conductivity which are comparable with ITO [10]. As such, it is an alternative material for electrode applications. It shows inferior control of carrier concentrations compared with a-IGZO, however, so a-IGZO is preferred for use as the channel [11].
Although ZnO based TTFTs are not a new concept [12,13], the new generation exhibits a high on-off ratio (>10^6) and a higher channel μ than the Si based devices which are currently used for state-of-the-art microelectronics applications such as select transistor drivers in commercial Liquid Crystal Displays (LCD) and systems-on-glass. Two main ZnO TTFT variants, employing either wurtzite or AOS ZnO alloys as channels, have emerged [6, 14-18].
These ZnO-based TTFTs offer several advantages over the incumbent Si based devices. First of all, they are transparent, so that generally more light can be transmitted through each pixel, yielding a brighter, more efficient, display. This also means that the aperture ratio can be increased, so as to give smaller pixels. Next, state-of-the-art wurtzite ZnO and a-IGZO TTFTs can now exhibit channel μ as good as 250cm^2/Vs and 12cm^2/Vs, respectively, as compared with typical values of 100cm^2/Vs and 1cm^2/Vs for poly-Si and a-Si [19]. This gives faster device operation, which leads to a quicker response and an increased refresh rate. In addition, because of their wide bandgap, the ZnO based TTFTs have reduced sensitivity to light (exposure to ambient light has no significant effect on the current–voltage characteristics) and less degradation on exposure to light compared with their a-Si counterparts. TTFTs made with a-IGZO are of particular significance because they give excellent performance when fabricated at room temperature and can be fabricated in large area format. This is often touted as resolving the trade-off between processing temperature and device performance so as to allow fabrication on inexpensive heat-sensitive substrates such as transparent polymers or paper (poly-Si deposition temperature is too high for many flexible polymer substrates). For the moment, however, an undesireable post-deposition annealing step at a temperature of about 200ºC is necessary in order to obtain suitable electrical and optical properties.

In this paper, we examine the possibility of avoiding such an annealing step through the use of Pulsed Laser Deposition (PLD) to engineer amorphous ZnO with good electrical and optical properties at RT. PLD has already shown potential for the fabrication of TFTs with wurtzite ZnO channels for operation with high device currents/powers and/or high frequencies [20]. Indeed, PLD has the capacity to grow wurtzite ZnO with superior crystallographic quality, a very large range of conductivities and excellent optical quality compared with other deposition techniques [21]. This is due to intrinsic advantages of PLD including the relatively high energy of the species in the ablation plume (typically ~10 to 100eV in PLD vs ~ 1 to 10eV for sputtering and 0.1 to 1 eV for MBE or CVD) and the extended range of oxygen partial pressures under which films can be grown (Fig. 1).

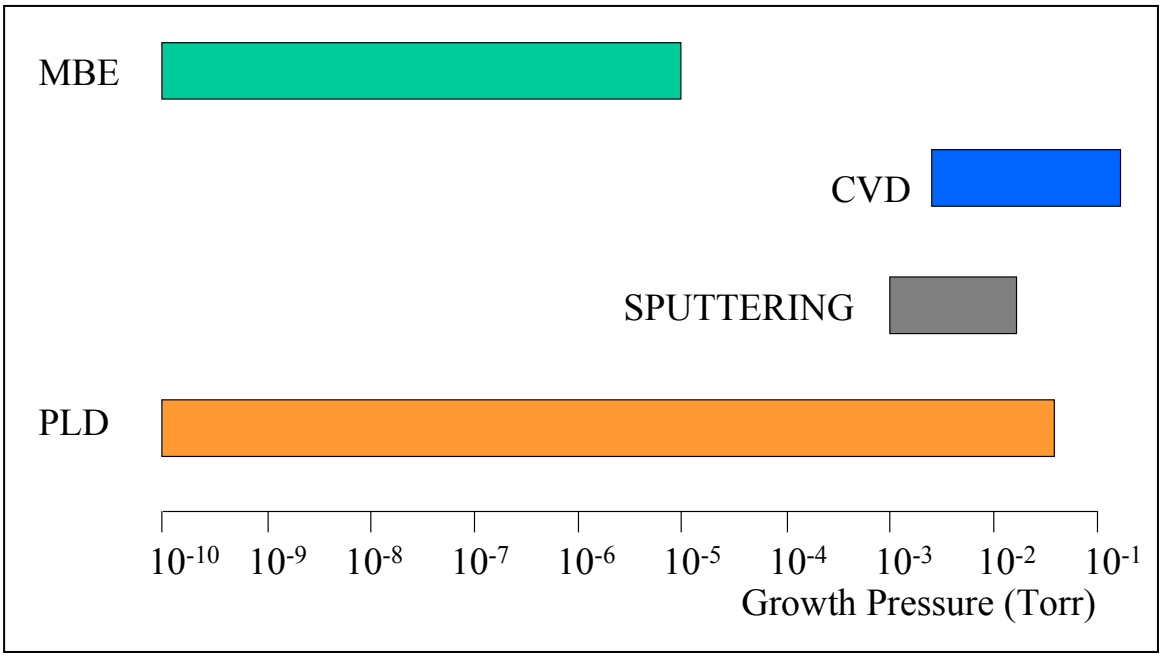

Figure 1. A comparison of typical dynamic operating pressure ranges for common thin film deposition techniques.

The combination of these features allows a great flexibility for tuning of the oxygen content over a very large range, of oxidant (or reducing gas) partial pressures plus the capacity to form wurtzite ZnO at temperatures down to RT.

To date, however, there have been very few studies into the fabrication of AOS ZnO by PLD. This is because ZnO tends to crystallize after a few nm of deposition, even at RT on amorphous substrates (e.g. glass [22]) under typical PLD conditions.

In this study the aim was to investigate the potential of PLD for the synthesis of conductive amorphous ZnO layers adapted for transparent electronics applications on heat-sensitive substrates.

2. EXPERIMENT

ZnO layers were deposited on (standard photocopy) paper and mylar (polymer) substrates held at room temperature (RT) by ablation of a 5N ZnO target with a KrF (248 nm) excimer laser. The sample morphology was studied using a Hitachi S4800 field emission-Scanning Electron Microscope (SEM) equipped with Energy Dispersive X-Ray (EDX) spectroscopy for compositional microanalysis. X-ray diffraction (XRD) studies were conducted with a High Resolution (HR) 4-circle Philips X-Pert MRD PRO system using Cu K□ radiation. Resistance measurements were made for injection currents of 0.01, 0.1 and 1 mA using an aligned 4-point measurement system with a Keithley 2400 source-meter. Optical properties were studied using Ultraviolet (UV) RT photoluminescence (PL) spectroscopy with a HeCd laser emitting at 325 nm.

3. RESULTS & DISCUSSION

Figure 2 shows SEM images for the ZnO/paper.

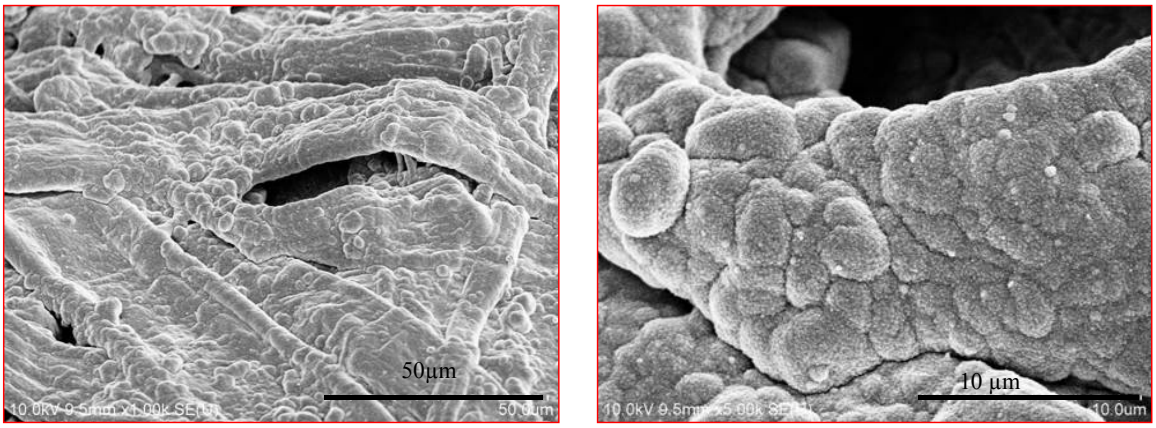

Figure 2. SEM images for ZnO deposited on paper using RT PLD.

The SEM studies showed the cellulose fibres of the paper but no evidence of a crystalline coating was observed. Figure 3 shows SEM images for the ZnO/mylar

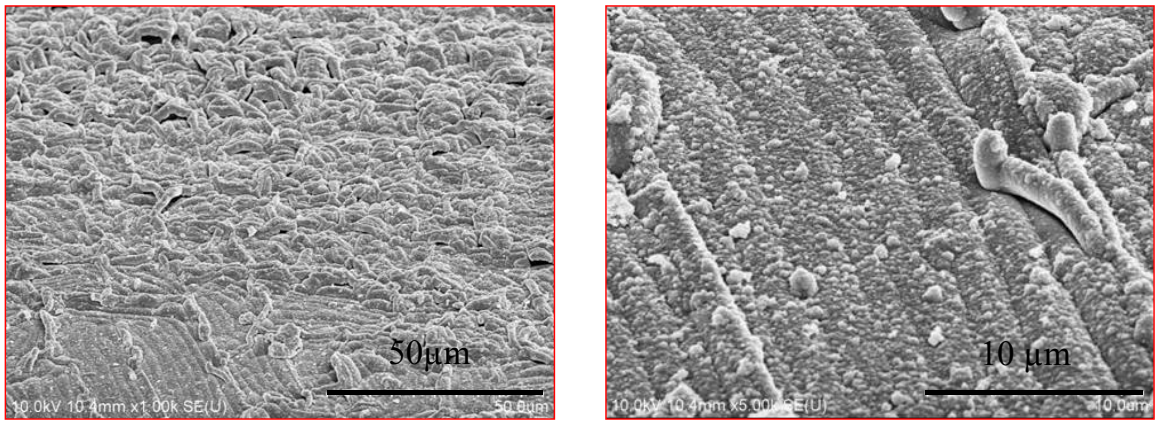

Figure 3. SEM images for ZnO deposited on mylar using RT PLD.

The SEM images show structure typical for a polymer substrate with no evidence of a crystalline coating.

EDX spectroscopy was conducted for the ZnO/paper and ZnO/mylar in order to verify the presence of a ZnO layer. A typical spectrum is shown in figure 4.

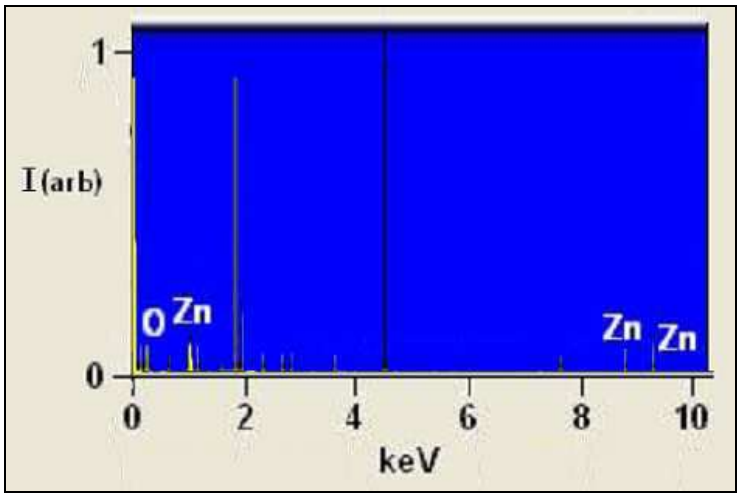

Figure 4. EDX spectrum for RT PLD of ZnO on mylar.

The spectra for both the ZnO/mylar and ZnO/paper showed peaks associated with Zn and O. Whilst the O peak could be from the substrate and/or microscope ambient, the Zn peak only appeared after the ZnO deposition. Thus it was concluded that a film had been formed by PLD. Four point electrical measurements before and after deposition confirmed this. Prior to deposition, both substrates showed infinitely high resistance. After deposition, the ZnO on mylar had a resistance of $575 \pm 20\ \Omega$ and the ZnO on paper had a resistance of $30\ 000 \pm 20\ 000\ \Omega$. Assuming that the deposition had formed continuous layers on the paper and mylar (rather than impregnating them) [23], film thickness was estimated from the deposition times to be about 950 nm. Thus the resistivities were estimated to be approximately $0.25 \pm 0.01\ \Omega$.cm for the ZnO on mylar and $13 \pm 9\ \Omega$.cm for the ZnO on paper. These are relatively low values.
Figure 5 shows XRD 2θ/ ω scans for mylar and ZnO/mylar.

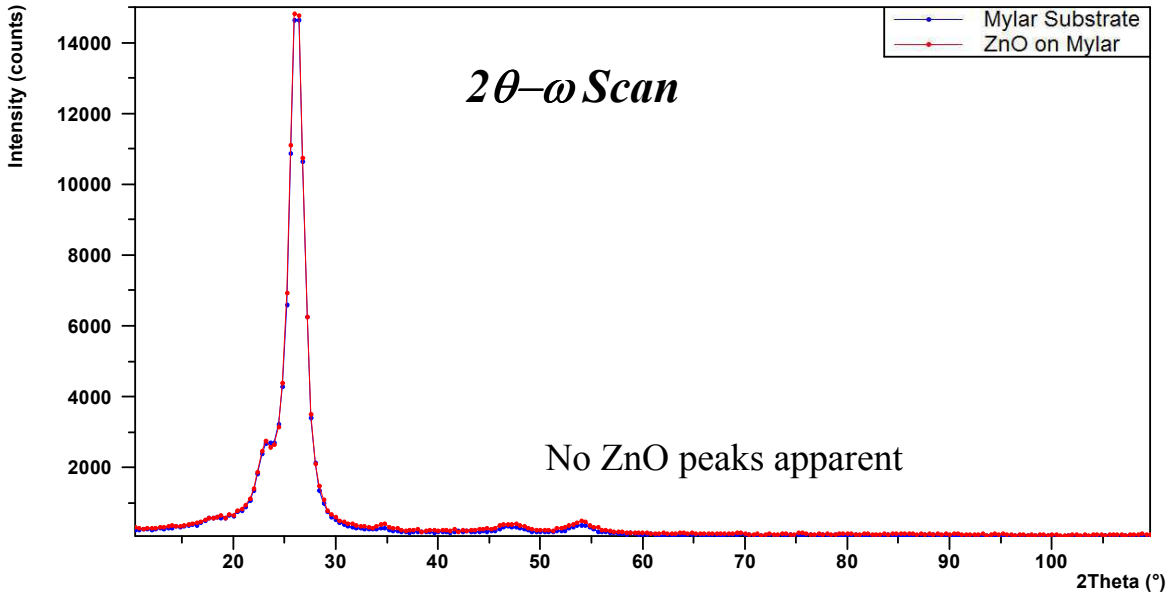

Figure 5. XRD 2θ/ω scans for the mylar substrate before and after RT PLD of ZnO.

The XRD scans were similar before and after ZnO deposition and no peaks associated with crystalline ZnO or Zn were apparent. Figure 6 shows XRD 2θ/ ω scans for paper and ZnO/paper.

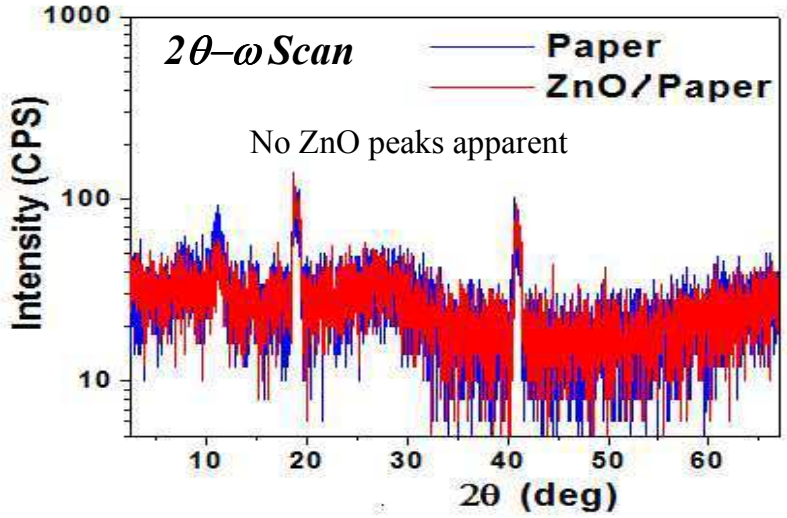

Figure 6. XRD 2θ/ω scans for a paper substrate before and after RT PLD of ZnO.

Once again, the scans were similar before and after the ZnO deposition and no peaks associated with crystalline ZnO or Zn could be found.
Figure 7 shows the PL spectra for mylar and ZnO/mylar.

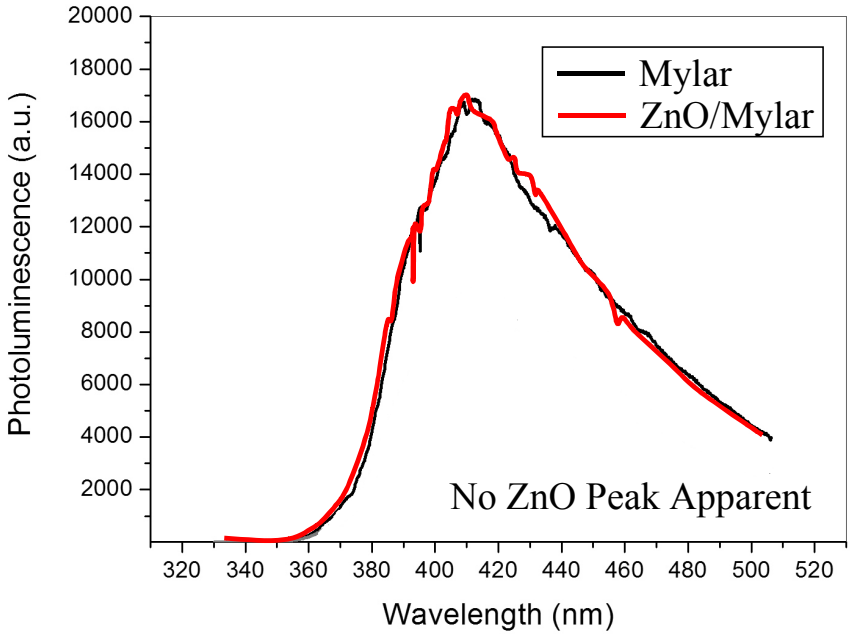

Figure 7. RT PL spectra for mylar before and after RT PLD of ZnO.

No peaks associated with the ZnO deposition could be found. PL studies for both the paper and the RT PLD ZnO on paper gave no significant signal.

4. Conclusion

ZnO thin films were made by PLD onto mylar and paper substrates held at RT. SEM and EDX studies indicated that a ZnO coating had been applied without destroying the integrity of the substrates. 4 point resistance measurements confirmed the presence of conductive layers having relatively low resistivities. XRD studies showed no supplementary peaks after ZnO deposition, and none which could be indexed to crystalline ZnO or Zn. UV RT PL studies showed no supplementary peaks after ZnO deposition and no response characteristic of wurtzite ZnO. Thus, there was no sign of crystallinity. Since the nature of PLD allows for significant flexibility in the adatom mobility and oxidant partial pressure, it is suggested, that RT PLD could be used to engineer ZnO-based AOS layers with enhanced electrical and optical properties directly at RT. It may thus be possible to avoid the inconvenient post-deposition annealing step that is generally required using other deposition techniques.

ACKNOWLEDGEMENTS

The authors would like to thank Dupont for providing the mylar substrates.

REFERENCES

[1] Rogers D. J., Hosseini Teherani F., Encyclopedia of Materials: Science and Technology, Elsevier, Oxford (2010) 1-5.
[2] Rogers D. J., Hosseini Teherani F., Sandana V. E., & Razeghi M. Proc. of SPIE 7605 (2010) 76050K-2
[3] Gordon R. G., MRS Bull 25, (2000) 52-7
[4] Hosono H., J. Non-Cryst. Solids 198-200, (1996) 165-9
[5] Denton E. P., Rawson H.,Stanworth J. E., Nature 173, (1954) 1030-2
[6] Nomura K., Ohta H., Takagi A., Kamiya T., Hirano M., Hosono H., Nature 432, (2004) 488-92
[7] Orita M., Ohta H., Hirano M., Narushima S., Hosono H., Phil. Mag. B 1, (2001) 501-15
[8] Hosono H., J. Non-Cryst. Solids 352, (2006) 851-8
[9] Fortunato E., Barquinha P., Pimentel A., Pereira L., Goncalves G., Martins R., Phys. Stat. Sol. (RRL) 1 (1), (2007) R34-6
[10] Sashabayashi T., Ito N., Nishimura E., Kon M., Song P. K., Utsumi K., Kaijo A., Shigesato Y., Thin Solid Films 445, (2003) 219-23
[11] Nomura K., Takagi A., Kamiya T., Ohta H., Hirano M., Hosono H., Jpn. J. Appl. Phys. 45, (2006) 4303-
[12] Boesen G. F., Jacobs J. E., Proc. IEEE 56 (11), (1968) 2094-5
[13] Ohya Y., Niwa T., Ban T., Takahashi Y., Jpn. J. Appl. Phys. Part 1 40, (2001) 297-8
[14] Carcia P. F., McLean R. S., Reilly M. H., Nunes G., Appl. Phys. Lett. 82, (2003) 1117-9
[15] Hoffmann R. L., Norris D. J., Wager J. F., Appl. Phys. Lett. 82, (2003) 733-5
[16] Masuda M., Kitamura K., Okumura Y., Miyatake S., Tabata H., Kawai T., J. Appl. Phys. 93, (2003) 3
[17] Nomura K., Ohta H., Ueda K., Kamiya T., Hirano M., Hosono H., Science 300, (2003) 1269-72
[18] Wager J. F., Science 300, (2003) 1245-6
[19] Nozawa T., Nikkei Electronics Asia November, (2007) 1024-30
[20] Rogers D. J., Sandana V. E., Hosseini Teherani F. & Razeghi M., Proc. of SPIE 7603 (2010) 760318
[21] Rogers D. J., Hosseini Teherani F., Sartel C., Sallet V., Jomard F., Galtier P. & Razeghi M., Proc. of SPIE Vol. 7217 (2009) 72170F-1
[22] Nakata Y., Okada T., Maeda M., Appl. Surf. Sci. 8028 (2002) 1-3
[23] Martins R., Brás B., Ferreira I., Pereira L., Barquinha P., Correia N., Costa R., Busani T., Gonçalves A., Pimentel A., Fortunato E., Proc. Of SPIE (2011)

Conclusion

Thin film transistors with wurtzite ZnO channels grown on Si3N4/SiO2/Si (111) substrates by pulsed laser deposition.
TFT were made by growing ZnO on Si3N4/SiO2/Si (111) substrates by pulsed laser deposition. X-ray diffraction and scanning electron microscope studies revealed the ZnO to have a polycrystalline wurtzite structure with a smooth surface, good crystallographic quality and a strong preferential c-axis orientation. Transmission studies in similar ZnO layers on glass substrates showed high transmission over the whole visible spectrum. Electrical measurements of a back gate geometry FET showed an enhancement-mode response with hard saturation, mA range Id and a VON ~ 0V. When scaled down, such TFTs may be of interest for high frequency applications.

Amorphous ZnO Films Grown by Room Temperature Pulsed Laser Deposition on Paper and Mylar for Transparent Electronics Applications.
There has been a surge of activity in the development of next-generation Transparent Thin Film Transistors (TTFT) for use in applications such as electronic paper and flexible Organic Light Emitting Diode panels. Amongst the TCOs attracting the most interest at present are AOS based on ZnO because they exhibit enhanced electron mobility (μ), superior capacity for processability in air and improved thermodynamic stability compared with conventional CAS and existing AOS. Moreover, they give excellent performance when fabricated at relatively low temperature and can readily be made in large area format. Thus they are projected to resolve the trade-off between processing temperature and device performance and thereby allow fabrication on inexpensive heat-sensitive substrates. For the moment, however, an undesireable post-deposition annealing step at a temperature of about 200ºC is necessary in order to obtain suitable electrical and optical properties. The experiments demonstrate the possibility of directly engineering amorphous ZnO with relatively high conductivity at RT on paper and mylar substrates using Pulsed Laser Deposition.

Conclusions de ce travail de recherche

Un résumé des conclusions sur les différents résultats obtenus lors de cette thèse est présenté ci-dessous.

Etape 1 : Choix d'approche de croissance de nanostructures

Le premier objectif de cette thèse était de fabriquer des reseaux homogènes de nanofils de ZnO en vue des applications optoelectroniques. Etape 1 etait de déterminer quel approche de croissance était le mieux adaptée (avec catalyseur (VLS) ou sans catalyseur).

Etape 1.1 Croissance avec catalyseur

Dans un premier temps, un bati d'evaporation a été fabriqué. Apres mise au point, des dépôts de l'or ont été faits sur des substrats de Si (111) et c-Al_2O_3 de 50 mm de diamètre. Ces deux substrats ont été couverts de 5 nm d'or. Ils ont ensuite été recuits afin de former des nano-gouttelettes d'or. Le développement de ces gouttelettes a été étudié en fonction des durées et des températures de recuit. Sous des conditions optimisées (duree = 60s, temperature = 800ºC), une distribution relativement homogène de gouttelettes de quelques nanomètres de diametre a été obtenue. Les gouttelettes d'or ont servi de catalyseur pour la croissance de nanostructures de ZnO par MOCVD, PVT et PLD. Les images obtenues par MEB ont revelé une grande variété de nanostructures : des nanopointes, des nanofils, des nanotubes et de nouvelles structures tel que des nanocolonnes multifacettées. Nous n'avons pas, cependant, reussi à faire croître des reseaux ordonnées de nanofils de ZnO et l'or n'était pas localisé à la pointe des nanostructures comme on attendrait pours le mecanisme VLS attendu.

Etape 1.1 Croissance sans catalyseur

L'étape suivante consistait à réaliser des nanostructures de tailles et formes homogènes sans utiliser de catalyseur. Les formes et les propriétés des nanostructures déposées sur Si(111) et c-Al_2O_3 ont été comparées en utilisant trois procédés de croissance : MOCVD, PLD et PVT. Une grande variété de nanostructures a encore été observée : nanocolonne, nanopointe et nanopeigne. La croissance par PVT a encore donné la plus grande variété de forme de nanostructures. La PLD a permis d'obtenir une forte densité de nanocolonnes de formes, tailles et espacement relativement homogènes et avec une forte orientation preferentiel perpendiculaire aux substrats. Ces nanostructures se sont autoformés sans l'utilisation de catalyseur. L'étude XRD a confirmé que les nanostructures réalisées par PLD sont mieux cristallisées et plus orientées (selon l'axe c) que celles élaborées par PVT ou MOCVD.

Une fois ces différents procédés étudiés, la PLD s'avère la technique la mieux adaptée à la fabrication de nanostructures de ZnO pour les applications optoélectroniques : réseaux de nanostructures autoformées, alignées, verticales, présentant un indice de réfraction effectif gradué et température de dépôt relativement basse. Les structures sont obtenues sans l'utilisation de catalyseur. Ces résultats positifs ont permis de passer à l'étape 2.

Etape2 : Etude de la croissance de réseaux de nanostructures de ZnO sans catalyseur sur different substrats

Le substrat, la pression/gaz dans la chambre et la temperature du substrat se sont revelés comme des paramètres clef pour la croissance des reseaux de nanostructure. D'abord, des nanostructures de ZnO ont été réalisées sur des substrats de Si(111) et c-Al_2O_3 par PLD. L'impact de la température et de la pression en argon lors du dépôt sur la morphologie, la structure cristalline et la photoluminescence ont été étudié. Différents types de nanostructures de ZnO ont été obtenus : en particulier, des réseaux de nanocônes et nanocolonnes, se sont autoformés à haute temperature. Ces reseaux ont montré une forte orientation cristallographique selon l'axe c (rocking curves de0.64º et 0.16º respectivement) et une bonne réponse en PL (emission excitonic bord de bande et peu de signal vert). En particulier, les resultats en PL et XRD pour les nanoreseaux sur Si(111) sont mieux que ceux pour les couches minces équivalents faits par PLD.

Nous avons ensuite réalisé un dépôt de nanostructures de ZnO sur de l'acier austénitique et sur un cristal de ZnO massif. Des nanocônes ont été obtenues par PLD. La XRD confirment que meme sur acier les nanostructures de ZnO sont de type würtzite et possèdent un axe cristallographique préférentiel selon l'axe c. La CL donne une émission de bord de bande caractéristique de ZnO.

On obtient ainsi des colonnes et des cônes dont les qualités structurales sont excellentes y compris sur des substrats avec lesquels ZnO n'a pas un bon accord paramétrique (e.g. SiO_2 amorphe et acier). Leurs propriétés d'émission sont aussi excellentes avec des bandes de défauts observables en photoluminescence relativement faibles.

Dans cette étude sur la fabrication de nano ZnO par PLD, nous avons egaelement mis en evidence des reseaux de nanofils de ZnO qui epaississent avec la croissance. Ces structures pourraient former un contact continu en surface si la croissance est poursuivi jusqu'au point de coalescence.

Etape 3 : Fabrications de composants

Etape 3.1 Couche antireflets

L'étude s'est portée sur les propriétés optiques de différents réseaux de nanostructures pour des applications PV et notamment les couches antireflets.

Les mesures de PL à basse température (4.2K) indiquent que les nanocolonnes sur les substrats de c-Al_2O_3 et de Si (111) de type n, présentent une émission similaire à celle observée dans le cas de cristaux massif de ZnO (dominante de l'émission de recombinaison par exciton lié à environ 3,36 eV) et une bande d'émission dans le vert. L'intensité du spectre PL des nanocônes sur Si (111) de type n est la plus élevée dans cette étude. Les mesures de réflectivité à température ambiante ont indiqué que toutes les structures agissent comme des couches antireflets (absorption > 95%) sur une

gamme spectrale de 450 à 750 nm et pour des angles d'incidence de 10° à 60°.

Etape 3.2 LED

Avec ces nanostructures régulières nous avons procédé à la fabrication d'un composant nano-LED utilisant une hétérojonction n-ZnO/p-Si.

Ces nanocônes ont été déposés par PLD sur un substrat de Si (111) de type p, afin de former une LED basée sur une hétérojonction nanostructurée. La nano-LED a une caractéristique I/V rectifiante et une électroluminescence bleue-blanche observable à l'œil nu. Leur indice de réfraction gradué permet de faciliter l'extraction des photons à l'interface LED/air.

Etape 3.3 PV

Les résultats de l'étape 2 prouvent que les nanostructures de ZnO peuvent être déposées sur des substrats très variés. L'étude s'est donc poursuivie dans l'optique d'effectuer une reprise de croissance de GaN sur des nanostructures de ZnO, sur des substrats sur lesquelles il est habituellement difficile de faire croître directement GaN. De plus la reprise de croissance de GaN couche mince sur du ZnO couche mince a déjà été demontrée dans des travaux précédents (cf. Annexe VI).

Des nanocônes de ZnO ont été déposés par PLD sur un substrat de Si (111). Les balayages XRD ont indiqué que ces nanocônes présentent une structure cristalline de type würtzite avec une orientation cristallographique selon l'axe c (correspondant aussi à l'axe de croissance). Les spectres de CL montrent une émission caractéristique d'une émission bord de bande de ZnO. Les nanostructures sur Si ont été utilisées comme « moule » pour la reprise de croissance de GaN par MOVPE. L'XRD, l'EDX, le MEB et la CL ont tous indiqué que les nanocônes de ZnO ont été encapsulés par GaN. Les mesures de réflectivité à température ambiante ont montré que les nanostructures de GaN/ZnO agissent comme des couches antireflets efficaces sur une large gamme spectrale (de 450 à 750 nm) et pour des angles d'incidence de 10° à 60°.

La faisabilité de composants à base de nano ZnO a été démontrée grâce à la réalisation d'une nanoLED de type n-nanoZnO/ p-Si et à la reprise de croissance de GaN par MOVPE sur des nanocônes de ZnO sur Si.

Etape 3.4 TFT

Une étude parallèle sur l'électronique transparente à base de couches minces de ZnO a été développée.

Un composant TFT a été réalisé par dépôt de ZnO par PLD sur un substrat de $Si_3N_4/SiO_2/Si$ (111). Les spectres de XRD et les images MEB montrent que ZnO présente une structure würtzite polycristalline, une qualité cristallographique relativement bonne et une orientation préférentielle selon l'axe c. Des dépôts de ZnO sur du verre dans les mêmes conditions ont été réalisés, et ce afin de pouvoir étudier les spectres de transmission. Les résultats ont indiqué une transmission élevée sur

tout le spectre visible. Un composant FET à géométrie « back-gate » a été fabriqué. Dans cette configuration le drain et la source sont situés sur la même surface alors que la grille est située sur la surface opposée (cf. chap. 4). Les mesures électriques montrent une amélioration de la réponse du composant pour une tension d'allumage de ~ 0V et un courant proche du courant de fuite. Réduit en taille, ce composant TFT pourrait avoir une utilisation intéressante dans les applications haute fréquence.

Etape 3.5 TCO

L'étude suivante porte sur l'utilisation de ZnO comme TCO sur des supports souples de type papier et mylar. L'expérience a démontré la possibilité de déposer par PLD ZnO amorphe à température ambiante directement sur des substrats souples : papier et mylar. La conductivité mesurée à température ambiante est de 13 ± 9 Ω.cm. Néanmoins, à l'heure actuelle, une étape de recuit post-déposition à une température d'au moins 200°C est nécessaire pour obtenir les propriétés électriques et optiques visées.

L'ensemble de ces étapes a donc démontré que ZnO pouvait être mis en œuvre par de nombreux procédés de fabrication (PLD, PVT, MOCVD…) mais aussi que les champs des applications optoélectroniques étaient extrêmement variés : couche antireflets, PV, LED, TFT et TCO.

ANNEXE I Outils de Caractérisations

I.1 Microscopie électronique à balayage

Au cours de cette thèse parmis les caractérisations de première imposrtance, l'une d'elle concerne l'étude morphologique des nanostructures de ZnO réalisés. Pour cela un microscope électronique à balayage (MEB) Hitachi SU 4800 a été utilisé.

Figure I.1 Photo du MEB Hitachi SU 4800

Le fonctionnement d'un MEB est basé sur le principe des interactions électrons-matière. Un faisceau d'électrons balaie la surface de l'échantillon à analyser qui, en réponse, réémet des électrons secondaires et rétrodiffusés. Dans le MEB que nous avons utilisé, la source d'électrons est un canon à effet de champs qui produit un faisceau d'électrons grâce à un filament de tungstène chauffé par un courant. Ce faisceau est accéléré par la haute tension (jusqu'à 20 kV) imposée entre le filament et une anode. Il est ensuite focalisé sur l'échantillon par une série de lentilles électromagnétiques.

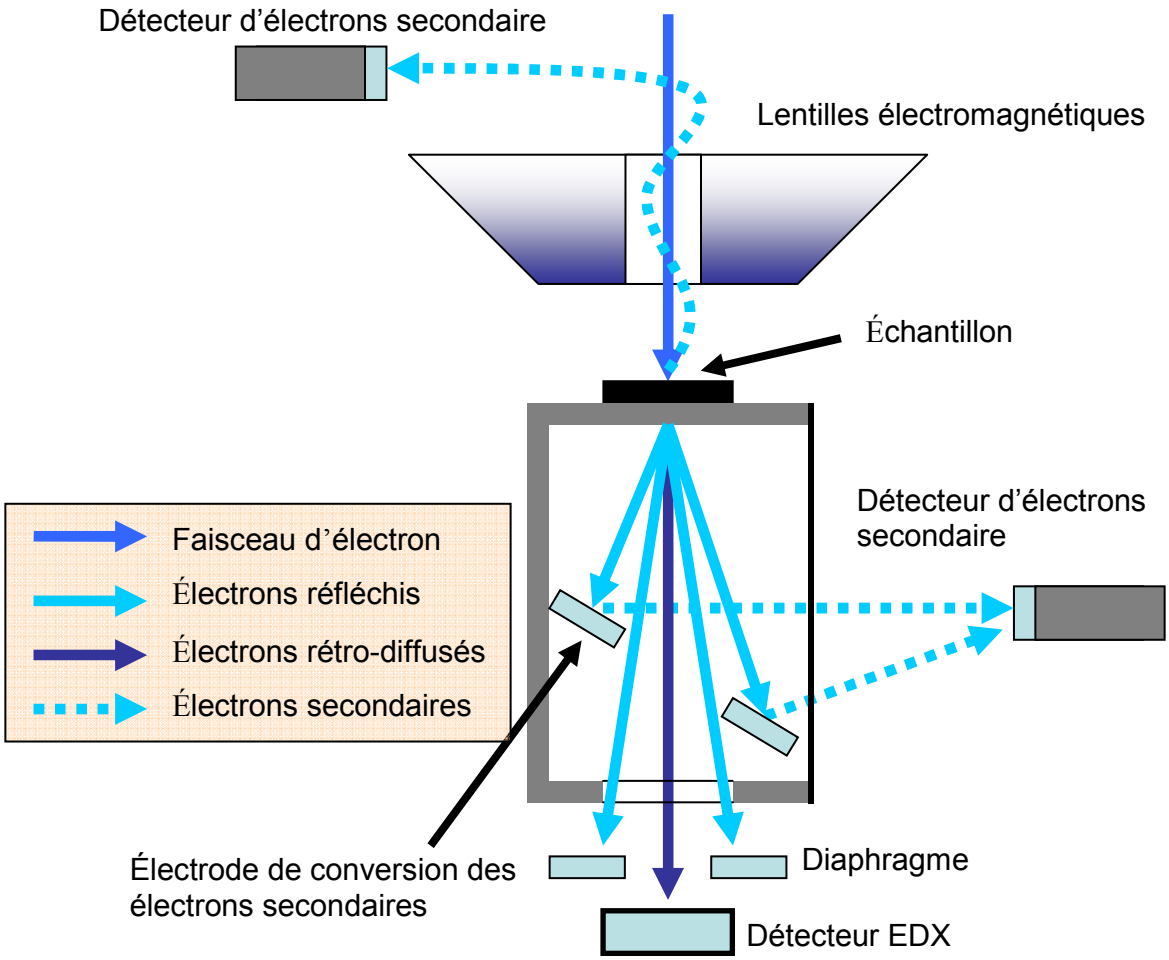

Figure I.2 : Schéma de fonctionnement du MEB Hitachi SU 4800

Les MEB sont équipés de différents détecteurs permettant d'analyser et de reconstruire une image de la surface avec une résolution comprise entre 1nm et 20 nm. Lorsque le faisceau d'électrons entre en collision avec l'échantillon, il va pénétrer dans celui-ci. Le faisceau d'électrons diffuse peu et définit un volume d'interaction (poire) dont les caractéristiques dépendent principalement de la tension d'accélération et du numéro atomique de l'échantillon (figure 2.6).

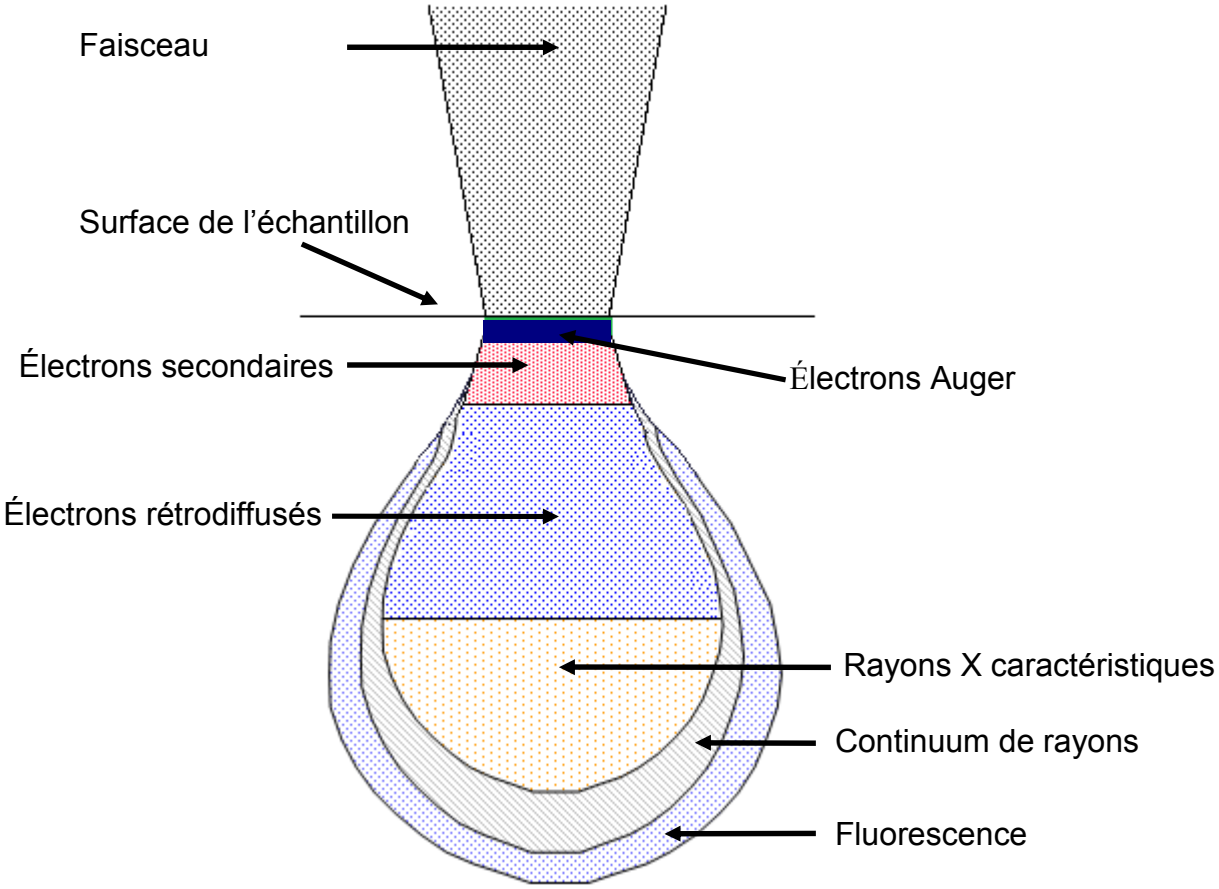

Figure I.3 : Poire d'interaction formée lors de la diffusion des électrons dans un matériau.

Dans ce volume, les électrons et les rayonnements électromagnétiques produits sont utilisés pour former des images ou pour effectuer des analyses physico-chimiques à l'aide d'un détecteur EDX (Energy Dispersive X-ray spectroscopy) d'une résolution de 128 eV à 1000 counts/s. Cet outil de caractérisation a permis de réaliser les images MEB présenté en figure 7 page 26 et figure 8 page 27.

I.2 Photoluminescence

La caractérisation par photoluminescence permet de caractériser la structure de bande des matériaux isolants et semi-conducteurs. Pour cela un rayonnement lumineux va exciter les électrons du matériau étudié. La lumière réémise par le matériau est ensuite anlysée. Afin d'avoir une lumière réemise assez forte pour pouvoir être détecter on utilise généralement un laser pour exciter le matériau et un systèle de détection adapté.

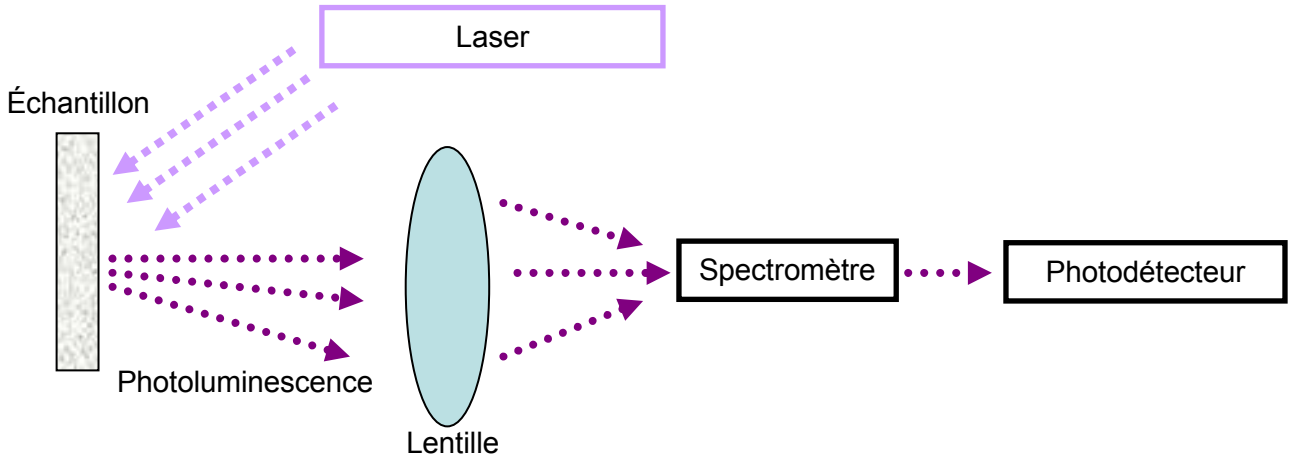

Figure I.4.: Schéma typique de mesure de photoluminescence. [21]

En plus de caractériser la structure de bande d'un matériau, la photoluminescence peut servir à determiner leurs niveaux d'impuretés. La photoluminescence est aussi utilisée pour mettre en évidence les niveaux quantiques provenant de l'empilement de semi-conducteurs ayant des gaps d'énergie différents. La photoluminescence est un domaine qui a connu beaucoup d'expansion et de raffinement depuis les années 70.

I.3 Microscopie à force atomique

L'AFM est utilisé pour l'étude de la morphologie de surface à une échelle comprise entre 1 et 20 µm². L'AFM est basé sur le balayage de la surface de l'échantillon avec une pointe de quelques micromètres de long et de diamètre inférieur à 10 nm. La pointe est localisée sur le côté libre d'un cantilever (microlevier) ayant une longueur comprise entre 100 et 200 µm. Les forces entre la pointe et la surface de l'échantillon causent des courbures ou des déflections du cantilever. Un détecteur mesure ces déflections et génère ainsi une carte topographique de la surface. Plusieurs forces participent à défléchir le cantilever. De façon schématique (Fig. I.5), ces forces peuvent être représentées par le potentiel de Lennard Jones. Les forces mises en jeu sont donc de deux sortes :
- Les forces attractives ou forces de Van Der Waals ;
-Les forces répulsives ou forces atomiques qui interviennent plus près de la surface, lorsque les nuages électroniques tendent à s'interpénétrer. Ces forces répulsives proviennent donc essentiellement du principe d'exclusion de Pauli.

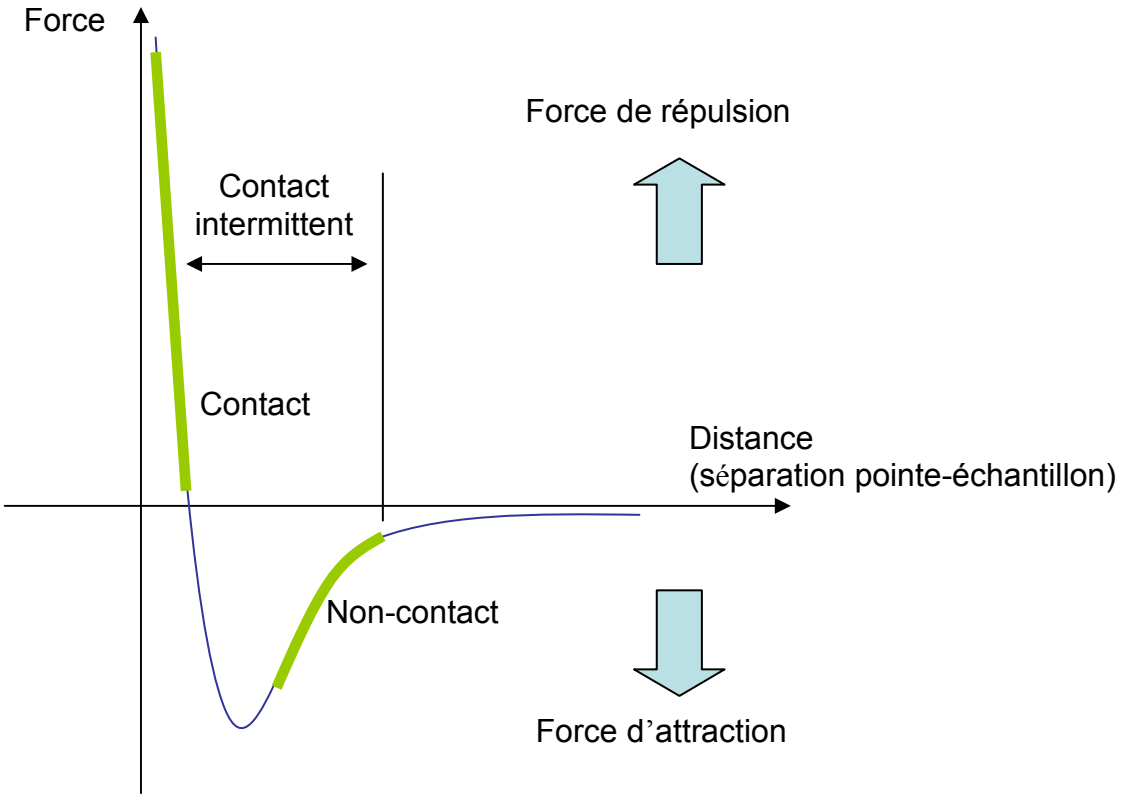

Figure I.5: Force interatomique en fonction de la distance.

Il existe de nombreux systèmes de détection de ces forces atomiques. Dans notre cas, l'AFM utilisé est muni d'un système de détection par déflection optique. Un translateur piézoélectrique sur lequel l'échantillon est déposé assure le déplacement de celui-ci et permet le balayage de la sonde par rapport à l'échantillon. Un faisceau laser est réfléchi sur le cantilever solidaire d'une sonde manométrique. Le spot réfléchi est alors centré sur une photodiode à quadrants, permettant ainsi la mesure des déflections.

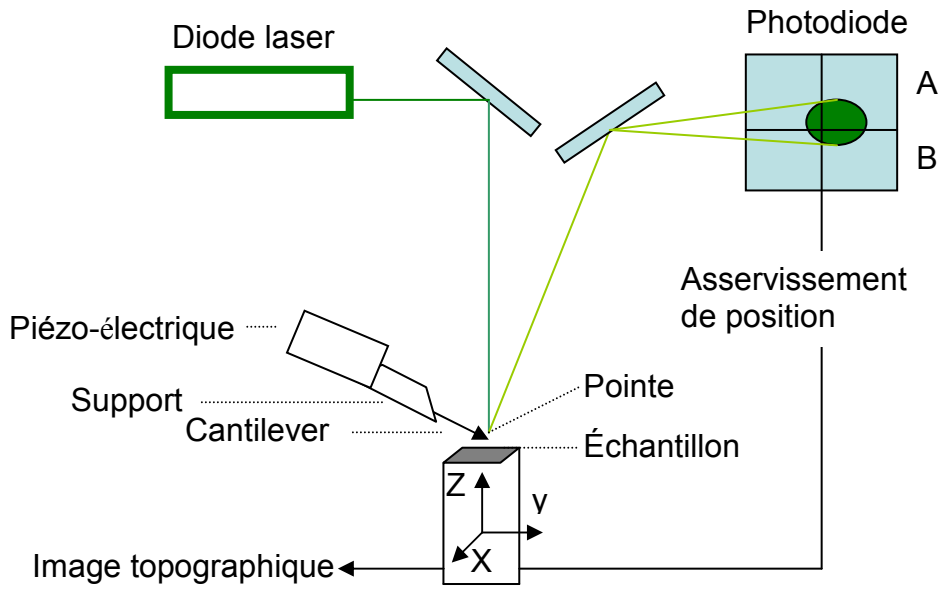

Figure I.6 : Principe de fonctionnement de l'AFM.

Une fois la déflection du microlevier détectée, l'AFM peut générer les informations topographiques par opération soit en maintenant la distance constante, soit en maintenant la force constante. Deux régimes de distance sont montrés sur la figure I.6 : le régime contact, où les forces interatomiques répulsives sont mises en jeu, et le régime non-contact, où la force de Van der Waals est utilisée.

I.4 Diffractométrie de rayons X

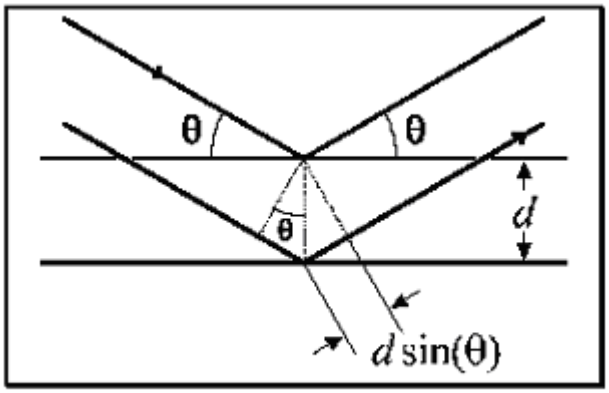

Figure I.7 : Principe de diffraction par rayons X.

L'analyse diffraction de rayon X permet la mesure et la qualité de l'orientation cristalline d'un matériau. Elle sert aussi à identifier les phase en présence dans un échantillon. Les rayons X induisent, dans un atome, une oscillation du nuage électronique par rapport au noyau Ce phénomène provoque la diffusion Rayleigh qui est une émission d'onde électromagnétique de même fréquence
Les rayons X ont des longueurs d'onde proche de distance inter-atomique, soit quelques Å Il y aura donc un phénomène d'interférences entre les rayons diffusés qui seront alternativement déstructives ou constructives Les photons X émis présenteront des flux importants ou très faibles en fonction de la direction dans l'espace. Ce sont ces variations selon les directions qui créent ce phénomène de diffraction X. On appel « pics de diffraction » les direction pour lesquelles les interférences sont constructives. Elles peuvent être déterminées par la loi de Bragg :

$$2d \sin\theta = n\lambda$$

d = distance inter-réticulaire, c'est-à-dire distance entre deux plans cristallographiques ;
θ = demi-angle de déviation (moitié de l'angle entre le faisceau incident et la direction du détecteur) ;
n = ordre de réflexion (nombre entier) ;
λ = longueur d'onde des rayons X.

Grâce à la loi de Bragg il est possible de calculer les périodicités du réseau cristallin à partir d'un spectre et ainsi d'identifier les phases cristallines avec orientation préférentielle perpendiculaires (ou presque) à la surface de l'échantillon. En particulier, les mesures de "Rocking curve" consistent à faire un balayage en Ω avec 2θ fixe, où 2θ correspond au maximum d'intensité du pic qui nous intéresse. La largeur à mi-hauteur du pic et la position angulaire obtenue avec ce balayage donnent respectivement une mesure de la dispersion de l'orientation cristalline et du décalage entre l'orientation de la couche et celle du substrat.

I.5 Cathodoluminescence

Le principe de la cathodoluminescence repose sur la réemission radiative d'un matériau suite à un bombardement de ce dernier par un d'électrons d'énergie importante (de 1 keV à ~20 keV)

Les techniques classiques comme la photoluminescence permettant de caractériser les propriétés d'émission de matériaux semiconducteurs ne sont pas forcément les plus adaptées pour obtenir le maximum de renseignements sur des nanostructure de ZnO.

En effet, le ZnO est un semiconducteur à grand gap (vers les 3,4 eV soit vers 360 nm) ce qui nécessite d'utiliser une source d'excitation ayant une énergie supérieure ce qui n'est pas le cas des lasers classiquement utilisés en photoluminescence. D'autre part, la photoluminescence ne permet que d'avoir une réponse globale d'un ensemble de nanostructures au contraire des expériences de cathodoluminescence [1]. Pour des diamètres inférieurs à quelques centaines de nanomètres, les dispositifs de type micro-photoluminescence ne permettront pas d'obtenir des cartographies de l'émission de nanofils pris individuellement.
Pour s'affranchir de ces inconvénients, le LMEN a développé un dispositif original de cathodoluminescence en champ proche inédit en France. Ce dispositif combine l'intérêt des techniques de cathodoluminescence classique pour l'imagerie et l'excitation et d'un dispositif de champ proche pour la collection des photons émis et la résolution des cartographies en émission.
La cathodoluminescence est une expérience idéale pour étudier les propriétés d'émission de matériaux de type ZnO. En effet, l'excitation s'effectue avec les électrons provenant du canon d'un microscope électronique à balayage (MEB) qui peuvent prendre des énergies importantes (de quelques keV à environ 20 keV) ce qui permet de visualiser la bande excitonique du ZnO. D'autre part, le MEB permet d'obtenir au préalable une image des structures à visualiser et il est donc possible de focaliser le faisceau électronique sur un point précis à exciter. En contrôlant le déplacement du faisceau du MEB, nous serons capables d'effectuer une cartographie des propriétés d'émission d'un film mince de ZnO en mettant en évidence, par exemple, les différences d'intensité pour une bande d'émission donnée. En fixant le détecteur à une longueur d'onde donnée, celle des défauts « verts/jaunes » du ZnO par exemple [2], il est possible de reconstituer une cartographie des défauts sur la surface du film. En plus des renseignements sur la qualité de l'émission des films, la cathodoluminescence permet donc d'obtenir des informations sur la qualité des films de ZnO (densité et localisation des défauts, mise en évidence de l'influence de la couche de mouillage…).
Néanmoins, les dispositifs classiques de cathodoluminescence sont limités au niveau de la résolution (quelques microns) ce qui limite les applications au niveau des nanostructures. Pour améliorer la résolution, nous avons couplé au MEB un microscope à force atomique (AFM). La collection des photons émis s'effectue grâce à une fibre optique couplée à la pointe de l'AFM [3], [4]. Ce dispositif MEB/SNOM permet d'améliorer la résolution jusqu'à une centaine de nanomètres ce qui est idéal pour l'analyse de nanofils.
Grâce à cette expérience, le LMEN a acquis de l'expertise sur l'analyse de couches minces de ZnO dans le cadre de plusieurs collaborations [5,6] dont dernièrement avec Nanovation [7] et sur l'étude d'autres nanostructures semiconductrices [8]. Un dispositif similaire mis au point en Allemagne a déjà donné des résultats très intéressants sur des nanofils de ZnO [9].

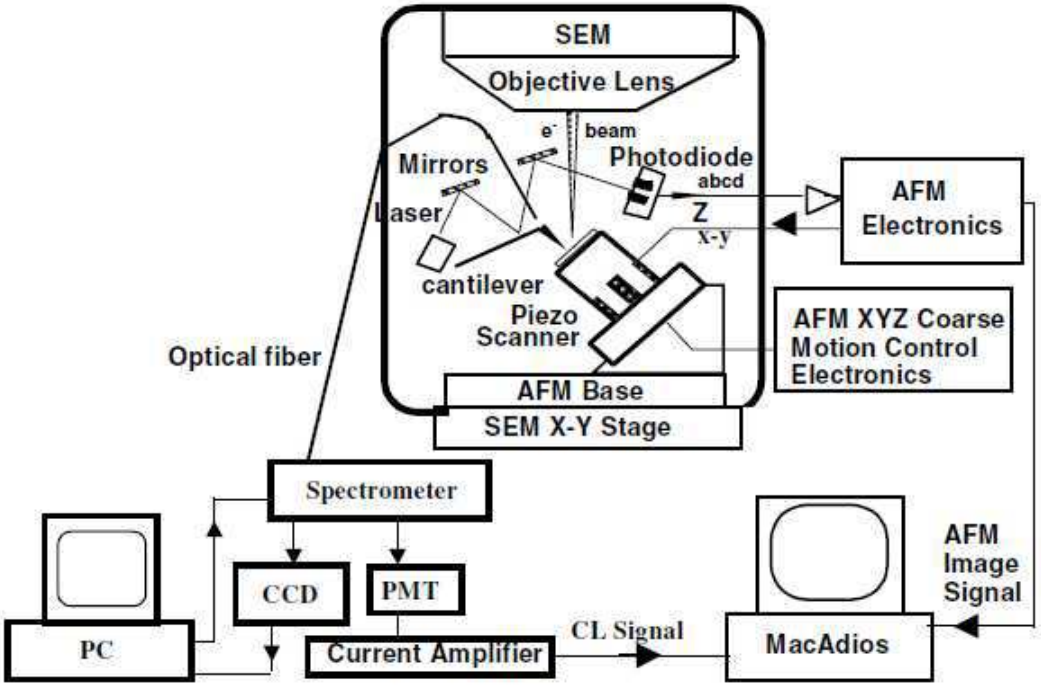

Figure I.8 : Schéma du montage cathodoluminescence. [10]

[1] JWP Hsu, Appl. Phys. Lett. 88, 252103 (2006),
[2] RC Wang et al., Appl. Phys. Lett. 86, 251104 (2005)
[3] D. Pastre, J-L. Bubendorff et M. Troyon Journal of Vacuum Science and Technology B 18 (2000) 1138-1143
[4] J-L. Bubendorff, D. Pastre et M. Troyon Journal of Microscopy 199 (2000) 191-196
[5 A. El Hichou, M. Addou, J. Ebothé and M. Troyon, Journal of luminescence, 113 (2005) 183-190
[6] J. L. Bubendorff, J. Ebothe, R. Dounia, A. El Hichou, M. Addou, Appl. Phys. 100 (2006) 014505 (1– 7).
[7] V. E. Sandana , D. J. Rogers, F. Hosseini Teherani, M. Molinari, M. Troyon, A. Largeteau, G. Demazeau, H.-J. Drouhin, C. Scott & M. Razeghi (To be published) Journal of crystal Growth 2011
[8] Bubendorff, J. L., Grandjean, N., Damilano, B., and Troyon, M.,(2003) J. Cryst. Growth., 247, 284-290.
[9]H J Fan et al 2004 Nanotechnology 15 1401-1404
[10] J. L. Bubendorff, D. Pastre & M. Troyon Journal of Microscopy, Vol. 199, Pt 3, 191-196.

I.6 Réflexion spéculaire

La lumière incidente à l'interface entre deux milieux peut être réfléchie, réfractée ou absorbée. De manière courante, le terme « réflexion » est utilisé pour décrire la réflexion spéculaire. La réflexion est dite spéculaire lorsque le rayon incident donne naissance à un rayon réfléchi unique. Idéalement, l'énergie du rayon incident se retrouve totalement dans le rayon réfléchi, en pratique une partie de l'énergie peut être absorbée ou diffusée au niveau de l'interface. La qualité de la réflexion dépend de la qualité de l'interface. Dès que la taille des défauts de l'interface est inférieure ou de l'ordre de grandeur de la longueur d'onde, l'interface tend à devenir parfaitement réfléchissante.

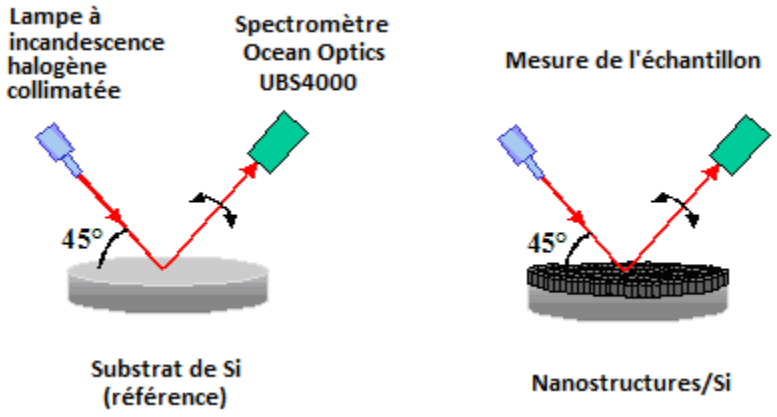

a) b)

Figure I.9 : Schéma du montage expérimental de mesure de la réflexion spéculaire. a) Mesure de la référence ; la source est une lampe à incandescence halogène collimatée qui a un angle de fixe de 45° avec la normal au substrat. Le spectromètre est un Ocean Optics UBS40000 et ses angles de mesure peuvent varier entre 10° et 60°. b) Mesure de l'échantillon.

En optique, la réflectivité est la réflectance qui est le rapport de l'énergie réfléchie sur l'énergie incidente exprimé en pourcentage. La réflexion peut être subdivisée en réflectance diffuse (de Beer-Lambert) et réflectance spéculaire ou miroitante. La réflectance efficace pour une surface idéale de Lambert est indépendante de l'angle de vision de l'observateur (loi de Rayleigh). La réflectance spéculaire est quant à elle très dépendante de l'angle de vision, étant maximale dans la direction du faisceau incident et à son opposé (théorie de Mie). La plupart des objets correspondent à un mélange de ces deux types de réflectance.

ANNEXE II Les matériaux semi-conducteurs

Un semi-conducteur est un solide dont la conductivité électrique est comprise entre celles des métaux (conducteurs) et celles des isolants. Cette distinction est donc quantitative. La figure II.1 montre les résistivités électriques de trois types de matériaux : isolants, semi-conducteurs et métaux.

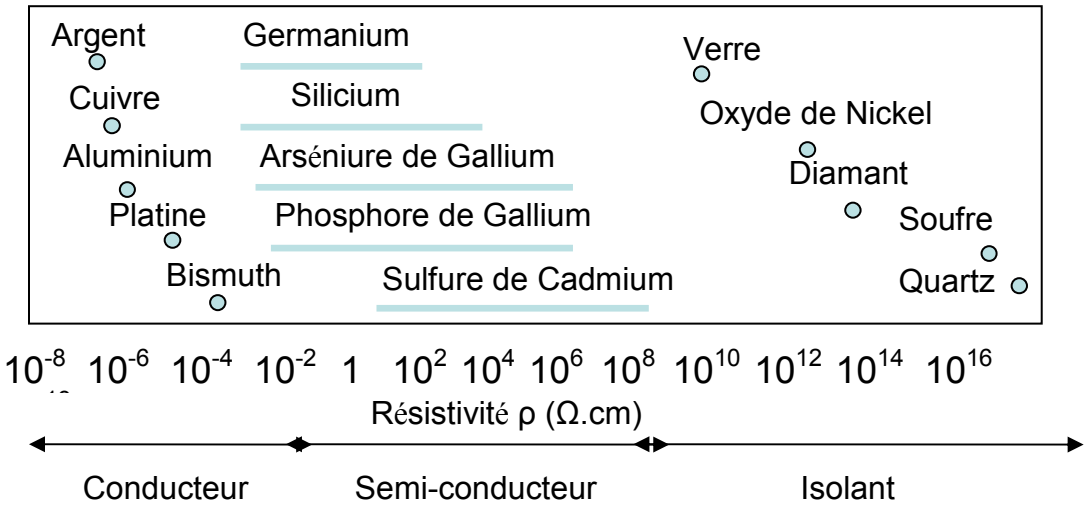

Figure II.1 :Résistivité en fonction de la nature des matériaux.

La figure II.2 illustre la position respective du niveau de Fermi, de la bande de valence et de la bande de conduction pour les isolants, semi-conducteurs et métaux. La couleur bleue indique la présence d'électrons.

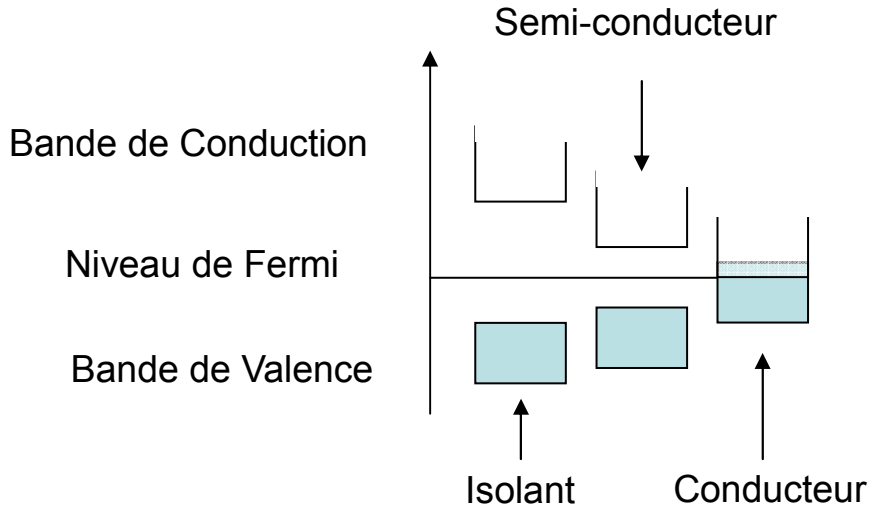

Figure II.2 Bande d'énergie selon le type de matériaux.

La conductivité des semi-conducteurs peut être contrôlée grâce au dopage (soit avec des défauts, soit

avec des impuretés), ce qui introduit des niveaux dans le gap et modifie ainsi la concentration de porteurs de charge libres. Si les électrons sont majoritaires par rapport aux trous, il s'agit alors d'un dopage n. Dans le cas contraire, il s'agit d'un dopage p.

	Classification périodique des élements				
Groupe	**II**	**III**	**IV**	**V**	**VI**
		B	C	N	O
		Al	Si	P	S
	Zn	Ga	Ge	As	Se
	Cd	In	Sn	Sb	Te

Figure II.3 : Tableau des éléments composant les semi-conducteurs usuels.

Il existe trois éléments semi-conducteurs appartenant tous au groupe IV qui sont :
- le germanium (Ge) premier semi-conducteur à avoir été utilisé ;
- le silicium (Si), devenu le matériau prédominant (98 % des composants actuels) ;
- l'étain gris (Sn), forme polymorphique et rare de l'étain.

Les semi-conducteurs composés usuels peuvent être constitués par :
- un élément du groupe III avec un élément du groupe V, par exemple GaAs, GaN, InAs ou AlAs ;
- un élément du groupe II avec un élément du groupe VI, par exemple CdTe, ZnSe, ZnTe, ZnO, MgS ou MgO ;
- un élément du groupe I avec un élément du groupe VII, par exemple CuBr, CuCl ou CuI.

ANNEXE III Structure de bande de ZnO

ZnO possède une bande interdite directe, c'est à dire que le minimum de la bande de conduction et le maximum de la bande de valence se trouvent alignés dans "l'espace des k" au centre de la zone de Brillouin (point Γ sur figure III.1 a). L'absorption et l'émission de lumière peuvent alors se faire avec conservation du vecteur d'onde sans impliquer d'interaction avec d'autres quasi-particules comme les phonons. Sous l'effet du couplage spin-orbite et du champ électrique nommé champ cristallin, trois bandes de valence distinctes apparaissent, conduisant ainsi à l'existence de trois excitons : A, B et C. [1]

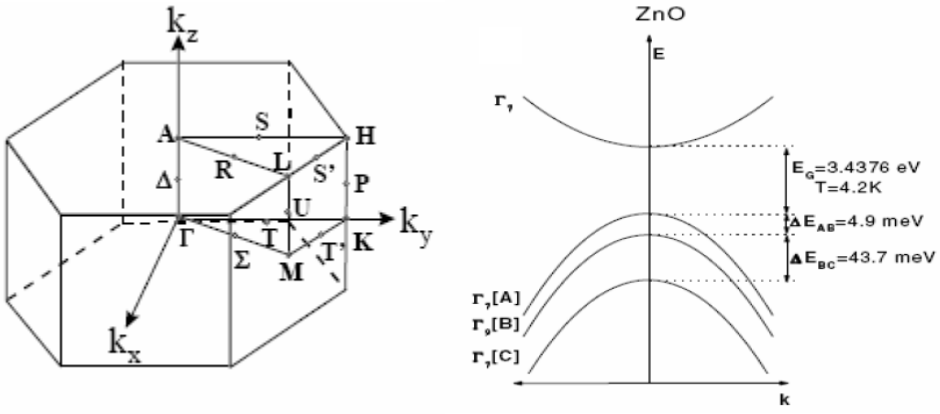

a) b)

Figure III.1 : a) Schéma de la première zone de Brillouin ; b) Diagramme des énergies des trois excitons, A, B et C de la bande de valence au point Γ dans le cas de ZnO. [1]

La figure III.2 représente la structure de bande de ZnO würtzite. [2, 3]

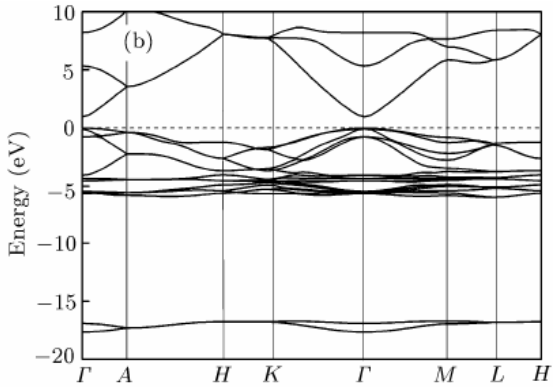

Figure III.2 : Structure de bandes de ZnO. En abscisses sont représentés les vecteurs d'onde du réseau réciproque selon les directions définies dans la figure IV.1 a. Structure de bande calculée par la méthode de « local-density approximation ». [4]

Références

[1] B. K. Meyer et al, Phys. Stat. Sol. b **241**, 231 (2007).
[2] X. Y. Zhang et al, Chinese Physical Letters, **24**, 1032 (2007).
[3] D. Vogel et al, Phys. Rev. B **52**, R14316 (1995).
[4] J. E. Jaffe, J. A. Snyder, Z. Lin, and A. C. Hess, Phys. Rev. B 62, 1660 (2000).

ANNEXE IV Luminescence d'un semi-conducteur et extraction de la lumière

Un matériau semi-conducteur est caractérisé par sa structure de bande électronique ayant un relativement faible gap énergétique (E_g) entre la bande de conduction et la bande de valence. Les électrons peuvent être excités de la bande de valence à la bande de conduction par énergie thermique ou par absorption d'un photon. [2]

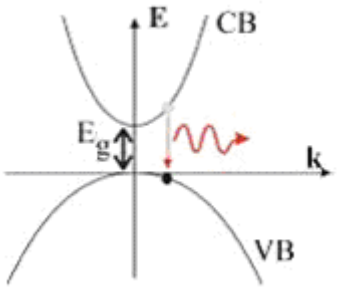

Figure IV.1: Luminescence dans un semi-conducteur direct. E_g est l'énergie de la bande interdite et k le vecteur d'onde de l'électron.

Une fois qu'un électron est dans la bande de conduction, il peut retourner dans la bande de valence (c'est-à-dire se recombiner avec un trou) via différents canaux de recombinaisons : radiatifs et non radiatifs. Le fonctionnement des diodes électroluminescentes (LEDs) est basé sur un phénomène de recombinaison radiative, appelé émission spontanée. La figure V.2 présente les énergies de gap et longueurs d'ondes d'émission en fonction de la longueur de liaisons (distance au plus proche voisin dans la maille élémentaire) de différents composés semi-conducteurs.

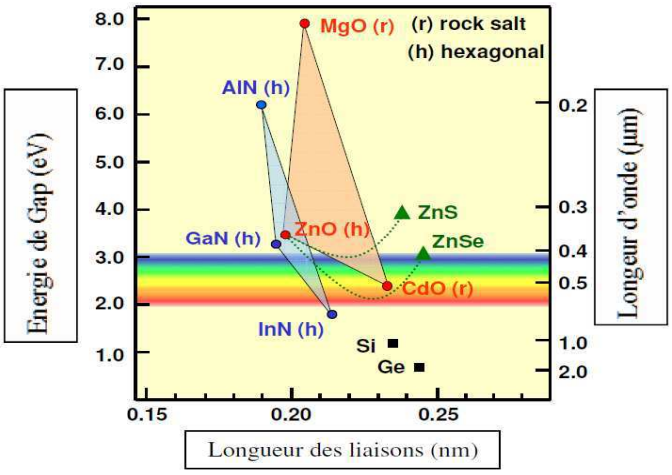

Figure IV.2: Energie de bande interdite (gap) et longueur d'onde d'émission en fonction de la longueur des liaisons.

Pour les matériaux cristallins on distingue ainsi deux types de semi-conducteurs, les semiconducteurs dit à gap direct pour lesquels dans l'espace des moments cinétiques le bas de la bande de conduction est situé en face du haut de la bande de valence, et les semi-conducteurs à gap indirect pour lesquels ce n'est pas le cas. Ces deux cas sont illustrés sur la figure ci-dessous pour deux semi-conducteurs classiques le silicium et l'arséniure de gallium. Cette différence est fondamentale pour les processus faisant intervenir des photons à cause de la condition de conservation du moment cinétique.

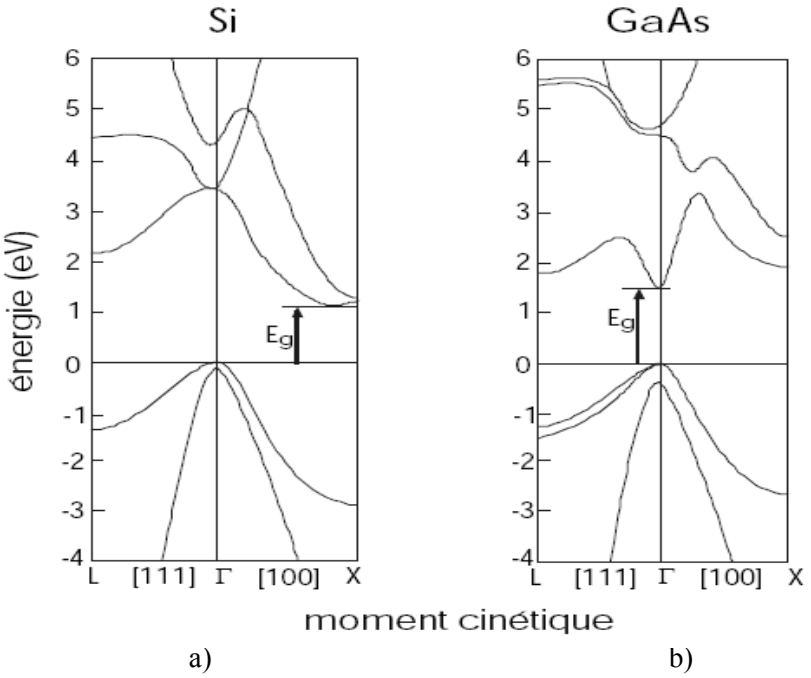

Figure IV.3 : Différence de structure de bandes entre un semi-conducteur à gap directe (b) et un semi-conducteur à gap indirecte (a)[3]

Recombinaisons radiatives

I) Émissions intrinsèques

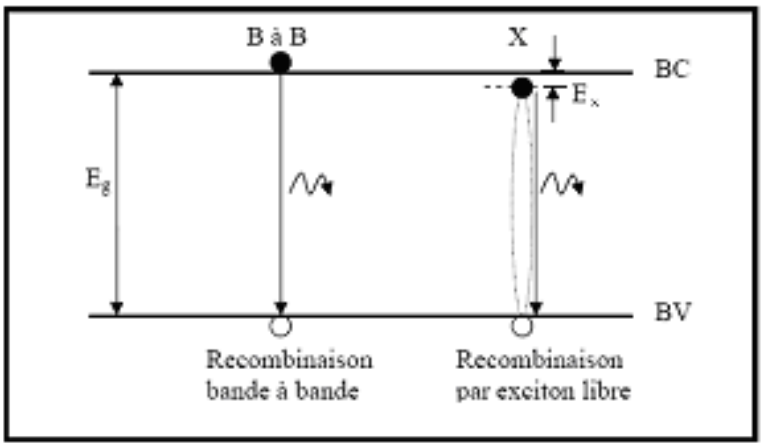

Figure IV.4 : Illustration des processus des recombinaisons radiatives.

1) Recombinaison bord de bande

Dans le cas de semi-conducteurs à gap direct, la recombinaison bord de bande s'effectue entre le maximum de la bande de valence et les états proches du minimum de la bande de conduction. Lorsque l'on diminue la température les recombinaisons excitoniques sont plus importantes par rapport à celle-ci.

2) Recombinaison par exciton libre

Dans les semi-conducteurs, l'attraction coulombienne entre l'électron et le trou entraîne la formation d'un nouvel état dans lequel les deux particules restent liées à la manière d'un atome d'hydrogène: l'exciton libre (Free Excitons). L'énergie libérée lors de la recombinaison des excitons libres est égale à la valeur du gap excitonique

$$h\nu = E_g - E_x$$

E_g : largeur de bande interdite du semi-conducteur ;
E_X : énergie de liaison de l'exciton libre ;
h: constante de planck ;
$\nu = c/\lambda$.

L'exciton libre est associée aux matériaux très purs. Ceci permet d'établir un critère de pureté du matériau étudié. La recombinaison excitonique peut s'accompagner de plusieurs émissions de phonons longitudinaux optiques (LO) d'énergie notée $h\omega_{LO}$.

II) Émissions extrinsèques

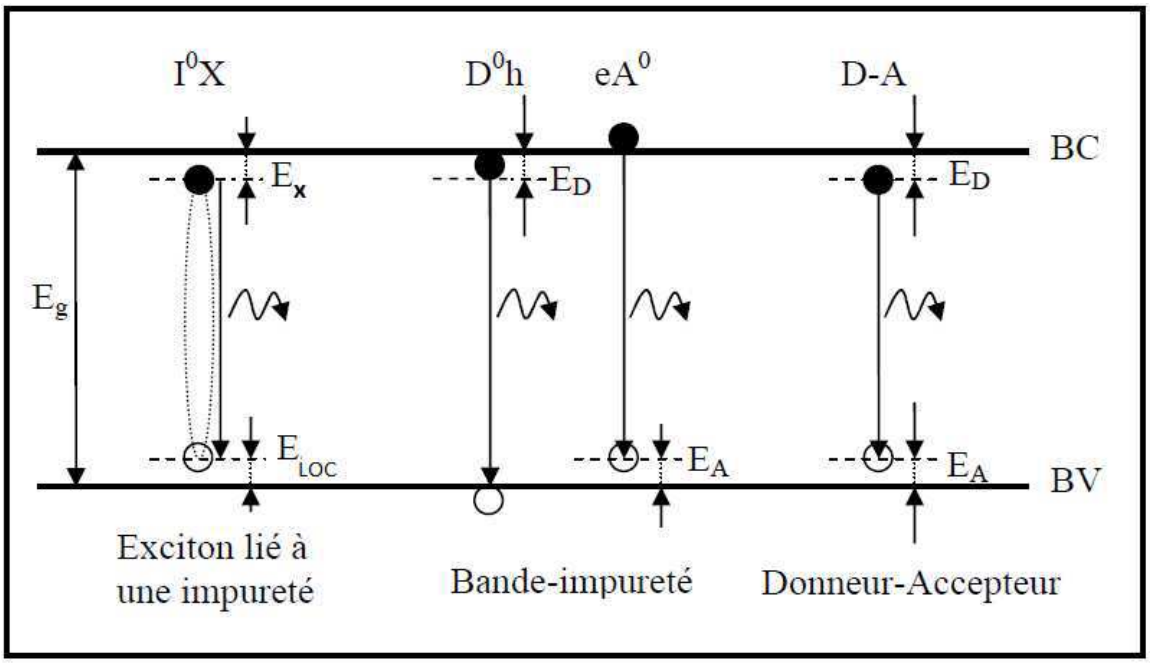

Figure IV.5 : Illustration des processus de recombinaisons radiatives : émissions extrinsèques.

1) Recombinaison par exciton lié

L'exciton peut se lier à une impureté lorsque celle-ci est à proximité, on l'appelle alors exciton lié (Bound Exciton). Ce sont des complexes formés entre une impureté et un exciton. L'exciton peut se lier avec un accepteur ou avec un donneur, qui peuvent être neutres ou ionisés. Lorsque les excitons liés se recombinent de façon radiative l'énergie des photons émis est :

$$h\nu = E_g - E_x - E_{LOC}$$

E_{LOC} est l'énergie de localisation de l'exciton sur l'impureté. On peut ainsi déterminer la nature de l'impureté.

2) Recombinaison bande-impureté

Cette recombinaison a lieu entre un accepteur neutre (eA^0) et un électron libre de la bande de conduction ou entre un trou libre de la bande de valence (D^0h) et un donneur neutre. L'énergie des photons émis est :

$h\nu = E_g - E_D$ pour la transition D^0h (E_D est l'énergie d'ionisation du donneur) ;
$h\nu = E_g - E_A$ pour la transition eA^0 (E_A est l'énergie d'ionisation de l'accepteur).

3) Recombinaisons donneur-accepteur (DAP)

Cette recombinaison se réalise entre un trou d'un niveau accepteur non ionisés et un électron d'un niveau donneur. Après recombinaison des deux impuretés celle-ci se retrouvent en interaction coulombienne. Lors d'une recombinaison donneur-accepteur (D-A) l'énergie du photon émis est :

$$h\nu = E_g - E_A - E_D + \frac{e^2}{4\pi\varepsilon r}$$

ε : constante diélectrique statique du matériau ;
e : charge de l'électron ;
r : distance entre atome donneur et atome accepteur.

Recombinaisons non radiatives

Les recombinaisons non radiatives et radiatives sont des processus concurrent. Les mécanismes de recombinaisons non radiatives les plus courants sont :
– la recombinaison par émission multiphonons sur les défauts cristallins ;
– la recombinaison Auger.
– les recombinaisons de surface provoquées par la discontinuité des liaisons atomiques et l'adsorption d'atomes étrangers ;

Extraction de la lumière

La performance d'une LED peut être réduite à deux valeurs quantitatives : l'efficacité quantique interne de la région active de la LED et l'efficacité d'extraction lumineuse. La première valeur, située entre 20 et 90%, reflète la qualité de la croissance épitaxiale de la structure. [4] La seconde valeur dépend fortement de la conception de la structure et peut être aussi faible que 2%. Pour les LEDs blanches d'aujourd'hui, l'efficacité quantique interne (c'est-à-dire le nombre de photons générés par électron traversant la diode) est inférieure à 50%. Pour les LEDs rouges l'efficacité quantique interne peut atteindre des valeurs très élevées, de l'ordre de 90 à 95 %. Il n'en est pas de même pour l'efficacité d'extraction, c'est-à-dire la fraction des photons produits qui parviennent à quitter la structure LED sans se faire absorber et qui constituent le flux lumineux utile. Celle-ci se situe généralement aux environs de 20 %, et de nombreuses recherches portent actuellement sur l'amélioration de ce facteur (optimisation de la géométrie, intégration de micro-réflecteurs, utilisation de structure type cristal photonique, nanostructuration de la surface). L'un des principaux problèmes des LEDs est l'extraction maximale de photons à l'air libre, le passage d'un mileu de fort indice optique (~ 2) à l'air. La lumière est totalement réfléchie à l'interface semi-conducteur-air pour un angle critique θc d'après la loi de Snell-Descartes (cf.figure IV.5) $n_1 \sin\theta_1 = n_2 \sin\theta_2$ où n_1 est l'indice du milieu 1, θ_1 est l'angle d'incidence du rayon lumineux à la normale de l'interface, n_2 est l'indice du milieu 2 et θ_2 est l'angle de réfraction du rayon lumineux à la normale de l'interface.

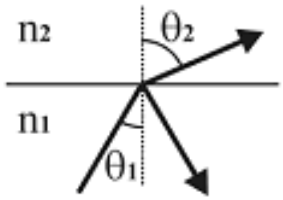

Figure IV.6: Schéma d'un rayon incident et réfracté entre un milieu 1 et 2.

La lumière générée peut être transmise dans l'air si elle se propage dans le matériau semi-conducteur avec un angle inférieur à l'angle critique $\theta_c = \sin^{-1}(n_2/n_1)$. La valeur de l'angle solide correspondant à θ_c est appelée cône d'extraction (Fig. IV.6). La lumière générée, dont l'angle de diffusion n'est pas situé dans le cône d'extraction, sera réfléchie à l'intérieur de la LED à l'interface air/semi-conducteur et éventuellement réabsorbée dans le semi-conducteur ou les contacts métalliques.

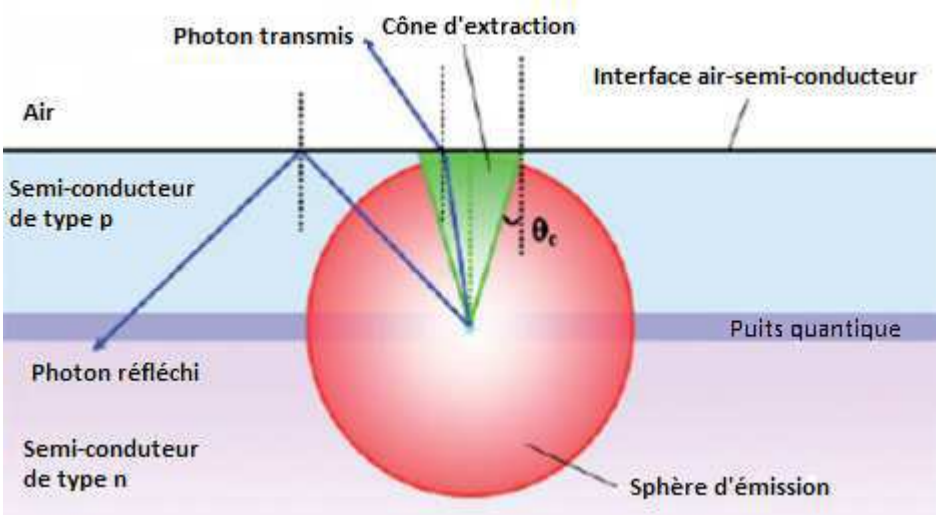

Figure IV.6 Représentation du cône d'extraction (en vert) d'angle solide θ_c , dans le cas d'une interface air-semi-conducteur. La sphère d'émission des photons est représentée en rouge. [5]

Une émission isotrope donne alors un rendement d'extraction de la lumière noté $\theta_{extract}$ tel que : $\theta_{extract} = (1/2)(1-\cos\theta_c)$. Ce qui correspond à un rendement d'environ 5% dans le cas d'une diode à base de ZnO (n = 2 pour $\lambda \approx$ 375 nm) et 4,5% dans le cas d'une LED GaN (n = 2,4 pour $\lambda \approx$ 365 nm).

La nanostructuration, pour la fabrication de dispositifs intégrant des nanostructures dont les propriétés spécifiques permettent un contrôle unique des propriétés d'émission d'un matériau, est clairement identifiée aujourd'hui comme un axe de développement important dans le domaine de l'éclairage et en particulier pour les LEDs à base de GaN. La structuration d'indice à l'échelle nanométrique permet en effet d'extraire plus efficacement les photons de la couche émettrice. Un gain de 70% en efficacité lumineuse a pu ainsi être démontré (cf. figure IV.7). [6]

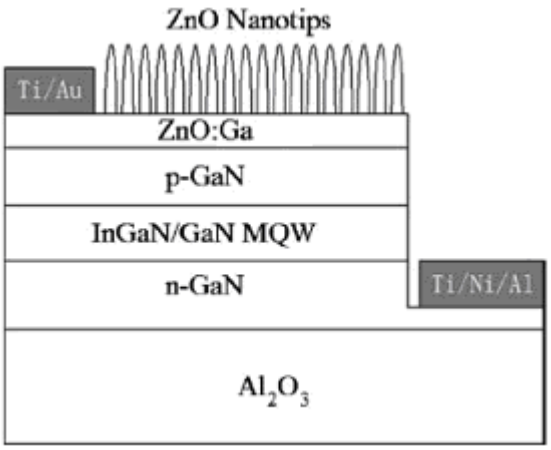

Figure IV.7 : Utilisation de nanocolonnes de ZnO dans une LED. [7]

Comportement électrique d'une jonction p-n

L'électroluminescence a été décrite, pour la première fois, par H. J. Round en 1907. Il observa une émission lumineuse sous injection courant dans un cristal de SiC. [8] Cependant la jonction p-n ne fut comprise qu'à partir de 1949 grâce aux travaux de Shockley, [9] travaux qui permirent à Lehovec d'interpréter le phénomène d'électroluminescence dans un cristal de SiC comme étant la recombinaison radiative d'une paire électron-trou dans une jonction p-n. [10]

La forme la plus simple d'une jonction p-n, appelé homojonction, est schématisée en figure IV.8. Il s'agit d'une jonction entre une région dopée p et une région dopée n. A l'interface entre les deux régions, les bandes de conduction et de valence se courbent afin que les niveaux de Fermi dans les deux régions soient alignés. Au niveau microscopique, cette déformation des bandes est dûe à la diffusion des porteur de charge vers les régions opposées (soit les électrons dans la région dopée p et vice-versa), ce qui, en retour va générer un champ électrique qui s'oppose au phénomène de diffusion. A l'état d'équilibre, le champ électrique produit un courant de conduction qui contrebalance le courant de diffusion. Lorsqu'une tension externe, telle que la polarisation soit directe, est appliquée à la jonction, l'équilibre entre les deux courants est rompu et la diffusion des porteurs de charge est favorisée. On obtient ainsi la loi de Schockley, qui décrit la caractéristique courant / tension I(V) :

$$I=I_0 \left(e^{eV/k_{BT}} -1\right)$$

-e = charge électron ;
V = tension externe ;
k_B = constante de Boltzmman ;
T = température.

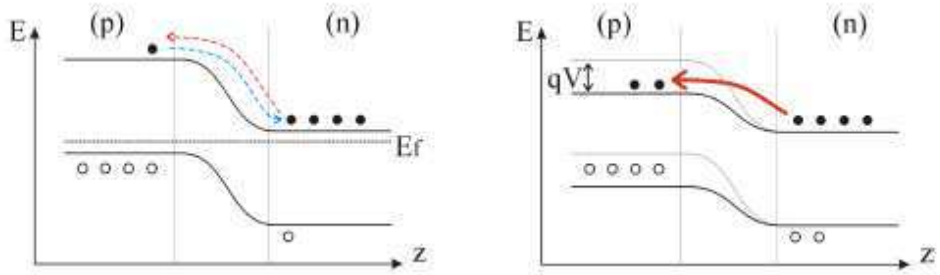

Figure IV.8 : (a) Homojonction sans courant injecté. Les courants de diffusion et de conduction dans la jonction se compensent à l'équilibre (flèches en pointillé) ; (b) Quand une tension directe V est appliquée, la hauteur de barrière diminue et la diffusion des porteurs de charges augmente. La région opposée présente plus de porteurs de charge minoritaires qui diffusent et peuvent se recombiner de façon radiative.

Il y a un excès de porteurs de charge minoritaires des deux coté de la jonction. Ces porteurs de charge diffusent et peuvent se recombinent de façon radiative. Cependant, l'efficacité de ce phénomène est limitée par l'absorption de la lumière générée (réabsorption à la jonction et recombinaison des porteurs de charge libre dans les régions p et n). Pour éviter cela, des hétérostructures sont utilisées. Dans celles-ci les énergies des bandes interdites à la jonction p-n sont inférieures à celles des régions p et n, ce qui a pour effet de diminuer la réabsorption de photons dans ces régions (cf. figure IV.9). Lorsque l'épaisseur de la région centrale diminue en dessous de la longueur d'onde de de Broglie des porteurs de charges, elle devient un puits quantique. Les structures intégrant des puits quantiques sont plus efficaces que de simples structures de type homojonction, car elles permettent une plus forte densité de porteurs de charge dans la région active (et conduisent à un temps de recombinaison plus court) pour une densité de courant donnée. Elles limitent ainsi le phénomène de réabsorption dans le matériau semi-conducteur. De plus, les puits quantiques permettent un meilleur contrôle de la longueur d'onde émise grâce au contrôle du déplacement énergétique lié au confinement quantique.

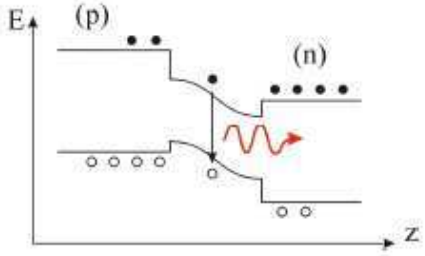

Figure IV.9 : Jonction p-n dans une hétérostructure ; la largeur de la bande est plus fine dans la région centrale ce qui empêche la réabsorption du photon émis dans les couches n et p. La flèche rouge représente un photon.

De fait, dans une jonction p-n idéale, tous les porteurs de charge injectés sont convertis en lumière ayant une longueur d'onde donnée : c'est ce qui constitue une efficacité de conversion électron-photon parfaite, comme illustré sur la figure IV.9.

Références

[1] G. Bastard, *Wave mechanics applied to semiconductor heterostructures,* Les Editions de Physique, Les Ulis, France (1992)
[2] C. Benoît à la Guillaume : Cours sur les processus de recombinaison radiative dans le semi-conducteur, Laboratoire de Physique de l'École Normale Supérieure, Paris (1998).
[3] H. Mathieu. *Physique des semi-conducteurs et des composants électroniques.* Les Editions Dunod, Paris, France (1997)
[4] Navigant Consulting, Inc., Radcliffe Advisors, Inc., and SSLS, Inc. Report on Solid-State Lighting Research and Development Building Technologies Program, Office of Energy Efficiency and Renewable Energy U.S. Department of Energy (2009);
http://apps1.eere.energy.gov/buildings/publications/pdfs/ssl/ssl_mypp2009_web.pdf
[5] M. Yamada, Y Narukawa, and T. Mukai, Jap. J. App. Phys. **41**, L246 (2002).
[6] J. Zhong, H. Chen, G. Saraf, Y. Lu, C. K. Choi, J. J. Song, D. M. Mackie, and H. Shen, App. Phys. Lett. **90**, 203515 (2007).
[7] H. J. Round, Electrical World, p. **309** (1907).
[8] W. Shockley, Bell System Technical Journal, **28**(3):435-489 (1949).
[9] K. Lehovec, C. A. Accardo, E. Jamgochian. Phys. Rev. **83**(3), 603-607 (1951).

ANNEXE V *Novel Green Light Emitting Diodes: Exploring Droop-free Lighting Solutions for a Sustainable Earth*

M. Razeghi et al. Journal of Light Emitting Diodes Vol 2 N0 1, April 2010

M. Razeghi*, C. Bayram and R. McClintock

Center for Quantum Devices, Department of Electrical Engineering and Computer Science, Northwestern University, Evanston, Illinois, USA 60208

F. Hosseini Teherani, D.J. Rogers and V. E. Sandana

Nanovation SARL, 103 bis Rue de Versailles, Orsay 91400, France

Abstract

The total annual energy consumption in the United States for lighting is approximately 800 Terawatt-hours and costs $80 billion to the public. The energy consumed for lighting throughout the world entails to greenhouse gas emission equivalent to 70% of the emissions from all the cars in the world. Novel solutions to lighting with higher efficiency will drastically reduce the energy consumption and help greenhouse gas emissions to be lowered. Novel green light emitting diodes are the key components of an affordable, durable and environmentally benign lighting solution that can achieve unique spectral quality and promise superior energy conversion efficiency.

Light-emitting diodes (LEDs), based on the InGaN alloy, are currently the most promising candidates for realizing solid state lighting (SSL). InGaN is a direct wide bandgap semiconductor with an emission that can span the entire visible spectrum via compositional tuning. However, InGaN LED performance remains wavelength-dependent. Indeed, ultrabright and efficient blue InGaN-based LEDs are readily available but the performance of InGaN-based green LEDs is still far from adequate for use in SSL.

Our recent work demonstrated hybrid green light-emitting diodes (LEDs) comprised of n-ZnO/(InGaN/GaN) multi-quantum-wells/p-GaN were grown on semi-insulating AlN/sapphire using pulsed laser deposition for the n-ZnO and metal organic chemical vapor deposition for the other layers.. We have shown that atop grown ZnO layer by Pulsed Laser Deposition can be a good replacement for GaN. The green wavelength emission requires significant indium content in the active layer (growth temperature ~ 700ºC) that makes InGaN quantum wells very susceptible to thermal degradation. With our technology, diffusion and segregation of indium in the green emitting active is inhibited thanks to the lower ZnO deposition temperatures (<600ºC) than is required for GaN (>1000ºC). Our novel technology preserves the integrity of the as-grown active layer and demonstrates superior green spectral quality (as demonstrated for LEDs on c-sapphire). The results indicate that hybrid LED structures could hold prospects for the development of green LEDs with superior performance.

Introduction

III-Nitride based emitters support promising applications from water purification to solid state lighting due to their tunable direct bandgap extending from deep ultraviolet towards green.

In section 1 "Ultraviolet Light Emitting Diodes", we are summarizing the research on ultraviolet light emitting diodes (LEDs). In section 2 "Hybrid Ultraviolet Light Emitting Diodes" we investigate some new ultraviolet LEDs based on silicon, zinc oxide and gallium nitride hybridization.

In section 3 "Comprehensive study of blue and green multi-quantum-well light emitting diodes grown on conventional and lateral epitaxial overgrowth GaN", growths of blue and green multi-quantum-wells (MQWs) and light-emitting diodes (LEDs) are realized on lateral epitaxial overgrowth (LEO) GaN, and compared with identical structures grown on conventional GaN. Atomic force microscopy is used to confirm the significant reduction of dislocations in the wing region of our LEO samples before active region growth. Differences between surface morphologies of blue and green MQWs are analyzed. These MQWs are integrated into LEDs. All devices show a blue shift in electroluminescence (EL) peak, and narrowing in EL spectra with increasing injection current, both characteristics attributed to the bandgap renormalization. Green LEDs show a larger EL peak shift and broader EL spectrum due to larger piezoelectric field and more indium segregation in the MQWs, respectively. Blue LEDs on LEO GaN show a higher performance than those on conventional GaN, however, no performance difference is observed for green LEDs on LEO GaN versus conventional GaN. The performance of the green LEDs is shown to be primarily limited by the active layer growth quality.

Increasing the In content of the active layer, an apparent decrease in the intensity is observed. In section 4 "Section 4 Green Light **Emitting Diodes**", we identify the problem, and apply our unique pulsed epitaxy approach to achieve green LEDs.

In section 5 "Section 5 Novel Hybrid Green LEDs Based on Substituting n-type ZnO for n-type GaN in an Inverted **p-n Junction**", we demonstrate our unique approach for green light emitting diodes. Although ultra-bright and efficient blue InGaN-based Light Emitting Diodes (LEDs) are readily available, the performance of InGaN-based green LEDs is still relatively poor. This is because the higher In content required in the active layers for green emission causes problems. In particular, the elevated substrate temperature (Ts) necessary for the *p*-type GaN top layer causes In to leak out of the active layers in the InGaN/GaN Multi-Quantum Wells (MQW). This significantly reduces the performance and lifetime of the LEDs. In this work, an *n*-type ZnO was substituted for the *n*-type GaN layer in an (In)GaN-based green LED with an inverted *p*-*n* structure. The top layer was thus the *n*-type ZnO rather than *p*-type GaN. Through use of Pulsed Laser Deposition (PLD) for this ZnO growth, the ultimate growth step could thus be performed at significantly lower Ts than is typically required for GaN growth in Metal-Organic Chemical Vapor Deposition (MOCVD). High crystallographic quality of the final hybrid LED structure and the integrity of the MQWs were confirmed by X-Ray Diffraction. The devices showed rectifying I/V characteristics with a turn-on voltage of 2.5 V and a discrete green Electroluminescence (EL) emission peaked at around 510 nm, which was readily visible to the naked eye. These results indicate that PLD-grown ZnO could be a good alternative to MOCVD-grown GaN for the *n*-type layer and that such inverted hybrid structures could hold the prospect for the development of green LEDs with superior performance.

In section 6 "**Section 6 Stranski-Krastanov growth of InGaN quantum dots emitting in green spectra**", we explain how to optimize InGaN quantum dots emitting in green spectra. In the 7th section,

"**Section 7 Phosphor-free White Light-Emitting Diodes based on InGaN Quantum Dots**", we demonstrate room temperature white LEDs based on InGaN QDS.

In section 8 "Phosphor-free white light emitting diodes based on InGaN quantum dots", we are demonstrating the optimization of green emitting InGaN quantum dots which are later integrated into LEDs. Thanks to the Stranski-Krastanov growth mode, white light emission is realized from these devices.

In summary, in this review we demonstrate the capabilities of III-Nitride devices emitting from ultraviolet through visible. We investigate novel hybrid green light emitting diodes as a means of cleaner green-light emission as well as develop quantum structures to be employed as active emitter material.

Section 1 Ultraviolet Light Emitting Diodes

Introduction

The ultraviolet (UV) portion of the electromagnetic spectrum lies between visible light and X-rays, spanning the wavelength range of ~10 nm to ~380 nm. It may further be classified into near UV (200 nm $< \lambda <$ 380 nm) and extreme or vacuum UV (10 nm $< \lambda <$ 200 nm), or alternatively UVA (380-315 nm), UVB (315-280 nm), and UVC (<280 nm). The wavelength range of 240 - 280 nm forms a strategic window for unique applications on earth [1]. This is due to the fact that even though the sun emits radiation in this wavelength region, the earth's atmosphere prevents these wavelengths from reaching the earth's surface. Therefore, in this window, commonly referred to as the solar blind region, there is a naturally low amount of radiation. That is, the only UV light present on the earth's surface in the solar blind region of the spectrum must be from a source on the earth's surface. Since there are few natural sources of light in this wavelength range, there is a very low level of background noise for applications using these strategic wavelengths.

The development of UV emitters and detectors has been primarily driven by the military applications of chemical / biological agent detection systems and non-line-of-sight (NLOS) communications. Chemical / biological agent detection using UV emitters and detectors is done through fluorescence-based detection, while NLOS communication takes advantage of the solar-blind portion of the spectrum in order to achieve short range, covert communications.

In fluorescence-based detection, the characteristic fluorescence of biological markers intrinsic to biological agents is used to detect the presence of biological agents in the environment. An ultraviolet light source (preferably a laser) illuminates the cloud of the unknown agent in short pulses. If fluorescent biological markers are present, they will emit light at a wavelength slightly longer than the absorption wavelengths. This emitted light is then detected by a sensor with a peak detection adjusted to the characteristic fluorescence of the marker. The detected signal is then analyzed for each laser pulse: threat discrimination is based upon comparison of the signal to the background in order to detect significant changes in bioaerosols.

By combining semiconductor-based UV Emitters with photodetectors, it becomes possible to devise a compact system that can rapidly detect and discriminate amongst various biological agents based upon their fluorescence signature. For this, UV emitters and detectors at several strategic wavelengths are required. The choice of wavelength is dictated by the specific absorption and fluorescence of the corresponding biological markers. The UV light sources are selected to emit at the peak absorption wavelength of the bio-marker in question, for example at 280 nm for tryptophan, 274 nm for tyrosine, and 257 nm for phenylalanine – the three important amino acids with fluorescence properties – and ~340

nm for NADH. The resulting signal is subsequently collected by a photodetector band-pass filter set at the appropriate waveband corresponding to the florescence wavelength of the agent. The use of efficient semiconductor-based UV light sources would enable the overall system to be more compact, inexpensive, and portable with lower power consumption than current existing biological and chemical agent detection systems. Additionally, the reduced size and lower power consumption of the semiconductor UV sources will enable the incorporation of multiple excitation sources at different wavelengths in the same compact enclosure. The use of additional sources is expected to increase the specificity of the biological agent detection system by targeting specific fluorescence excitations from a variety of biological markers.

NLOS communication takes advantage of the solar blind region of the spectrum ($\lambda<280$ nm) for its very low background noise, high atmospheric scattering, and high absorption rate for UV signals. The very low background noise allows for easy signal detection; any UV signal less than 280 nm seen by the detector must be man-made. The high atmospheric scattering allows for the signal to be transmitted without direct line of sight restrictions. The high absorption rate combined with the high atmospheric scattering leads to a strong extinction coefficient, which means that the signal cannot be detected from a distance, allowing for covert communications.

The system would consist of a transmitter unit with a UV source (wavelength of less than 280 nm) and a receiver with a solar-blind detector (cutoff wavelength of 280 nm). The receiver would be able to detect a signal from the transmitter as long as the distance between them is between approximately 10 and 250 meters. This form of covert communication would be invaluable to troop communication on the battlefield.

In addition to these two major defense applications, there are many civilian applications for UV emitters. Shorter wavelength lasers (into the UV end of the spectrum) would provide a means for higher density optical data storage and higher resolution laser printing, since the resolution of both of these applications is directly proportional to the wavelength of the laser. UV LEDs would enable fabrication of white LEDs for efficient, low cost lighting. UV-C light ($100 \text{ nm} < \lambda < 280 \text{ nm}$) deactivates the DNA of bacteria, viruses, and other pathogens, thus destroying their ability to multiply and cause disease. UV emitters in the UV-C range may be used for food sterilization and water / air purification. UV emitters may also be used for activation of photochemically sensitive resins and in-situ activation of drugs through optical stimulus.

Combinations of emitters and detectors would provide systems for free-space UV communications, and covert space communications, which would be secure from eavesdropping from anyone on earth.

UV detectors may be integrated into a watch or pager type device that could then be used to test for sun exposure, alerting the wearer when they had overexposed themselves to harmful UV rays. UV focal plane arrays (FPAs), or large arrays of mini UV detectors, provide UV imaging capabilities that have several possible applications. Visible and/or solar blind detectors eliminate a lot of background noise and thus FPAs made of such detectors are ideal for monitoring power lines for possible fault locations and UV flame detection and combustion monitoring in engines. The military desires solar blind UV FPAs for early missile threat warning, and aerial and terrestial UV countermeasures. UV astronomy would also benefit from UV FPA development.

For most of the applications described above, it is critical to have a compact and lightweight, chemically and physically robust UV detector and / or UV source in order to meet the needs of the applications and withstand the operating demands placed on the device. As will be discussed later, the nitride material system is uniquely matched to fulfill these demands.

The nitride material system has several important properties that make it ideal for visible to deep UV optoelectronic devices. These properties also allow InAlGaN material to withstand demanding applications that require harsh operating conditions.

The nitrides posses a wide band gap which, through alloying, can be tuned from about 0.9 eV for InN to 3.4 eV for GaN to 6.2 eV for AlN. This covers the wavelength range of IR radiation into to the deep UV end of the spectrum. III-Nitrides are the only semiconductor material system that covers the deep UV portion of the spectrum. Alloying allows for heterostructure devices, which improves device performance over a straight p-n junction. The III-nitride bandgap is a direct bandgap, which is ideal for optoelectronic devices.

First 280 nm LEDs

Our group achieved the first published 280 nm LED in early 2002 [2]. The structure, shown in Figure 1, was based on AlInGaN / AlInGaN multiple quantum wells and was top-emission. The LED was fabricated using the 400 μm × 400 μm mask without a ring contact. The IV curve, shown in Figure 2(a), demonstrates a turn-on voltage of approximately 5 volts, a differential resistance of 40 Ω, and reverse leakage at -3 V of approximately -10 μA. Figure 2(b) displays the EL spectra at various pulsed mode currents, showing a peak emission wavelength of 281 nm for low current injection with a slight red-shift to 282 nm at higher injection currents.

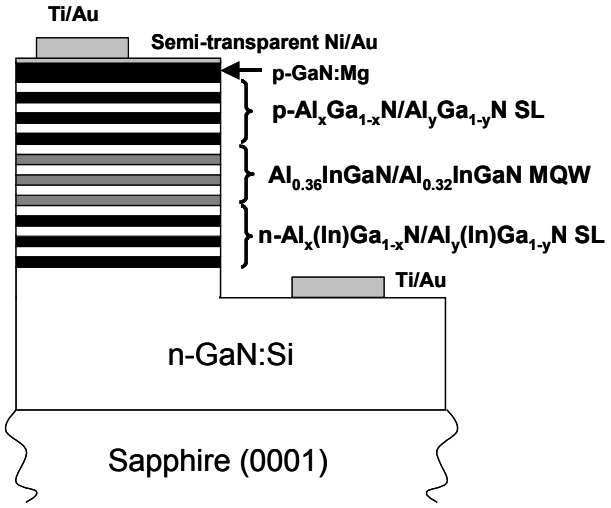

Figure 1: Device structure of first 280 nm device.

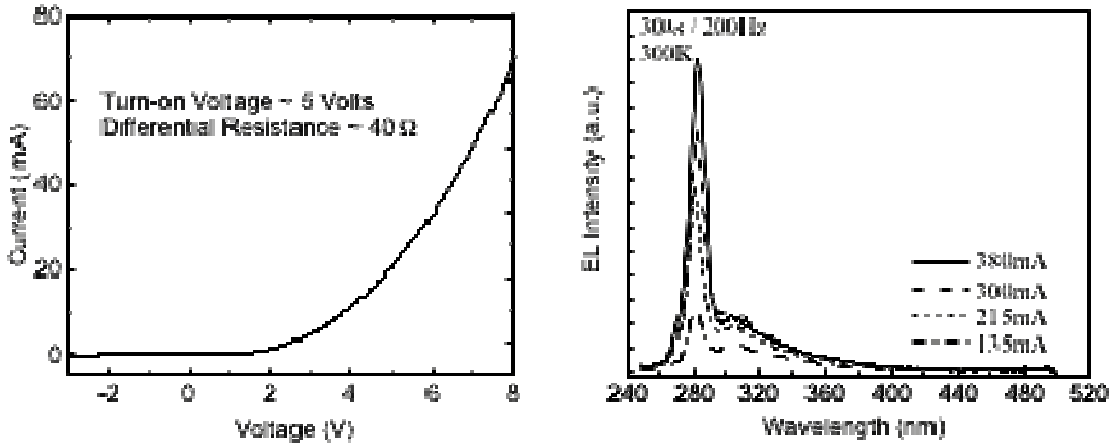

(a) **(b)**

Figure 2: (a) IV curve and (b) EL spectra of first 280 nm device.

High power 280 nm LEDs

In fall 2003, we demonstrated mW power from our 280 nm LEDs due to an improvement in material quality and device structure, as well as improvements in device geometry and packaging [3].

The device structure of the mW LED consists of an asymmetric single-quantum well (SQW) active layer confined between *p*- and *n*-type AlGaN on top of a high-quality AlGaN/AlN template. Deposition was initiated with a 20 nm low-temperature AlN buffer layer, followed by a 350 nm thick AlN layer, and a 30 period $Al_{0.85}Ga_{0.15}N$/AlN (50 Å/50 Å) superlattice topped with a 50 nm AlN layer. Next, 600 nm of Si–In codoped n-$Al_{0.5}Ga_{0.5}N$ was deposited forming the n-type contact layer which preceded a 100 nm thick n-$Al_{0.45}Ga_{0.55}N$ layer. The active region consisted of a 10nm $Al_{0.4}Ga_{0.6}N$ barrier, followed by a 5nm $Al_{0.36}Ga_{0.44}N$ quantum well, and ending with a second 5 nm $Al_{0.4}Ga_{0.6}N$ barrier. A 10 nm $Al_{0.6}Ga_{0.4}N$ current blocking layer was then deposited to help prevent an overflow of electrons out of the active region. The asymmetric design of the active region is intended to compensate for the lower mobility of holes compared to electrons. This allows more of the injected electrons to contribute to recombination in the quantum well, which in turn increases the efficiency of the LED. The structure was completed with a 50 nm thick p-$Al_{0.45}Ga_{0.55}N$ layer followed by a 50 nm thick p-GaN contact layer. After growth, the sample was examined with both an optical and a scanning electron microscope and was found to be crack free. A schematic diagram of the device structure including the metallic contacts is shown in Figure 3.

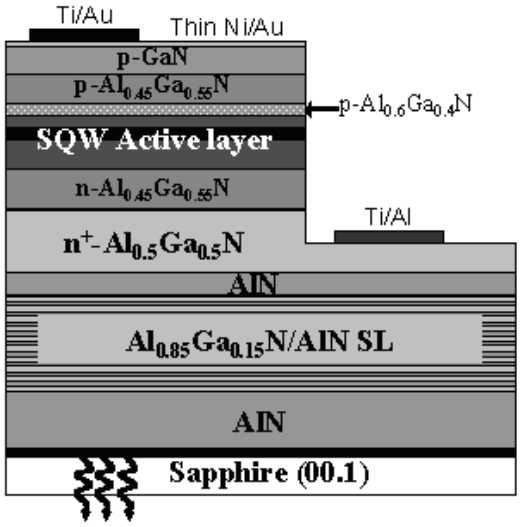

Figure 3: Device structure of high-power 280 nm LED.

The standard deep UV LED fabrication process was utilized for these devices, using the 300 µm × 300 µm AlN submount set of masks in order to have a ring contact and be able to package the devices.

After processing, we analyzed the I–V characteristics of the devices. Figure 4(a) displays the I–V curve of a single device, which has a series resistance of approximately 25 Ω and a turn-on of approximately 6 V. By fitting the I–V curve an ideality factor of 5.6 is estimated. Next, we measured the EL spectra from a single diode under various pulsed injection currents (5 µs pulse width, 2 kHz frequency). These spectra, displayed in Figure 4(b), demonstrate an approximately linear increase in intensity with increasing current. The dominant single peak occurs at ~280 nm. By fitting a Gaussian to the curve, we determined the peak to have a full-width at half-maximum value of 9.2 nm.

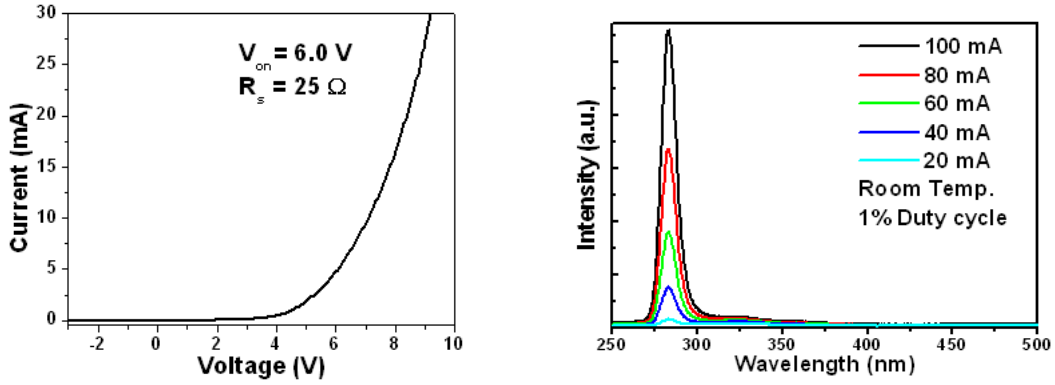

(a) **(b)**

Figure 4: (a) IV curve and (b) EL spectra of high-power 280 nm LED.

Finally, we measured the optical output power of the diodes. Figure 5 shows the pulsed (200 ns, 200 Hz) P-I curve of a single diode and an array of four diodes connected in parallel.

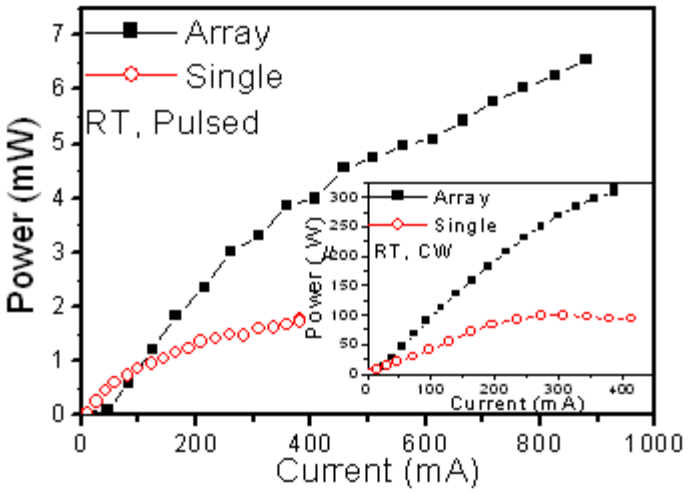

Figure 5: Pulsed (200 ns, 200 Hz) P-I curves for a single device and an array of four devices. Inset displays the continuous wave power for a single devices and array of four devices.

Under 400 mA injection current, the output powers of the single diode and the array are 1.8 mW and 3.9 mW, respectively, with the array reaching a high power of 6.5 mW at 880 mA. The array is able to reach higher power at the same current as the single device because the current is spread across a larger area, which alleviates local heating effects. A clear decrease in slope efficiency is noticeable on both curves when comparing the low and high injection current regions. The curve for the diode array gives an initial slope efficiency of 14.7 μW/mA, which falls off to 4.8 μW/mA at higher current. This change is attributed to device heating caused by current crowding. The inset of Figure 5 displays P– I curves measured under continuous-wave operation for both a single diode and an array of four diodes. At 300 mA, the single device and the array produced output powers of 100 μW and 270 μW, respectively. At 390 mA, the array reaches a power of 310 μW. Figure 6 shows the EQEs corresponding to the P–I curves in Figure 5.

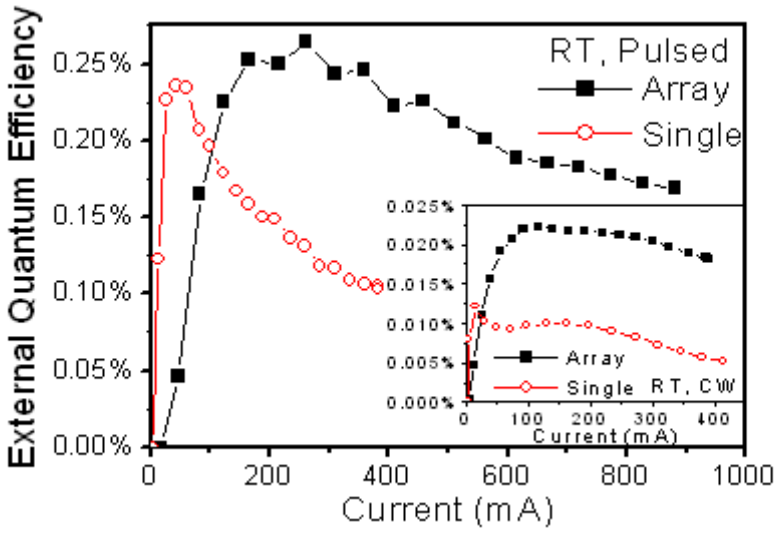

Figure 6: External Quantum Efficiency (EQE) curves for a single device and an array of four devices under pulsed (200 ns, 200 Hz) current operation. The inset displays the EQE curves under continuous-wave operation for a single device and an array.

Under pulsed current operation, the single device reaches a peak EQE value of 0.24% at a current of 40 mA while the array reaches 0.26% at 265 mA. After reaching the maximum value, the EQE curves roll off, a second demonstration of the decrease in device efficiency due to internal heating. The array reaches its peak efficiency at a later current because the current is spread across a larger area. However, after this peak value, the array EQE drops at a slower rate than the single device because, as discussed earlier, there is less localized device heating. Similarly, the continuous-wave EQE of the array reaches a higher value and stays relatively constant as compared to the continuous-wave EQE of the single device. The continuous-wave EQE curves reach peak values of 0.012% and 0.022% for the single device and the array, respectively.

LEDS with $\lambda < 280$ nm

At approximately the same time that we achieved high power 280 nm LEDs, we also achieved a similar result with 265 nm LEDs [4], and not long thereafter also achieved mW power from 250 nm LEDs, demonstrating our ability to produce high quality, high aluminum content AlGaN based devices, as well as successful device processing techniques applied to such difficult material. These devices were processed using the standard 300 μm × 300 μm mask set and flip chip bonded to the AlN submounts.

The I-V curve for the 265 nm LED, shown below in Figure 7(a), has a series resistance of 55 Ω with a turn-on voltage of approximately 6.5 V. The EL spectra, shown in Figure 7(b), demonstrate a strong dominant peak at 267 nm that increases approximately linearly with increasing injection current, as expected, while the secondary defect related peak saturates with increasing current.

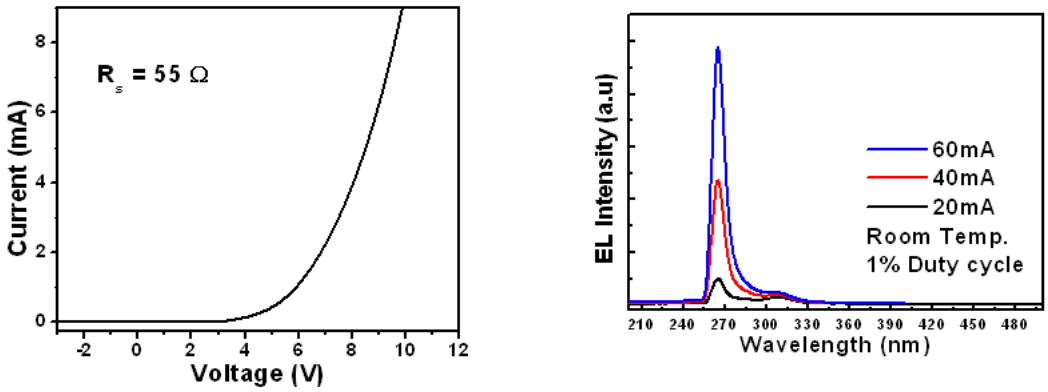

(a) **(b)**

Figure 7: (a) IV curve of a single 265 nm LED and (b) EL spectra at various currents showing a dominant peak at 265 nm [Error! Bookmark not defined.**].**

Figure 8(a) shows the pulsed P-I curves of a single 265 nm LED and an array of four 265 nm LEDs connected in parallel. Both curves have an initial slope efficiency of ~12.8 μW/mA, however the single diode rolls off to a slope efficiency of ~4.3 μW/mA while the array is able to maintain a higher 7.4 μW/mA at the same current range. This is attributed to current spreading over more devices, which alleviates the localized heating effects. Thus, the array is able to reach 5.3 mW at a current of 700 mA.

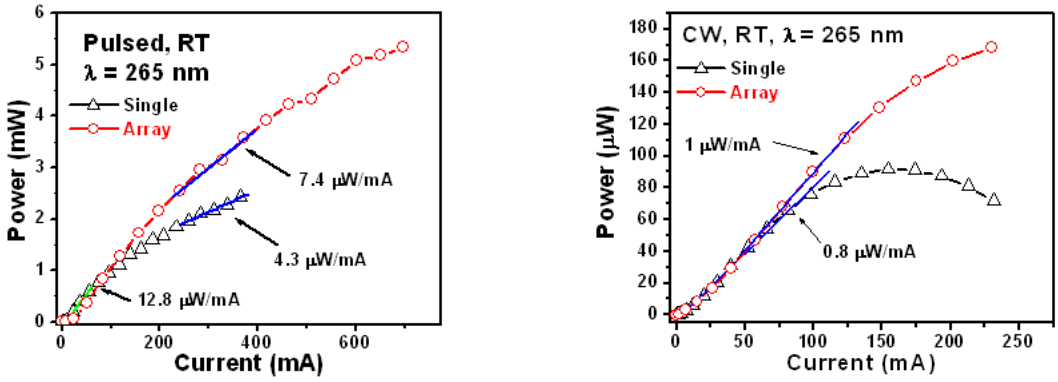

(a) **(b)**

Figure 8: (a) Pulsed P-I measurements of a single 265 nm diode and an array of four 265 nm diodes connected in series and (b) continuous wave measurements of a single 265 nm diode and an array of four 265 nm diodes connected in series.

Figure 8(b) shows a similar trend for the continuous wave measurements from both a sinigle 265 nm LED and an array of four 265 nm LEDs. Again, the array is able to avoid the thermal roll-over seen for

the single device, which is attributed to current crowding causing device heating, in order to achieve a power of 170 μW at a current of 230 mA.

Similarly, the I-V curve for a single 250 nm LED, shown below in Figure 9(a), demonstrates a series resistance of approximately 43 Ω, and a turn on voltage of ~10 V. The EL, shown in Figure 9(b), has a strong single peak at ~254 nm.

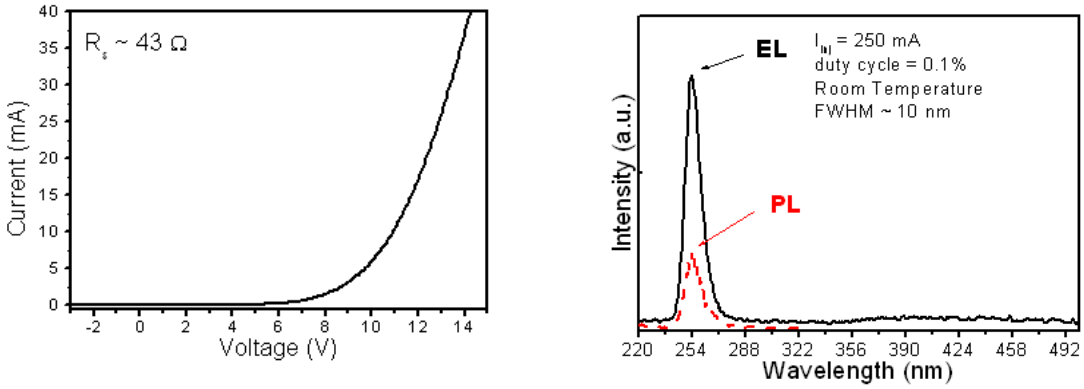

(a) **(b)**

Figure 9: (a) IV curve of a single 250 nm LED and (b) EL spectrum at an injection current of 250 mA of a single LED showing a single peak at 254 nm. The photoluminescence (PL) is shown for reference.

Figure 10 shows the P-I-V curves, measured under pulsed current operation (200 ns pulse at 2 kHz), for a single diode and an array of five diodes connected in parallel. It is clearly shown that the array has a much lower resistance than the single diode, as expected. The array clearly outperforms the single diode. This is again attributed to current spreading across the five diodes; due to the higher aluminum content and thus lower conductivity, current crowding becomes a much larger issue as the wavelength of the devices is lowered. Through connecting the devices in parallel, however, it was possible to achieve 3.2 mW at an injection current of 930 mA.

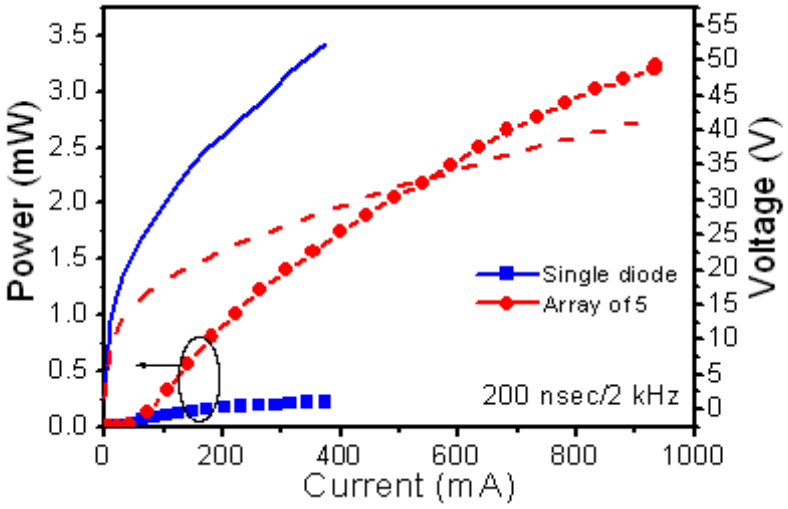

Figure 10: P-I-V curves of a single 250 nm LED and an array of five 250 nm LEDs connected in parallel.

Finger geometry / extended area UV LEDs

The finger geometry / extended area UV LEDs demonstrated an improvement in performance through effectively decreasing current crowding, as shown by the near field image. This was confirmed by the wall-plug efficiency curve measured under continuous-wave operation, shown in Figure 11.

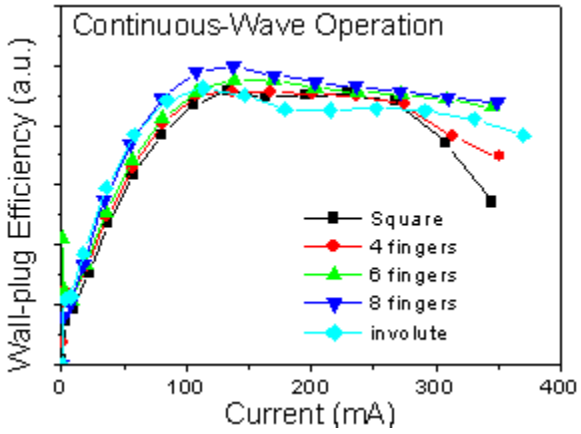

Figure 11: Wall-plug Efficiency under continuous-wave operation for the 300μm x 300 μm square mesa, the four-, six- and eight-finger mesas, and the involute geometry mesa.

In Figure 11, the square mesa and the four-finger mesa reach thermal roll-over at about 300 mA, after which the four-finger mesa slightly outperforms the square mesa. This was expected since the four n-type contact fingers should slightly reduce the current crowding by increasing the perimeter and thus the area that the current will flow through as compared the square geometry. The six- and eight-finger

geometry and the involute geometry mesas do not reach a definitive thermal roll-over point, with the eight-finger geometry outperforming the six-finger geometry, again due to better current spreading with an increase in the number of n-type contact fingers, and therefore for an increased perimeter and current area.

Micro-LEDs

Preliminary microLED results indicating successful device improvements due to the RAE method have been achieved. Due to an inconsistency within the processing procedure, described below, the devices did not perform perfectly, however they do show a significant difference between the samples that cracked and the samples that were effectively crack-free.

Three pieces of the same sample were patterned for re-growth with the micro-LED mask set: a 12×12 piece, an 8×8 piece, and a 4×4 piece. The etch depth was ~1 μm so that the etch depth would be larger than the thickness of the re-grown device structure in order to take advantage of the RAE method. The three samples were then thoroughly cleaned using the process. The rest of the LED device structure was then grown on these three samples along with an un-patterned piece, for comparison.

After growth, the four pieces were examined by optical microscope. The 4×4 sample had cracks on the mesas, which was not unexpected since the mesa dimensions were at threshold size according to our RAE experiments. The un-patterned piece was also cracked, as expected. The 8×8 sample was found to have very few cracks on the mesas, and the 12×12 sample was to found to have virtually no cracking on the mesas.

Micro-LEDs were then fabricated on the four samples following a similar procedure, in order to insulate the thick p-type bonding contact from the n-type material. The un-patterned device was processed with the 8×8 micro-LED mask set, for comparison. The SiO_2 insulating layer was not uniformly etched during the buffered oxide etch step, and therefore windows through which to make contact to the p-type thin contacts on top of the mesas were not uniformly opened.

After processing, I-V curves of the devices were measured. The I-V curves revealed that the re-grown, crack-free 12×12 and 8×8 samples tended to have a sharper (less leaky) device turn-on and a lower differential resistance while the cracked 4×4 sample had a sluggish (leaky) device turn-on and a higher differential resistance, as shown in Figure 12(a). When comparing the 8×8 re-grown sample to the 8×8 standard sample, the re-grown sample had a slightly lower turn-on voltage and lower resistance than the standard sample, as shown in Figure 12(b).

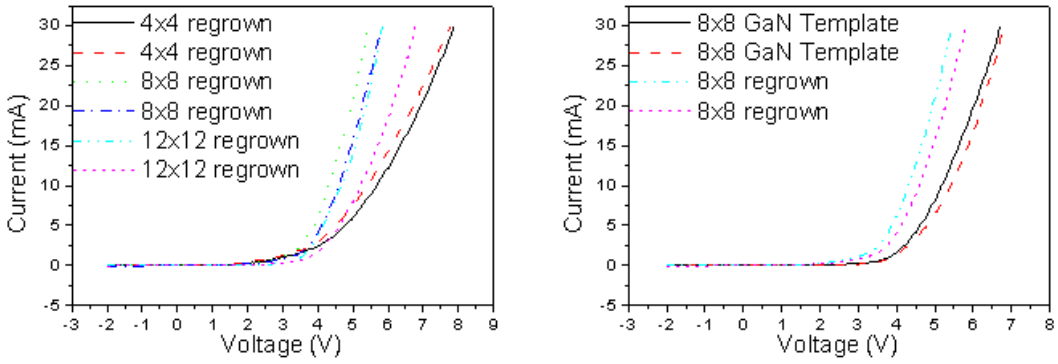

(a) **(b)**

Figure 12: Measured I-V curves for (a) the three re-grown samples, and (b) the re-grown 8×8 sample and the standard 8×8 sample.

Next, EL measurements were performed on the four samples. All displayed strong, single peak EL, however the peak wavelength tended to slightly shift between the samples, as displayed in Table 1.

Table 1: Peak wavelengths of the micro-LED samples	
Sample	***Peak Wavelength***
Standard (8×8 mask)	350.5 nm
4x4 re-grown	349.0 nm
8×8 re-grown	348.0 nm
12×12 re-grown	347.0 nm

This may possibly be attributed to the amount of strain induced in each situation. The amount of strain can roughly be correlated to the density of cracks present on the sample: the more cracks, the more strain relief, and thus the lower the strain. Similarly, the sample with the fewest cracks would have the highest strain. Therefore, the un-patterned standard sample, which appeared to have the highest crack density, would have the lowest strain, followed by the 4×4 re-grown sample and then the 8×8 re-grown sample, with the 12×12 re-grown sample having the highest strain. The more strain, the thinner the device layers would be, and therefore the quantum well would be slightly thinner, shifting the energy levels up and the wavelength down.

Next, pulsed P-I measurements were taken. It should be noted that since the SiO_2 windows did not open uniformly, 100% of the mesas generally do not light up for each device. Since the three device designs were meant to all have the same overall mesa area, so that only the individual mesa size is varied, this processing issue does somewhat affect the comparison of the four devices. However, care was taken to

perform P-I measurements on those devices with the highest percentage of mesas lighting up. These measurements, shown in Figure 13, show that the 8×8 and 12×12 re-grown samples outperform the 8×8 standard and 4×4 re-grown samples; they are able to reach higher powers at a similar current, as well as reach higher currents without device degradation. This first observation, crack-free samples achieving higher power at a similar current, may be attributed to a combination of the following three scenarios: current crowding effects due to variance in individual mesa size, total device mesa area not lighting up due to processing difficulties, or device performance degradation due to cracking. In the case of the 4×4 re-grown device, since there is a significant difference in mesa size, current crowding may play a significant factor. It was observed via optical microscope that the 8×8 and 12×12 individual mesas light up much more uniformly than the 4×4 individual mesas. However, since this trend is also seen between the re-grown 8×8 sample and the 8×8 standard sample, it most likely also is partially due to cracking. The second observation, crack-free samples able to reach higher currents without device degradation, clearly demonstrates that the two samples with few to no cracks were able to outperform the samples with cracking since this observation is independent of output power; the RAE method was effective in improving device performance.

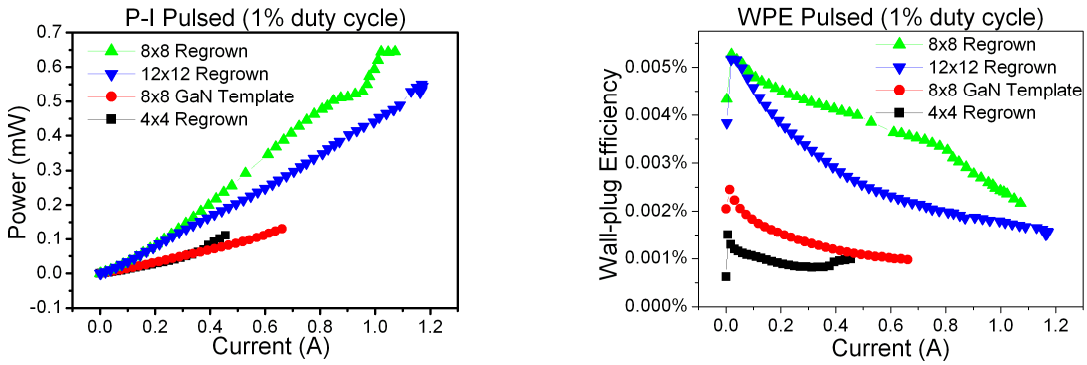

(a) **(b)**

Figure 13: (a) Pulsed P-I curves for the four samples and (b) corresponding WPE curves.

Figure 13(b), the wall-plug efficiency for the four samples, also confirms this result. The two samples with little to no cracking reach a much higher WPE value than the two samples with cracking. Figure 13(a) and (b) also show that the 8×8 re-grown sample outperformed the 12×12 re-grown sample. This may be due to the 8×8 re-grown LED lighting up more uniformly than the 12×12 re-grown sample, and therefore this result would need to be confirmed with an improved processing procedure.

A similar, yet less definite trend is shown by the CW P-I and corresponding WPE measurements, shown in Figure 14(a) and (b). At lower currents, the 8×8 re-grown sample and 12×12 re-grown sample outperform the 4×4 re-grown sample and the 8×8 standard sample. However all four samples reach thermal roll-over at approximately 200-225 mA, with the 8×8 standard sample eventually reaching a

higher power than the 12×12 re-grown sample. Again, this may be attributed to perhaps a slightly larger percentage of the total area lighting up, and therefore again, this result should be confirmed with a more reliable processing procedure.

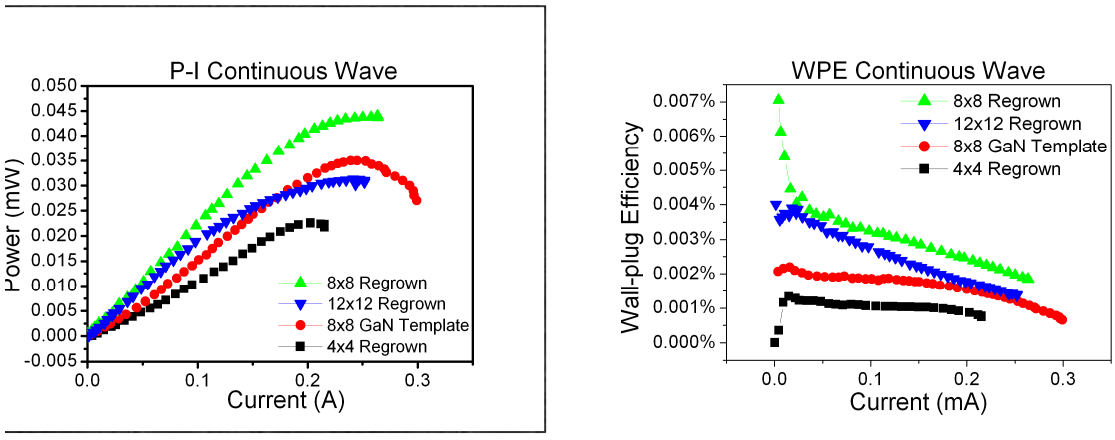

(a) **(b)**

Figure 14: (a) CW P-I curves for the four samples and (b) corresponding WPE curves.

Conclusion

Through an understanding into the processing procedures as they are applied to the III-nitride materials system combined with improvements to device geometry and packaging and the excellent material improvements made by my peers, many significant deep-UV emitter and detector technologies have been achieved. These include demonstration of first ever 280 nm LEDs, [2] demonstration of first ever RT milliwatt operation of 280 nm LEDs, [3] demonstration of first ever RT milliwatt operation of 265 nm LEDs, [4] and demonstration of RT milliwatt operation of sub-255 nm LEDs,

Section 2 Hybrid Ultraviolet Light Emitting Diodes

p-GaN / n-ZnO LED

In early 2005, we were able to demonstrate a hybrid p-GaN / n-ZnO device [5].

The device was processed using the circular LED mask The device was first annealed to activate the acceptors in the p-GaN at 1000°C in nitrogen ambient. Since ZnO is easily wet-etched by most acids, the photolithographically defined mesas were etched down to the p-GaN material via wet-etching with weak Acid solution. The photoresist was then removed and the sample was cleaned. The thin Ni/Au p-type contact was deposited using the ring contact mask for lift-off, followed by the standard anneal for the p-GaN contact. Next, a Ti/Au n-contact was deposited using the wire bonding contact mask, which was then annealed at 350°C in nitrogen ambient. Finally a thick Ti/Au contact was deposited directly over the thin p-contact for wire bonding purposes, again using the ring contact mask for lift-off. Since ZnO is slowly etched in developer solutions and even very slowly etched by DI water, special care was taken in order to avoid damage to the ZnO whenever possible by minimizing its exposure to harmful chemicals.

The results from this hybrid LED are shown below in Figure (a), (b), (c), and (d).

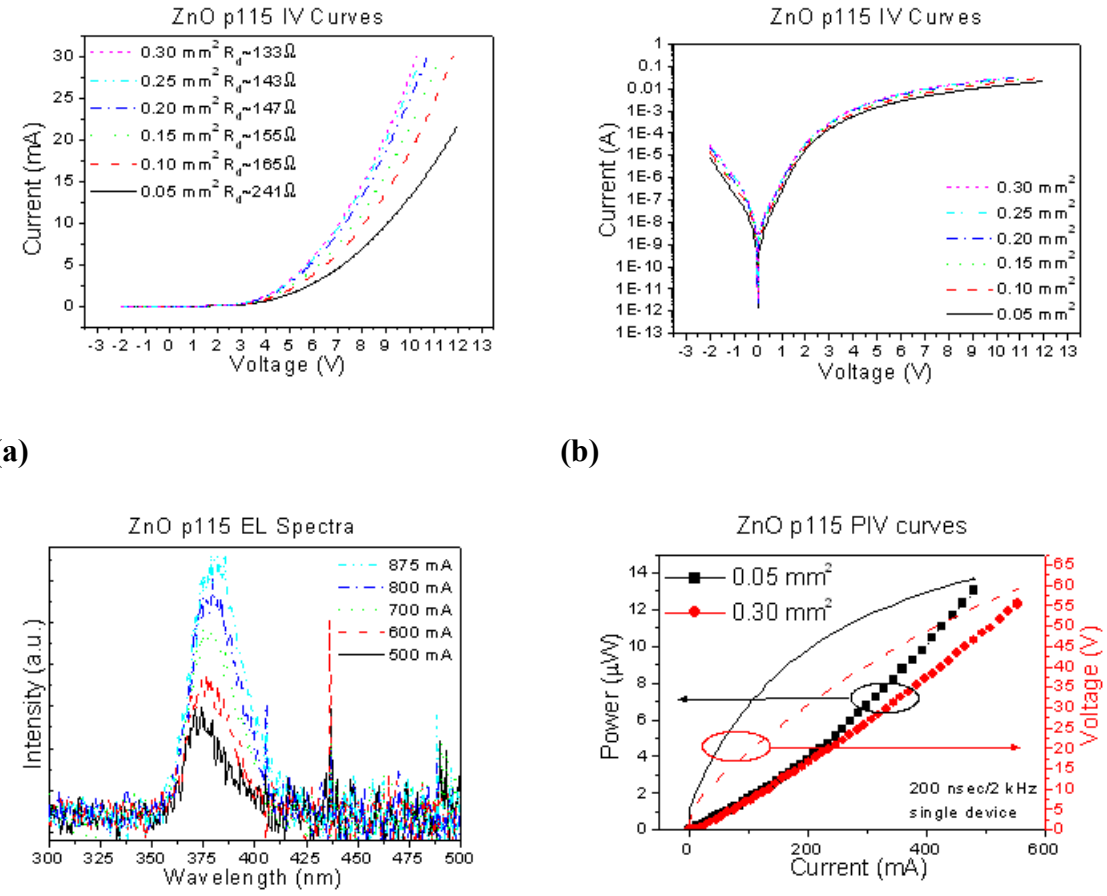

Figure 15: (a) linear I-V curve of various sized mesas, (b) semi-logarithmic I-V curve of various sized mesas, (c) EL spectra at various currents, and (d) P-I-V measurements of the smallest and largest mesa sizes.

The I-V curves demonstrate a fairly constant turn-on voltage of approximately 5 V independent of mesa size, as well as a decrease in differential resistance with an increase in size. The reverse leakage current shows a slight increase with an increase in size as expected due to the increase of both area (possible bulk leakage) and circumference (possible edge leakage). The reverse leakages range from -7.06 μA at -2 V for the smallest sized LED to -28.2 μA at -2 V for the largest sized LED, which are fairly high values as compared to our non-hybrid LEDs. The EL demonstrates emission at a peak wavelength of approximately 374 nm at 500 mA and redshifts slightly with increasing current, approximately linearly, to about 382 nm at an injection current of 875 mA, attributed to device heating. This peak wavelength agrees with the photoluminescence spectrum, which had a peak wavelength of ~375 nm, and is characteristic of near-band-edge emission from ZnO. The P-I-V demonstrates ~12 μW peak power emission from both the largest and the smallest sized devices, which indicates that there is a good lateral homogeneity of the layer / device properties.

ZnO:N / n-Si LED

In June 2007, we observed rectifying behavior and discrete luminescence from a ZnO on n-Si LED structure. The ZnO was grown on n-Si substrates using pulsed laser deposition with a KrF excimer laser, as described elsewhere [6]. p-type conduction was targeted using N as a dopant. Photoluminescence, Hall measurements, and ECV measurements were performed, however the results were inconclusive as to whether the material was definitively p-type, and therefore it was decided that device characterization would be used to further investigate.

After material characterization, the sample was annealed in order to activate the ZnO:N material. Mesas were then defined via photolithography and a wet etch in a dilute phosphoric and acetic acid solution [7]. A Pt / Ni / Au contact was then deposited and annealed in order to form an ohmic contact to the ZnO:N [8]. Finally, a Ti / Au contact was deposited on the n-Si as the n-type ohmic contact [9]. Prior to deposition, the n-Si surface was subjected to a brief buffered oxide etch in order to minimize the SiO_2 barrier between the semiconductor and the metallic contact. The cross section of the device structure is shown schematically in Figure 16.

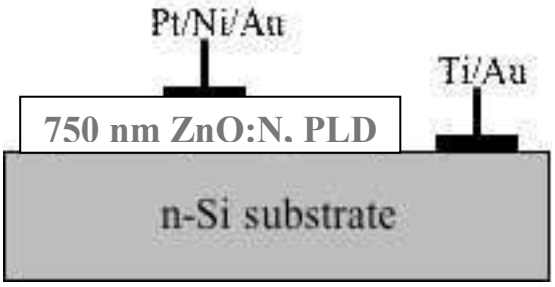

Figure 16: Cross-sectional schematic of the ZnO:N / n-Si heterojunction device structure.

Following device processing, electrical characterization of the devices was carried out. The inset of Figure 17 shows the I-V curve of the Pt / Ni / Au contact, demonstrating that a good ohmic contact is formed on the ZnO:N material. The linear I-V curve of a device with a mesa area of 0.15 mm2 is displayed in Figure 17, demonstrating rectifying behavior. A linear fit to the higher voltage regime of this curve allows for the calculation of a differential resistance of 99 W and a turn-on voltage of 3.36 V. This turn-on voltage corresponds to the ZnO band gap, suggesting a junction with electron injection into the ZnO. Through modeling of the I-V curve in the high current regime, a series resistance of 56 W was found. A linear fit to the low current regime of this I-V curve in log scale results in the determination of an ideality factor of $n = 2.34$ for this diode [3]. This value, which lies slightly outside of the expected range of $1 < n < 2$, indicates that an additional process is contributing to the conduction in the diode.

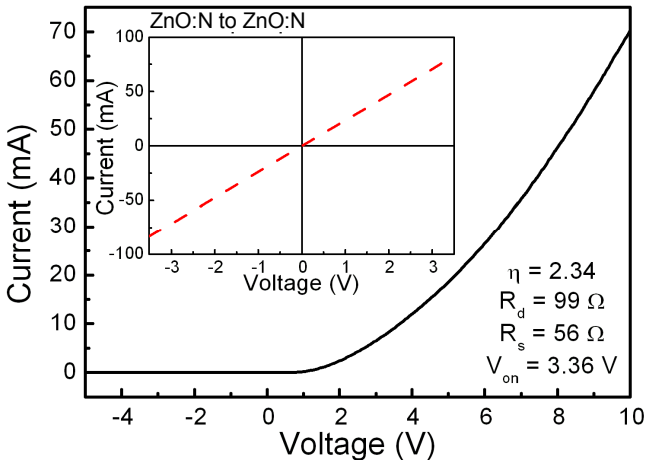

Figure 17: RT I-V characteristic for a 0.15 mm^2 mesa structure. Inset displays the I-V curve for a ZnO:N to ZnO:N metallic contact, demonstrating ohmic behavior.

The I-V curve of this same device in log scale is shown in Figure 18. This curve demonstrates relatively low reverse leakage, with a dark current density of 2.24 mA/cm^2 at -5 V.

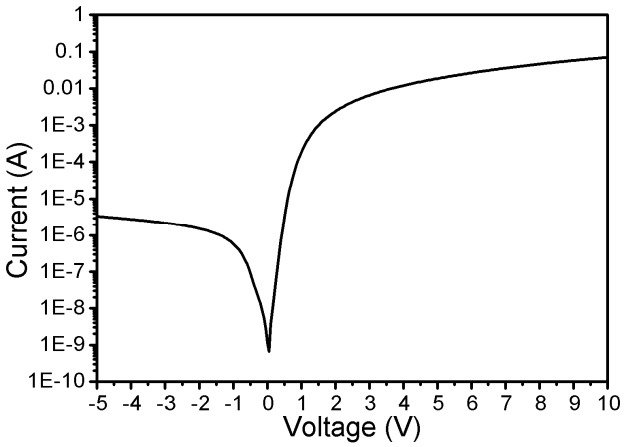

Figure 18: RT log (I-V) characteristic for a 0.15 mm^2 mesa structure.

For currents over 1mA, electroluminescence was observed with a main broadband emission centered at about 600 nm plus a small 380nm peak, which corresponds to the energy of ZnO near band edge. The relatively low injection current at which this luminescence appears indicates that the luminescence is not due to impact ionization. An image of the top view of a 0.05 mm^2 mesa under 0 V bias is shown in Figure 19(a), while Figure 19(b) is a picture of the same diode (in the dark) with an injection current of approximately 100 mA operated under DC bias. This image shows the electroluminescence of the mesa, with discrete spots which were visible to the naked eye. Experiments on similar samples grown in the absence of nitrogen showed no light emission.

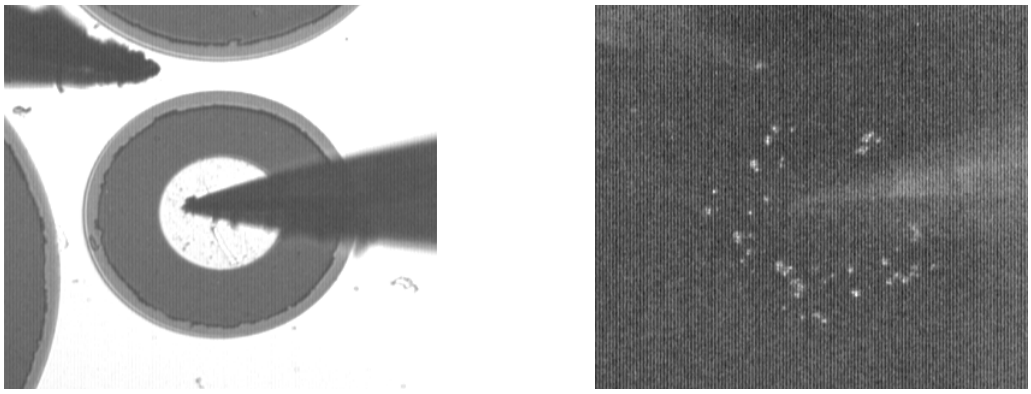

(a) **(b)**

Figure 19: (a) Image of the mesa while being probed for electrical characterization. (b) Image of the mesa operated under DC bias with a current injection of approximately 100 mA demonstrating electroluminescence from discrete spots within the mesa area.

Section 3 Comprehensive study of blue and green multi-quantum-well light emitting diodes grown on conventional and lateral epitaxial overgrowth GaN

Introduction

Solid state lighting (SSL) holds the promise of a more energy-efficient, longer-lasting, more compact, and lower maintenance substitute for today's incandescent and fluorescent light sources. Since lighting currently represents about 22% of all electricity consumption, the adoption of SSL could significantly reduce greenhouse gas emissions. [10] Light-emitting diodes (LEDs) based on $In_xGa_{1-x}N$ alloys, are currently the most promising candidates for realizing efficient SSL. InGaN is a direct wide bandgap semiconductor with an emission which can span the entire visible spectrum via compositional tuning. However, InGaN LED performance is highly wavelength-dependent. Indeed, ultra-bright and efficient blue InGaN-based LEDs are readily available [11] but the efficiency of InGaN-based green LEDs is still far from adequate for use in SSL. [10,11,12]

The lack of economical lattice-matched substrates for the growth of III-Nitrides necessitates the usage of GaN-mismatched silicon carbide (SiC) or sapphire (Al_2O_3) substrates, which leads to dislocation densities on the order of 108 cm-2. The high performance of blue LEDs in spite of these dislocations is attributed to indium segregation in the InGaN layers that produces nanometer-wide indium-rich regions that behave like quantum dots. [15,16] These quantum dots (QDs) localize the carriers, and prevent them from recombining non-radiatively at the dislocation sites. [17, 18] Difficulty in realizing high power green LEDs has three major parts (1) the limited solubility of indium in InGaN [19] imposes a restricted growth window for the green-emitting InGaN active layer, (2) InGaN with high indium content becomes unstable at elevated growth temperatures required for other layers in the device [20] leading to indium migrating out of the active layers, which reduces the LED spectral quality, [14], [21] (3) InGaN with high indium content generates dislocations leading to lower performance. [21]
Blue and green LEDs grown on conventional GaN have been compared in order to study the wavelength-dependent device performance. [22, 23, 24] Blue LEDs and laser diodes (LDs) grown on LEO GaN have also been studied in other works, showing superior performance to those grown on conventional GaN. [25,26] Devices on LEO GaN offer lower leakage current [25], [27], [28], higher stability, better thermal properties [26], and longer device lifetime. [29] Despite these advantages, there are no studies of green

active layers and LEDs on LEO GaN. In this work, we analyze blue and green active layers on conventional and high quality LEO GaN by X-ray diffraction (XRD), atomic force microscopy (AFM) and photoluminescence (PL). Then, we integrate them into LEDs, compare and correlate the material characteristics and device performance [30].

Experiment

Growth and Material Characterization

MQWs and LEDs were grown on double side polished *c*-plane sapphire substrate in an Aixtron 200/4-HT, horizontal flow, low pressure, metal organic chemical vapor deposition (MOCVD) reactor. Trimethlyaluminum (TMAl), Trimethylgallium (TMGa), and Trimethlyindium (TMIn) were the metalorganic cation precursors for Al, Ga, and In sources, respectively. Bis(cyclopentadienyl)magnesium (Cp_2Mg) and Silane (SiH_4) were used as the *p*- and *n*-type doping sources, respectively. Ammonia (NH_3) was used as the nitrogen anion source. Nitrogen was used as the carrier gas for growth of the MQWs to help increase indium incorporation whereas hydrogen was used during the rest of the layers.

Preparation of high quality LEO GaN

Growth began with desorption of the sapphire substrate at 1100ºC under H_2. Then, a thin low-temperature GaN buffer layer was grown, followed by 2 μm of GaN, grown at 1050ºC. In order to create a mask for lateral overgrowth, the wafer was removed from the reactor and 50 nm of silicon nitride (SiN) was deposited by plasma enhanced chemical vapor phase deposition (PECVD) [31] and patterned along the GaN $<1\bar{1}00>$ direction with openings of 2 μm and a period of 15 μm. This pattern direction exposes the A-planes $(11\bar{2}0)$ for lateral growth and is known to give fastest lateral growth rate and high quality wing regions.[32] For higher device performance, smaller fill factors (ratio of mask opening width to stripe period) are desired, which makes regrowth more challenging. [33] We have used a fill factor of 0.13 to have a larger wing area and to perform better analysis.

Etching of the opening in the SiN layer was performed by electron cyclotron resonance reactive ion etching (ECR-RIE) using an SF_6 based chemistry; we have observed that this ECR-RIE chemistry does not etch GaN appreciably, however, some surface damage is observed by scanning electron microscope (SEM). Some SiN residuals were observed on the GaN opening regions via AFM. However, when GaN regrowth tests were conducted in these opening regions, a smooth GaN surface was observed via SEM, showing that slight remaining SiN residues did not have a detrimental effect on the GaN regrowth. Proper trade-off must be made between etching time and surface damage, and amount of SiN residual atoms in the GaN opening in correlation with the regrowth characteristics.

After etching, samples were cleaned with trichloroethylene, acetone, methanol, and rinsed thoroughly. Then, samples were placed inside the reactor for our optimized five-step LEO GaN re-growth. A cross-sectional sketch of the LEO GaN steps is shown in Figure 20.

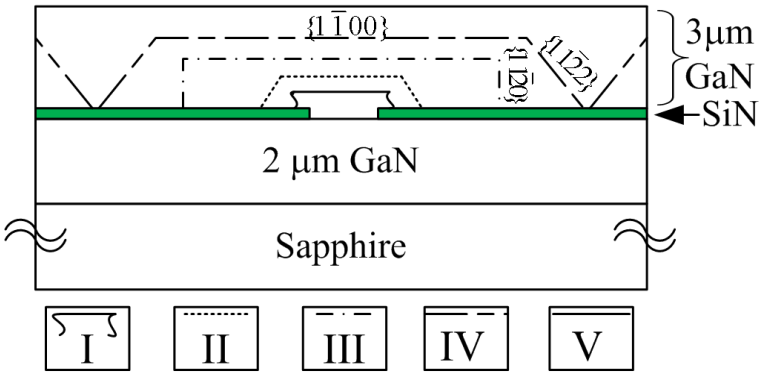

Figure 20: Schematic sketch of our optimized five-step LEO GaN growth process.

Step I is designed for high surface diffusion to minimize nucleation on the SiN mask and promote vertical growth on the GaN in the SiN openings in order to create an initial well-formed seed from which the vertical growth will progress. The vertical thickness should be around double the SiN layer thickness. Important growth parameters such as growth temperature, V/III ratio, effective lateral to vertical growth rate ratio, and growth time are given in Table 2.

Step II is similar to Step I except the growth conditions are adjusted to favor both lateral and vertical growth in order to obtain straight side walls. [34] Growth temperature is increased and V/III ratio is decreased, as given in Table 2. If Ga and N adatoms are too mobile, then they tend to align themselves exactly as the etching pattern. However, since the edges of the SiN mask are not perfectly straight lines, this step is needed to achieve better straight sidewalls. At the end of this step well formed inclined $\{11\bar{2}2\}$ facets are observed.

Step III is the lateral growth phase, during which the lateral to vertical (L/V) growth rate is enhanced by increasing the growth temperature.[32] Increasing effective lateral to vertical growth rate ratio (L/V) decreases the growth time required for coalescence, and helps bend the threading dislocations sideways.[31] During the first part of Step III the initially inclined $\{11\bar{2}2\}$ sidewalls begin to tilt, and are replaced with vertical $\{11\bar{2}0\}$ sidewalls (Figure 20). This change in the growth direction over the first three steps, from vertical to lateral, helps to bend the threading dislocations sideways so that they do not propagate to the surface.

Step IV is the coalescence step; after the distance between the side walls is close enough, the side wall slope is increased, as shown in Figure 20 in order to realize a void free coalescence front. This is achieved by decreasing the growth temperature sufficiently so that growth favors the formation of inclined $\{11\bar{2}2\}$ facets.[32] This inclination minimizes the voids and prevents the dislocations spreading at the coalescence front. Failure to control the lateral to vertical growth rate during coalescence results in the formation of voids and leads the LEO GaN surface to bend, both can be observed by SEM. During this phase, the lower temperature necessary to realize inclined planes results in less surface diffusion, and the lack of exposed SiN removes the supply of excess adatoms at the facet edge. [35] This results in a slow lateral growth rate, requiring a longer time for full coalescence.

Step V is similar to conventional GaN growth and promotes vertical growth. *n*-type doping is achieved by introducing SiH_4 during in this step, as LEDs will be grown on this template. Typically up to 0.6 μm is grown in this layer. The GaN vertical growth height at full coalescence is ~5 μm, small enough that wafer bending effects are minimal. [36]

LEO Step No:	T_{growth}(°C)	V/III Ratio	L/V Ratio	t_{growth} (mins)
I	1080	6000	1.1	4
II	1100	2930	2.4	60
III	1130	2930	2.6	60
IV	1100	2930	1.4	195
V	1040	2400	1.0	30

Table 2: Important growth parameters for LEO GaN (2 µm opening 15 µm period): LEO Step number, growth temperature (T_{growth}(°C)), V/III ratio, effective lateral to vertical growth rate ratio (L/V), and growth time (t_{growth}).

Table 2 summarizes the basic growth parameters for the above explained five-step LEO growth process (Figure 20) for an opening of 2 µm and period of 15 µm. It should be possible to reach high quality LEO GaN for different filling factors and periods, by employing the ideas described in each growth step.

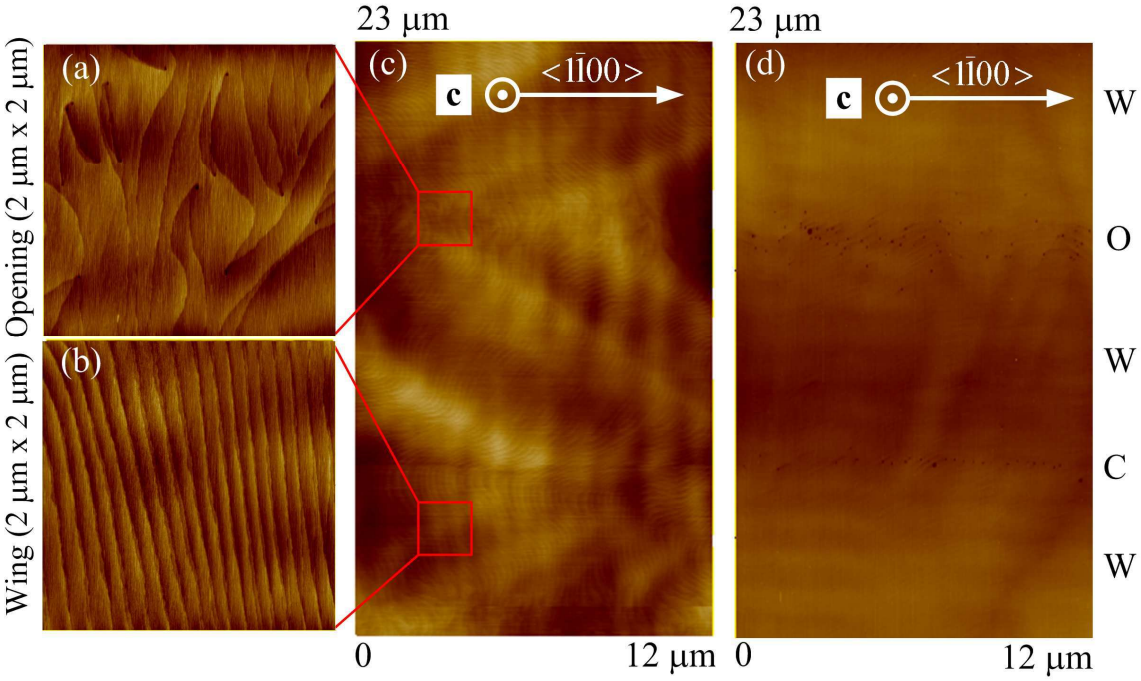

Figure 21. AFM images of coalesced LEO GaN. (a) opening (2 µm x 2 µm) and (b) wing (2 µm x 2 µm) have root mean square (RMS) roughness of 1.9 Å and 1.5 Å, respectively. (c) displays larger area (12 µm x 23 µm) AFM scan. (d) displays dislocations, revealed by hot phosphoric acid treatment, which are seen as dark spots. 'W', 'O' and 'C' corresponds to wing, opening and coalescence regions, respectively.

Figure 21 displays the AFM of the fully coalesced LEO GaN templates. The surface above the opening region (Figure 21(a)), is similar to that of conventional GaN, exhibiting chaotic atomic steps, the surface termination of which identify screw/mixed type threading dislocations.[34] Contrarily, the wing region

(Figure 21(b)), where lateral growth occurs, possesses well ordered parallel atomic steps with no atomic step terminations. The entire surface, including the coalescence region, where the neighboring atomic steps interfere, is observed in Figure 21(c). In order to study the dislocations, a hot (170ºC) phosphoric acid (85% H3PO4) treatment [27], [36] for 15 minutes was used. This etch-pit-density study reveals no discernable dislocations in the wing areas, whereas in the LEO GaN coalescence area, and opening region dislocation densities of (2±1) × 108 cm-2, and (9±2) × 108 cm-2 are observed, respectively (Figure 21(d)). For comparison, conventional GaN was observed to have a dislocation density of (9±1) × 108 cm-2. This phosphoric acid treatment is capable of distinguishing between edge and screw or mixed type dislocations.[27], [36] The bigger pits correspond to dislocations with screw component whereas smaller ones correspond to edge type dislocations. It is know that edge type dislocation may exist in the wing region as their bending is very sensitive to growth conditions. [28,37] The non-existence of any discernable dislocations on our wing regions show the quality of the five-step LEO GaN developed, and establish a baseline from which we can study the effect of dislocations on blue and green InGaN based LEDs. For LEO GaN, no GaN peak separation is observed (in Figure 22) which shows that there is no significant plane tilt [39], supporting our high quality growth scheme described.

After preparation of LEO templates as described above, blue and green MQWs and LEDs are grown simultaneously on these templates, and on conventional GaN for comparison purposes. Each quantum well was composed of 3.5-nm-thick InGaN with a 7.0-nm-thick GaN barrier. The thicknesses of the blue and green MQW layers are arranged to be the same in order to have a better comparison. Growth temperatures of the MQWs are adjusted to ensure blue and green luminescence from the InGaN QWs. These MQWs were capped with 550 nm thick *p*-GaN complete the LED structure.

Blue and green active layers on conventional and LEO GaN

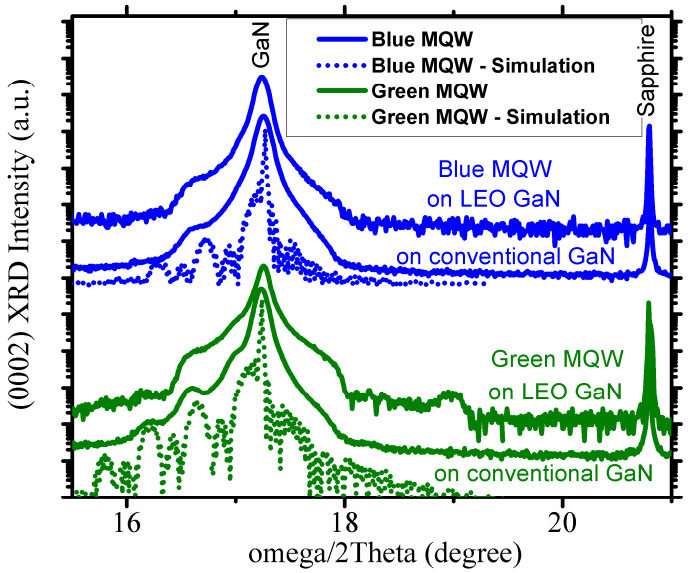

Figure 22. (0002) XRD omega/2Theta scan of blue and green MQWs on conventional and LEO GaN. The XRD simulation is realized to compare with experimental results.

Open detector X-ray diffraction (XRD) studies and XRD simulations are carried out to confirm the indium composition, and InGaN and GaN thicknesses of the active layer. Figure 22 displays the (0002) XRD (omega/2Theta) scan for blue and green three-MQWs on LEO and conventional GaN. The XRD

simulations of these MQWs are also plotted, and show good agreement with the experimental data. The InGaN and GaN thicknesses are determined as 3.5 and 7.0 nm, respectively. The indium content in the InGaN well is calculated to be 20% for blue MQWs and 28% for green MQWs. The 0^{th} order MQW peak is more distinctly observed in green MQWs due to higher average indium content in these structures.

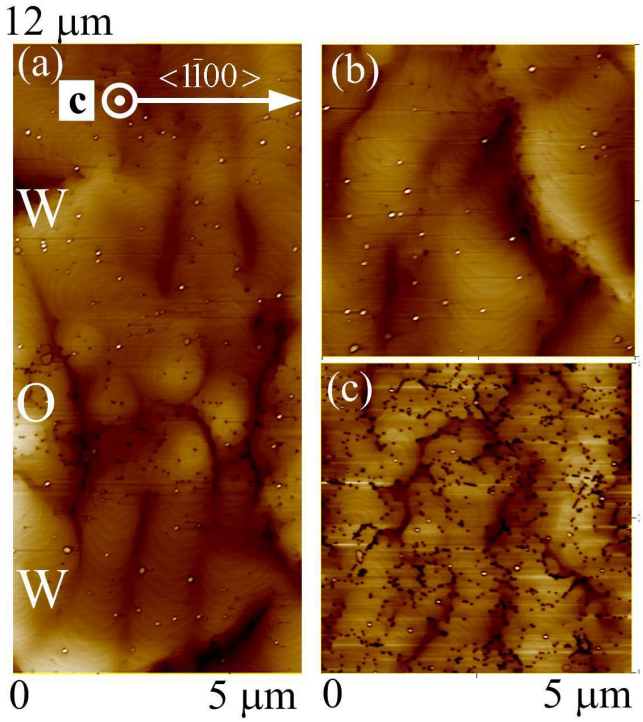

Figure 23. AFM images of blue MQWs on (a) LEO GaN (5 µm x 12 µm), (b) wing area of LEO GaN (5 µm x 5 µm), (c) conventional GaN (5 µm x 5 µm). 'W', and 'O' corresponds to the wing and opening regions, respectively.

Atomic force microscopy is used to study the surface morphology of the MQW active layers. Figure 23 shows the AFM images of the last barrier of blue MQWs on LEO and conventional GaN. Screw type threading dislocations are observed to be dominant on the opening (Figure 23(a)). Figure 23(b,c) show that active layer on wing area has much fewer dislocations and a much smoother surface than that on conventional GaN. This is directly related to the lower dislocation density in the wing area. Figure 24 shows the AFM images of green MQWs on LEO and conventional GaN. Screw type dislocations are still dominant in the opening region. Although less dislocations are observed on the wing than that on the conventional GaN (Figure 24 (b,c)), an island-like (2-D) growth is observed to be dominant across the LEO stripe, different from the blue active layer case (Figure 23). The lower deposition temperature necessary to realize a green active layer results in an island-like growth rather than a layer-by-layer growth as was observed for blue layer. In summary, the wing regions are observed to be smoother than opening regions.

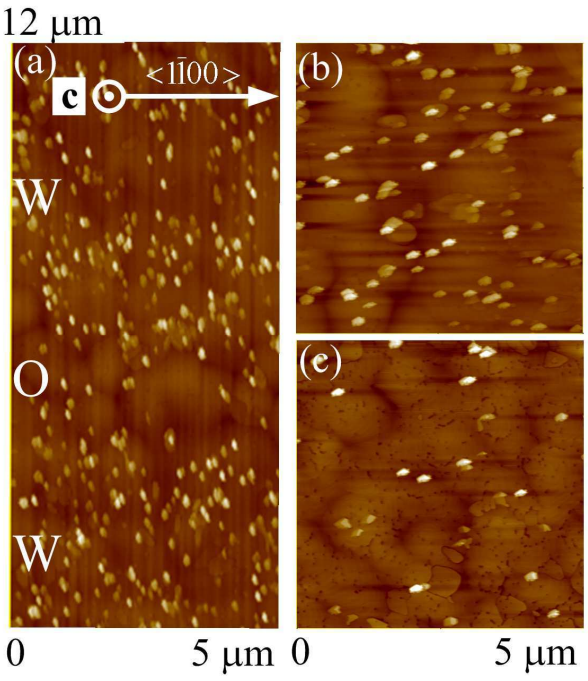

Figure 24. AFM images of green MQWs on (a) LEO GaN (5 µm x 12 µm), (b) wing area of LEO GaN (5 µm x 5 µm), (c) conventional GaN (5 µm x 5 µm). 'W', and 'O' corresponds to the wing and opening regions, respectively.

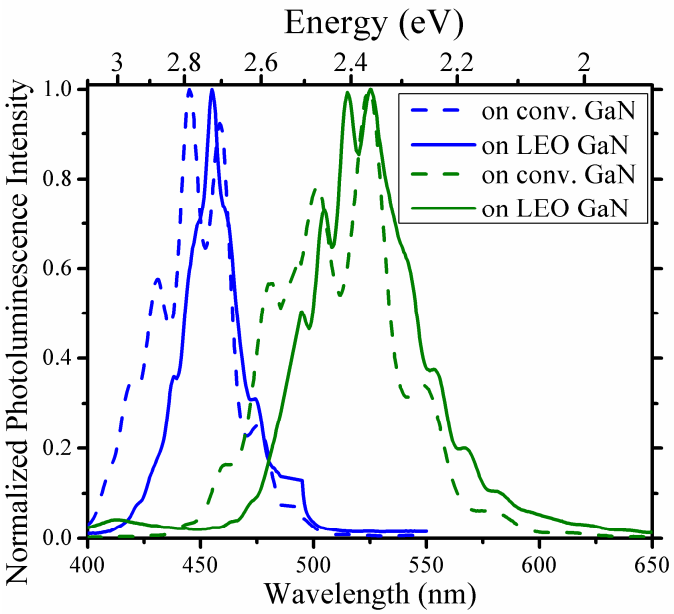

Figure 25. Room temperature PL of blue and green active layers.

Room-temperature (RT) photoluminescence of these blue and green emitting MQWs are shown in Figure 25. The PL wavelength of MQWs on LEO GaN is observed to be slightly higher than that of the same structure grown on conventional GaN. This could be due to increase in *c*-plane lattice constant of LEO

GaN [40], leading to a smaller compositional pulling effect [41], thus allowing slightly more indium into the InGaN.

Fabrication of blue and green LEDs

Blue and green active layers composed of seven-MQWs were grown as described above with the addition of a 550 nm thick *p*-GaN capping layer to complete the LED structure. Activation of the *p*-type GaN is achieved by rapid thermal annealing (RTA) at 1000ºC for 30 s in nitrogen ambient. After this the surface is treated with HCl:H_20 (1:1), 30Å Ni/ 30Å Au is deposited and annealed for 10 mins under air to achieve a transparent ohmic contact to *p*-GaN. ECR-RIE ($SiCl_4$:Ar based chemistry) is used to etch 300 μm x 300 μm mesas, thus, each LED mesa spans many opening, wing, and coalescence regions. Finally, 400Å Ti/1200Å Au is deposited as a thick *n*-type contact and to serve as a central bond pad on top of the thin transparent *p*-contact in order to complete the LED fabrication.

Device Results and Discussions

The blue and green LED on conventional GaN are hereinafter referred as "$B_{Conv.}$" and "$G_{Conv.}$" whereas those on LEO GaN as "B_{LEO}" and "G_{LEO}", respectively. Figure 26(a, b) show the I-V curves of blue and green LEDs on conventional and LEO GaN. A clear improvement in reverse-bias leakage characteristics is observed between samples B_{LEO} and $B_{Conv.}$ whereas no significant difference is observed between samples $G_{Conv.}$ and G_{LEO}.

Reverse bias characteristics of the LEDs are studied in detail. The majority of the leakage current is expected to flow through the LED, with only a small portion contributed by surface leakage. [42] The leakage current through nitride *p-i-n* devices is known to be dominated by hopping of charged carriers via localized defect-related states (traps) in the depletion region. [43,44] In the case of defect dominated reverse conduction, the reverse I-V characteristics of LEDs can be modeled as [27]

$$I = I_0 e^{qV/E_0} \qquad (1),$$

where V and E0 are the diode voltage and the energy parameter, respectively, with I0 being a pre-exponential factor. E0 represents the electrical activities of dislocations with a screw component, and is known to be dependent on the voltage at which the fitting is realized. [27], [42], [43] For electrical fields $E << (2kT/qa) \approx 5\times105$ V/cm (assuming a, the localization radius of the electron wave function, is 10 Å), thermionic emission over a barrier dominates the leakage current. [26] We have used the fitting at low voltage range ($1 < V < 5$). In this range, I0 and E0 are related to the density and to the electrical activities of dislocations with a screw component, respectively. [27], [41], [42], [43], [46] Using Eqn. (1) to fit the I-V curves, reverse bias parameters I0 and E0 are calculated, and given in Table 3.

Identifier	Device	I_0 (μA)	E_0 (eV)
$B_{Conv.}$	Blue LED on conventional GaN	7.86×10^{-6}	1.34
B_{LEO}	Blue LED on LEO GaN	3.17×10^{-10}	0.73
$G_{Conv.}$	Green LED on conventional GaN	2.01×10^{-6}	0.91
G_{LEO}	Green LED on LEO GaN	2.16×10^{-6}	0.80

Table 3: Important calculated/fitted LED parameters: leakage current pre-exponential factor (I_0), electrical activities of dislocations with a screw component factor (E_0).

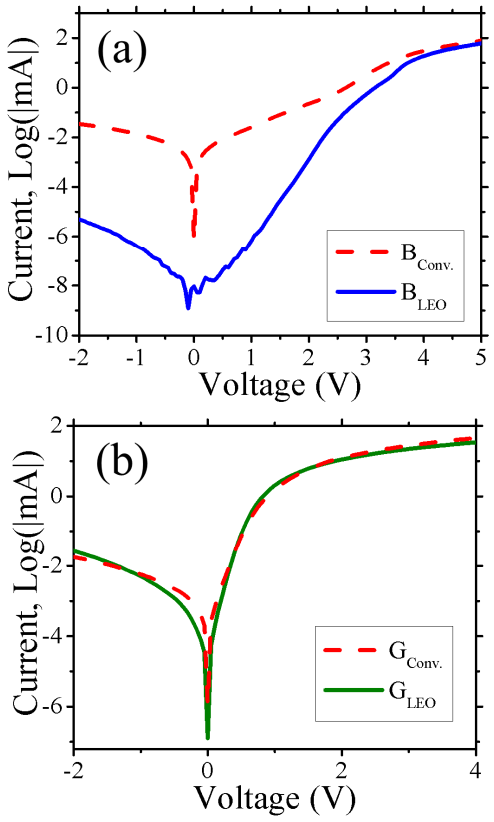

Figure 26. Current-Voltage curves (logarithmic scale) of blue and green LEDs on conventional ($B_{Conv.}$, $G_{Conv.}$) and LEO GaN (B_{LEO}, G_{LEO}).

I_0 is related to square of the density of dislocations with a screw component.[27] Comparing I0 values among the different samples in Table 3 suggests BLEO has approximately two orders of magnitude

lower dislocation density than BConv.. This agrees with the etch-pit-density study of the LEO GaN (Figure 21). For GConv. and GLEO, no significant difference in I0 is observed. As the same LEO GaN templates are used for BLEO and GLEO, the active layer used in samples GConv. and GLEO is the dominant dislocation generator leading to uniform dislocation distribution through the active layer. This helps explaining why we do not see a significant difference in I0 between samples BConv., GConv., and GLEO.

E_0 is very sensitive to the growth conditions [27] thus blue (BConv. and BLEO), and green (GConv. and GLEO) emitters should be considered separately. The lower value for sample BLEO compared to BConv. could be due to periodic alignment of the dislocations leading to a stronger voltage dependency of leakage current. A similar trend is observed between GLEO and GConv.; however, it is less pronounced, due to the generation of additional dislocations in the active layer creating an almost homogeneous dislocation density similar to conventional GaN (Figure 23, Figure 24). The higher active layer quality of sample BConv. compared to GConv. could be the reason for higher value of E0 leading to smaller dependency of leakage current on voltage.

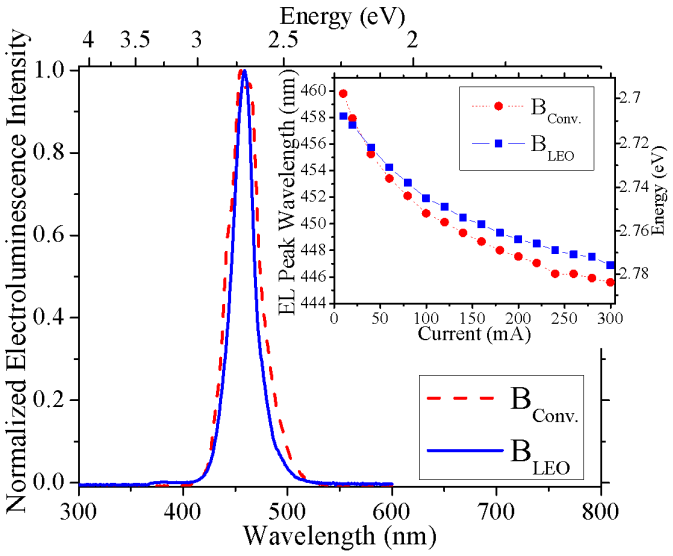

Figure 27. Electroluminescence spectra of blue LED on conventional ($B_{Conv.}$) and LEO GaN (B_{LEO}) under 20 mA current injection. Inset displays the peak wavelength at different current injections.

Electroluminescence (EL) spectra were acquired for the LEDs under pulsed current injection (duty cycle of 10% and frequency of 5 kHz) in order to help reduce heating effects under higher current injection (Figure 27, Figure 28). The minimal role heating was confirmed by measuring the peak intensity versus power and noting that, for the currents used in this study, no thermal roll-over was observed to occur. The EL spectra of blue LEDs are shown in Figure 27. The inset shows that both devices demonstrate a blue shift (from 465 to 446 nm) with increasing current. The decrease in wavelength with injection current is attributed to bandgap renormalization (due to free carrier screening of the piezoelectric (PE) field). At all but the lowest currents, BLEO has a slightly longer wavelength emission than BConv. (Figure 27 inset). In previous blue LED studies, a similar observation has been reported. [24] This observation is in agreement with the PL that was discussed in section II-(b). Device BLEO has a narrower EL spectra then BConv. (Figure 29). This suggests a more uniform indium distribution throughout the active layer. [17] Indeed, Figure 23 directly illustrates the more uniform surface of blue MQWs on LEO GaN, supporting the advantage of LEO templates.

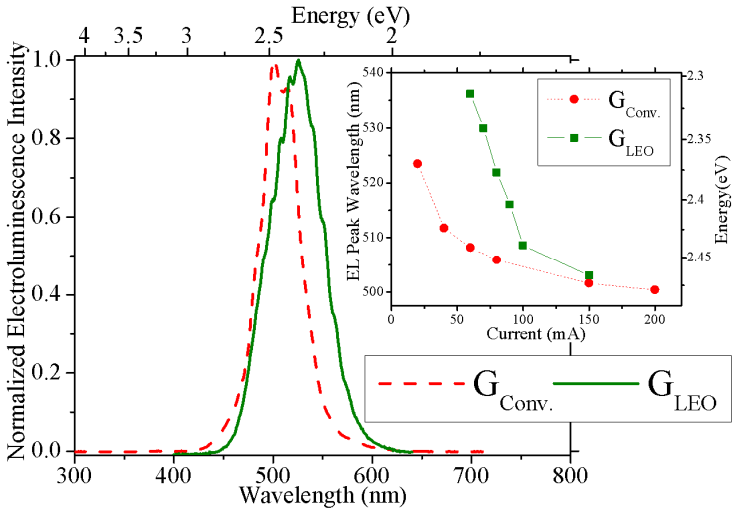

Figure 28. Electroluminescence spectra of green LED on conventional ($G_{Conv.}$) and LEO GaN (G_{LEO}) under 80 mA current injection. Inset displays the peak wavelength at different current injections.

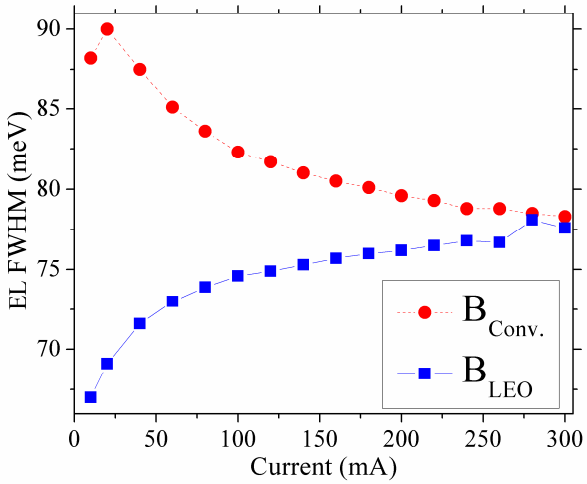

Figure 29. EL FWHM dependency on current for blue LED on conventional ($B_{Conv.}$) and LEO GaN (B_{LEO}).

In Figure 29, the EL FWHMs of the blue LEDs are plotted as a function of the injection current; the FWHM of device on conventional GaN can be seen to decrease with current, while the FWHM of the device on LEO GaN can be seen to increase. The EL FWHM broadening in B_{LEO} could be related to dislocation alignment in the LEO openings resulting in an electric field built up.

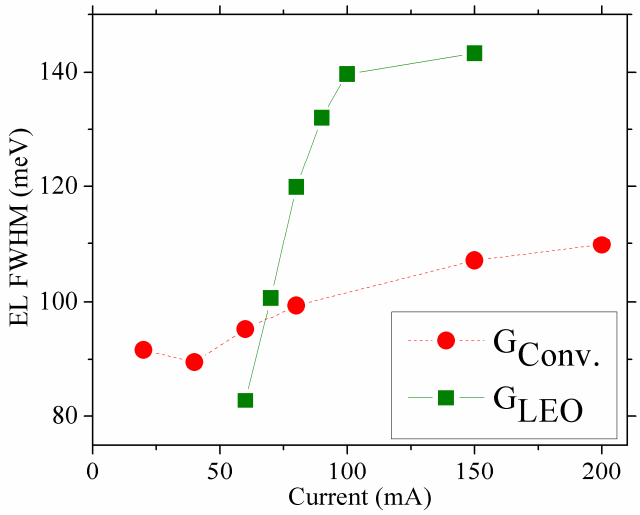

Figure 30. EL FWHM dependency on current for green LED on conventional ($G_{Conv.}$) and LEO GaN (G_{LEO}).

The EL spectra of the green LEDs are shown in Figure 28. Device G_{LEO} is observed to have longer peak wavelength than device $G_{Conv.}$ (Figure 28 inset). With increasing current, the EL FWHM increased for both devices (Figure 29); however, the EL peak-shift of sample G_{LEO} is larger than that of G_{LEO}, possibly due to the effects of piezoelectric fields. These piezoelectric fields may also be responsible for the broader EL FWHM observed in green LEDs. (This could be seen by comparing the ordinates of Figure 29, and Figure 30)

Comparing blue and green LEDs, a more pronounced EL peak shift is observed for green LEDs. This suggests stronger piezoelectric effects in the active layer. Piezoelectric effects are expected to be more pronounced in green MQWs due to the higher indium content of the layers. [24] The broader EL-FWHM of green LEDs than those of blue ones indicates a bigger indium fluctuation through the green active layer. [15] This is in agreement with the AFM measurements we have discussed in section II-(a)(Figure 23, Figure 24).

The radiant power of the various devices was measured as a function of injection current in continuous wave injection (not shown). Device BLEO achieved 2.6 times more power than BConv. whereas GLEO and GConv. had almost the same peak power independent of the template. In near field EL studies of device BLEO, we have observed a stronger luminescence originating from the wing regions compared to the opening regions. This luminescence difference should be related to the density of dislocations on the corresponding regions, demonstrating the role of dislocations as non-radiative recombination centers.[17] For GConv. and GLEO, we did not observe any difference between luminescence in the wing and opening regions. This supports our reverse bias analysis, and reinforces that the green LED performance is dominated primarily by the active layer quality. In summary, green MQW quality should be improved to reveal the benefits of GaN LEO templates in green LEDs.

Conclusion

A five-step LEO GaN growth technique for high quality LEO GaN growth is introduced. Blue and green

emitting active layers and LEDs on conventional GaN and five-step-grown LEO GaN templates are realized. AFM, XRD and PL are used to study the structural and optical properties of the active layers, and the effects of dislocations on blue and green active layers are identified. Significant differences in blue and green active layer surfaces are analyzed. The high quality LEO templates are observed to be important for smoother active layer surface morphologies. Blue and green LEDs on conventional GaN and high quality LEO GaN are studied. Green LEDs are observed to be leakier than blue ones, and no significant differences between green LEDs on conventional GaN and LEO GaN in terms of I-V behavior and peak power are observed. Green MQW quality is determined to be the bottleneck for high performance green emitters, not template dislocation density.

Section 4 Green Light Emitting Diodes

Introduction

We have performed room temperature photoluminescence (PL) studies on active layers with peak emission wavelengths of 406 nm, 424 nm, 448 nm, 481 nm, 501 nm, 517 nm, 542 nm, 560 nm, and 570 nm as seen in Figure 31(a). With increasing emission wavelength, a significant decrease in peak emission intensity as shown in Figure 31(b) is observed. In addition, the longer the emission wavelength the broader the emission spectrum becomes, as seen in Figure 31(c). The decrease in the intensity is related to dislocations generated due to the high indium content InGaN and GaN. The similar intensity decrease is observed even on our high quality LEO samples.

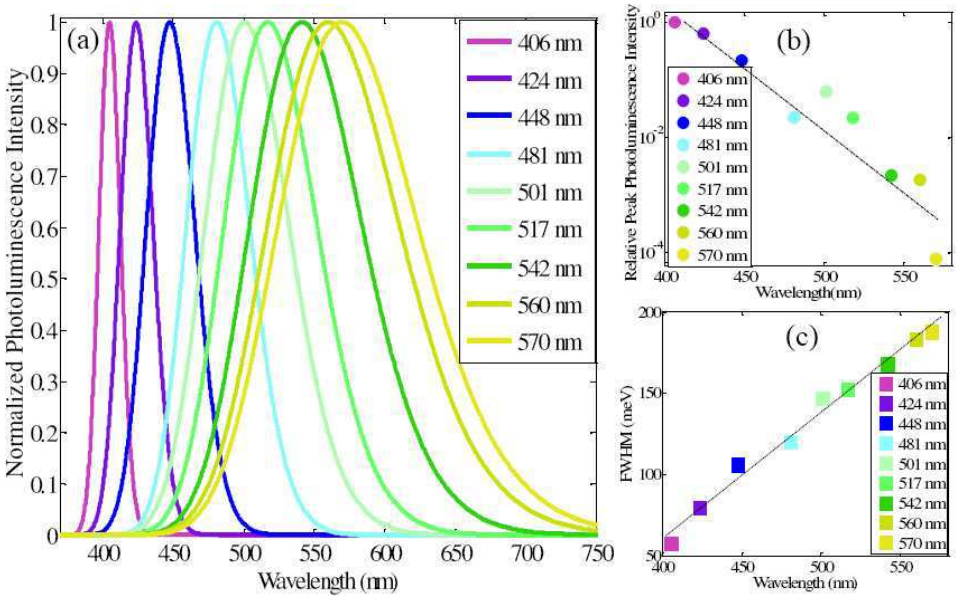

Figure 31. (a) Normalized Photoluminescence Intensity versus Wavelength at room temperature, (b) Relative Peak PL Intensity (logarithmic scale) versus Wavelength, (c) FWHM versus Wavelength

In order to improve the performance of longer wavelength devices we investigate a novel pulsed growth technique. Using pulsed growth can increase the mobility of the adatoms helping them to diffuse till they settle on the correct lattice site. Mobility could be increased by increasing temperature, decreasing the group III element amount, decreasing the pressure. However, increasing temperature and decreasing pressure results in much lower In content in the layers. We have decreased the total group-III amount as feasible as possible, to a growth rate value of 1.18 nm/min. To give the adatoms more mobility, we

developed a pulsed layer epitaxy method, without sacrificing emission wavelength, which improved the active layer significantly.

Experiment

The pulsed atomic layer epitaxy of InGaN is developed to increase the material quality through increasing the mobility of the adatoms. According to our research, a continuous supply of indium is used whereas gallium is pulsed as indium desorbs from the surface quickly and results a decrease in wavelength.

T_{In}	T_{Ga}	T_{Total}	No of Periods	AFM Roughness (1μmx1μm)
4	1	4	39	2.68 A
4	2	4	39	3.81 A
4	3	4	39	3.75 A
4	4	4	39	4.42 A
2	1	2	78	3.75 A

Table 4: Effect of pulsing time and period on the surface roughness.

In Table 4, the effect of the pulsing time of gallium and pulsing period time is summarized. The active layers are capped with 7 nm GaN. It is seen that with increasing Ga duration time, the surface roughness increases (Figure 32). In contrast, by decreasing the pulsing period a smoother surface is achieved, as shown in Figure 33.

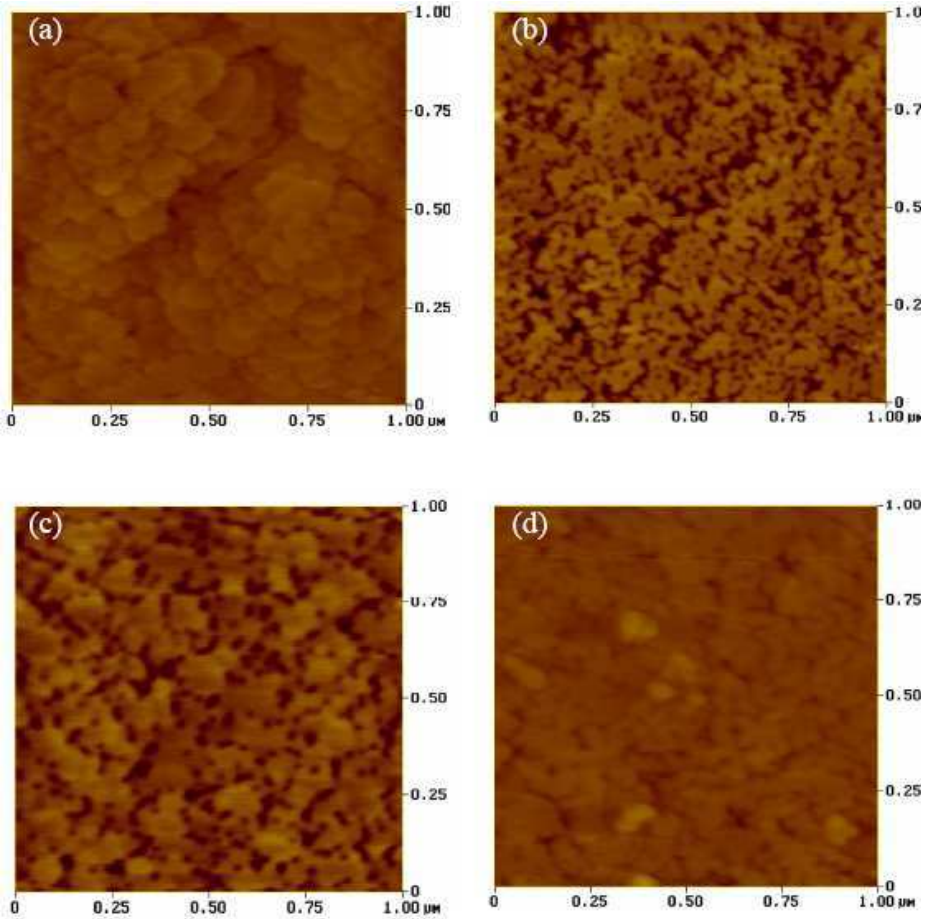

Figure 32. Effect of Ga pulsing time on surface morphology: (a) 1 sec, (b) 2 sec, (c) 3 sec, and (d) 4 sec.

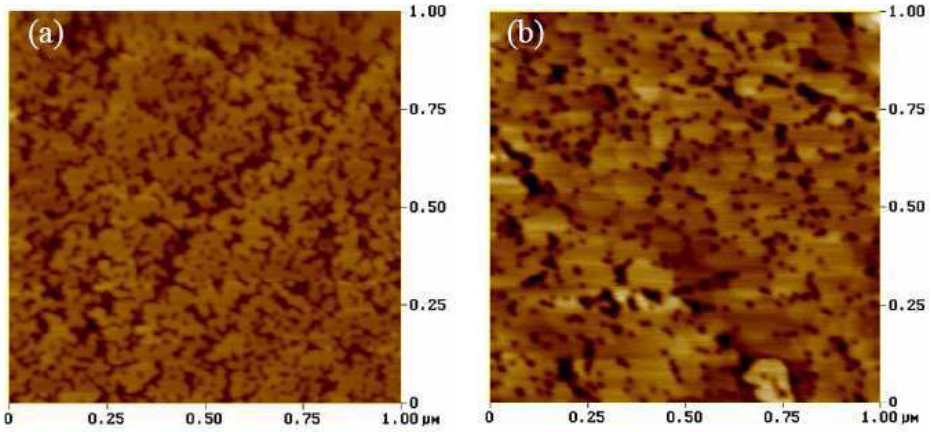

Figure 33. Effect of one period time on surface morphology: (a) 4 sec total, (b) 2 sec total.

During our research, we have observed that the amount of indium in the active layer is strongly effected by the surface on which active layer is grown. At the same growth temperature, on higher quality GaN,

InGaN has a lower indium composition. This also suggests that for multiquantum well growths, as the barrier material is grown at low temperatures and layer quality decrease, the indium content of the resulting active layers increase. This results in a broader emission, and if indium is clustered too much, the failure of light emission. We have resolved this problem by employing a temperature cycling in the active layer (Figure 34). To achieve a narrower emission, first a low temperature layer thick enough to keep indium inside at barrier growth temperature is grown. After this low temperature layer, higher temperature GaN is grown.

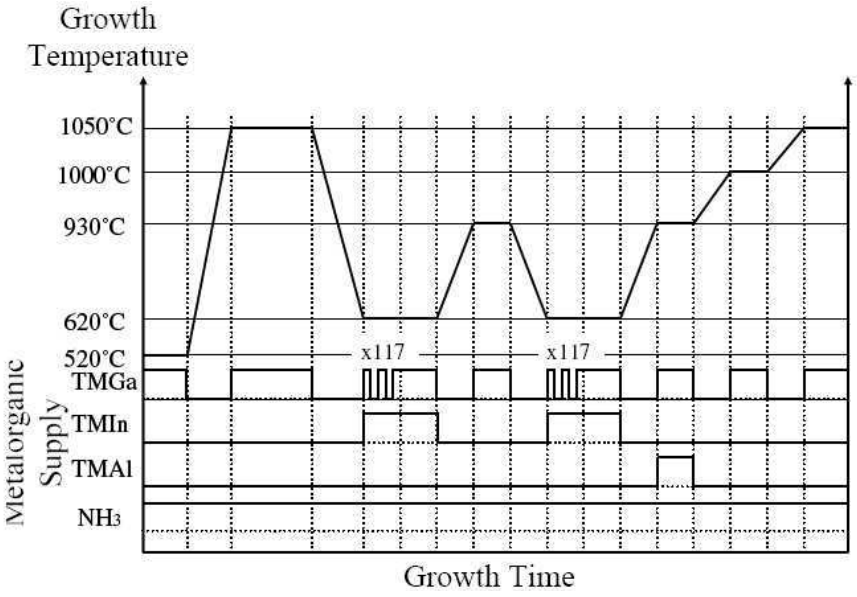

Figure 34. Growth Temperature and Metalorganic Supply throughout the LED growth

Once the LEDs are grown, activation of the p-type GaN is achieved by rapid thermal annealing (RTA) at 1000 °C for 30 seconds. After surface treatment with HCl:H_20 (1:1), 30 Å Ni / 30 Å Au is deposited as transparent contact and is annealed to achieve ohmic contact to p-type material. ECR-RIE system (using a $SiCl_2$ and Ar chemistry) is then used to etch 300 μm x 300 μm mesas. 400 Å Ti / 1200 Å Au is finaly deposited as the thick contact metal for both n- and p-type GaN.

Result and Discussion

The devices have a turn on voltage of 6.2 V with turn-on resistance ~90 Ω (Figure 35). The electroluminescence spectrum is shown in Figure 36.

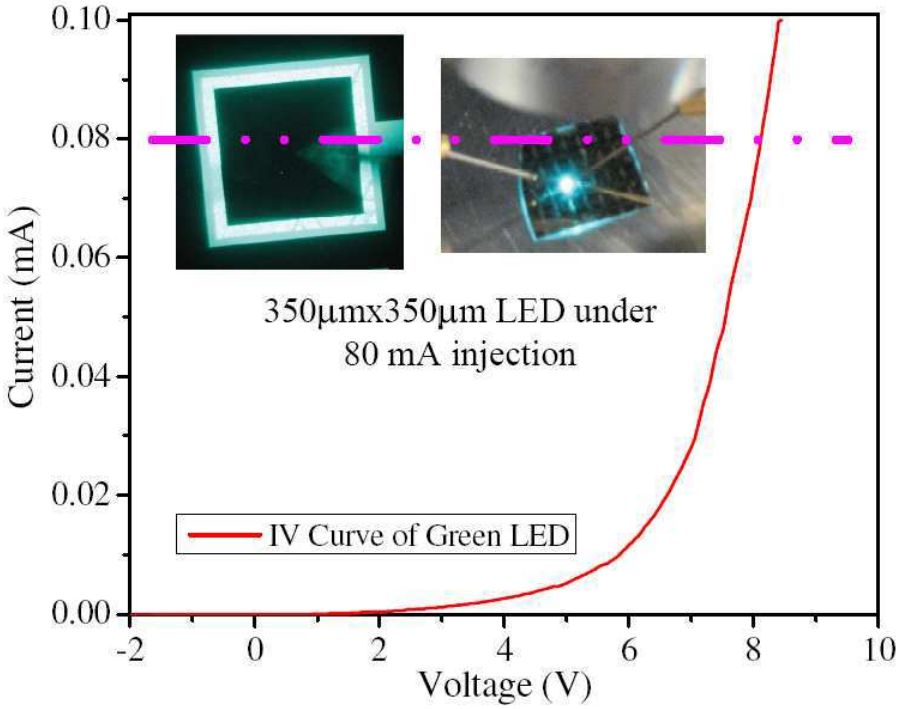

Figure 35. Current Voltage characteristics of a green LED. Inset pictures display a 300 μm × 300 μm LED under 80 mA current injection.

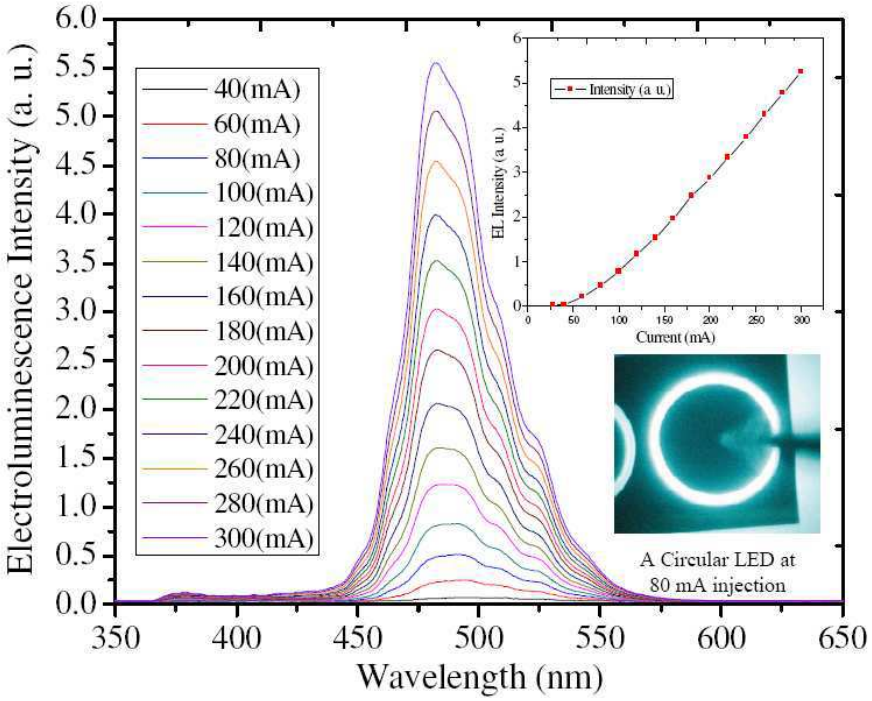

Figure 36. Current Dependent Electroluminescence of the Green LED. Inset displays the current dependence of the peak intensity.

Conclusion

The active layer quality is improved by using pulsed atomic layer epitaxy for InGaN. Thermal cycling in the active layer is developed to ensure uniformity and quality of the quantum wells. We have demonstrated green LEDs with emission wavelength 510 nm at 20 mA. A blue shift with injection current similar to blue LEDs are observed.

Future Work

In future work, we plan to integrate aluminum inside the barriers to help ensure higher indium contents in the well layers are preserved. This should also lead to a higher device performance due to better confinement. The drawback is the strain-related blue shift in the active layer emission. We will prepare high quality LEO GaN substrates to study the effect of these substrates on green light emitting diodes.

Section 5 Novel Hybrid Green LEDs Based on Substituting n-type ZnO for n-type GaN in an Inverted p-n Junction

Introduction

Solid state lighting (SSL) holds the promise of a more energy-efficient, longer-lasting, more compact, and lower maintenance substitute for today's incandescent and fluorescent light sources. Since lighting currently represents about 22% of all electricity consumption, the adoption of SSL could significantly reduce greenhouse gas emissions. [9] Light-emitting diodes (LEDs) based on the InGaN alloy, are currently the most promising candidates for realizing SSL. InGaN is a direct wide bandgap semiconductor with an emission which can span the entire visible spectrum via compositional tuning. InGaN LED performance remains wavelength-dependent, however. Indeed, ultra-bright and efficient blue InGaN-based LEDs are readily available [10] but the performance of InGaN-based green LEDs is still far from adequate for use in SSL.[11], [12]

The higher In content required in the active layers for green emission causes problems. Firstly, the limited solubility of In in GaN [18] imposes a restricted growth window for the green-emitting InGaN active layer. Secondly, InGaN with high In content becomes unstable at elevated substrate temperature (Ts). [19] Conventionally, a p-GaN layer is grown on top of an InGaN multi-quantum-well (MQW) active layer. The p-GaN layer is grown at significantly higher Ts than the InGaN MQW active layer in order to obtain high structural quality. This leads, however, to In leaking out of the active layers, which reduces the LED output. [12]Thus, it is important to combat In diffusion in order to obtain InGaN based green LEDs with superior performance.

ZnO is a wide bandgap material (Eg=3.3 eV) with a large exciton binding energy (60 meV). It has a low toxicity and the same wurtzite structure as GaN. The small in-plane lattice mismatch (~1.8%) with GaN makes ZnO a good candidate for integration in nitride devices.[4], [47] Recently, there have been many reports of ultraviolet emitters based on n-ZnO/p-GaN heterostructures. [3], [46], [47] In this work, ZnO is adopted as the n-layer in a new kind of hybrid green LED. [13]

In conventional GaN-based LEDs, the *p*-layer is deposited on top of the *n*-layer, because the *n*-layer can be grown with higher crystallographic and morphological quality than the *p*-layer. In this work, we

adopted an inverted LED structure employing an *n*-ZnO layer grown on top of (In)GaN MQW/*p*-GaN/AlN/Sapphire. Through the use of pulsed laser deposition (PLD), a high quality *n*-ZnO layer could be grown at significantly lower Ts than is typically required for GaN growth in metalorganic chemical vapor deposition (MOCVD). This approach could be beneficial, particularly for green light emitters, in which, the high In content InGaN active layers are adversely affected by the high Ts required for the GaN growth. Furthermore, the refractive index of ZnO at 500 nm is 2.0 compared with 2.5 for GaN. Thus, lower critical angle loss is expected for light extraction through ZnO-capped LEDs.

In this chapter, we explain the fabrication of these hybrid LEDs, and investigate the optical, structural, and electrical characteristics of the fabricated devices.

Experiment

The AlGaInN compounds were grown in an AIXTRON 200/4-HT horizontal flow, low pressure MOCVD reactor. Trimethlyaluminum (TMAl), Trimethylgallium (TMGa), Trimethlyindium (TMIn), and Bis(cyclopentadienyl)-magnesium (DCpMg) were the metalorganic cation precursors for Al, Ga, In, and Mg sources, respectively. Ammonia (NH_3) was used as the nitrogen source. Hydrogen was used as the carrier gas in the AlN and *p*-GaN layers.

First, a 600 nm-thick AlN layer was grown on the *c*-sapphire in order to improve the quality of the subsequent *p*-GaN layer. [49] Rapid thermal annealing was realized at 1000°C for 30 seconds in order to activate the Mg dopant. Then, a five period multi-quantum well structure was grown in a nitrogen ambient. Each period consisted of a 2-nm-thick InGaN quantum-well with a 4-nm-thick GaN barrier. An *n*-ZnO layer was grown on top of the (InGaN/GaN) MQW/*p*-GaN using PLD of a sintered ZnO target with a KrF (248nm) excimer laser. A ZnO layer was also simultaneously grown directly on *c*-sapphire as a reference for characterization studies.

Result and Discussion

First the structural, electrical and optical properties of hybrid LED layers were reported, and then the effects of solvents, annealing and etching on *n*-ZnO were shown. Thanks to these studies, integration of ZnO in (In)GaN based green LEDs was realized.

Structural characterization of the layers

Scanning Electron Microscopy (SEM) was performed in a Hitachi S4500 microscope equipped with an Oxford Energy Dispersive X-ray microanalysis (EDX) system and Atomic Force Microscopy (AFM) was conducted using a Veeco Dimension 3100 Scanning Probe system.

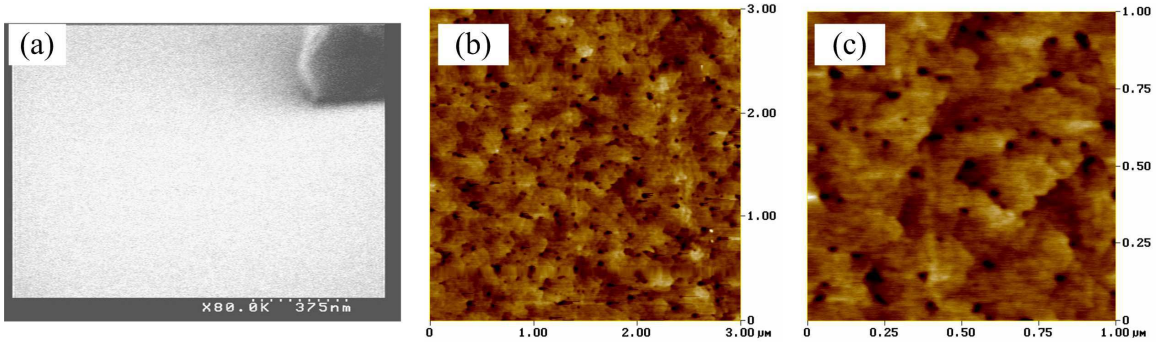

Figure 37. (a) SEM surface micrograph, (b) AFM scan (3 µm ×3 µm), (c) AFM scan (1 µm ×1 µm) of the surface of *n*-ZnO/Sapphire.

SEM images of the ZnO reference sample surface revealed a relatively featureless morphology (Figure 37 (a)), free of the particulates or droplets, which can be an issue with PLD growth. Tapping mode AFM gave root mean square (RMS) roughnesses of 5.6Å and 4.7 Å for (3 µm ×3 µm) and (1 µm ×1 µm) scans, which are shown in Figure 37 (b) and (c), respectively.

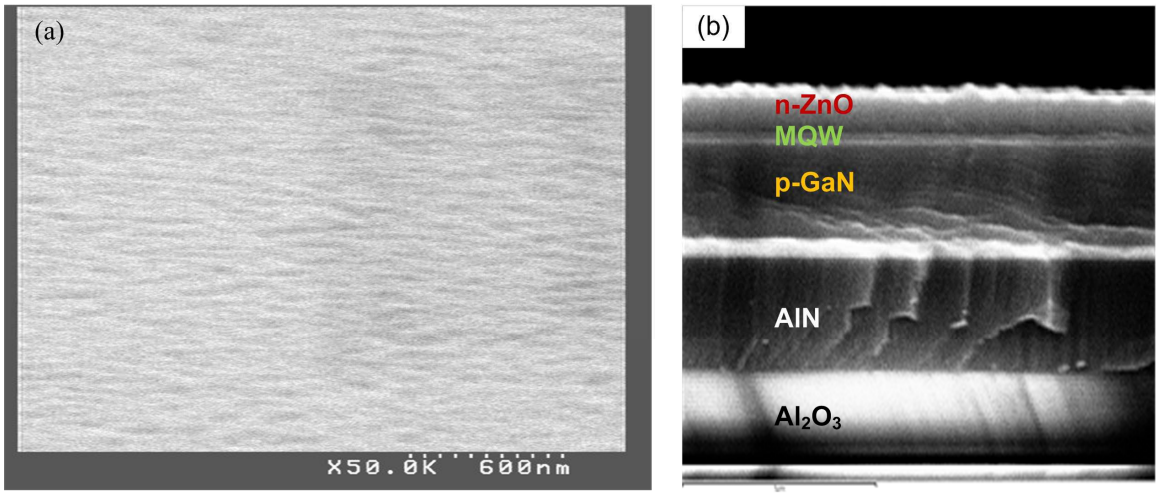

Figure 38. SEM micrographs of the hybrid LED: (a) Surface and (b) Cross-sectional view.

Figure 38 (a) shows an SEM micrograph of the top surface of the *n*-ZnO layer of the fabricated hybrid LED. The surface morphology appears slightly rougher than the as-grown *n*-ZnO on sapphire (Figure 37 (a)). Figure 38(b) shows an SEM fracture cross-sectional image. The *n*-ZnO / MQW/ *p*-GaN/ AlN/ Sapphire (Al_2O_3) LED layers can clearly be distinguished.

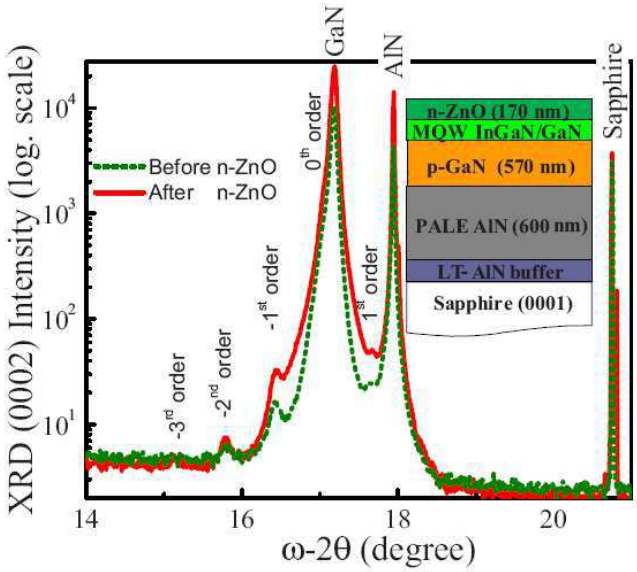

Figure 39. RT XRD ω/2θ scans for the (0002) peak before- and after- growth of *n*-ZnO on the (InGaN/GaN) MQW/*p*-GaN/AlN/Sapphire.

X-ray diffraction (XRD) studies were performed using a High Resolution Panalytical MPD-Pro system Diffractrometer. ω-2θ scans for the (0002) peak of the LED structure are shown in Figure 39. The ZnO and GaN peaks are indistinguishable, suggesting a good lattice match. The MQW-related, satellite peaks are similar before and after the ZnO growth. This indicates that the active layers maintained their compositional and structural integrity.

Electrical characterization of the layers

Room temperature Hall effect measurements were performed on the *n*-ZnO/Sapphire in Van der Pauw configuration (with a magnetic field strength of 0.3 T) with 400Å Ti/300Å Pt/1200Å Au contacts. The *n*-contacts proved ohmic and carrier concentration was determined to be 2.8×10^{19}cm^{-3} with a mobility of 10.0 cm^2/V·s, and a resistivity of 0.02Ω·cm. Similarly, hole carrier concentration for the *p*-GaN was determined to be 7.8×10^{17} cm^{-3} and 30Å Ni / 30Å Au transparent *p*-contacts were observed to be ohmic.

Optical characterization of the layers

Photoluminescence (PL) measurements were carried out at RT with a frequency-doubled argon-ion laser at 244 nm. Room temperature PL for the *n*-ZnO/sapphire reference sample revealed a single peak at 377 nm corresponding to the *n*-ZnO band-edge. The spectrum also had relatively low green signal, which implies that there is a relatively low defect/dislocation density in the sample. Laser power dependent measurements showed no significant peak shift or full-width-at-half-maximum (FWHM) broadening (Figure 40(a,b)). A linear increase in PL main peak intensity with increasing laser radiant power was observed. These results indicate high optical quality of the ZnO layer.

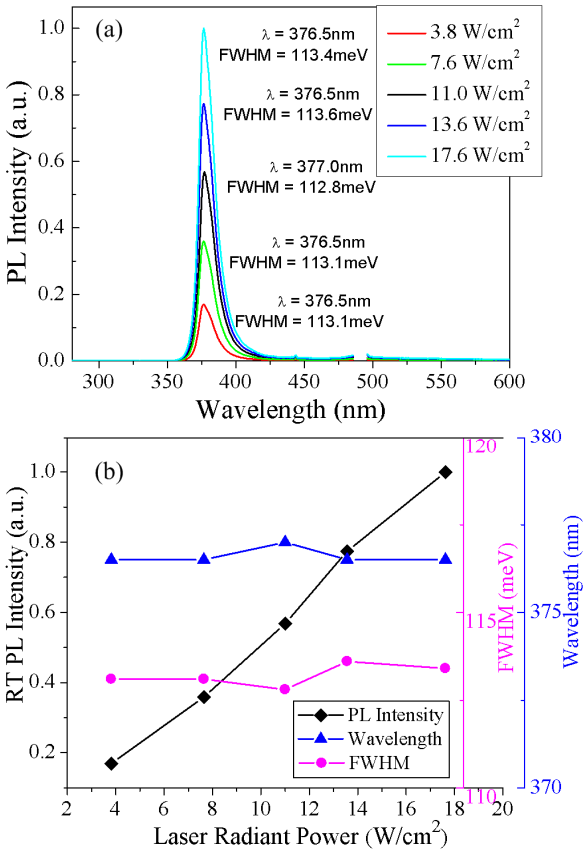

Figure 40. (a) RT PL spectra at different laser powers for *n*-ZnO/sapphire, (b) Peak PL intensity, PL FWHM and wavelength dependency on radiant laser power for *n*-ZnO/sapphire.

Normalized RT PL spectra for the hybrid device are shown in Figure 41. The spectrum for the *p*-GaN is dominated by a 426 nm Mg-related peak, which was attributed to defect-related deep level centers. [50] The PL spectrum, once the InGaN/GaN MQWs were grown on the *p*-GaN, shows a strong emission peaked at 496 nm without the 426 nm Mg-related peak. The PL spectrum for the completed hybrid LED structure (including the *n*-ZnO top layer) shows the strongest main emission peak, centered at 376 nm, corresponding to the ZnO band-edge and is similar to the PL observed for the ZnO/sapphire reference sample.

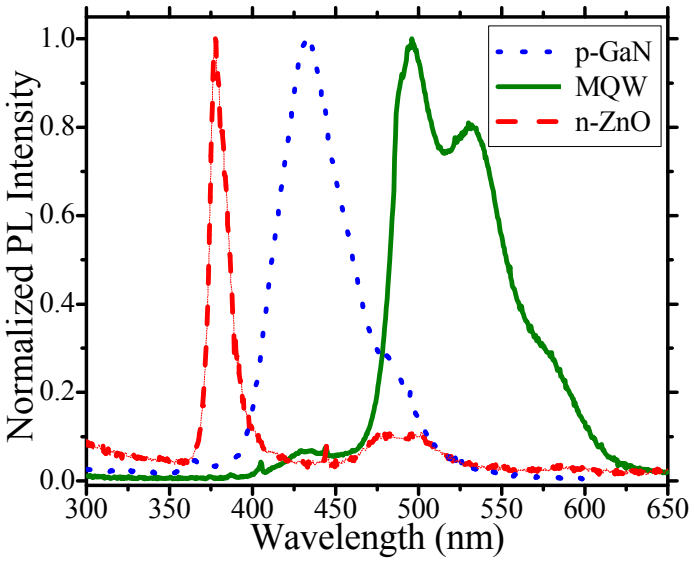

Figure 41. RT normalized PL spectra as consecutive *p*-GaN, InGaN/GaN MQW, and *n*-ZnO layers were grown on AlN/Sapphire.

Effects of common solvents on ZnO

The effect on ZnO of the common solvents used in the fabrication of the InGaN LEDs (deionized (DI) water, acetone, trichloroethylene (TCE), methanol and stripper) was studied. After each step, SEM was used to investigate any potential impact on the *n*-ZnO surface. Figure 42 displays SEM micrographs of the initial ZnO surface (a) and the surface after consecutive immersion in (b) DI water, (c) acetone, (d) TCE, (e) methanol, and (f) stripper. No significant degradation of the *n*-ZnO surface was observed after treatment with these solvents.

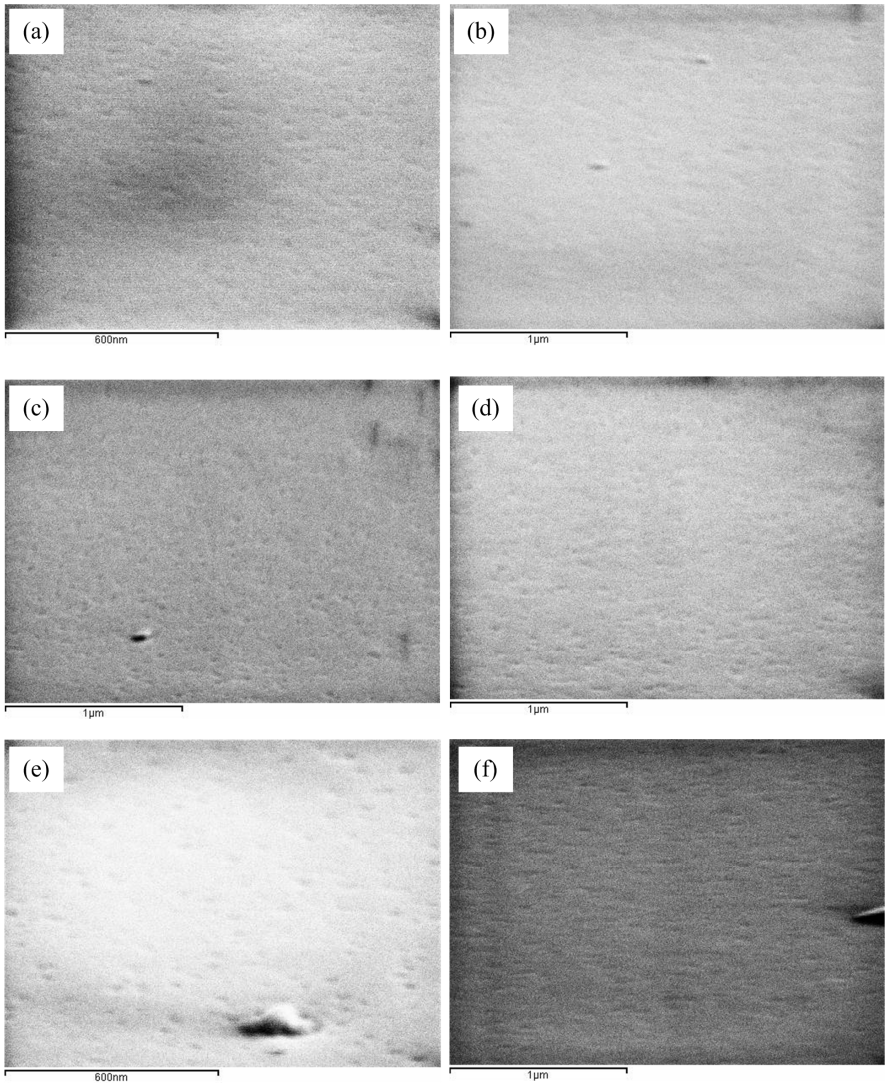

Figure 42. SEM micrographs of (a) the initial *n*-ZnO surface and after treated with (b) DI water, (c) acetone, (d) TCE, (e) methanol, and (f) stripper, consecutively.

Effect of annealing

Annealing is a crucial parameter in order to obtain low resistance ohmic contacts to *p*-GaN. Our studies established that 30Å Ni/ 30 Å Au contact to *p*-GaN was least resistive when annealed at 500ºC for 10 mins in air. Thus, an annealing test of the *n*-ZnO layer was realized under this condition. This annealing was determined to damage the *n*-ZnO surface. Thus, *p*-contacts were not annealed for these hybrid LEDs. Evaporated 30Å Ni / 30Å Au / 400Å Ti / 1200Å Au were found to be ohmic, however. Further studies are being carried on for optimization of annealing with regard to overall LED performance.

Etching study

Dry etching was preferred to wet-etching for consistency and for the realization of better side-wall profiles. A systematic study of dry etching (with a Plasmatherm electron cyclotron resonance reactive ion etching (ECR-RIE) system) was conducted. For the GaN, a ($SiCl_4$ + Ar) chemistry was adopted based on our prior studies. For the *n*-ZnO, (CH_4 + Ar) chemistry was employed, with Ar at 5 mTorr. A common

side-wall angle of ~70º was observed (Figure 43). The *n*-ZnO etch rate was determined to be 53 nm/min.

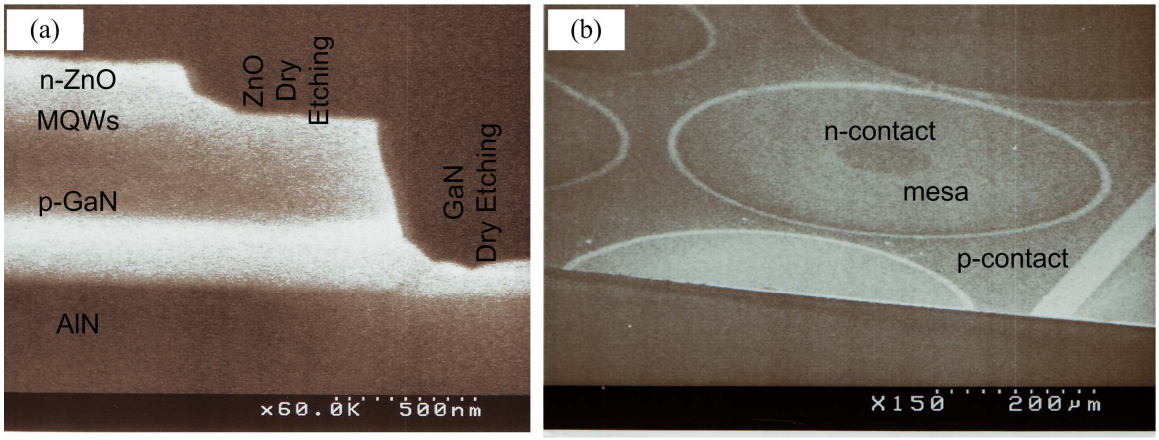

Figure 43. SEM micrographs of a fabricated hybrid LED (a) Side view, (b) Top (angled) view.

X-ray microanalysis gives information about the elemental composition of the specimen, in terms of both quantity and distribution. An etch-test EDX study shown in Figure 44 indicated that etched layers of *n*-ZnO had a lower Zn atom density than the as-grown layer. Al and O atom densities were also observed to be higher on the etched surface relative to those on the as-grown mesa area. Figure 44 (b,c) gives the normalized scale for the EDX count rates for Zn, Al and O atoms for the etched and as-grown layers showing the spatial distribution of elements.

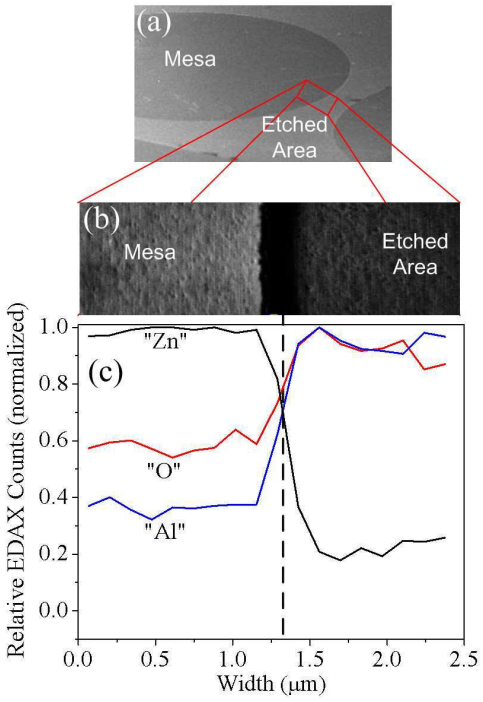

Figure 44. (a) Dry etching of *n*-ZnO on sapphire, (b,c) EDX system analysis shows the relative concentrations of O, Al and Zn atoms through 2.46 µm (from mesa through etched area). The EDX scale is normalized and relative.

Device performance

After optimization of the fabrication process, hybrid green LEDs were fabricated using optimized processing techniques. First of all, the samples were cleaned chemically. The cleaning steps included TCE, acetone, methanol treatment and rinsing. Circular LED mesas, with an area of 0.30 mm^2, were fabricated by masking the surface and dry etching right through the *n*-ZnO layer to a depth of 500 nm into the *p*-GaN.

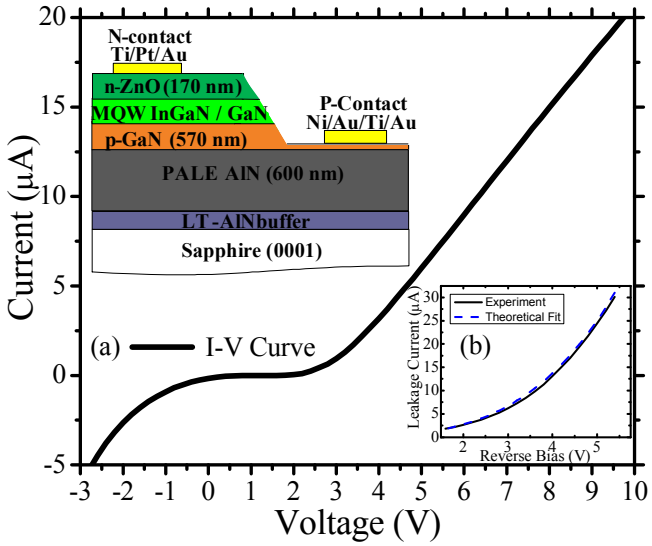

Figure 45. (a) I-V Curve of the fabricated LED. The device structure is illustrated in the inset. (b) Leakage current versus reverse bias voltage: Experimental and theoretical fit for the reverse-bias voltage range -1.6 to -5.4 V.

Figure 45(a) shows a typical I-V curve for a green emitting hybrid LED. The turn-on voltage is around 2.5 V, which is close to the bandgap energy observed in the PL spectrum (Figure 41). The on-series resistance (R_S) is calculated via a linear fit to the equation [51] $I\,dV/dI = R_S I + kT/e$ for $V >> kT/e$, and determined to be 4.75 MΩ. This relatively high value is most likely due to (1) high contact resistance because the metal contacts to the *p*-GaN were not annealed, and (2) the closeness (~70 nm) of the *p*-contact to GaN/AlN interface, which could lead to interface effects such as a 2-D electron gas or elevated dislocation densities corrupting the ohmic nature of the contact. R_S could be lowered through use of a lower *p*-GaN etch depth to increase the separation between the contact and GaN/AlN interface. The Ni/Au was not annealed to make a better ohmic contact with the *p*-GaN because the ZnO surface morphology was observed to be modified by annealing at 500ºC. Decreasing the *p*-GaN etch depth and annealing the *p*-contact could improve the forward-bias (FB) I-V characteristics. Under FB, green light was easily observed with the naked eye at RT under continuous-wave (CW) operation.

Reverse-bias characteristics are zoomed in Figure 45(b). As the p-GaN contact is close to the GaN/AlN interface, where there are many dislocations, a highly non-linear increase in leakage current with respect to reverse bias voltage was observed. The leakage current is known to be proportional to the square of the density of dislocations. [27] At high reverse bias, there is field-assisted thermal ionization of carriers from the defect-associated traps, which is known as Poole-Frenkel effect. Thus, the leakage current is expected to obey [41], [43]

$$I = I_0 \exp\left(\frac{\beta_{BF} E^{1/2}}{kT}\right), \qquad (2)$$

The average electric field (E) dependence on the reverse bias (V) was found from $E = (V + V_i)/w$, where V_i is the built-in junction voltage, and w is the depletion width. [52] Figure 44(b) plots the best fit of Eqn. 2 to our experimental data. From this fit, we obtain $\beta_{BF} = 7.6\times10^{-4}$ eV $V^{1/2}$ $cm^{1/2}$. This value is slightly higher than that for GaN (4.5×10^{-4} eV $V^{1/2}$ $cm^{1/2}$). For higher density of dislocations, β_{BF} tends to be bigger [52]. Since leakage current scales with the square of the density of dislocations, the effective density of dislocations was calculated to be 8.2×10^{-8} cm^{-2}. This theoretical fit shows that under reverse bias, hopping conduction is dominant in these hybrid LEDs similar to conventional *p-n* (In)GaN diodes. [53] Further optimization of the hybrid LED design and fabrication process are in progress.

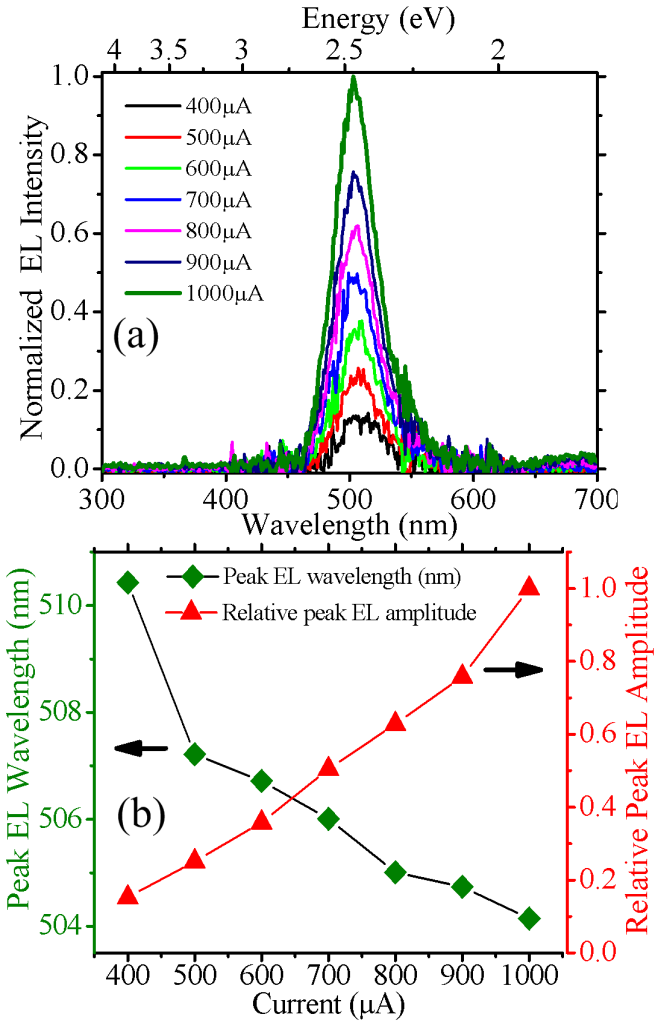

Figure 46. (a) Normalized electroluminescence (EL) intensity of the hybrid green LED at room temperature, (b) Peak EL wavelength and amplitude with respect to injection current.

Output power of the hybrid LED was measured utilizing a calibrated integrated sphere. Under forward

bias, green light was easily observed with the naked eye at RT under continuous-wave (CW) operation. Optical output power was on the order of μW. Electroluminescence spectra were acquired under pulsed operation (duty cycle of 10%, frequency = 5 kHz) in order to reduce heating effects under higher current injection. EL spectra (Figure 46) revealed an emission peaked in the green regime with a blueshift from 510 nm to 504 nm as the current increased from 400 μA to 1000 μA. The FWHM decreased simultaneously from 194 meV to 179 meV. These effects were attributed to free-carrier screening of the piezoelectric field, which led to bandgap renormalization. The spectral narrowing for the device demonstrated no band-filling effects, even for higher current injections, and thus indicated superior quality of the active layer [23]. This was consistent with the high compositional and structural integrity of the MQWs inferred from the XRD studies (Figure 39) and can be attributed to the lower Ts employed for PLD of the ZnO top n-layer. More device details can be found in refs.[13], [53].

Further optimization of the hybrid LED design and fabrication process are in progress, including improvement of electron and hole current spreading through adjustment of the *n*-ZnO and *p*-GaN layer thicknesses. *p*-GaN etch-depth is also under investigation, in order to inject holes more uniformly. Thicker green active layers are also being developed, which should give higher output in the green (since the ZnO growth temperature is lower than that for the InGaN, thicker InGaN layers should be more stable).

Conclusion

Novel hybrid green LEDs were developed. These devices employed an inverted *p*-*n* structure and the substitution of *n*-ZnO for the *n*-GaN layer. Conventional MOCVD growth was used for the *p*-GaN and MQWs. Lower temperature PLD was adopted for the ZnO growth in order to combat thermal degradation of the InGaN layers. High structural and optical quality of the ZnO, GaN and (In)GaN layers were confirmed using XRD and PL analyses, which suggested that the integrity of the MQW was maintained.

The effects of common solvents, etchants and annealing on *n*-ZnO were investigated. No significant degradation of the *n*-ZnO surface was observed after consecutive treatment with DI water, acetone, TCE, methanol, and stripper. Dry etching of *n*-ZnO with (CH_4 + Ar) chemistry was found to give good side-wall profiles for the device fabrication. Some minor degradation of the *n*-ZnO surface was observed after the 10-minute anneal at 500°C in air, which is commonly adopted for *p*-GaN transparent contact optimization. Evaporated 30Å Ni / 30Å Au / 400Å Ti / 1200Å Au and 400Å Ti / 300Å Pt / 1200Å Au contacts were found to give ohmic contacts to the *p*-GaN and *n*-ZnO, respectively, without annealing.

Under these processing conditions, a hybrid LED giving green EL between 510 and 504 nm, with a CW output on the order of μW, at RT was realized. Such an inverted hybrid structure approach could hold the prospect for the development of future green LEDs with superior performance.

Section 6 Stranski-Krastanov growth of InGaN quantum dots emitting in green spectra

Self-assembled InGaN quantum dots (QDs) were grown on GaN templates by metalorganic chemical vapor deposition. 2D–3D growth mode transition through Stranski–Krastanov mode was observed via atomic force microscopy. The critical thickness for $In_{0.67}Ga_{0.33}N$ QDs was determined to be four monolayers. The effects of growth temperature, deposition thickness, and V/III ratio on QD formation were examined. The capping of InGaN QDs with GaN was analyzed. Optimized InGaN quantum dots emitted in green spectra at room temperature.

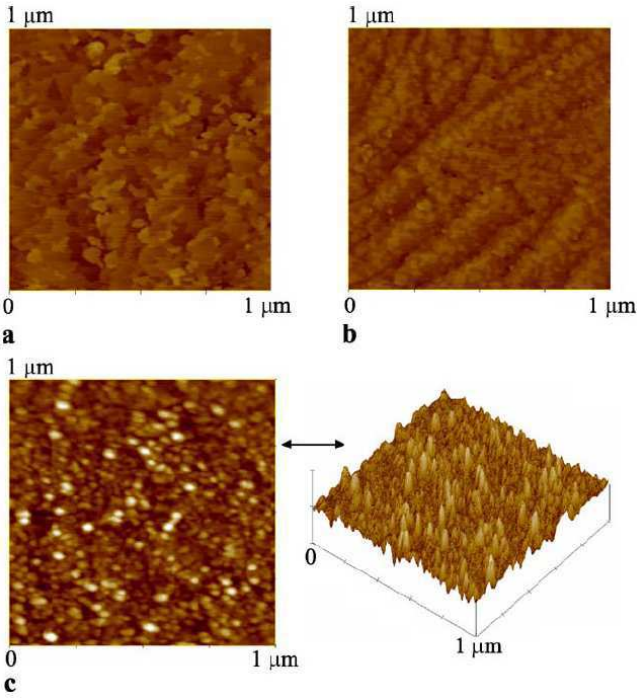

Figure 47. AFM (1 μm × 1 μm) images of 5.8 ML InGaN grown at (a) T = 734ºC, (b) T = 679ºC, and (c) T = 633ºC.

Introduction

Solid state lighting (SSL) holds the promise of a more energy-efficient, longer-lasting, more compact, and lower maintenance substitute for today's incandescent and fluorescent light sources. Since lighting currently represents about 22% of all electricity consumption, the adoption of SSL could significantly reduce greenhouse gas emissions. [9] Light-emitting diodes (LEDs) based on the InGaN alloy are currently the most promising candidates for realizing SSL. InGaN is a direct wide-band-gap semiconductor with an emission that can span the entire visible spectra via compositional tuning.

With increasing indium content (from violet to green emission) a significant decrease in performance is observed in light emitters based on quantum wells. [11], [13] One of the crucial reasons is that the large lattice mismatch between high indium content InGaN and GaN induces the generation of dislocations in the active region [11], [31], [55]. This explains how the performance decreases for high indium content light emitters, even on low-dislocated templates [29], [56]. The use of quantum dots may be one way to overcome these limitations in high-indium-content devices. Strain due to high indium content can be channeled into quantum dot (QD) formation which can decrease the overall strain otherwise which would form dislocations [57]. Besides, optoelectronic devices based on QDs have many advantages over those based on QWs, such as temperature stability and higher efficiency [58].

Room temperature blue emission from QDs was reported earlier [59,60]. The strong luminescence from these QDs was attributed to the exitonic transitions [61]. The blue QDs have been integrated into LEDs [62]. However, there are few studies of InGaN quantum dots in the green spectra [63]. In this work, we study the formation of high-indium-content InGaN

QDs, and study the effect of growth temperature, deposition thickness and V/III ratio on QD formation. We also report the stability of GaN capped InGaN QDs grown by Stranski–Krastanov (SK) mode.

Experiment

The samples are grown in an AIXTRON 200/4-HT horizontal flow, low-pressure metalorganic chemical vapor deposition (MOCVD) reactor. Trimethylgallium (TMGa) and trimethlyindium (TMIn) are the metalorganic cation precursors for Ga and In sources, respectively. Ammonia (NH_3) is used as the nitrogen source. All QD growths are realized under N_2 to facilitate the incorporation of indium.

The InGaN layers were grown on 2-µm-thick GaN on double side polished (DSP) (0001) sapphire (Al_2O_3) substrate. The growth rate was 11.8 Å⁄min and growth was interrupted for 15 s under ammonia before cool down. We studied the effect of temperature, deposition thickness, and V⁄III ratio on the formation and optical quality of the InGaN QDs.

Result and discussion

Atomic force microscopy (AFM) was used to study the QD formation. Figure 47 (a, b, c) displays the (1 µm × 1 µm) AFM images of 5.8 monolayer (ML) InGaN grown at 734°C,

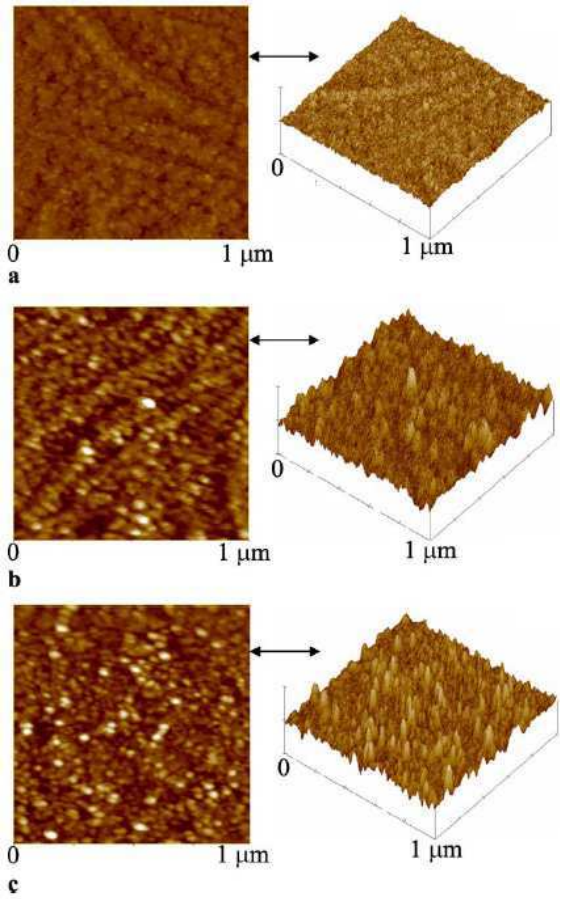

Figure 48. AFM (1 µm × 1 µm) images of (a) 2.9 ML, (b) 4.4 ML, and (c) 5.8 ML InGaN grown at T=633ºC.

679°C, and 633°C, respectively (1 ML ≈ 2.7 Å). At 734°C, as seen in Figure 47(a), only island like 2-D quantum disks (Q-disks) formed. Lowering the growth temperature (Ts) further resulted in smaller disks and surface roughening (Figure 47 (b)). This behavior was attributed to the decrease in adatom mobility and increase in the indium content of Q-disks. The adatom mobility decreased as a result of lowered Ts, and indium content increased due to higher indium thermodynamic equilibrium at low temperatures.

Effecting both the thermodynamic (indium content in InGaN) and kinetic (mobility) equilibrium on the surface, temperature is observed to be the most crucial parameter of high-quality QD growths. We have determined 633°C to be a proper growth temperature for green emitting InGaN QDs.

Figure 48 (a, b, c) displays the (1 μm×1 μm) AFM images of 2.9-, 4.4-, and 5.8-ML-thick InGaN grown at 633°C, respectively. At this Ts, critical thickness for QD formation is determined to be ~4.0 ML. Below the critical thickness, no QDs are observed (and the surface is similar to Figure 48 (a)). Above critical thickness, increasing the deposited InGaN results in increase in the density of the QDs in the expense of uniformity (Figure 48(b, c)).

The effect of V/III ratio on the surface morphology is studied. Figure 49 displays the AFM root-mean-square (RMS) roughness (1 μm × 1 μm) of 4.0 ML InGaN layer with respect to V/III ratio at Ts of 633°C. For this deposition thickness and temperature no QDs are observed. As seen in Figure 49, V/III ratio strongly effects the surface roughness. We have determined 13.88×10^3, where the roughness is maximized in Figure 49, to be a proper V/III ratio for QD formation at 633°C.

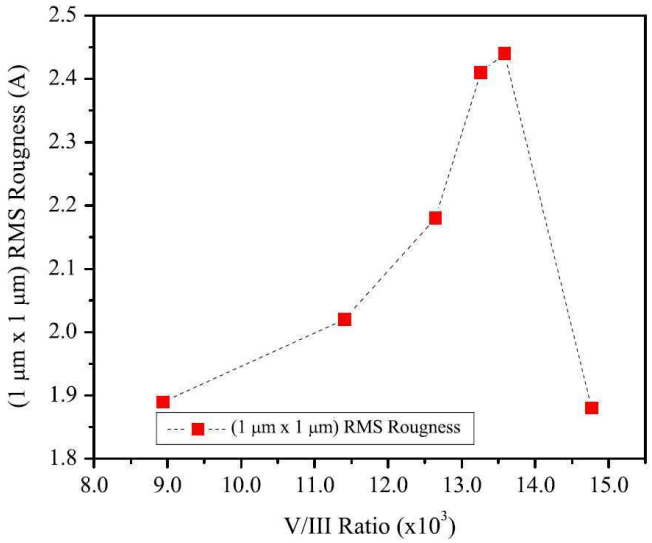

Figure 49. AFM RMS roughness (1 μm × 1 μm) versus V/III ratio for 4.0 ML InGaN grown at T=633ºC.

Effect of V/III ratio on QD formation is studied separately. Figure 50 (a, b) displays the (1 μm × 1 μm) AFM images of 5.8-ML-thick InGaN grown at 633°C with V/III ratio being 13.88 × 103 and 13.57×10^3, respectively. As seen, higher V/III ratio results in bigger quantum dots, similar to increased RMS roughness in Figure 49. V/III ratio being 13.88×10^3, increasing or decreasing V/III ratio results in less uniform quantum dots. Thus, we have kept the V/III ratio at 13.88×10^3 thereafter.

Maintaining the growth temperature at 633°C, and V/III ratio at 13.88×10^3, we have identified formation of two different quantum structures: quantum disks and quantum dots. When InGaN is deposited less than critical thickness of 4 ML, some kind of 2-D structure similar to Figure 48 (a) was observed. As the height of these structures were much smaller than their width (as observed via AFM analyses), they are referred to as quantum disks. Deposited more than 4 ML, QD formation was observed via AFM (Figure 48 (b, c)).

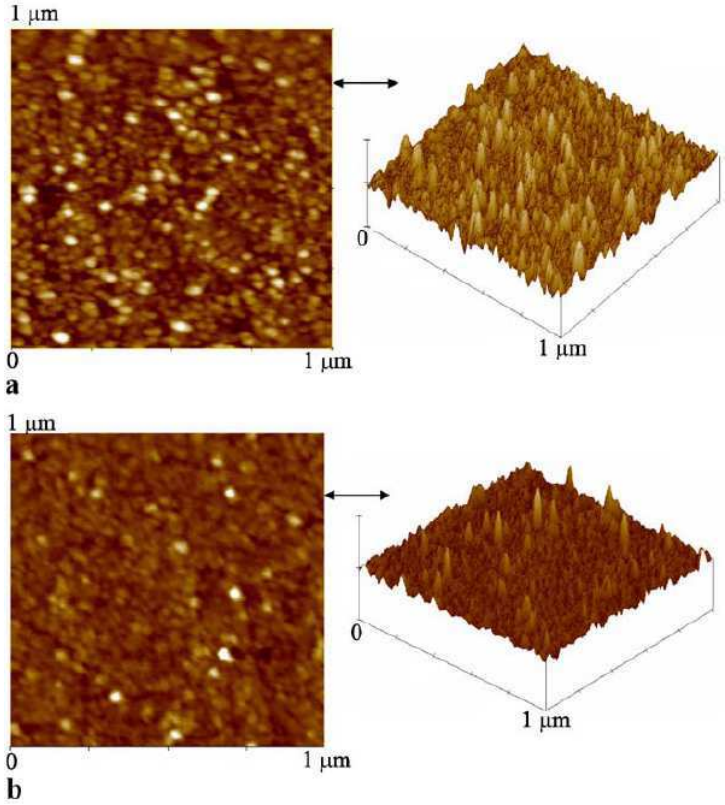

Figure 50. AFM (1 μm × 1 μm) images of 5.8 ML InGaN grown at T=633ºC with a V/III ratio (a) 13.88 × 10^3, and (b) 13.57 × 10^3.

The photoluminescence of the InGaN quantum structures were studied at room temperature (Figure 51) via 244 nm line of Argon laser. Due to low excitation (18 W/cm^2), the main transition in QDs is from ground levels of conduction and valance bands. Fabry–Perot reflections (in Figure 51) are observed due to 2-μm-thick GaN cavity. At 558 nm calculated Fabry–Perot peak separation is 34 nm not far from what we experimentally observe.

At our optimized growth conditions, InGaN relaxes into two different quantum structures, quantum disks or quantum dots depending on the deposited thickness. For ~2.4ML InGaN deposition, the layer is pseudomorphic, and broad band emission from 420 to 520 nm is observed. For InGaN deposition ≥3 ML, the layer tends to partially relax by forming quantum disks, as shown in Figure 48 (a), which leads to two distinct PL bands in Figure 51. The first

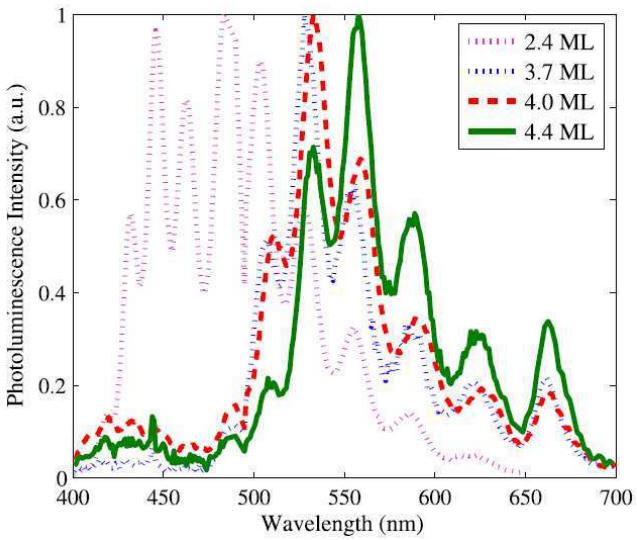

Figure 51. Normalized photoluminescence intensity versus wavelength at room temperature for 2.4-, 3.7-, 4.0-, and 4.4-ML-thick InGaN.

band (420–460 nm) presenting a low PL emission intensity is attributed to a wetting layer. The existence of this wetting layer is due to SK mode. The high-intensity band has a peak at 525 nm and corresponds to emission from the (higher indium content) quantum disks. At a thickness of 4.4 ML, quantum dot formation occurs, as shown in Figure 48 (b). Two PL bands are also observed, but the high-indium-content band corresponding to QD emission has a longer wavelength (558 nm) than that of the quantum disk. In conclusion, QD formation takes place after deposition of critical thickness of about 4.0 ML with an apparent PL redshift. When 4.4 ML InGaN is deposited, the average size of the quantum dots are 0.8 nm in height and 36 nm in bottom diameter, and their density is 1×10^{10} cm^{-2}.

In Ref. [64], the detrimental effect of quantum dot height on radiative lifetime is reported. The strong room temperature luminescence of our QDs should be due to smaller QD height leading to a higher overlap between electron and hole wavefunctions. Thus, achieving high-optical-quality InGaN QDs requires precise control of the InGaN growth rate and is attainable at low growth rates via MOCVD.

Integrating the QDs in LEDs requires an appropriate means of capping. A low-temperature GaN capping layer is investigated to cap 4.4 ML InGaN QDs. For a 2-nm-thick capping layer we can still resolve the QDs by AFM (Figure 52 (a)). However, with 5-nm-thick capping, the QDs are completely covered (Figure 52 (b)). The PL intensity dependence on capping thickness is shown in Figure 52 (c). When just covered, the PL intensity increases. However, a thicker capping layer reduces the emission intensity possibly due to the absorption losses in the thick GaN capping layer.

Figure 52. AFM Surface Plot for (a) 2 nm capped (1 µm ×1 µm), (b) 5 nm capped (5 µm ×5 µm) 4.4 ML InGaN QDs. (c) Peak photoluminescence intensity dependence on capping thickness.

Calculation of indium content

Iterative calculation of strain and piezoelectric effects on the band gap are used along with ground energy levels to estimate the indium content of the InGaN QDs using experimental PL data as input. The set of parameters used in this work could be found in Ref. [65]. Vegard's Law is used to interpolate values for $In_xGa_{(1-x)}N$.

The InGaN QDs are known to have trapezoidal shape, which can be observed via transmission electron microscope studies [66]. Thus, InGaN QDs are assumed to have a trapezoidal shape with 35° side wall angle while calculating the ground state energies by finite-element modeling (FEM). The relation between band gap determined from PL (E_g^{PL})and real compositional band gap (E_g^x) is approximated as follows:

$$E_g^{PL} = E_g^x + E_x^{g-g} + \Delta E_g \quad (3)$$

where strain and piezoelectric field effects are included in ΔE_g. E_x^{g-g} is the sum of the conduction and valance band ground energy levels relative to their respective bands. Finite-element modeling is used to calculate the ground energy levels of the quantum dots. Assuming an initial indium composition, E_x^{g-g} and ΔE_g is calculated giving E_g^x. From this result of E_g^x the new indium content (x_{In}) and the new value for strain and ground states are calculated. This new strain and ground state transition energy lead to a new E_g^x .Iteration continues until indium content (x_{In}) converges.

The band gap of the InGaN is calculated from

$$E_g^x = x_{Ga}E_g^{GaN} + x_{In}E_g^{InN} - bx_{Ga}x_{In} \quad (4)$$

where $b = 2.77 / (1 + 1.007x_{In})$ gives indium content dependent InGaN bowing parameter to match experimental data [67]. The effect of strain and piezoelectric effect on bandgap at room temperature can be calculated by separating the effect of strain (ε) and piezoelectric fields (QCSE) as follows:

$$\Delta E_g = \Delta E_g^{\varepsilon} + \Delta E_g^{QCSE} \quad (5)$$

As only the lowest possible transition in room temperature is of interest, the total change in band gap due to strain could be written as sum of the contributions from change in conduction and valance (heavy hole) bands, as in (6).

$$\Delta E_g^{\varepsilon} = \Delta E_c^{\varepsilon} - \Delta E_{v,hh}^{\varepsilon} \quad (6)$$

For pseudomorphic wurtzite films grown along (0001) *z*-axis, the nonzero strain elements are [68]

$$\varepsilon_{xx} = \varepsilon_{yy} = \frac{c_{GaN} - c_{InGaN}}{c_{InGaN}} \quad (7)$$

$$\varepsilon_{zz} = -\frac{2C_{13}}{C_{33}}\varepsilon_{xx} \quad (8)$$

where c is the in-plane lattice constant and C_{ij} is the elastic constant.

The change in conduction band due to strain (ΔE_c^{ε}) is calculated [69,70] as

$$\Delta E_c^{\varepsilon} = a_c^z \Delta\varepsilon_{zz} + a_c^{x,y}(\Delta\varepsilon_{xx} + \Delta\varepsilon_{yy}) \quad (9)$$

$$= a_c^z\left(-\frac{2C_{13}}{C_{33}}\Delta\varepsilon_{xx}\right) + a_c^{x,y}(2\Delta\varepsilon_{xx}) \quad (10)$$

where a_c^z, and $a_c^{x,y}$ are hydrostatic deformation potential constants.

The calculation of valance band shift due to strain is as follows:

$$\Delta E_{v,hh}^{\varepsilon} = \lambda_{\varepsilon} + \theta_{\varepsilon} \quad (11)$$

$$\lambda_{\varepsilon} = D_1\Delta\varepsilon_{zz} + D_2(\Delta\varepsilon_{xx} + \Delta\varepsilon_{yy}) \quad (12)$$

$$\theta_{\varepsilon} = D_3\Delta\varepsilon_{zz} + D_4(\Delta\varepsilon_{xx} + \Delta\varepsilon_{yy}) \quad (13)$$

where D_1, D_2, D_3, and D_4 are deformation potential constants. By using Eqns. (6, 9, 11) the effect of strain on the band gap (ΔE_g^{ε}) is calculated for any indium content in InGaN. Our result agrees that increasing the compressive strain ($\Delta\varepsilon_{xx} < 0$) increases the band gap.

Polarization related electric field has two components: spontaneous and strain induced. Spontaneous

component is independent of the strain and dependent on the composition. Strain induced one depends on composition via strain. Piezoelectric field is calculated from surface charge density. The surface charge density for both components can be calculated as [71,72]:

$$\sigma^z = \sigma^z_{st} + \sigma^z_{sp} \quad (14)$$

$$\sigma^z_{st} = 2\varepsilon_{xx}\left(\varepsilon_{31} - \varepsilon_{33}\frac{C_{13}}{C_{33}}\right) \quad (15)$$

$$\sigma^z_{sp} = x_{Ga}P^{sp}_{GaN} + x_{In}P^{sp}_{InN} \quad (16)$$

where P^{sp}_{AN} is the spontaneous polarization coefficient of binary compound AN. Piezoelectric field (ε^{PE}) follows the charge density as:

$$\varepsilon^{PE} = \frac{\sigma^z}{2\varepsilon_0\varepsilon_r} \quad (17)$$

where ε_0 and ε_r are the vacuum and relative permittivity constants. Thus change in the band gap due to electric field, quantum-confined Stark effect (QCSE), could be approximated as [73]:

$$\Delta E_g^{QCSE} = \frac{C_1(m_e^* + m_h^*)m_0e^2\varepsilon^2L_{eff}^4}{\hbar^2} \quad (18)$$

where C1 = −2.19 × 10^{-3} and L_{eff} = 8 × 10^{-10} m are used. m_0 is the electron mass, e is the unit charge, and ħ is the Planck's constant over 2π. m_e and m_h are the effective masses of the electron and heavy hole, respectively. L_{eff} is the effective thickness, and assumed to be the biggest QD height not to underestimate the change in the band gap due to electric field (ΔE_g^{QCSE}). ε is the electric field due to spontaneous and strain-induced charges. From (18), decreasing the electric field results in a larger band gap, as expected.

By using (10, 11, 18) in (19)

$$\Delta E_g = (\Delta E_c^{\varepsilon} - \Delta E_{v,hh}^{\varepsilon}) + \Delta E_g^{QCSE} \quad (19)$$

and iterating, indium content is determined to be 67.4% resulting a strain of 6.3%. The minus sign of strain indicates compressive nature. Due to small height of QDs, change in band gap due to electric field (~3.3 MV/cm) is on the order of 2.0 meV whereas change in band gap due to strain is 78.4 meV. The signs indicate the opposing processes. Thus, in QDs the effect of strain on band gap is dominant rather than that of piezoelectric fields. From FEM simulations, the converged ground energy levels of 0.217 eV for conduction band and 0.158 eV for valance band (measured from their

respective bands) are reached as for $In_{0.67}Ga_{0.33}N$ QDs.

In quantum-well-based nitride light emitters, the emission blue shifts with increasing injection current due to free carrier screening that occurs due to the high piezoelectric field [74]. This injection-dependent wavelength shift is undesirable for lasers as the gain structure is typically optimized for a single wavelength. Thus, QDs band gap being less affected by electric field should help more wavelength stable emission in nitride light emitters. As InGaN is sensitive to regrowth of GaN at high temperatures, these QDs could be particularly beneficial in hybrid structures [13] that employs ZnO layers grown atop of InGaN QDs at lower temperatures than that of (In)GaN layers.

Conclusion

Stranski–Krastanow growth of InGaN quantum dots (QDs) on GaN templates are realized. Effect of growth temperature, deposition thickness and V/III ratio on QD formation are studied. InGaN QDs with a peak emission wavelength of 558 nm at room temperature are realized. These QDs are capped to be integrated into optoelectronic devices. Theoretical analysis suggests that due to low QD height, piezoelectric field effect on band gap is small which should lead to more stable emission wavelength with injection current. InGaN QDs promises applications in conventional and hybrid green-light emitters.

Section 7 Phosphor-free White Light-Emitting Diodes based on InGaN Quantum Dots

High indium content (67%) room temperature green emitting InGaN quantum dots (QDs) are grown on GaN templates using Stranski-Krastanov (SK) growth mode. A two-step-grown GaN cap layer is employed for stacking QDs. Three-, seven- and fourteen-stack QD structures are integrated into light-emitting diodes from which cool white light emission is observed. The white light emission is attributed to the SK growth mode of InGaN QDs leading to blue and green emission from wetting layer and multi-stack QDs, respectively. Theoretical calculations identify compressive strain as the dominant effect on the emission characteristics of these QDs.

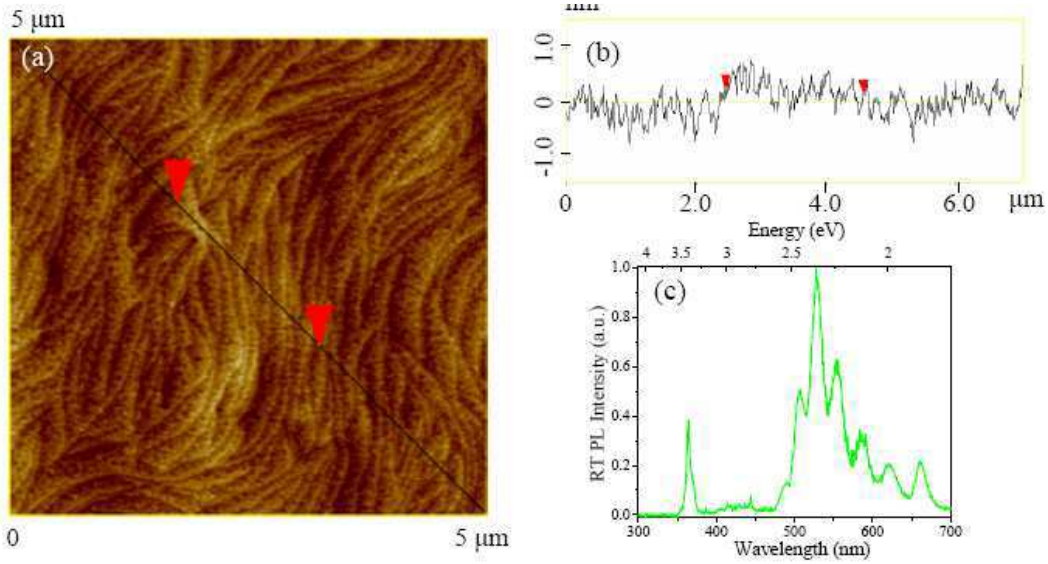

Figure 53. (a)Atomic force microscopy (5 µm × 5 µm) contour images of InGaN on GaN after 6.5 ML InGaN, (b) Height variation across the cross section; The average quantum dot height is 0.8 nm (~3 ML), bottom diameter is 36 nm, and their density is 1×10^{10} cm^{-2} (c) Room temperature photoluminescence of the uncapped self-assembled QDs (Peak wavelength is 528.0 nm, and Full-width-at-half- maximum (FWHM) is 89.3 meV)

Introduction

Solid state lighting (SSL) holds the promise of a more energy-efficient, longer-lasting, more compact, and lower maintenance substitute for today's incandescent and °uorescent light sources. Since lighting currently represents about 22% of all electricity consumption, the adoption of SSL could significantly reduce greenhouse gas emissions [9].

The development of high efficiency and reliable white lighting is a crucial milestone for SSL research. One way to achieve white light is via mixing three-standard-color (red, green, and blue) light-emitting diodes (LEDs). This approach has the potential problems such as (1) the color of the light may change considerably with viewing angle, (2) color tuning individual diodes is difficult, (3) the operation life of different color LEDs are variable [75]. Development of high power blue LEDs [10], and lack of performance in green ones [11], [13] has led to another approach; the usage of a single (blue or ultraviolet) LED and one or more phosphors, as a means of white light generation [75]. Although recent phosphor-converted white LEDs show high efficiencies [76], phosphor-free white LEDs are more convenient in design, and more liable for mass production [77,78].

With increasing indium content (from violet to green emission), a significant decrease in performance is observed in light emitters based on quantum wells [11]. One of the reasons is that the large lattice mismatch between high indium content InGaN and GaN induces the generation of dislocations in the active region. [11], [55] This explains how the performance decreases for high indium content light emitters, even on low dislocated templates. [48], [46] The use of quantum dots may be one way to overcome these limitations in high indium content devices. Besides, optoelectronic devices based on quantum dots (QDs) have many advantages over those based on quantum wells such as temperature stability and higher efficiency. [58]

Room temperature blue emission from InGaN QDs has been reported earlier. [59], [61] The strong luminescence from these QDs is attributed to the exitonic transitions. [61] The blue QDs are being integrated into LEDs. [62] However, there are few reports of InGaN quantum dots in the green spectral range luminescing at room temperature. This is mainly due to the diffculty in growing high indium content high quality InGaN quantum dots. The uniformity, density and size of the QDs are essential parameters controlled by material growth. Besides, successful integration of these QDs into LEDs requires their stability at high temperatures so that stacking could be realized and contact layers can be grown upon. In this respect, the instability of InGaN at high temperature adds another challenge for device applications [18]. However, the phase separation in InGaN can be suppressed by strain [79]. Thus, among high indium content InGaN active layers, InGaN QDs grown using Stranski-Krastanov (SK) growth mode [80] may be more phase-stable at higher temperatures than quantum wells as strain could be channelled for self-assembly rather than misift dislocation generation. In this work, the structural and optical properties, and the capping of green emitting InGaN QDs grown via SK growth mode is studied. Integration of these QDs into LEDs is realized, and electro-optical characteristics of these LEDs are reported.

Experiment

InGaN QDs are self-assembled by SK growth on 2 μm GaN on double side polished (0001) sapphire (Al_2O_3) substrate using horizontal-fow low-pressure metal organic chemical vapor deposition (MOCVD) reactor. During the active layer growth, N_2 is used as the carrier gas to facilitate the incorporation of indium. InGaN deposition thickness is calculated based on bulk growth rate which was 1.2 nm/min at 100 mbar. In order to achieve high quality QDs, the deposition temperature from 734℃ to 634℃ , V/III ratio from 9×10^3 to 15×10^3 , deposition thickness from 2 ML to 8 ML (1 ML ≈ 2.7Å), interruption time from 15 s to 60 s are varied. Eventually, the growth temperature of ~634ºC, V/III ratio of ~13.9×10^3, deposition thickness of 6.5 ML and interruption time of 15 s were determined to give well-ordered InGaN QDs emitting in green regime at room temperature.

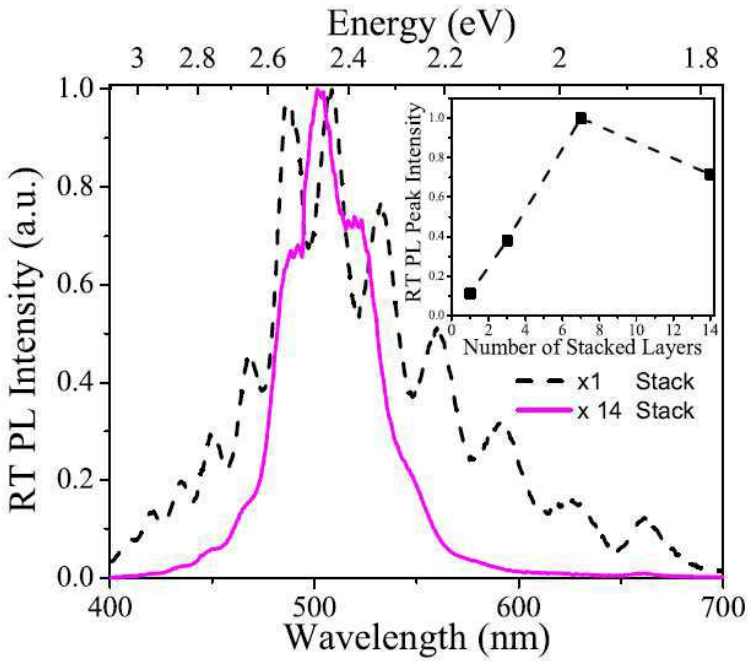

Figure 54. Room temperature normalized photoluminescence intensity of a single- and fourteen-stack QD layer. Inset displays the relative PL intensity dependence on the number of stacked QD layers.

Result and Discussion

Growth and Characterization of InGaN QDs

No QD formation for layers thinner than critical thickness of 4.0 ML suggests the SK growth mode. [66], [80] After deposition of 6.5 ML and 15 s growth interruption under ammonia, quantum dots form (Figure 53). The average size of the quantum dots are 0.8 nm (~3 ML) in height and 36 nm in bottom diameter, and their density is 1×1010 cm-2, as seen in Figure 53(a-b). It is observed in Figure 53(a) that the QDs form at the step edges of the epitaxial layer as step edges increase the nucleation probability.

The photoluminescence of the InGaN QDs is studied at room temperature (Figure 53 (c) and Figure 54). Figure 53(c) displays the room temperature luminescence from these uncapped QDs. The GaN energy level is observed at 364 nm as well as strong green luminescence related to high indium content InGaN QDs peaking at 528 nm. Fabry-Perot reflections (in Figure 53(c) and 2) are observed due to 2 μm thick GaN cavity. Due to low excitation (18 W/cm2), the main transition in QDs is from ground levels of conduction and valance bands. The emission band (400-450 nm) attributed to a wetting layer is observed at photoluminescence studies. The existence of this wetting layer is due to SK growth mode verified by AFM studies. The detrimental effect of quantum dot height on radiative lifetime is reported. [64] The strong room temperature luminescence of our QDs should be due to smaller QD height leading to a higher overlap between electron and hole wavefunctions, and higher QD uniformity and density leading to stronger luminescence. In conclusion, the critical thickness is determined to be 4.0 ML, and QDs with room temperature green emission is achieved by MOCVD growth optimization.

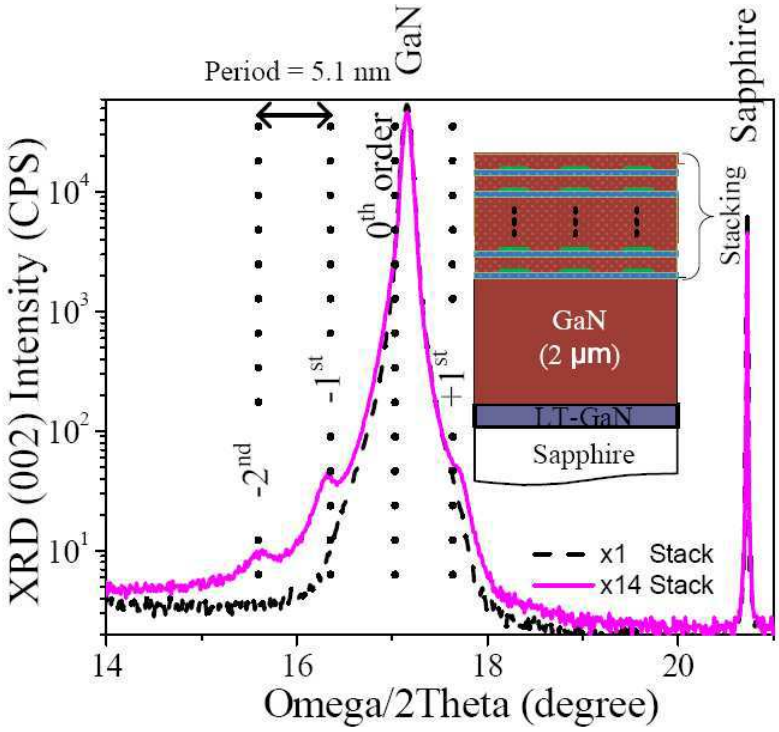

Figure 55. Room temperature XRD (002) intensity of a single-and fourteen-stack QD layer. Inset displays the stacked structure.

Capping and stacking InGaN QDs

Integrating the QDs in LEDs requires an appropriate means of capping. Besides, achieving strong emission necessiates embedding many QD layers that are similar in characteristics. QD preservation and QD multi-stacking requirements are fulfilled by developing a two step cap layer: 2 nm low temperature ((~634℃)) GaN layer followed by 2 nm high temperature (~1020ºC) GaN layer. The low temperature cap layer increases the QDs stability and durability under high temperatures, and high temperature growth creates a high quality GaN epilayer (verified by AFM) for the next stack of QDs. By this scheme, up-to fourteen QD layers are stacked up. The slight blue shift of the peak wavelength (83 meV) before (Figure 53(c)) and after (Figure 54) capping is attributed to the interdiffusion of indium atoms. The photoluminescence (PL) of a single stack and fourteen-stack QD layer is compared in Figure 54. The narrowing of the PL spectra suggests successful capping. The peak wavelength is 510 nm and is not affected significantly by number of stacked QD layers. The Figure 54 inset displays the dependence of the PL peak intensity on the number of QD stack layers. The linear increase in intensity up to seven stacks shows our stacking quality. Slight decrease for the fourteen-stack QD layer could be due to slight degradation in material surface with respect to seven-stack QD layer.

The stacked active layers are studied by X-ray diffraction (XRD) for monitoring crystal quality. Although no InGaN peaks can be identified for a single stack, fourteen-stack QD layer displays clear satellite peaks, as seen in Figure 55. The increase in clarity of the satellite peaks with increase in stacked layer confirms the quality of the stacked active layers. The indium composition of the individual layers (wetting layer and QDs) is difficult to determine by XRD as all layers are under high stress, and their thicknesses are relatively comparable. Thus, optical luminescence results are used to determine the

indium content of the QDs as explained in Section III C. XRD data determines the active layer period as 5.1 nm, which is comparable to expected period 5.8 nm, considering SK growth formation of active layer material: 1.8 nm (6.5 ML) active layer material (wetting

layer and QDs), and 4 nm GaN cap layer. In conclusion, AFM, photoluminescence and XRD results show proper GaN capping scheme for green emitting InGaN QDs as being first a low temperature (2 nm), then a high temperature (2 nm) cap layer. Successful stacking up to fourteen QD layers is achieved.

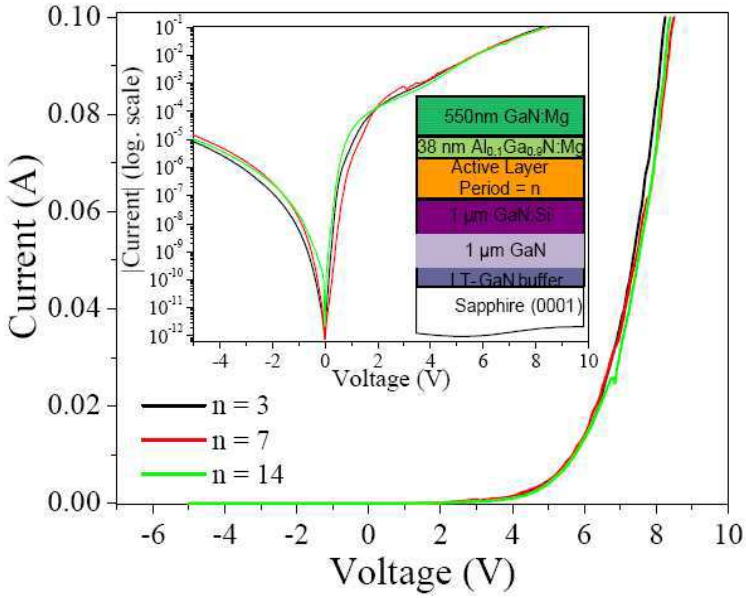

Figure 56. *I -V* Curves of the LEDs for three-, seven-, and fourteen-stack QD layers. Inset displays the logarithmic scale *I -V* curves and the final LED device structure.

Integration of InGaN QDs into LEDs and Results

The integration of multi-stack QD layer in an LED is achieved by growing 38 nm thick $Al_{0.1}Ga_{0.9}N$:Mg as a current blocking layer, and followed by 550 nm GaN:Mg deposition as current spreading and contact layer. Complete device structure is shown in Figure 56 inset.

Activation of the *p*-type GaN is achieved by rapid thermal annealing at 1000℃ for 30 s. After surface treatment with HCl:H_20 (1:1), 30Å Ni / 30Å Au is deposited as transparent contact and is annealed to achieve ohmic contact to *p*-type material. ECR-RIE system (etchants being $SiCl_2$ and Ar) is used to etch the mesa. 400Å Ti / 1200Å Au is deposited as the thick contact metal for both n- and p-type GaN.

The *I -V* curves of the LEDs with three-, seven-, and fourteen-stack QD layer is shown in Figure 56. No significant difference in the *I -V* characteristics of the LEDs with respect to number of QD stack in the active layer is observed. The electrical equivalent values are calculated.[Error! Bookmark not defined.] The on-series resistance (R*s*) is ~17.2 Ω .Parallel resistance, which is inversely related to leakage current, is calculated as ~5GΩ. The turn-on voltage is 6.1 V.

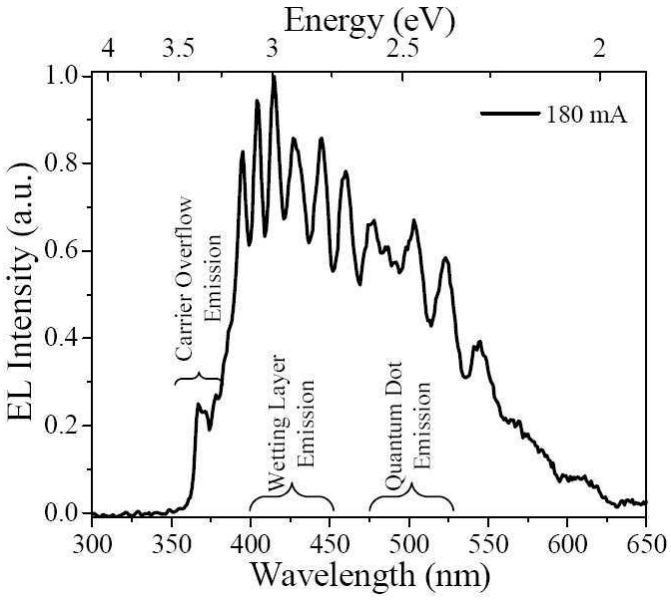

Figure 57. ***A typical room temperature electroluminescence of the QD-based LED at 180 mA injection.***

A typical electroluminescence (EL) of an LED is shown in Figure 57. The ~380 nm peak is due to electron overflow into *p*-type material, and their subsequent recombination

in (Al)GaN:Mg layers. The broad electroluminescence from blue to green regime is due to the superimposition of emission from wetting layer and QDs. The wetting layer emitting from 400 nm to 450 nm (observed in Figure 53(c)) has a stronger effect in EL due to higher carrier injection and carrier overflow from the QDs. The green emission band from 480 nm to 530 nm is attributed to the embedded InGaN QDs which demonstrated strong room temperature PL before integration into the LEDs (Figure 54). Thus, LEDs employing self-assembled InGaN QDs are shown to be a good source of phosphor-free cool white light emission, that may be vital for SSL.

Conclusion

InGaN QDs are grown by SK growth mode and shown to have strong green luminescence at room temperature. A low temperature GaN cap layer followed by a high temperature one is developed for stacking up to fourteen-layer of QDs, which are later integrated into LEDs. Cool white light emission is observed from these LEDs that is applicable for SSL.

CONCLUSION

A five-step LEO GaN growth technique for high quality LEO GaN growth is introduced. Blue and green emitting active layers and LEDs on conventional GaN and five-step-grown LEO GaN templates are realized. Significant differences in blue and green active layer surfaces are analyzed. The high quality LEO templates are observed to be important for smoother active layer surface morphologies. Blue and green LEDs on conventional GaN and high quality LEO GaN are studied. Green LEDs are observed to be leakier than blue ones, and no significant differences between green LEDs on conventional GaN and LEO GaN in terms of I-V behavior and peak power are observed. Green MQW quality is determined to be the bottleneck for high performance green emitters, not template dislocation density.

The green active layer quality is improved by using pulsed atomic layer epitaxy for InGaN. Thermal

cycling in the active layer is developed to ensure uniformity and quality of the quantum wells. We have demonstrated green LEDs with emission wavelength 510 nm at 20 mA. A blue shift with injection current similar to blue LEDs are observed.

Employment of ZnO atop of green emitting high indium content InGaN LEDs brings up a new era of designs as it solves a major problem of conventional green LEDs: it prevents the much-needed indium for green emission from leaking out. Low indium incorporation in QWs grown on nonpolar substrates raises the interest in semipolar structures which promise higher rate of indium incorporation and significantly decreased piezoelectric fields. Combined with the semipolar freestanding GaN substrate, our innovative ZnO – InGaN hybridization promises efficiency-droop-free green LEDs with superior green spectral quality that fulfills the green gap and enables white LEDs based on color-mixing (the most energy efficient method of white light generation) as well as other commercial applications such as portable hand-held projectors/communicators, TVs and novel display systems.

Green emitting InGaN QDs are realized, and integrated into LEDs. Thanks to the S-K growth mode, white light emission is observed. These quantum structures could be of interest to phosphor-free lighting technologies.

In summary, III-Nitrides are quite promising materials from ultraviolet towards visible emitters. Their direct bandgap and its tunibility makes them great candidates for portable energy efficiency alternatives whereas their durability and radiation hardness make them longer life time solutions for harsh environments. From quantum structures (such as dots) to bulk material systems, AlGaInN compounds promise a very bright future for the world.

Acknowledgment
The authors would like to thank Dr. J.L. Pau, Dr. R. McClintock, Dr. P. Kung, Dr. K. Minder, Dr. S.R. Darvish, Dr. S. Slivken and Dr. B. Movaghar from Center for Quantum Devices at Northwestern University for their support and feedback throughout the research.

References

[1] J.D. Brown, Jizhong Li, P. Srinivasan, J. Mathews, J. F. Schetzina, MRS Internet J. of Nitride Semicond. Res. 5, 9 (2000).
[2] A. Yasan, R. McClintock, K. Mayes, S. R. Darvish, P. Kung, and M. Razeghi, Appl. Phys. Lett. 81, 801 (2002).
[3] K. Mayes, A. Yasan, R. McClintock, D. Shiell, S. R. Darvish, P. Kung, and M. Razeghi, Appl. Phys. Lett. 84, 1046 (2004).
[4] A. Yasan, R. McClintock, K. Mayes, D. Shiell, L. Gautero, S. R. Darvish, P. Kung, and M. Razeghi, Appl. Phys. Lett. 83, 4701 (2003).
[5] D. J. Rogers, F. Hosseini Teherani, A. Yasan, K. Minder, P. Kung, and M. Razeghi, Appl. Phys. Lett 88, 141918 (2006).
[6] D. J. Rogers, F. Hosseini Teherani, A. Yasan, R. McClintock, K. Mayes, S. R. Darvish, P. Kung, M. Razeghi and G. Garry, Proc. SPIE, 5732, 412 (2005).
[7] J. Fryar, E. McGlynn, M. O. Henry, A. A. Cafolla, C. J. Hanson, Physica B, 340-342, 210 (2003).
[8] J. Lee, K. K. Kim, H. Tampo, A. Yamada, and S. Niki, Journal of the Electrochemical Society, 153, G1047 (2006).
[9] X. Shao, S. L. Rommel, B. A. Orner, J. Kolodzey, and P. R. Berger, IEEE Electron Device Letters, 18, 411 (1997).
[10] C. J. Humphreys, MRS Bulletin 33, 459 (2008).
[11] N.F. Gardner, G.O. Muller, Y.C. Shen, G. Chen, S. Watanabe, W. Gotz, and M.R. Krames, Appl. Phys. Lett. 91, 243506 (2007).
[12] Y.H. Cho, S.K. Lee, H.S. Kwack, J.Y. Kim, K.S. Lim, H.M. Kim, T.W. Kang, S.N. Lee, M.S. Seon, O.H. Nam, and Y.J. Park, Appl. Phys. Lett. 83, 2578 (2003).
[13] I.K. Park, M.K. Kwon, J.O. Kim, S.B. Seo, J.Y. Kim, J.H. Lim, S.J. Park, and Y.S. Kim, Appl. Phys. Lett. 91, 133105 (2007).

[14] C. Bayram, F. H. Teherani, D. Rogers, and M. Razeghi, Appl. Phys. Lett. 93, 081111 (2008).
[15] Y. Narukawa, Y. Kawakami, M. Funato, S. Fujita, and S. Nakamura, Appl. Phys. Lett. 70, 981 (1996).
[16] M. Takeguchi, M.R. McCartney, and D. J. Smith, Appl. Phys. Lett. 84, 2103 (2004).
[17] S. J. Rosner, E.C. Carr, M.J. Ludowise, G. Girolami, and H.I. Erikson, Appl. Phys. Lett. 70, 420 (1996).
[18] S.F. Chichibu, H. Marchand, M.S. Minsky, S. Keller, P.T. Fini, J.P. Ibbetson, S.B. Fleischer, J.S. Speck, J.E. Bowers, E. Hu, U.K. Mishra, S.P. DenBaars, T. Deguchi, T. Sota, and S. Nakamura, Appl. Phys. Lett. 74, 1460 (1999).
[19] I. Ho and G.B. Stringfellow, Appl. Phys. Lett. 69, 2701 (1996).
[20] B. Van Daele, G. Van Tendeloo, K. Jacobs, I. Moerman, and M.R. Leys, Appl. Phys. Lett. 85, 4379 (2004).
[21] C. Wetzel, T. Salagaj, T. Detchprohm, P. Li, and J.S. Nelson. Appl. Phys. Lett. 85, 866 (2004).
[22] S. Nakamura, M. Senoh, N. Iwasa, and S. Nagahama, Jpn. J. Appl. Phys. 34, L797-799 (1995).
[23] S.J. Chang, W.C. Lai, Y.K. Su, J.F. Chen, C.H. Liu, and U.H. Liaw, IEEE J. on Select. Top. On Quant. Elect. 8, 278 (2002).
[24] Y.D. Qi, H. Liang, D. Wang, Z.D. Lu, W. Tang, and K.M. Lau, Appl. Phys. Lett. 86, 101903 (2005).
[25] T. Mukai, K. Takekawa, and S. Nakamura, Jpn. J. Appl. Phys. 27 L839-L841 (1998).
[26] D.I. Florescu, V.M. Asnin, F.H. Pollak, A.M. Jones, J.C. Ramer, M.J. Schurman, and I. Ferguson, Appl. Phys. Lett. 77, 1464 (2000).
[27] P. Kozodoy, J.P. Ibbetson, M. Marchand, P.T. Fini, S. Keller, J.S. Speck, S.P. Denbaars, and U.K. Mishra, Appl. Phys. Lett. 73, 975 (1998).
[28] D.S. Li, H. Chen, H.B. Yu, H.Q. Jia, Q. Huang, and J.M. Zhou, J. Appl. Phys. 96, 1111 (2004).
[29] S. Tomiya, T. Hino, S. Goto, M. Takeya, and M. Ikeda, IEEE J Sel. Top. Quant. Elect. 10, 1277 Nov./Dec. (2004).
[30] C. Bayram, J. L. Pau, R. McClintock, and M. Razeghi, Applied Physics B 95, 307 (2009).
[31] S. Tomiya, K. Funato, T. Asatsuma, T. Hino, S. Kijima,T. Asano, and M. Ikeda, Appl. Phys. Lett. 77, 636 (2000).
[32] A.E. Romanov, P. Fini, and J.S. Speck, J. Appl. Phys. 93, 106 (2003).
[33] H. Marchand, J.P. Ibbetson, P.T. Fini, S. Keller, S.P. DenBaars, J.S. Speck, and U.K. Mishra, J. Cryst. Growth 195, 328 (1998).
[34] D. Kapolnek, S. Keller, R. Vetury, R.D. Underwood, P. Kozodoy, S.P. Denbaars, U.K. Mishra, Appl. Phys. Lett. 71, 1204 (1997).
[35] H. Marchand, X.H. Wu, J.P. Ibbetson, P.T. Fini, P. Kozodoy, S. Keller, J.S. Speck, S.P. Denbaars, and U.K. Mishra, Appl. Phys. Lett. 73, 747 (1998).
[36] M. Takeya, K. Yanashima, T. Asano, T. Hino, S. Ikeda, K. Shibuya, S. Kijima, T. Tojuo, S. Ansai, S. Uchida, Y. Yabuki, T. Aoki, T. Asatsuma, M. Ozawa, T. Kobayashi, E.Morita, and M. Ikeda, J. Cryst. Growth 221, 646 (2000).
[37] X. Xu, R.P. Vaudo, J. Flynn, and G.R. Brandes. J. Electron. Mater. 31, 402 (2002).
[38] A. Sakai, H. Sunakawa, and A. Usui, Appl. Phys. Lett. 73 481 (1998).
[39] P. Fini, H. Marchand, J.P. Ibbetson, S.P. Denbaars, U.K. Mishra, and J.S. Speck, J. Cryst. Growth 209, 581 (2000).
[40] J.Z. Domagala, Z.R. Zytkiewicz, B. Beaumont, J. Kozlowski, R. Czernetzki, P. Prystawko, amd M. Leszczynski, J. Cryst. Growth 245, 37 (2002).
[41] K. Hiramatsu, Y. Kawaguchi, M. Shimizu, N. Sawaki, T. Zheleva, R.F. Davis, H. Tsuda, W. Taki, N. Kuwano, and K. Oki, MRS Internet J. Nitride Semicond. Res. 2, 6 (1997).
[42] M.S. Ferdous, X. Wang, M. N. Fairchild, and S.D. Hersee, Appl. Phys. Lett. 91, 231107 (2007).
[43] D. V. Kuksenkov, H. Temkin, A. Osinsky, R. Gaska, and M.A Khan, J. Appl. Phys. 83, 2142 (1998).
[44] D. V. Kuksenkov, H. Temkin, A. Osinsky, R. Gaska, and M.A Khan, Appl. Phys. Lett. 72, 1365 (1998).
[45] J.W.P. Hsu, M.J. Manfra, D.V. Lang, S. Richter, S.N.G. Chu, A.M. Sergent, R.N. Kleiman, L.N. Pfeiffer, and R.J. Molnar, Appl. Phys. Lett. 78, 1685 (2001).
[46] S.J. An, J.H. Chae, G.C. Yi, and G. H. Park, Appl. Phys.Lett. 92, 121108 (2008).
[47] Ya.I. Aliyov, J.E. Van Nostrand, and D.C. Look, Appl.Phys. Lett. 83, 2943 (2003).
[48] D.J. Rogers, F.H. Teherani, P. Kung, K. Minder, and M. Razeghi, Superlattice Microst. 42, p. 322-326 (2007).
[49] C. Bayram, J. L. Pau, R. McClintock, and M. Razeghi, Journal of Applied Physics. 104, 083512 (2008).
[50] M. Smith, G. D. Chen, J. Y. Lin, H. X. Jiang, A. Salvador, B.N. Sverdlov, A. Botchkarev, H. Morkoc, and B. Goldenberg, Appl. Phys. Lett. 68, 1883 (1996).
[51] E. F. Schubert, Light-Emitting Diodes, (Cambridge, Cambridge University Press, 2003).
[52] S.M. Sze, Physics of Semiconductor Devices, 2nd ed. (Wiley, New York, 1981).
[53] T. Takeuchi, C. Wetzel, S. Yamaguchi, H. Sakai, H. Amano, and I. Akasaki, Appl. Phys. Lett. 73, 1691 (1998).
[54] C. Bayram, F. H. Teherani, D. Rogers, and M. Razeghi, Vacuum Science and Technology B 27, 1784 May/June 2009.

[55] F.A. Ponce, S. Srinivasan, A. Bell, L. Geng, R. Liu, M. Stevens, J. Cai, H. Omiya, H. Marui, S. Tanaka, Phys. Status Solidi 240, 273 (2003)
[56] T. Kozaki, H. Matsumura, Y. Sugimoto, S. Nagahama, T. Mukai, Proc. SPIE 6133, 613306 (2006).
[57] D.J. Eaglesham, M. Cerullo, Phys. Rev. Lett. 64, 1943 (1990)
[58] M. Petroff, A. Lorke, A. Imomoglu, Phys. Today 54, 46 (2001)
[59] K. Tachibana, T. Someya, Y. Arakawa, Appl. Phys. Lett. 74, 383 (1999).
[60] B. Damilano, N. Grandjean, S. Dalmasso, J. Massies, Appl. Phys. Lett. 75, 3751 (1999).
[61] O. Moriwaki, T. Someya, K. Tachibana, S. Ishida, Y. Arakawa, Appl. Phys. Lett. 76, 2361 (2000).
[62] Y.K. Su, S.J. Chang, L.W. Ji, C.S. Chang, L.W.Wu,W.C. Lai, T.H. Fang, K.T. Lam, Semicond. Sci. Technol. 19, 389 (2004).
[63] S. Choi, J. Jang, S. Yi, J. Kim, W. Jung, Proc. SPIE 6479, 64791F (2007).
[64] V. Ranjan, G. Allan, C. Priester, C. Delerue, Phys. Rev. B 68, 115305 (2003).
[65] I. Vurgaftman, J.R. Meyer, L.R. Ram-Mohan, Appl. Phys. Rev. 89, 5815 (2001).
[66] K.S. Kim, C.H. Hong,W.H. Lee, C.S. Kim, O.H. Cha, G.M. Yang, E.K. Suh, K.Y. Lim, H.J. Lee, H.K. Cho, J.Y. Lee, J.M. Seo, MRS Int. J. Nitride Semicond. Res. 5S1, W11.74 (2000).
[67] M. Androulidaki, N.T. Pelekanos, K. Tsagaraki, E. Dimakis, E. Iliopoulos, A. Adikimenakis, E. Bellet-Amalric, D. Jalabert, A. Georgakilas, Phys. Status Solidi 6, 1866 (2006)
[68] S.L. Chuang, C.S. Chang, Phys. Rev. B 54, 2491 (1996)
[69] M. Grundmann, O. Stier, D. Bimberg, Phys. Rev. B 52, 11969 (1995).
[70] C.G. Van de Walle, M.D. McCluskey, C.P. Master, L.T. Romano, N.M. Johnson, Mat. Sci. Eng. B 59, 274 (1999)
[71] O. Ambacher, J. Majewski, C. Miskys, A. Link, M. Hermann, M. Eicjkhoff, M. Stutzmann, F. Bernardini, V. Fiorentini, V. Tilak, B. Schaff, L.F. Eastman, J. Phys. Condens. Matter 14, 3399 (2002)
[72] V.A. Fonoberov, A.A. Balandin, J. Appl. Phys. 94, 7178 (2003)
[73] S.L. Chuang, Physics of Optoelectronic Devices (Wiley, New York, 1995)
[74] S. Chichibu, T. Azuhata, T. Sota, S. Nakamura, Appl. Phys. Lett. 69, 4188 (1996)
[75] Eric D. Jones. Light Emitting Diodes for General Illumination (OIDA, Washington, 2001).
[76] S.C. Allen, and A. J. Stecki, Appl. Phys. Lett. 92, 143309 (2008).
[77] C.-F. Huang, C.-H. Lu, T.-Y. Tang, J.-Jie Huang, and C.C. Yang, Appl. Phys. Lett. 90, 151122 (2007).
[78] C. B. Soh, W. Liu, J. H. Teng, S. Y. Chow, S. S. Ang, and S. J. Chua Appl. Phys. Lett. 92, 261909 (2008).
[79] S.Yu. Karpov. MRS Internet J. Nitride Semicond. Res. 3, 16 (1998).
[80] R. A. Oliver, M. J. Kappers, C. J. Humphreys, and G. A. D. Briggs, J. Appl. Phys. 97, 013707 (2005).

ANNEXE VI *Epitaxial MOVPE growth of highly c-axis oriented InGaN/GaN films on ZnO-buffered Si (111) substrates*

A. Ougazzaden et al. Proc. of SPIE Vol. 7603 76031D-1

A. Ougazzaden[(a)], D. J. Rogers[(b)], F. Hosseini Teherani[(b)], G. Orsal[(c)], T. Moudakir[(c)], S. Gautier[(c)], V. E. Sandana[(b)], F. Jomard[(d)], M. Abid[(a)], M. Molinari[(e)], M. Troyon[(e)], P. L. Voss[(a)], D. McGrouther[(f)] & J. N. Chapman[(f)]

[(a)]Georgia Institute of Technology/GT-Lorraine-UMI 2958 Georgia Tech-CNRS, 2-3 rue Marconi, 57070 Metz, France
[(b)]Nanovation SARL, 103 bis Rue de Versailles, Orsay, 91400, France
[(c)]LMOPS - UMR CNRS 7132, Université de Metz et SUPELEC, 2 rue Edouard Belin, 57070 METZ, France
[(d)]GEMAC, Université de Versailles-Saint-Quentin1, place Aristide Briand, 92195 Meudon Cedex France
[(e)]LMEN, University of Reims Champagne-Ardennes, 21 rue Clement Ader, 51685 Reims, France
[(f)]Department of Physics and Astronomy, University of Glasgow, G12 8QQ, Scotland.

ABSTRACT

InGaN/GaN layers were grown on ZnO-buffered Si (111) substrates by metalorganic vapour phase epitaxy (MOVPE). The dissociation of ZnO observed during conventional MOVPE growth of InGaN/GaN was combated through the use of a low pressure/temperature MOVPE approach with N_2 as a carrier gas and dimethylhydrazine added to the ammonia (nitrogen precursor) in order to enhance the concentration of atomic nitrogen at relatively low temperature. Electron Microscopy of cross-sections, High Resolution X-Ray Diffraction (HR-XRD), secondary ion mass spectroscopy and cathodoluminescence studies suggested that single phase wurtzite InGaN layers with between about 17.5 and 21.5% indium were grown epitaxially, with no evidence of back-etching of the ZnO templates. HR-XRD revealed highly pronounced c-axis texture for both the InGaN/GaN and ZnO. Immersion in dilute nitric acid dissolved the ZnO such that the InGaN/GaN could be lifted-off from the substrate.

1. INTRODUCTION

Recently, the Gallium Nitride (GaN) and Zinc Oxide (ZnO) materials systems have attracted considerable attention because of their use in a broad range of emerging applications including light-emitting diodes [1-2] and solar cells [3-4]. GaN and ZnO are similar in that they have direct wide bandgaps, wurtzite crystal structure, high thermal stability and comparable thermal expansion coefficients. GaN has the advantage, however, of a mature know-how for p-type doping, while ZnO has proven to be more crystallographically compliant to non-native substrates than GaN. With a view to exploiting both of these strong points, ZnO layers have been proposed as buffer layers for the regrowth of GaN-based p-n devices on amorphous and mismatched substrates [5-9].
Alloying with In is important for engineering a reduced bandgap in GaN and thus facilitating quantum wells and devices which can function over the whole visible range. Previously, epitaxial

growth of InGaN on ZnO has been reported on sapphire (Al_2O_3) substrates [10-11]. However, Al_2O_3 substrates are insulating, limited in size and relatively expensive. Silicon (Si) substrates, on the other hand, are cheaper, available in larger formats, have higher thermal/electrical conductivities and offer the potential for integration with mature Si-based electronics [12-13]. In this paper, we investigate the growth of InGaN/GaN on ZnO-buffered Si (111) substrates using metalorganic vapour phase epitaxy (MOVPE), which is the dominant growth technology for InGaN-based materials and devices.

One serious obstacle to the epitaxy of InGaN on ZnO is the stability of ZnO in the MOVPE process. In particular, exposure to ammonia (NH_3) precursor and H_2 carrier gas at growth temperatures over about 650°C results in the decomposition of the ZnO [14-15]. This can lead to the formation of interfacial layers/compounds, poor epitaxy and the unintentional incorporation of liberated Zn and O into the InGaN epilayer, which is detrimental for the optical and electrical properties.

2. EXPERIMENT

ZnO thin film templates were grown on 2-inch diameter Si (111) substrates using Pulsed Laser Deposition (PLD) with a Coherent KrF excimer laser (248nm) [5]. PLD was chosen because the high adatom mobility in this growth technique allows the ZnO to crystallise readily on amorphous substrates, such as the native SiO_2 passivation layer on the surface of the Si substrate. 40 nm thick GaN and InGaN layers (of various thicknesses) were then grown on the ZnO films using a low pressure, T-shaped, MOVPE reactor [16] with Trimethylgallium (TMG) as the Ga source and Trimethylindium (TMIn) as the In source. A combination of NH_3 and Dimethylhydrazine (DMHY) was used as a source of atomic nitrogen. DMHY was added because of its' low decomposition temperature, which enhances the concentration of atomic nitrogen in the gas phase compared to NH_3 alone, allowing GaN growth at lower temperatures. Nitrogen was employed as a carrier gas [17] during the whole growth process, in order to avoid etching of the ZnO surface and ensure In incorporation [18]. The impact of In content was studied by adjusting the TMIn flow at constant TMGa flow.

The surface roughness and growth rate of InGaN layers were monitored during the growth using in-situ reflectometry. Images of fracture cross-sectional samples were obtained using a Hitachi S-4800 field-emission scanning electron microscope (SEM). For transmission electron microscopy (TEM) investigation, cross-sectional samples were prepared using the in-situ liftout technique in a Dualbeam FIB (FEI Nova Nanolab 200). High resolution (HR-TEM) imaging was performed using an FEI Tecnai F20 equipped with a field emission gun source operated at 200 keV. The crystalline quality and indium composition of the InGaN layers were characterized by high resolution x-ray diffraction (HR-XRD), using Cu K_α radiation in Panalytical MRD-Pro system equipped with a hybrid monochromator.

Concentration profiles of In, Ga, N and Zn along the growth direction were obtained by MCs+ Secondary Ion Mass Spectroscopy (SIMS) in a Cameca IMS4F system. The primary (incident) ions were 133Cs+ with an impact energy of 5.5 keV. Positively charged secondary ions were detected. The optical properties of the InGaN/GaN/ZnO were studied using a home-made cathodoluminescence (CL) system in an SEM [19].

3. RESULTS & DISCUSSION

Figure 1 shows an SEM image of a fracture cross-section of an InGaN/GaN/ZnO/Si sample with approximately 21.5% In. The sample shows continuous InGaN/GaN and ZnO layers. A well-defined interface between ZnO and GaN can be clearly observed but the InGaN/GaN interface is not obvious. The thicknesses of the InGaN/GaN and ZnO are about 180nm and 140nm, respectively.

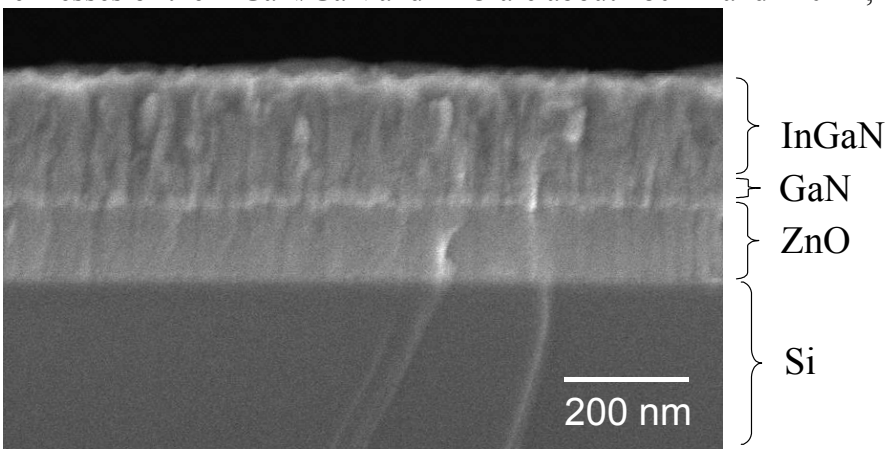

Figure 1. SEM fracture cross-section image of the InGaN/GaN/ZnO/Si heterostructure.

Figure 2 shows a HR-TEM image of the ZnO/Si interface. In this image, the regular lattice fringes in the Si substrate are interrupted at the interface with the ZnO due to the presence of the amorphous SiO_2 overlayer (~3nm thick). The subsequent ZnO layer shows established lattice fringes after only 2 nm of growth, confirming the capacity of PLD-grown ZnO to crystallise on amorphous substrates.

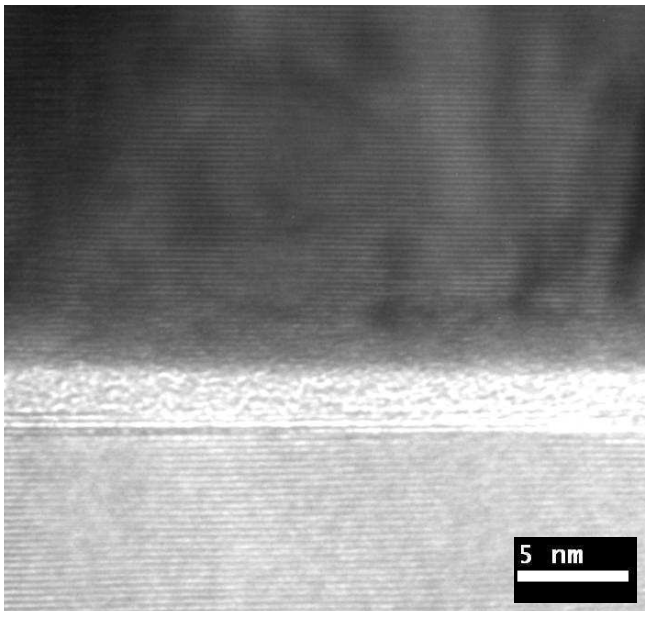

Figure 2. A HR-TEM image of the interface between the PLD-grown ZnO layer and the Si substrate.

Figure 3 shows a HR-TEM image of the interfaces between the InGaN, GaN and ZnO layers plus the result of a Fast Fourier Transform (FFT) analysis.

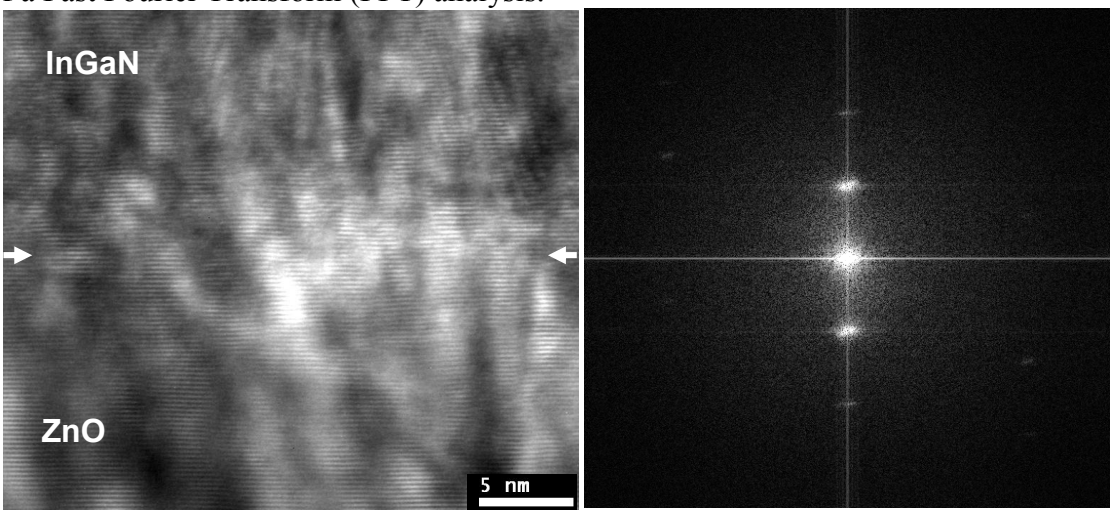

Figure 3. A HR-TEM image of the InGaN/GaN/ZnO interfaces plus a FFT analysis of the image (the arrows, in the former, suggest the position of GaN/ZnO interface).

The image shows continuous lattice fringes across the InGaN/GaN/ZnO interfaces, with no evidence of a misfit layer, or any interfacial compounds. The FFT confirms that both the lattice plane alignment and lattice spacing are similar in the InGaN/GaN and ZnO layers. Thus the TEM studies suggest that there has been epitaxial growth.
Figure 4 shows the XRD 2θ-ω scans as a function of TMIn/III ratio during growth.

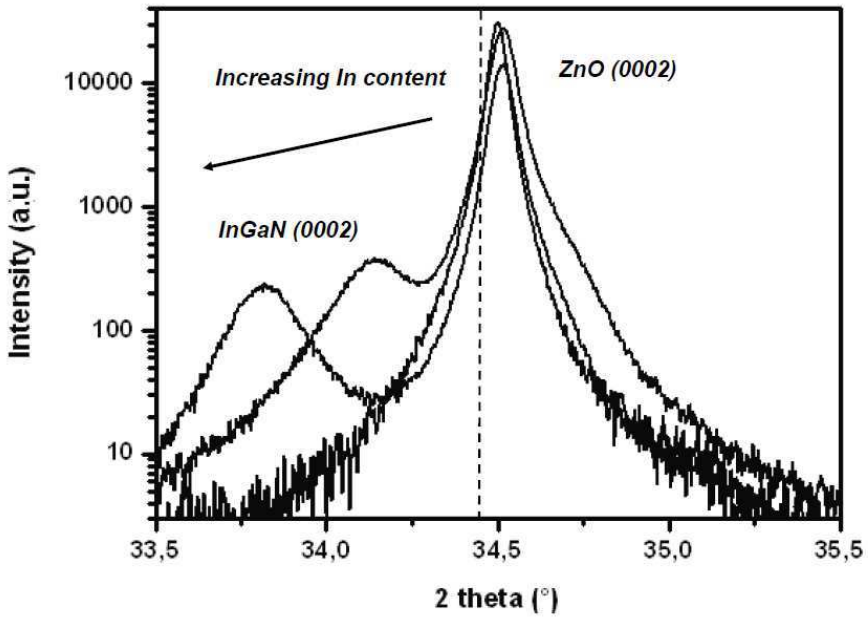

Figure 4. XRD 2θ-ω scans of the (0002) peak for ZnO/Si and the InGaN/GaN/ZnO/Si with varying In contents. The dashed line shows the peak position (34.43°) for a ZnO powder reference sample.

XRD study revealed the InGaN/GaN/ZnO layers to have single-phase wurtzite structure with strong c-axis orientation. The scans in Figure 4 present two distinct peaks, which were indexed as the (0002) peaks of the ZnO and the InGaN. An increase of the TMIn/III ratio led to a shift of the InGaN peak to lower angle and thus a higher out-of-plane "c" lattice parameter. The scans in Figure 4 also exhibited a small shoulder on the right of the ZnO peak, which was not visible in the XRD scans for the ZnO films prior to InGaN/GaN growth. This shoulder might be from the GaN layer. The concentration of In in the InGaN layer with higher In content (peak on left) was calculated from the (0002) InGaN peak position via Vegard's law to be about 21.5%. The (0002) ZnO peaks for all samples grown on Si were observed to be shifted to a higher 2θ angle than expected for bulk ZnO, which suggests that they were under tensile strain in the a-plane. This has been reported elsewhere for ZnO grown on Si substrates [20]. After InGaN/GaN growth, the ZnO peaks shifted slightly higher in 2θ (Figure 4). Thus the ZnO films absorbed some stress (tensile in this case) from the InGaN/GaN layers (as was observed in previous experiments on the MOVPE growth of GaN on ZnO/c-Al_2O_3 [6]).

Figure 5 shows the SIMS concentration profiles for Ga, In, N and Zn along the growth direction (in a sample with a thicker ZnO layer than that shown in Figure 1). The profile for Zn indicates some diffusion of Zn into the InGaN/GaN near the GaN/ZnO interface [8-9].

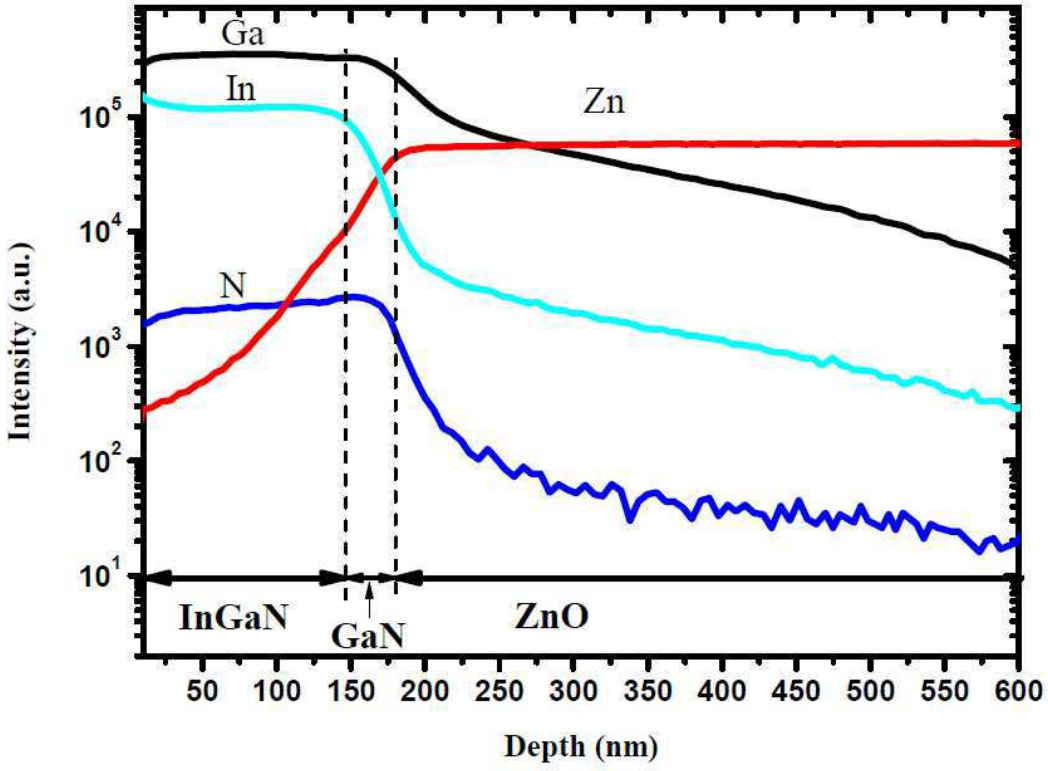

Figure 5. SIMS elemental concentration depth profiles for the Zn, Ga, N and In signals for the InGaN/GaN/ZnO-buffered Si (log. scale). It should be noted that the tails in the concentration profiles for In, Ga, and N, which extend into the ZnO, are probably artifacts due to residual particles of InGaN in the probe crater.

Figure 6 shows a normalized, room temperature (RT), CL spectrum plus a Monte Carlo simulation of the respective primary and back-scattered electron diffusion.

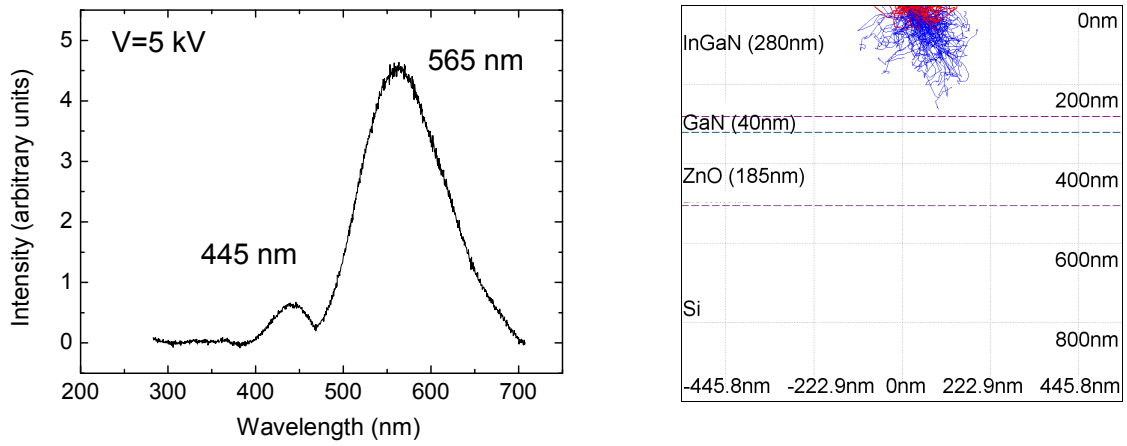

Figure 6. Normalized, RT, CL spectrum under 5kV accelerating voltage, plus a Monte Carlo simulation of the primary (red) and back-scattered (blue) electron diffusion.

The simulation suggested that an incident electron beam, with an energy of 5kV, stimulated a response from most of the InGaN/GaN layer depth. The spectrum itself shows two peaks located at about 445 nm (2.79 eV) and 565 nm (2.20 eV). The first of these peaks was indexed as InGaN with an In concentration of about 17.5 + 5 % [21], which is coherent with the value calculated from the XRD scan. The second (565 nm) peak has been observed in InGaN grown on bulk ZnO in the past and has been attributed to emission from Zn-related impurity centers in the InGaN [22]. This is coherent with the slight diffusion of Zn into the InGaN/GaN near the interface with ZnO, which was observed by SIMS.
Finally, the InGaN/GaN was lifted-off the substrate by immersion in dilute HNO3.
After several minutes, the ZnO dissolved completely and the InGaN/GaN separated from the substrate.

4. CONCLUSIONS

InGaN/GaN films were grown on ZnO-buffered Si (111) substrates by MOVPE. The dissociation of ZnO observed during conventional MOVPE growth of InGaN/GaN was combated through the use of a low pressure/temperature MOVPE approach with N_2 as a carrier gas and DMHY added to the NH_3 in order to facilitate atomic nitrogen production at lower temperatures. XRD, SEM, TEM, SIMS and CL characterisations showed smooth, highly c-axis oriented InGaN/GaN films having a well-defined interface with the ZnO underlayer, continuous lattice fringes across the interfaces and no evidence of any back-etching of ZnO. XRD and CL suggest that between 17.5 and 21.5% of In was integrated in the GaN, without any phase separation. Slight Zn diffusion into the InGaN/GaN was observed near the interface with ZnO.
Thus it was demonstrated that use of a PLD-grown ZnO buffer layer allows highly c-axis oriented wurtzite InGaN/GaN to be grown on Si substrates without removal of the amorphous SiO2 layer.

Such an approach may open the way to the integration of InGaN based devices with Si-based electronics. The feasibility of chemical lift-off of the InGaN/GaN from the substrate was also demonstrated via dissolution of the ZnO in dilute HNO3. Such a wet-etching approach would allow wafer bonding of the InGaN/GaN onto alternative substrates, with advantages such as superior transparency, and/or electrical/thermal conductivity.

ACKNOWLEDGEMENTS

The authors would like to thank the French "Agence National de la Recherche" for financial support.

REFERENCES

[1] X. Duan, Y. Huang, Y. Cui, J. Wang, C. M. Lieber, Nature 409 (2001) 66.
[2] T. Mukai, S. Nakamura, M. Senoh, Appl. Phys. Lett. 64 (1994) 1687.
[3] N. Golego, S. A. Studenkin, M. Cocivera, J. Electrochem. Soc. 147 (2000) 1592.
[4] S. C. Jain, M. Willander, J. Narayan, R. Van Overstraeten, J. Appl. Phys. 87 (2000) 965.
[5] D. J. Rogers, F. Hosseini Teherani, A. Yasan, R. McClintock, K. Mayes, S.R. Darvish, P. Kung, M. Razeghi, G. Garry, Proc. SPIE 5732 (2005) 412.
[6] D. J. Rogers, F. Hosseini Teherani, A. Ougazzaden, S. Gautier, L. Divay, A. Lusson, O. Durand, F. Wyczisk, G. Garry, T. Monteiro, M. R. Correira, M. Peres, A. Neves, D. McGrouther, J. N. Chapman, M. Razeghi, Appl. Phys. Lett. 91 (2007) 071120.
[7] A. Ougazzaden, D. J. Rogers, F. Hosseini Teherani, T. Moudakir, S. Gautier, T. Aggerstam S. Ould Saad, J. Martin, Z. Djebbour, L. Divay, O. Durand, G. Garry, A. Lusson, D. McGrouther, J. N. Chapman, J. Cryst. Growth 310 (2008) 944.
[8] D. J. Rogers, F. Hosseini Teherani, F. Jomard, M. Molinari, M. Troyon, D. McGrouther, J. N. Chapman, T. Moudakir, S. Gautier, A. Ougazzaden, M. Razeghi, J. Vac. Sci. Technol. B 273 (2009) 1655.
[9] R. Paszkiewicz, B. Paszkiewicz, M. Wosko, A. Szyszka, L. Marciniak, J. Prazmowska, W. Macherzynski, J. Serafinczuk, J. Kozowski, M. Tlaczala, J. Kovac, I. Novotny, J. Skriniarova, D. Hasko, J. Cryst. Growth 310 (2008) 4891.
[10] S.-J. Wang, N. Li, E.-H. Park, S.-C. Lien, Z. C. Feng, A. Valencia, J. Nause, I. Ferguson, J. Appl. Phys. 102 (2007) 106105.
[11] J.-B. Huang, S.-S. Wei, L.-C. Chen, L.-S. Hong, Solid-State Electronics (2008), doi:10.1016/j.sse.2008.03.007.
[12] M. Benyoucef, M. Kuball, B. Beaumont, P. Gibart, Appl. Phys. Lett. 81 (2002) 2370.
[13] J.W Lee, S.W Park, J.B. Yoo, Phys. Stat. Sol. A 176 (1999) 583.
[14] S.J. An, W.I. Park, G.C. Yi, Y.J. Kim, H.B. Kang, M. Kim, Appl. Phys. Lett. 84 (2004) 3612.
[15] K. Black, A.C. Jones, P.R. Chalker, J.M. Gaskell, R.T. Murray, T.B. Joyce, S.A. Rushworth, J. Crystal Growth 310 (2008) 1010.
[16] A. Mircea, A. Ougazzaden, R. Mellet, Prog. Cryst. Growth Charact. 19 (1989) 39.
[17] S. Gautier, C. Sartel, S. Ould-Saad, J. Martin, A. Sirenko, A. Ougazzaden, J. Cryst. Growth 298 (2007) 428.
[18] F. Scholz, V. Harle, F. Steuber, H. Bolay, A. Dornen, B. Kaufmann, V. Syganow, A. Hangleiter, J. Crystal Growth 170 (1997) 321.
[19] M. Troyon, D. Pastre, J. P. Jouart, and J. L. Beaudoin, Ultramicroscopy 75 (1998) 15.
[20] M. Suchea, S. Christoulakis, C. Tibeica, M. Katharakis, N. Kornilios, T. Efthimiopoulos, E. Koudoumas, Applied Surface Science, 254 (2008) 5475.
[21] S. Stepanov, W.N. Wang, B.S. Yavich, V. Bougrov, Y.T. Rebane, Y.G. Shreter, MRS Internet J. Nitride Semicond. Res. 6 (2001) 6.
[22] N. Li, S.-J. Wang, E.-H. Park, Z. C. Feng, A. Valencia, J. Nause, C. Summers, I. Ferguson, Proc. of SPIE Vol. 6669 (2007) 66690X-3.

RESUMÉ DE LA THÈSE EN FRANÇAIS :

Ce travail a pour objectif la maitrise de la croissance et l'analyse des propriétés des nanostructures d'oxyde de zinc (ZnO). Trois procédés de fabrication de nanostructures de ZnO ont été étudiés : dépôt chimique en phase vapeur de composés organométalliques (MOCVD), dépôt par ablation laser (PLD) et dépôt par transport physique en phase vapeur (PVT). Les substrats utilisés pour cette étude sont : saphir, silicium, ZnO massif, acier austénitique, mylar et papier. Les nanostructures ont été caractérisées par différentes techniques, notamment la microscopie électronique à balayage, la photoluminescence, la cathodoluminescence, la diffraction de rayon X et des mesures de réflectivité. Une grande variété de formes de structures a été obtenue par les trois procédés de croissance : nanofiles, nanocolonnes, nanocônes, nanopeignes. Mais par PLD on obtient des réseaux de nanocolonnes et nanocônes autoformées, alignées, verticales, homogènes dont les qualités structurales sont excellentes y compris sur des substrats avec lesquels ZnO n'a pas un bon accord paramétrique. Ces nanostructures sont obtenues sans utiliser de catalyseur. Leurs propriétés d'émission sont aussi excellentes avec des bandes de défauts, observables en PL, relativement faibles. La faisabilité de composants à base de nano ZnO a été démontrée grâce à la réalisation d'une nanoLED de type n-nanoZnO/ p-Si, mais aussi par la reprise de croissance de GaN sur des nanocônes de ZnO/Si qui agissent comme une couche antireflet (~95% d'absorption de la lumière visible). L'étude a aussi porté sur la fabrication d'un composant transistor couche mince dont les caractéristiques de transfert rectifiante ont été obtenues.

RESUMÉ DE LA THÈSE EN ANGLAIS :

The objective of this work was to grow, study & control the properties of ZnO thin films & nanostructures. Three growth processes were studied: Metal-Organic Chemical Vapour Deposition (MOCVD), Pulsed Laser Deposition (PLD) & Physical Vapour Transport (PVT). The substrates used were: c-Al2O3; Si, ZnO, steel, mylar & paper. The ZnO was characterized using scanning electron microscopy, photoluminescence, cathodoluminescence, X-ray diffraction & optical reflectivity. A very wide range of ZnO nanostructures was observed, including nanorods, nanoneedles, nanocombs & some novel structures. Self-forming arrays of vertically aligned nanostructures (moth-eye nanocones & nanocolumns (vertical & broadening)) could be obtained by PLD without the use of a catalyst. The various characterisation techniques indicated that these arrays were significantly better crystallized & more highly oriented than those grown by PVT/MOCVD. The feasibility of devices was also demonstrated. A nanoLED (n-nanoZnO/p-Si) had a rectifying I/V characteristic & gave blue/white electroluminescence. Moth-eye coatings on Si, resembling black-silicon, were used as templates for the growth of GaN by MOCVD. Angular-dependent specular reflection indicated that the GaN/ZnO nanostructures were broadband antireflection coatings with < 1% reflection over the visible spectrum for incidence angles < 60°. A back-gate geometry ZnO/Si3N4/SiO2/Si transparent thin film transistor was fabricated. It demonstrated a rectifying transfer characteristic, hard saturation & enhancement mode operation. Id was in the mA range & the VON was ~ 0V. Finally, conductive Amorphous Oxide Semiconductor ZnO was grown at RT on paper & mylar.